*Università degli Studi di Pavia*

*Dipartimento di Scienze della Terra e dell'Ambiente*

SCUOLA DI ALTA FORMAZIONE DOTTORALE

MACRO-AREA SCIENZE E TECNOLOGIE

DOTTORATO DI RICERCA IN SCIENZE DELLA TERRA E DELL'AMBIENTE

**Elisabetta Marchionda**

# Facies analysis and stratigraphic-sedimentological modelling of the Upper Jurassic Arab Formation (onshore field, Abu Dhabi, UAE)

Anno Accademico 2016-2017
Ciclo XXX

Coordinatore
Prof. Roberto Sacchi

Tutors
Prof. Andrea Di Giulio
Dr. Andrea Ceriani

Co-tutors
Dr. Fadi H. Nader
Dr. Rémy Deschamps

# CONTENTS

**FIGURES AND TABLES LIST …….. v**

**ABSTRACT…… ix**

**RIASSUNTO…….. xi**

## Chapter 1

**INTRODUCTION……. 1**

1.1 General introduction and aims of the work…….. 1

1.2 Data set acquisition, elaboration and fundings……...…….. 3

1.3 Thesis outline…… 4

## Chapter 2

**GEOLOGICAL BACKGROUND……...…… 7**

2.1 The Arabian Plate tectonic framework…….. 7

2.2 The United Arab Emirates structural assessment and the field of study…….. 9

2.3 The present-day of Abu Dhabi (UAE)……... 12

2.4 The Upper Jurassic stratigraphic scheme of the Abu Dhabi region……... 13

2.4.1 Previous stratigraphic studies on the Arab Fm. in the onshore Abu Dhabi… 16

2.5 Diagenesis of the Arab Fm. D Member in the onshore Abu Dhabi field…….. 18

2.5.1 The Arab D Member reservoir quality evolution…… 20

## Chapter 3

**FACIES ANALYSIS AND FIELD-SCALE CONCEPTUAL DEPOSITIONAL MODEL…….. 23**

3.1 Methods……. 23

3.1.1 Core and thin section analysis……. 23

3.1.2 Well log analysis and correlations…….. 24

3.2 Results…… 26

3.2.1 Facies associations……..…… 26

3.2.2 Field-scale stratigraphy and sedimentary evolution of the Arab Fm. …… 35

3.2.3 Well correlations……. 39

3.2.4 Lateral changes and paleofacies maps…… 42
3.3 Discussion……. 44
3.3.1 Progradational trend……. 44
3.3.2 Field-scale temporal and spatial evolution……. 45
3.3.3 A single interpretation? ……. 47
3.3.4 The Arab Fm. cyclicity: local controls…… 48
3.3.5 A regional overview: a new piece of the puzzle…… 49
3.4 Conclusions…… 51

# Chapter 4

**3D FORWARD MODELLING OF A PROGRADING CARBONATE RAMP: A QUANTITATIVE ANALYSIS…… 53**
4.1 Model set up……... 53
4.1.1 3D stratigraphic forward modelling…… 53
4.1.2 Workflow…… 54
4.2 Dataset and inputs…….. 56
4.2.1 Sediment classes and carbonate production…… 56
4.2.2 Age model, eustasy and greenhouse conditions…….. 57
4.2.3 Domain and basinal settings…… 58
4.3 Results…… 60
4.3.1 The Reference Model (REF)…….. 60
- *Facies distribution*…… 60
- *Calibration: simulated vs. real wells*……..……. 63

4.3.2 Sensitivity analysis……. 64
- *Initial bathymetry*…….. 66
- *Subsidence*……..... 68
- *Carbonate production*…… 70
- *Transport parameters*…… 70
- *Evaporites calibration*…….. 71

4.4 Discussion…….. 72
4.4.1 Salt dome evolution: two depositional scenarios…… 72
4.4.2 Subsidence and carbonate production rates…… 75
4.4.3 Cyclicity and evaporites precipitation…… 78

4.4.4 Conceptual vs. 3D stratigraphic forward model……. 80
4.5 Conclusions…… 81

# Chapter 5

**CONCLUSIONS…… 83**

# Chapter 6

**FUTURE WORKS……. 87**
6.1 The predictive power of the model: blind well tests…….. 87
6.2 Regional forward stratigraphic assessment…… 87
6.3 Thermal-burial history and basin modelling: new insights on the diagenetic impact… 88

**ACKNOWLEDGEMENTS…….. 91**
**REFERENCES……... 93**

# Appendix

**Appendix 1 - Core logging…… 109**
**Appendix 2 - Thin sections analysis……. 111**
**Appendix 3 - Sensitivity analysis……. 123**
**Appendix 4 - 3D forward modelling…… 133**

# FIGURES AND TABLES LIST

**CHAPTER 2**

**Figure 2.1** *Map of the major tectonic elements of the Arabian Plate (simplified from Konert et al., 2001)*……...7

**Figure 2.2** *List of the major tectonic events occurred in the Phanerozoic on the Arabian Platform (simplified and modified from Haq and Al-Qahtani, 2005)* ……..…….……. 8

**Figure 2.3** *Main tectonic provinces of the UAE (redrawn and modified from Alsharhan, 1989)*…… .10

**Figure 2.4** *A) Paleofacies map of the Late Jurassic (Kimmeridgian to Tithonian), during the deposition of the Arab Fm. (modified and simplified from Ziegler, 2001 and from Hughes, 2004b). Approximate location of the field of study southward Abu Dhabi. B) Sketch map of the field of study. The location of the five wells available for this study is circled in red*……. 11

**Figure 2.5** *General map of the sedimentary facies along the coastal areas of the Abu Dhabi Emirate (simplified from Alsharhan and Kendall, 2011)*……... 13

**Figure 2.6** *Summary of the stratigraphic column of the Upper Jurassic of the Abu Dhabi region (modified from Al-Silwadi et al., 1996). The ages of the Arab Fm. are suggested from the orbital forcing model of the AROS J/C Chart and following updates (Al-Husseini and Matthews, 2008; Al-Husseini, 2008; Al-Husseini, 2009)*…..…...14

**Figure 2.7** *Biozones identified for the Arab Fm. (simplified and modified from Al-Silwadi et al., 1996)*… …… 15

**Figure 2.8** *Facies distribution across the wells studied in Lawrence et al., 2015 (modified from Lawrence et al., 2015).* ……. 17

**Figure 2.9** *Paragenetic sequence from Morad et al. (in review) for the Arab Fm. in relation to burial and tectonic events (? = uncertain event; from Morad et al. in review)*…… …….. 20

**CHAPTER 3**

**Table 3.1** *Major characteristics of the facies recognized, including lithology, structures, genetic processes and depositional environment interpretation*…… 27

**Figure 3.1** *Core pictures. Some examples of the identified facies.* …….. 30

**Figure 3.2** *Optical photomicrographs in plane polarized light. Some examples of the identified facies*…….. 31

**Figure 3.3** *Schematic carbonate ramp model with the prevalent textures of the Arab Fm. for the different environments encompassed (modified from the depositional model in Morad et al., 2012)*……. 32

**Figure 3.4** *A) Core log drawing of well A4. B) Highlight of the upper part of the core drawing of well A4. C) Legend comprehensive of all the symbols used in all the Figures of this chapter*……. 32

**Figure 3.5** *Micropaleontological distribution in the well A1, A2, A3, A5. The biozones refer to the work of Al-Silwadi et al. (1996). Optical photomicrographs of some samples of the main biota: A) B;) C); and D*…….. 38

**Figure 3.6** *Correlation panel CP1 encompassing wells A1, A5 and A4*…… 40

**Figure 3.7** *Correlation panel CP2 encompassing wells A2, A3 and A4*…… 41

**Figure 3.8** *Schematic summary of the Arab Fm. representing the eleven transgressive surfaces, the subaerial unconformity, and the division in cycles and the top of the Stromatoporoid Zone. The vertical facies distribution is pictured in a synthetic/schematic column*……42

**Figure 3.9** *Paleofacies maps showing the distribution of the facies associations through time across the area. The maps are pictured in correspondence to the eleven transgressive surfaces and the subaerial unconformity identified within the Arab Formation*……. 43
**Figure 3.10** *Progradation of the system towards southwest at time step TS4 and SU5. The direction of progradation can be locally different and oriented towards many directions (little red arrows TS3), but comprises into the southwest main direction of progradation (black arrows TS3, TS4, And SU5)*…….. 45
**Figure 3.11** *Well panel representing the intra-cycle thickness variations*……46
**Figure 3.12** *A) Correlation of the Stromatoporoid Zone from the "offshore transect" (redrawn, modified and simplified from Al-Silwadi et al., 1996) and the onshore studied field. B) Interpretation of the paleofacies distribution at the top of the S.Z. of the Arab Fm. in a regional overview*……. 50

**CHAPTER 4**
**Table 4.1** *List of the Reference Model (REF) input parameters*…… 55
**Figure 4.1** *A) Curves of production versus depth for each sediment class. B) Composite eustatic curve computed in the simulations (lilac curve).* ……. 57
**Figure 4.2** *Bathymetry, thickness and subsidence maps inserted in the Reference (REF) Model.* …….. 59
**Figure 4.3** *3D representation of the Reference Model (REF), according to different simulated output parameters: A) bathymetry; distribution of the sediment classes: B) Carbo_Grains; C) Carbo_Mud; D) Carbo_Evapo; variations in E) wave energy; and F) salinity*…… 61
**Table 4.2** *Properties of the different simulated facies (SF)*…….. 62
**Figure 4.4** *Distribution of the simulated facies in the Reference Model.* ……. 63
**Figure 4.5** *Comparison between the real (R.W.) and simulated wells (S.W.)*…… 63
**Table 4.3** *List of the models presented in the thesis with the values assigned at the main inputs* …… 64
**Figure 4.6** *A) Bathymetry and subsidence maps inserted in the Salt Dome (SD) model, and the 3D bathymetry output. B) Diagram comparing the SD and REF models. On the right: cross section cutting the SD model across the five wells, picturing the distribution of facies*……... 67
**Figure 4.7** *A) Diagrams that compares the models in which the subsidence (A) and the Carbo_Grains production (B) were tested. The S14 and the G218 models (highlighted in yellow) gave a higher TOT value (higher calibration). On the right: cross section cutting the S14 model (A) and the G218 model (B) across the five wells, picturing the distribution of facies*…… 69
**Table 4.4** *Different subsidence rates applied by the software for the simulations: S0, S12, SD, S14 and S26 (average between the wells values)*…… 69
**Figure 4.8** *Diagrams showing the percentages in average matches of the different macro environments considering the five available wells and the TOT values, according to the parameters tested: production rate of A) Carbo_Mud; B) Carbo_Evapo; and C) diffusion coefficients (transport). D) Comparison of the percentages of the matches between the total thickness of the simulated and real evaporites, testing the Carbo_Evapo production and the evaporation rate*…….. 71
**Figure 4.9** *Evolution of the output bathymetries and facies distribution in the REF and SD model*…….. 73
**Figure 4.10** *Evolution of the bathymetries and facies distribution of the model T0.01-0.05*……75

**Figure 4.11** *Simulated sedimentation rates for the three macro environments according to the different wells and their averages in the G218 model*…….. 77
**Figure 4.12** *A) Summary of the vertical stacking pattern of the Arab A-B-C in the real wells. B) Panel of correlation of the simulated wells (G218 model, Arab A-B-C)*…….. 78

**APPENDIX 1**
**Figure A11** *Core logs*…….. 109

**APPENDIX 2**
**Table A21** *Range chart of well A1*……... 114
**Figure A21** *Optical photomicrographs for well A1*…… 115
**Table A22** *Range chart of well A2*…….. 116
**Figure A22** *Optical photomicrographs for well A2*…… 117
**Table A23** *Range chart of well A3 (MD values corrected for core-log shift*)……. 118
**Figure A23** *Optical photomicrographs for well A3*…… 119
**Table A24** *Range chart of well A5*…….. 120
**Figure A24** *Optical photomicrographs for well A5*…… 121

**APPENDIX 3**
**Table A31** *Punctual matches for the simulations computed for well A1*……..126
**Table A32** *Punctual matches for the simulations computed for well A2*……. 127
**Table A33** *Punctual matches for the simulations computed for well A3*……..128
**Table A34** *Punctual matches for the simulations computed for well A4*……..129
**Table A35** *Punctual matches for the simulations computed for well A5*……... 130
**Table A36** *Matches for the total thicknesses of the evaporitic deposits*…….. ……... 130
**Table A37** *Averages for each macro environment between the five wells and the TOT value*……... 131

**APPENDIX 4**
**Figure A41** *S0 model*……133
**Figure A42** *S12 model*……. 134
**Figure A43** *S14 model*……. 134
**Figure A44** *S26 model*……..……135
**Figure A45** *G106 model*…….. 135
**Figure A46** *G206 model*…….. 136
**Figure A47** *G218 model*…….. 136
**Figure A48** *G318 model*…….. 137
**Figure A49** *M22 model*…… 137
**Figure A410** *M42 model*…….. 138
**Figure A411** *M46 model*…….. 138
**Figure A412** *M66 model*…….. 139

**Figure A413** *CE8 model*……...139
**Figure A414** *CE24 model*…… 140
**Figure 415** *E500 model*…… 140
**Figure A416** *E2500 model*…….. 141
**Figure A417** *T0.01-0.05 model*…… 141
**Figure A418** *T0.002-0.01 model*…….. 142
**Figure A419** *T0.005-0.025 model*…… 142

# ABSTRACT

This study aims to achieve, by means of qualitative and quantitative approaches, new stratigraphic and sedimentological insights on an ancient carbonate ramp, providing, as far as possible, robust models illustrating the temporal and spatial evolution of the depositional system in analysis.

The research is focused on the Upper Jurassic Arab Formation on a giant gas field, onshore Abu Dhabi (UAE), where five wells were investigated throughout different methodologies.

In the first part of the study a new field-scale conceptual sedimentary depositional model was built by means of: i) subsurface high-resolution facies analysis; ii) well correlations; and iii) paleofacies maps. The facies analysis was based on 540 m of cores and 277 thin sections. Eighteen facies were defined and grouped into five facies associations, representative of a shallow marine carbonate ramp. The depositional system ranges from outer ramp to supratidal/sabkha and intertidal environments, with a shoal complex protecting a lagoon. A micropaleontological analysis helped at defining the field-scale evolution of the different sedimentary environments through time and space. The results were integrated with well log data (Gamma Ray and Density-Neutron Log), and used to establish the stratigraphic architecture. The Arab Formation is characterized by a shallowing upward carbonates succession, punctuated in its upper part by the alternation with evaporitic deposits. Well correlations were useful to generate several new paleofacies maps corresponding to key stratigraphic surfaces identified within the succession. Different directions of progradation were detected suggesting a local topographic control on the deposition of the Arab Formation, due probably to syn-sedimentary salt diapirism. The cyclical arrangement of the facies associations and the peculiarities of this new model were discussed at regional scale, in order to propose a new paleogeographic scenario.

The second part of the research integrated and enhanced the new onshore field conceptual model with the use of a 3D forward diffusion-based dynamic modeling tool. Stratigraphic forward models are commonly used to investigate the global and local parameters that control the sedimentary deposition that are not usually quantified in conceptual models. In this study the modelling tool was used to: i) simulate the temporal shallowing upward trend and spatial evolution of a shallow marine carbonate ramp that represents the field-scale depositional scenario; ii) test by trial and error the response of the model to changes of the input parameters; and iii) quantitatively assess the main factors that affected the most the carbonate ramp depositional geometries and facies distribution. Twenty-one models were developed to

systematically test: the initial bathymetry, the subsidence, the carbonate production and the transport parameters. Twenty models illustrates a prograding shoal complex with a seaward relative deep domain (outer and mid-ramp deposits), and a landward shallow cyclical depositional pattern characterized by lagoonal/intertidal and supratidal environments.

All the simulations were calibrated in correspondence to the wells (control points) available in the studied area. This helped to verify and refine the calibration of the models in terms of resulting thickness and facies distribution. Various timing of salt movements in the substratum, subsidence and carbonate production rates, and controls on cyclicity were evaluated in order to discuss the geological consistency of the models.

The multi-attractive research, presented in this dissertation provides: i) an exhaustive case of study, calibrated on a field-scale, that could be successfully applied to other ancient and modern analogues for academic and/or hydrocarbon exploitation purposes; and ii) new results and interpretations pertaining to the Upper Jurassic Arab Formation, which includes one of the most economically important oil and gas reservoir in the world.

# RIASSUNTO

Questo studio ha lo scopo di ottenere, tramite un'analisi qualitativa e quantitativa, nuovi rilevanti risultati riguardo alla stratigrafia e sedimentologia di una successione di rampa carbonatica, sviluppando modelli che illustrino l'evoluzione temporale e spaziale del sistema deposizionale in esame.

La ricerca è stata incentrata sullo studio dell'Arab Formation (Tardo Giurassico) in un campo petrolifero nell'*onshore* di Abu Dhabi (UAE), dove cinque pozzi sono stati analizzati attraverso diverse metodologie.

Nella prima parte del lavoro, un nuovo modello concettuale a scala di campo è stato sviluppato per mezzo di: i) analisi di facies ad alta risoluzione; ii) correlazioni di pozzo; e iii) mappe di paleofacies. L'analisi di facies si è basata sullo studio di 540 m di carote e di 277 sezioni sottili. Diciotto facies sono state definite e raggruppate in cinque associazioni caratteristiche di un sistema di rampa carbonatica di mare basso. La rampa si estende da ambienti relativamente profondi (*outer ramp*) ad intertidali/sopratidali, con un complesso oolitico che protegge e racchiude una laguna. I risultati sono stati integrati con lo studio dei log di pozzo (Gamma Ray e Density-Neutron), utilizzati per definire l'architettura stratigrafica. L'Arab Formation è caratterizzata da una successione carbonatica *shallowing upward*, intervallata a depositi evaporitici nella sua parte superiore. Le correlazioni stratigrafiche tra i pozzi sono state indispensabili per generare diverse mappe di paleofacies in corrispondenza delle superfici stratigrafiche chiave identificate nella successione. Diverse direzioni di progradazione sono state individuate, dovute ad un controllo locale sulla topografia legato probabilmente alla risalita di duomi salini. L'arrangiamento ciclico delle associazioni di facies e le caratteristiche di questo nuovo modello sono state discusse a scale regionale, con lo scopo di proporre una nuova mappa paleogeografica.

La seconda parte della ricerca ha integrato e potenziato il modello concettuale, attraverso l'uso di uno strumento di modellizzazione *forward* tridimensionale basato su principi fisici di diffusione. I modelli *forward* di tipo stratigrafico sono comunemente usati per investigare i processi globali e locali che controllano i sistemi sedimentari, che non sono di solito quantificati nei modelli di tipo concettuale. In questa ricerca lo strumento di modellizzazione è stato usato per: i) simulare l'evoluzione temporale (trend complessivo *shallowing upward*) e spaziale di una rampa carbonatica di mare basso che rappresenta il sistema deposizionale in analisi; ii) testare la risposta del modello al cambiamento dei parametri di input; e iii) valutare in modo quantitativo i principali fattori che impattano sulle geometrie deposizionali e sulla

distribuzione delle facies. Ventuno modelli sono stati sviluppati testando sistematicamente: la batimetria iniziale, la subsidenza, la produzione di carbonato e i parametri di trasporto. Venti modelli illustrano la progradazione dello *shoal complex*, che divide la simulazione geologica in un dominio relativamente profondo verso mare e uno di acque basse verso terra, dove facies lagunari/intertidali e sopratidali sono ciclicamente alternate. Tutte le simulazioni sono state controllate in corrispondenza dei pozzi disponibili, allo scopo di verificare e migliorare la calibrazione dei modelli in termini di spessori e distribuzione delle facies. Movimenti salini nel *substratum*, tassi di subsidenza e di produzione carbonatica, e controlli sulla ciclicità sono stati valutati al fine di discutere la consistenza geologica dei modelli.

Il pluri-interessante lavoro presentato in questa tesi costituisce un'esaustiva analisi di un sistema di rampa carbonatica, che può essere applicata ad altri casi di studio analoghi, sia fossili sia recenti per scopi scientifici e/o industriali. Lo studio inoltre fornisce nuovi dati e interpretazioni riguardo l'Arab Formation, la quale include uno tra i *reservoir* di idrocarburi più importanti al mondo.

# Chapter 1

# INTRODUCTION

## 1.1 General introduction and aims of the work

Carbonate ramps are traditionally sites of interest in exploration activities looking for hydrocarbons sources and reservoirs (Burchette and Wright, 1992; e.g. Burchette et al., 1990; Palermo et al., 2010; Kietzmann et al., 2014). Facies distribution on ramps, and on carbonate platforms in general, is controlled by multiple factors such as relative sea-level changes, type of carbonate-producing biota, hydraulic energy, local tectonic, seafloor morphology, ecological parameters and climatic impact (Pomar, 2001; Pomar and Hallock, 2008; Pomar and Kendall, 2008; Pomar and Haq, 2016 with references therein). These parameters constrain the sediment production and distribution, giving rise to complex, diverse and heterogeneous depositional systems (see Pomar and Haq, 2016). The investigation of these controlling factors is a necessary challenge in order to deeply understand the vertical and lateral development of carbonate systems at the change of the different depositional conditions.

In this framework, this Ph.D. project has been designed in order to provide new qualitative and quantitative models concerning the evolution of an ancient carbonate ramp, deciphering how the depositional setting changes through space and time. The attention is given to unravel new sedimentological and stratigraphic insights into the study of the Upper Jurassic Arab Formation (Fm.; lithostratigraphic members A-B-C-D) in an onshore Abu Dhabi (UAE) field.

The Arab Fm. extends over a large area of the Arabian Platform and includes one of the most prolific Upper Jurassic reservoirs in the world (Alsharhan, 1989). The Arab D grainstones are the major producing reservoir in several giant fields, such as the Ghawar field (Saudi Arabia), the world's largest oil field (Durham, 2005; Lindsay et al., 2006; Al-Awwad and Pomar, 2015 with references therein).

In the United Arab Emirates (UAE), major reservoirs were discovered offshore and onshore Abu Dhabi (e.g. in the Arab Fm.), making the UAE the seventh-largest petroleum producer in the world (yr: 2017 www.eia.gov with references therein). The Arab Fm. was extensively studied, following various relevant discoveries, offshore Abu Dhabi (e.g. Azer and Peebles, 1995, Al-Silwadi et al., 1996; Lehmann et al., 2008; Morad et al., 2012). Yet, only a few publications are available for the onshore area concerning specifically the stratigraphy of the Arab Fm. (e.g. Grötsch et al., 2003; Lawrence et al., 2015), promoting primary this research.

The scope of this study was initially reached developing a new field-scale conceptual model based on an integrated workflow that combines core analysis and micropaleontological/petrographic thin section examinations with well log analysis. High-resolution cores and well-log studies are fundamental in order to understand the spatial and temporal evolution of a subsurface sedimentary system, reconstructing from 1D data conceptual depositional scenarios (e.g. Al-Awwad and Pomar, 2015; Abdolmaleki et al., 2016; Wang et al., 2016; Beigi et al., 2017).

In this study, the subsurface high-resolution facies analysis and well correlations allowed building several paleofacies maps that show the evolution of the Arab Fm. through time and space. Moreover, the detected biota allowed to assess the vertical recurrence of depositional environments and to interpret their evolution in the not drilled area. The new results were fundamental to discuss previous existent models scattered in the Abu Dhabi area, not only to highlight the differences, but to propose an innovative regional paleogeographic map.

Conceptual models may not fully investigate all the geological processes that rule the strata development and architecture, because of limited sedimentological observations, lacking in a quantitative evaluation of processes uncertainties and complexities (Warrlich et al., 2002; Burgess et al., 2006; Granjeon, 2010). To fill this gap, stratigraphic forward modelling can be applied to quantify and simulate geological processes and their interplay (Warrlich et al., 2002). The resulting stratigraphic simulations are commonly used in petroleum exploration and reservoir characterization to better predict reservoir plays distribution (Matthews and Frohlich, 1998; Nordlund, 1999; Griffiths et al., 2001; Shafie and Madon, 2008; Warrlich et al., 2008; Hawie et al., 2015; Huang et al., 2015; Hawie et al., 2016; Hawie et al., 2017).

In this project, DionisosFlow™ software package (Granjeon, 1997; Granjeon and Joseph, 1999) was used to model the step by step depositional evolution of the Arab Fm. carbonate ramp in the field of study and surrounding area. The 3D stratigraphic forward modelling was applied to systematically assess the key factors that control the deposition of the carbonate ramp and to determine the stratigraphic evolution and facies distribution of the Arab Formation. The models were calibrated on five available wells in the field of study and tested in accordance to the main controlling parameters in order to: i) evaluate the response of the model upon tuning/changing the values of the different inputs; ii) unravel which of the different bio-physico-chemical processes affected most the sedimentation of the Arab Fm.; and iii) further improve the geological consistency of the models.

This Ph.D. project provides a successful example of how an integrated workflow, that combines together traditional with cutting-edge methodologies, can help to unravel, in a qualitative and quantitative way, the spatial and temporal evolution of an ancient carbonate ramp, assessing the role played by the main controlling parameters. The resulting stratigraphic and sedimentological insights not only add novelty in the study of the Arab Fm., but could be extended to modern and ancient analogue carbonate successions. Moreover, this work can be potentially applied for further hydrocarbon exploitation and petroleum system assessment in the onshore studied field and in other fields presenting a similar depositional scenario.

The work of this thesis was carried out in synergy with my tutors, professors and researchers belonging to different institutions: the University of Pavia (Italy), the Khalifa University of Science and Technology - Petroleum Institute of Abu Dhabi (Abu Dhabi, UAE), the IFP Energies nouvelles (IFPEN, Rueil-Malmaison, France), and Al Hosn Gas (Abu Dhabi, UAE; now ADNOC Sour Gas). Moreover in parallel, a Ph.D. project is currently performed at the University of Oslo by Mr. Daniel Morad, entitled: "Burial diagenesis and thermochemical sulfate reduction in the Arab gas reservoirs - clues to control on $H_2S$ distribution", investigating the same field and wells used in this study. Between the two Ph.D. projects a constant exchange of knowledge and scientific discussions took place in these three years, enhancing the outcomes of both works.

## 1.2 Data set acquisition, elaboration and fundings

Core logging activity was performed in the ADCO cores lab in Abu Dhabi by me in teamwork with: Dr. Rémy Deschamps (IFPEN), Dr. Marta Gasparrini (IFPEN), Daniel Morad (University of Oslo), and Prof. Sadoon Morad (Khalifa University-Petroleum Institute).
Thin sections were analyzed with a polarizing microscope at the laboratories of IFPEN and University of Pavia by me under the supervision of Prof. Miriam Cobianchi (Unipv). I performed data elaboration, the 3D stratigraphic forward modelling, and sensitivity analysis at IFPEN and University of Pavia. All the necessary field-data (such as well log-tracks and internal reports) and samples were kindly provided by courtesy of Al Hosn Gas. The software DionisosFlow™ has been provided by Beicip-Franlab (Rueil-Malmaison, France) with a constant technical support (for all the details concerning the methodologies that I have applied see the dedicated sections in Chapter 3 and 4).

This Ph.D. project was funded by the Petroleum Institute of Abu Dhabi (Abu Dhabi, UAE) and University of Pavia (Italy).

## 1.3 Thesis outline

The chapters of this thesis are mainly based on two comprehensive papers prepared during the course of the Ph.D. that address the aims of the project:

- **Marchionda, E**., Deschamps, R., Cobianchi, M., Nader, F.H., Di Giulio, A., Morad, D.J., Al Darmaki, F., Ceriani, A., 2018. Field-scale depositional evolution of the Upper Jurassic Arab Formation (onshore Abu Dhabi, UAE).
  Marine and Petroleum Geology, vol. 89, part 2, pp. 350-369 http://dx.doi.org/10.1016/j.marpetgeo.2017.10.006

- **Marchionda, E**., Deschamps, R., Nader, F.H., Di Giulio, A., Al Darmaki, F., Ceriani, A.. 3D stratigraphic forward modelling of a carbonate ramp: a quantitative field-scale analysis of the Arab Formation (Upper Jurassic, onshore Abu Dhabi, UAE). *Submitted to Sedimentary Geology*

The introduction and the geological setting of the two papers were unified and implemented in order to provide a common thread between the two main parts of the research.

**Chapter 1** contains an overview on the dissertation, outlining the aims and the achievements. The chapter explains the structure of the thesis, addressing the reader to the different sections.

In **Chapter 2** a summary of the geological background is provided. The aim is to present to the reader the principal notions about: i) the tectonic evolution of the Arabian Platform and the UAE; ii) the Late Jurassic stratigraphy of the Abu Dhabi region, useful for the comprehension of all the work; and iii) the principal literature review concerning the Arab Formation stratigraphy in the onshore of Abu Dhabi. In addition, a closer view of the present-day of Abu Dhabi is briefly reported in order to provide an example of a modern analogue of the studied system.
Sections **2.5** and **2.5.1** contain a very short summary of the detailed study on the diagenesis of the Arab Fm. D Member that is the outcome of the Ph.D. project by Mr. Daniel Morad at the

University of Oslo. These sections aim to give a brief overview of the diagenetic alterations that affected the D Member of the Arab Formation.
The results of this companion study are the content of the paper:

- Morad, D., Nader, F.H., Gasparrini, M., Morad, S., Rossi, C., **Marchionda, E.**, Al Darmaki, F., Martines, M., Hellevang, H.. Comparison of the diagenetic and reservoir quality evolution between the anticline crest and flank of an Upper Jurassic carbonate gas reservoir, Abu Dhabi, United Arab Emirates. *In review at Sedimentary Geology*

The main analytical parts and the related interpretations of this dissertation are enclosed in **Chapter 3** and **4**, which contain the major part of the two papers prepared.

**Chapter 3** is focused on the facies analysis of the Arab Fm. and the field-scale conceptual model. The different methods applied are explained (core logging, petrography of thin sections and well log analysis). Subsequently, the results are reported and discussed at the field-scale and, eventually, in a regional overview.

The 3D stratigraphic forward modelling is reported and discussed in **Chapter 4** that starts highlighting the model set up and the simulations workflow. After the presentation of the various inputs, the resulting models are listed and discussed according to the tested parameters.

**Chapter 5** concludes and summarizes the work presented in this dissertation, focusing on the main achievements reached.

Research never ends! Possible further continuations of the project are enclosed in **Chapter 6**.

Additional material is enclosed in the Appendices that was not possible to insert in the concise and fluid structure of the papers on which this thesis is based on. The Appendices act as a "data repository" containing significant data achieved and produced during the Ph.D. fundamental to extrapolate the essential scientific insights of the two papers prepared.
**Appendix 1** reports the core drawings of all the wells analyzed in the cores lab. **Appendix 2** includes the range charts and several additional photomicrographs of the thin sections

analyzed. The data sheets of the sensitivity analysis are reported in the **Appendix 3**. The main inputs and some outstanding outputs of the simulated models are pictured in the **Appendix 4**.

# Chapter 2

# GEOLOGICAL BACKGROUND

## 2.1 The Arabian Plate tectonic framework

The Arabian Plate tectonic framework includes the Arabian Shield (with extensive basement exposures; Stern and Johnson, 2010), the Arabian Platform (with a Phanerozoic succession; Stern and Johnson, 2010) and the surrounding sedimentary basins (Haq and Al-Qahtani, 2005). The Arabian Plate (Figure 2.1) is characterized by the three principal types of tectonic boundaries:

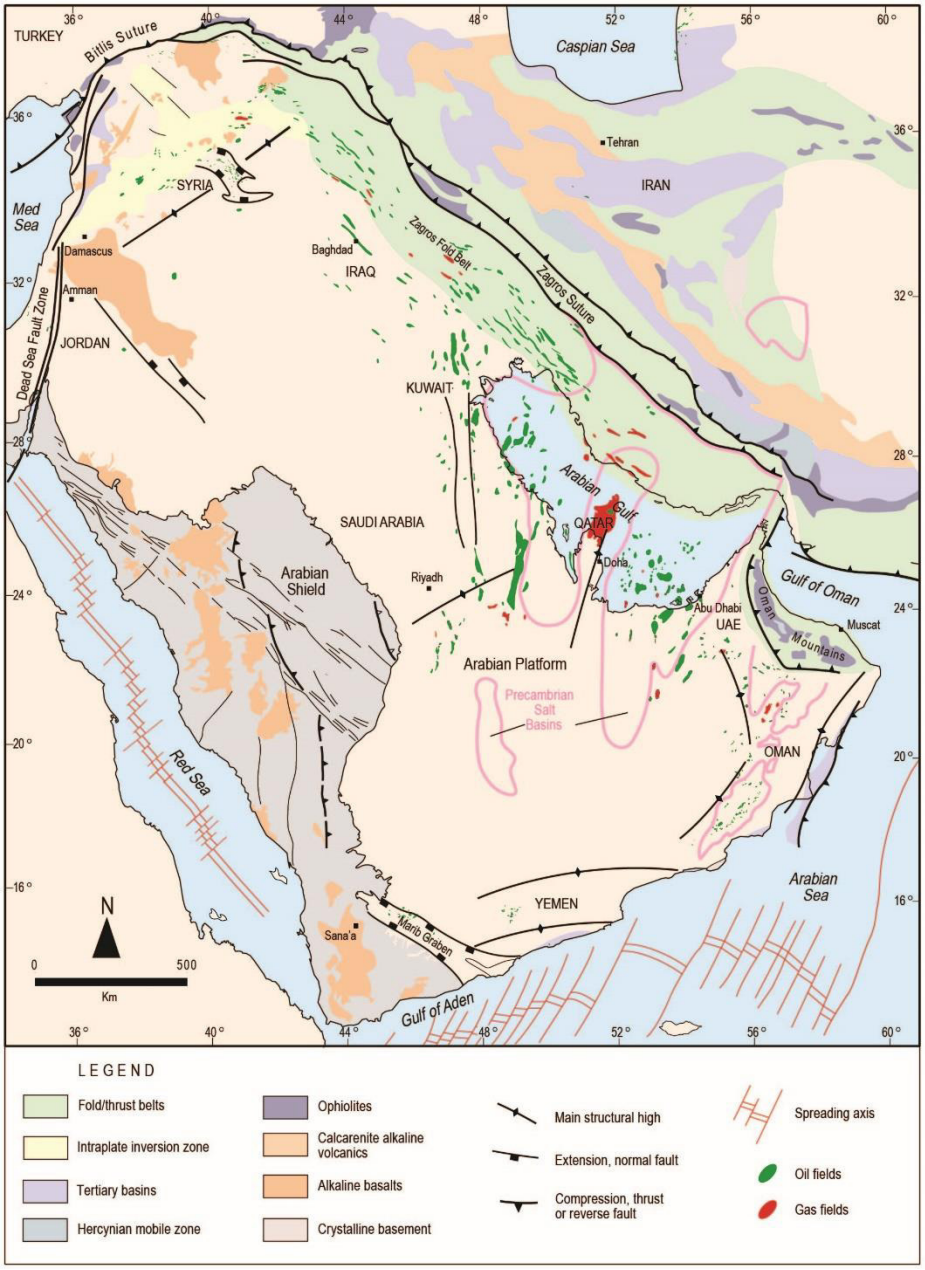


**Figure 2.1** *Map of the major tectonic elements of the Arabian Plate (simplified from Konert et al., 2001).*

i) extensional, due to rifting in the Gulf of Aden and Red Sea (in the south and west); ii) compressional, related to the Arabian Plate convergence and collision with Eurasia, giving rise to the Taurus and Zagros (in the north and northeast) and to the Oman Mountains (in the southeast); iii) transform, resulting from the northward strike-slip displacement of the Arabian Plate along the Levant fault zone (Dead Sea) in the west (Beydoun, 1998; Konert et al., 2001). The tectonic history of the Arabian Plate started in the Proterozoic and was characterized by a series of structural deformation (summarized in Figure 2.2) alternated with relative quiescent time periods (Haq and Al-Qahtani, 2005).

| System/Series | Structural Event → | Subsequent Arabian Plate Effects |
|---|---|---|
| Late Precambrian | Najd shear-zone-related rifting begins | Development of rift salt basins |
| Early Cambrian | Subsidence starts after peneplanation | Transgressions of the Platform in Late Cambrian and Early Ordovician |
| Latest Devonian | 'Hercynian' Orogeny begins on Arabian Plate | Multiple phases of compression and block faulting. Widespread inversion, erosion of several km of sediments on the Platform |
| Latest Carboniferous | End of 'Hercynian' Orogeny on Arabian Plate | Plate tilts gently to the northeast |
| Late Permian | Neo-Tethys opens and the NE passive margin begins to subside | Transgression and beginning of dominantly carbonate sedimentation over the Platform (tropical latitude) |
| Late Early Jurassic | Rifting starts in eastern Mediterranean and western margin of the Plate | Uplift of western margin of the Plate, beginning of a passive margin along northwestern margin of the Plate |
| Late Middle - Early Late Jurassic | Differential intraplate subsidence + global sea-level rise | Several intrashelf basins on the Platform |
| Early Cretaceous | South Atlantic begins to open | Plate tilts more to the east and dominant sediment transport is now from west to east. |
| Late Cretaceous | Ophiolite obduction along NE margin begins | Fault reactivation and uplift of NE margin of Platform |
| Early Paleocene | Ophiolite obduction ends | Erosion along NE margin of the Platform |
| Late Eocene | Closure of Tethys Seaway | Arabian Plate begins its collision with Asia and tilts again to the northeast |
| Late Oligocene/Miocene | Gulf of Aden and Red Sea starts to open | Eastern branch of Tethys closed by this time |

**Figure 2.2** *List of the major tectonic events occurred in the Phanerozoic on the Arabian Platform (simplified and modified from Haq and Al-Qahtani, 2005 according to the papers reported in this chapter).*

From Late Ordovician to Early Devonian, the Plate resided at relative high latitudes and it was affected (during Late Ordovician) by a glaciation with related evidences on the Arabian Shield such as broad-deeply incised subglacial valleys (Konert et al., 2001, with references therein; Haq and Al-Qahtani, 2005). During Late Devonian-Late Carboniferous the Hercynian

orogeny widely affected the Arabian Plate, with multiple phases of compression and block faulting (Haq and Al-Qahtani, 2005).

The post-Hercynian period (until Turonian) was characterized by stable conditions on the Arabian Platform (Murris, 1980), with the onset (late Permian) of dominant carbonate deposition, subsequent to the opening of the Neo-Tethys ocean in the east and the formation of a passive margin along most of the boundary in the northeast of the Arabian Plate (Murris, 1980; Haq and Al-Qahtani, 2005). The stretching of the crust caused an increase in the accommodation space (Konert et al., 2001). By Permian times, tropical latitudes were reached (Haq and Al-Qahtani, 2005) and maintained during the Mesozoic and Cenozoic, where organic productivity and carbonate deposition were dominant (Beydoun, 1998). During late Middle-early Late Jurassic (Callovian-Oxfordian) several scattered intrashelf basins developed on the Arabian Platform (four according to Ziegler, 2001), as result of differential intraplate subsidence coupled with a global sea-level rise (Murris, 1980; Ziegler, 2001; Al-Suwaidi and Aziz, 2002; Hughes, 2004b). These shallow basins favored water density stratification, with euxinic conditions and subsequent conservation of organic matter; on the margins, carbonate reservoir rocks were deposited, and periodic evaporites and shales sealed the area (Murris, 1980; Beydoun, 1998).

The exceptional combination of these petroleum system elements (source-reservoir-seal) in the Jurassic (and Paleozoic) made the Arabian Peninsula one of the major hydrocarbon-producing province in the world (Pollastro, 2003).

The stable conditions were interrupted (Late Cretaceous, Turonian to Maestrichtian; Murris, 1980) by the convergence between the Arabian and Asian Plates with the obduction of the Neo-Tethys ophiolites along the margin in the northeast of the Arabian Plate (Haq and Al-Qahtani, 2005). The continuous convergence between the Arabian Plate and Eurasia (i.e. Zagros orogeny) resulted in the progressive closure of the eastern portion of the Neo-Tethys seaway, completed by the Late Oligocene, following the collision with the Asian Plate started in the Late Eocene (Haq and Al-Qahtani, 2005). In the Mid-Cenozoic/Miocene, the opening of the Red Sea and Gulf of Aden set the separation between Arabian and African Plate (Glennie, 2010).

## 2.2 The United Arab Emirates structural assessment and the field of study

The United Arab Emirates (UAE; Figure 2.3) are located within the Arabian Platform, and are characterized by an intracratonic basin (passive plate-margin region), including Abu Dhabi and part of Dubai regions (Alsharhan, 1989).

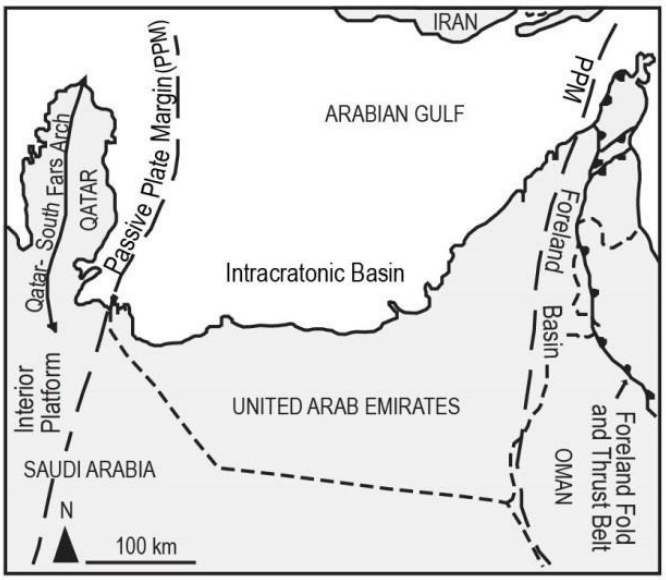


**Figure 2.3** *Main tectonic provinces of the UAE: the intracratonic basin (passive plate-margin region) and the foreland basin and adjacent foreland fold- and thrust-belt region (redrawn and modified from Alsharhan, 1989).*

This basin is bounded to the northwest by the Qatar-South Fars Arch (a broad regional high; Murris, 1980), and to the east by the foreland basin and adjacent foreland fold- and thrust-belt region of onshore northern UAE and Oman (Alsharhan, 1989). Large, gentle folds with flanks less than 5° characterize the intracratonic basin and are the results of: i) differential regional subsidence; ii) uplift along deep-seated basement faults; and/or iii) deep-seated diapiric movements of Eocambrian salt (Alsharhan, 1989; Alsharhan and Scott, 2000).

The foreland fold- and thrust-belt region shows different tectonic styles. The basin is defined by a foreland sequence following a rift margin sequence, where the Late Cretaceous ophiolite nappes are stacked onto the old rifting of the Arabian continental margin (Alsharhan, 1989).

The Mesozoic-Cenozoic structural evolution of the UAE is related to the opening (Permian) and closure (Late Cretaceous-Paleogene) of the Neo-Tethys (Alsharhan, 1989; Alsharhan and Scott, 2000). The tectonic deformations combined with eustatic fluctuations asserted the control on the sedimentation mainly characterized from Permian to Holocene by deposition of carbonates on an epeiric shelf (Alsharhan, 1989).

The studied field is located onshore, southward Abu Dhabi City (Figure 2.4), where five wells were made available for this research (by courtesy of Al Hosn Gas). According to the paleofacies maps of Murris (1980), Al-Husseini (1997) and Ziegler (2001), the field is located in one of the intrashelf basins mentioned above, specifically in the south-eastern margin of the so-called Rub' Al Khali basin (Figure 2.4) according to Al-Awwad and Collins (2013) and Al-Awwad and Pomar (2015). From a structural point of view, the field lies on a northeast-southwest trending anticline that started to develop during Early Cretaceous with its climax in the Late Cretaceous (Alsharhan and Nairn, 1997). The northeast-southwest fold trend could be linked to the Late Tertiary Oman overthrusting, occurred during the Zagros Mountains folding (Alsharhan and Scott, 2000).

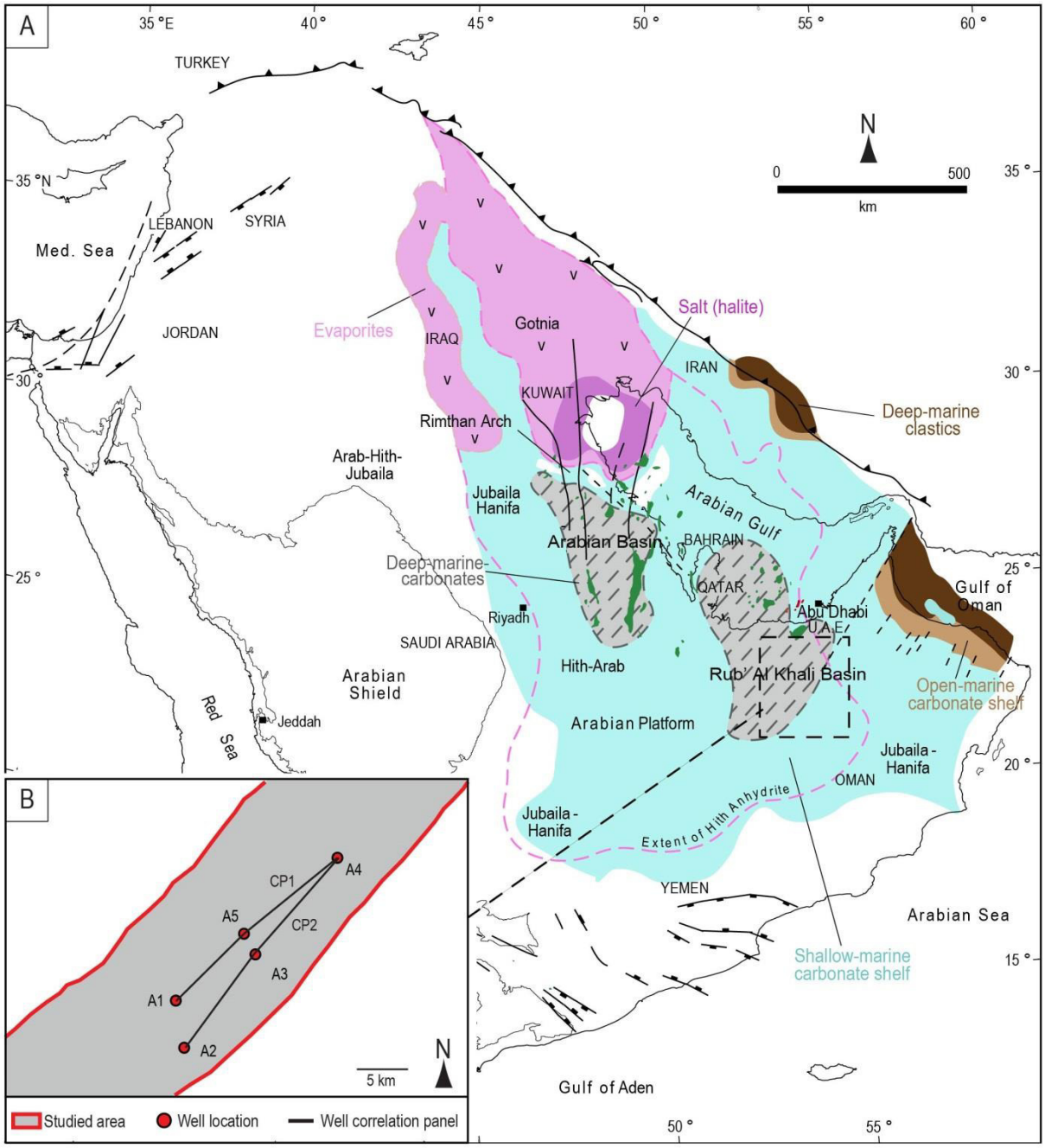


**Figure 2.4** *A) Paleofacies map of the Late Jurassic (Kimmeridgian to Tithonian), during the deposition of the Arab Fm. (modified and simplified from Ziegler, 2001 and from Hughes, 2004b). Some of the main fields on the Arabian Platform are pictured in green and red. The dashed-line rectangle represents the southward Abu Dhabi area where the field of study (frame B) is inside somewhere located (on purpose undefined). The names of the two intrashelf basins (Arabian and Rub' Al Khali) are gathered from Al-Awwad and Collins, 2013 and Al-Awwad and Pomar, 2015. B) Sketch map of the field of study shaped on a northeast-southwest anticline structure. The studied area borders are underlined in red. The location of the five wells available for this study is circled in red. The black lines represent the two transects encompassed by the well correlation panels CP1 (Figure 3.6) and CP2 (Figure 3.7).*

## 2.3 The present-day of Abu Dhabi (UAE)

The present-day ramp system of the southern Arabian Gulf is considered as a modern analogue for the Arab Fm., due to its similar alternation of shallow marine carbonates and evaporites (Alsharhan and Kendall, 2003; Alsharhan and Kendall, 2011). The UAE coast runs for around 600 km in the southeastern of the Arabian Gulf between Qatar Peninsula and Oman and it is dominated by relative pure carbonates, local evaporites, and minor siliciclastic components (Alsharhan and Kendall, 2003; Kendall and Alsharhan, 2011a).

An arid sub-tropical climate influences the UAE region: on the coastline, humidity percentages values range from 40% for the day to 90% for the night, with temperatures of 28-45 °C in summer, and around 12 °C in winter (Kendall and Alsharhan, 2011b). Strong winds, high temperatures, and low rain precipitation (less than 40 mm/yr) are the causes of significant evaporation (124 cm/yr) and high salinity (40-50‰ in the shallow area of the UAE, 60-70‰ in lagoon and embayments; Alsharhan and Kendall, 2003, with references therein).

Schematically, the UAE Arabian Gulf sedimentary system is characterized by seaward reefs, islands and tidal delta enclosing inner saline lagoons and supratidal evaporite/carbonates flats and sabkhas (Kendall and Alsharhan, 2011b). The Holocene facies belts of Abu Dhabi comprise: i) different types of shallow marine carbonates such as coral and coralline algae, oolitic sand, grapestones and pellets, carbonate mud and pellets, molluscan sand, and cyanobacterial mats; ii) supratidal evaporites; and iii) aeolian sands (Kendall and Alsharhan, 2011a). The Abu Dhabi coastal area is divided in three main geomorphological provinces (Figure 2.5): the open Khor Al Bazam lagoon and seaward bank, the Al Rufayq – Bu Sharah Shelf and channel region, the Abu Dhabi barrier island and protected lagoon (Kendall and Alsharhan, 2011a)

Five major environments can be detected: open marine shelf, offshore bank-shoal/channel and barrier island system, lagoons, coastal terrace, mainland coastal plain/sabkha (Kendall and Alsharhan, 2011b). The marine geomorphologies are the results of waves, currents, and biological processes (Kendall and Alsharhan, 2011a). According to these authors: waves and currents mainly shape intertidal sand flats, located on shoals, the offshore break, and coastal terrace. Currents mainly model tidal channels, that cut the offshore banks, shoals and channels area, and between barrier islands (Kendall and Alsharhan, 2011a). The biological activity is giving rise to corals growth, seaweed covered areas, cyanobacterial flats, and mangroves areas (Kendall and Alsharhan, 2011a). Sabkha barriers and plains are listed as marine and subaerial

features; coastal dunes, hills and alluvial fans characterized the subaerial geomorphologies (Kendall and Alsharhan, 2011a).

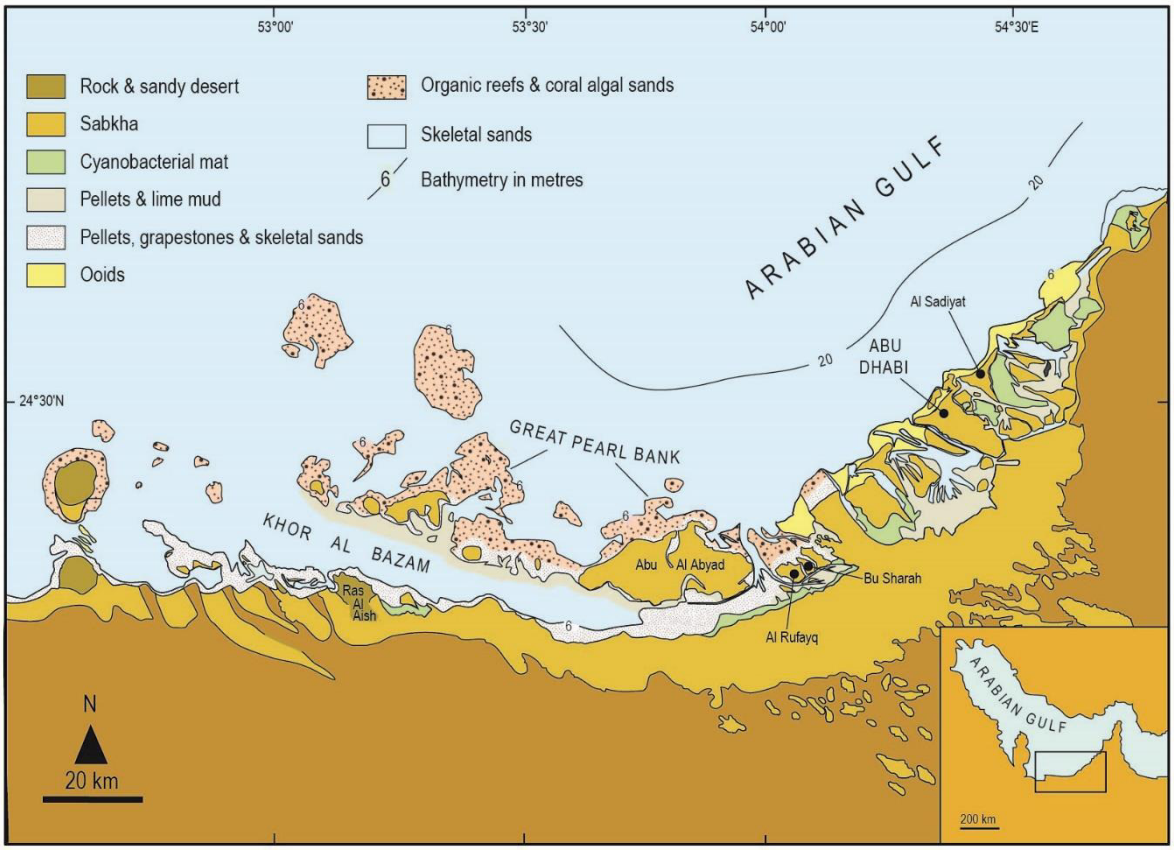


**Figure 2.5** *General map of the sedimentary facies along the coastal areas of the Abu Dhabi Emirate. The localities of the three main geomorphological provinces are indicated (simplified from Alsharhan and Kendall, 2011).*

## 2.4 The Upper Jurassic stratigraphic scheme of the Abu Dhabi region

During Late Jurassic, a widespread deposition of predominantly shallow marine carbonates occurred on the Arabian Platform (Ziegler, 2001) characterized by cyclic deposition of carbonates and evaporites of the Arab Fm. that filled the intrashelf basin. In the Abu Dhabi region, the Arab Fm. conformably overlays the Diyab Fm., and it is overlain by the Hith Fm. (Alsharhan, 1989). Different nomenclatures are used in literature to describe the different units forming the Arabian Platform sedimentary succession. The present thesis adopts the stratigraphic nomenclature reported in works such as Alsharhan and Nairn (1997), Al-Silwadi et al. (1996), and Grötsch et al. (2003).

The simplified stratigraphic scheme of the study area is summarized, from base to top, as follows (Figure 2.6):

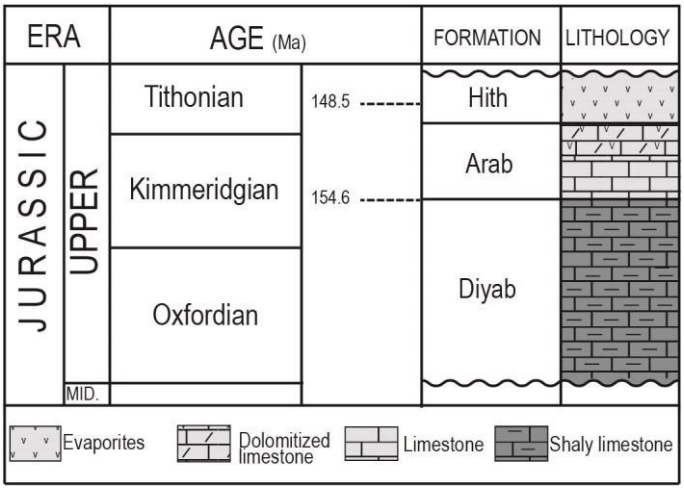


**Figure 2.6** *Summary of the stratigraphic column of the Upper Jurassic of the Abu Dhabi region (modified from Al-Silwadi et al., 1996). The ages of the Arab Fm. are suggested from the orbital forcing model of the AROS J/C Chart (Al-Husseini and Matthews, 2008) reported in the Middle East Geological Time Scale (Al-Husseini, 2008), and in the Al-Husseini (2009) updates. The age collocation is approximated and not on scale.*

- DIYAB FM. (Oxfordian-Early Kimmeridgian): the lower part consists of highly radioactive/clean mudstones, containing abundant organic matter. The middle part is made up of mudstones/wackestones in the western and central Abu Dhabi area, while in the eastern Abu Dhabi oolitic, peloidal, bioclastic grainstones/packstones/wackestones are recorded, including the occurrence of stromatoporoids, corals, green algae and foraminifera (Al-Suwaidi et al., 2000). The upper part is mainly characterized by limestones rich in organic matter (Alsharhan and Nairn, 1997). The Diyab carbonate sediments enclosed the Abu Dhabi region intrashelf basin, causing restricted water circulation (Al-Suwaidi et al., 2000). The high content of preserved organic matter made the Diyab Fm. to be the major source rock for the Jurassic and Lower Cretaceous reservoirs in the UAE (Alsharhan and Nairn, 1997). The Diyab Fm. is also called Dunkhan Fm. in onshore Abu Dhabi, and the Hanifa (Qatar) and Jubaila Fms. (Saudi Arabia) are its lateral equivalent (Alsharhan and Nairn, 1997; Al-Suwaidi et al., 2000). Generally, the thickness of the Diyab Fm. ranges from 260 to 313 m (853-1027 ft; Alsharhan and Nairn, 1997). In the southern onshore Abu Dhabi, it can reach up to 395 m (1300 ft; Al-Suwaidi et al., 2000).
- ARAB FM. (Kimmeridgian-Early Tithonian): it consists of a cyclic sequence of shallow marine carbonates and evaporites (Alsharhan and Nairn, 1997), deposited during a period of overall sea level rise (Alsharhan and Magara, 1995; Ziegler, 2001) and arid climatic conditions (Alsharhan, 1989). The well type section of the formation is the Dammam-7 in eastern Saudi Arabia, described by Powers et al. (1966), where the Arab Fm. is divided in four members called Arab A-B-C-D (from top to bottom), with the D Member is considered as the upper part of the Arab D reservoir (Hughes, 2004b; Al-Awwad and Pomar 2015). The four members consist each of a lower carbonate unit capped by anhydrite deposits, exception for the A Member, where the

evaporite section is considered as a separate formation (the Hith Fm.; Powers et al., 1966). The reference section for the D Member was designated in the Abqaiq well 71 in Saudi Arabia (Powers et al., 1966).

According to the orbital forcing model of the AROS J/C Chart (Al-Husseini and Matthews, 2008) reported in the Middle East Geological Time Scale (Al-Husseini, 2008), and in the update by Al-Husseini (2009), the Arab Fm. can be almost comprised between 148.5 and 154.6 Ma.

The formation was widely studied (especially the D Member) in Saudi Arabia, Qatar, Iran and offshore area of Abu Dhabi both for stratigraphic/sedimentological and diagenetic perspectives (e.g. Alsharhan and Whittle, 1995; Azer and Peebles, 1995; Al-Silwadi et al. 1996; Al-Saad and Sadooni, 2001; Cantrell and Hagerty, 2003; Hughes, 2004b; Al-Saad and Ibrahim, 2005; Swart et al., 2005; Al-Emadi et al., 2009; Morad et al., 2012; Nader et al., 2013; Daraei et al., 2014; Al-Awwad and Pomar, 2015).

Al-Silwadi et al. (1996) developed a regional Abu Dhabi biozonation scheme for the Arab Fm., including seven main biozones of Kimmeridgian-Tithonian interval.

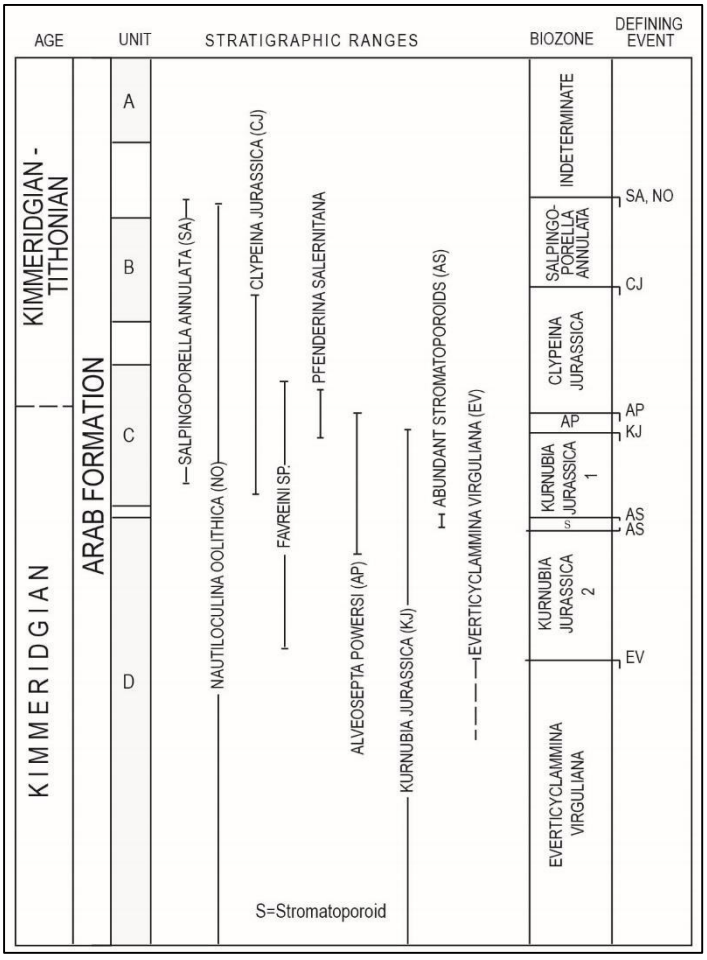


From bottom to top the scheme comprises (Figure 2.7): *Everticyclammina virguliana* Zone, *Kurnubia jurassica* Zone 2, Stromatoporoid Zone, *Kurnubia jurassica* Zone 1, *Alveosepta powersi* Zone, *Clypeina jurassica* Zone, *Salpingoporella annulata* Zone.

**Figure 2.7** *Biozones identified for the Arab Fm. members (simplified and modified from Al-Silwadi et al., 1996).*

The different biozones are capped by the Indeterminate Zone (Arab A), characterized by absence of fossils (Al-Silwadi et al., 1996).

In the wells available for this study, the thickness of the Arab Fm. ranges from 162-192 m (531-630 ft).

- HITH FM. (Tithonian): it consists of massive beds of chicken wire anhydrite, interbedded with sucrosic dolomites and pellet-rich wackestones and packstones (Alsharhan and Nairn, 1997) deposited under an arid climate (Alsharhan and Magara, 1995), during the final phase of restriction of the basin (Al-Silwadi et al., 1996).

  A mixture of playa and sabkha environments is suggested as sedimentary setting (Alsharhan and Kendall, 1994). The formation gradually thins toward east across Abu Dhabi, passing laterally into the intertidal carbonates of the Asab Fm. (Ayoub and En Nadi, 2000). Where deposited, the Hith Fm. forms a regional cap rock that seals the major oil and gas accumulations of the Arab reservoirs (Alsharhan and Nairn, 1997). Across Abu Dhabi, the general thickness of the Hith Fm. varies from 0 m (central Abu Dhabi) to 146 m (480 ft; western Abu Dhabi). In the studied area, the formation is thick 55-79 m thick (180 to 259 ft).

### 2.4.1 Previous stratigraphic studies on the Arab Fm. in the onshore Abu Dhabi

In the onshore Abu Dhabi, the Arab Fm. was previously described in papers such as Grötsch et al. (2003) and Lawrence at al. (2015).

Grötsch et al. (2003) studied the Arab Fm. in order to develop a 3D geological model for the Upper Jurassic sedimentary succession on the onshore Abu Dhabi Bab field (from bottom to top: Upper Diyab, Arab, Hith and Manifa formations). The lithofacies associations identified by Grötsch et al. (2003) from west to east highlight the following depositional environment for the Arab Fm.: i) supratidal to intertidal with alternation of evaporitic sabkha and salinas deposits; ii) intertidal to lagoon with algal laminites; iii) shoreline to inner ramp with oolitic and bioclastic grainstones; iv) mid-ramp defined by a transition from oolitic grainstones to bioturbated wackestones; and v) outer ramp characterized by micrtic, bioturbated limestones. The first four listed associations characterized the Arab A-B-C, instead the top of the Arab D Member is picked in correspondence of the top of the oolitic and bioclastic grainstones. The Arab A-B-C members are defined time-equivalent to the Upper Arab D Member in Grötsch et al. (2003).

In the work of Lawrence et al. (2015), the attention is focused on the Arab D Member investigated in the same onshore field studied on this dissertation. The main environments identified by Lawrence et al. (2015) for the Arab D Member are (from bottom to top): a) outer

ramp and mid-ramp dominated by mudstones interbedded with thin skeletal-rich beds (wackestones to floatstones); b) foreshoal characterized by skeletal-rich peloidal packstones (benthic foraminifera, bivalves and echinoderms); c) offshore active shoal with planar skeletal grainstones, produced by offshore reworking and currents; d) active shoal punctuated by trough cross-bedded oolitic grainstones. The bidirectionality of cross bedding is interpreted as the results of tidal sedimentation within parabolic bars, under ebb and flood currents; e) shoal margin and backshoal with planar skeletal oolitic and bioturbated oolitic grainstones respectively.

These deposits are comprised between two sequence boundaries (SB), where the Upper SB (USB) is located almost at the top of the Arab D grainstones, and the lower SB (LSB) was recognized approximately 10 m below the base of the oolitic grainstones (Figure 2.8; Lawrence et al., 2015). Between the two SBs a maximum flooding surfaces (MFS) was detected within the lowermost part of the Arab D grainstones in correspondence of a mudstones and skeletal wackestones interval (Lawrence et al., 2015).

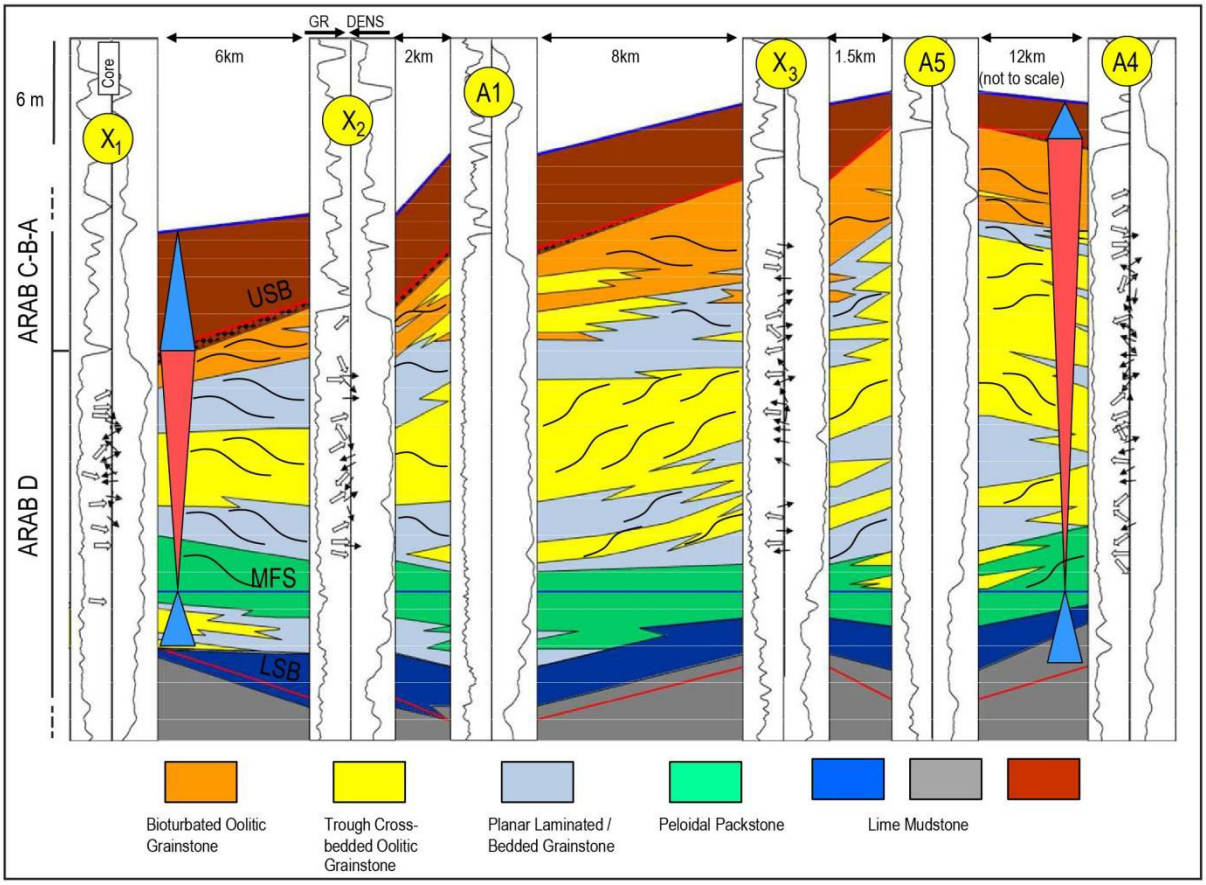


**Figure 2.8** *Facies distribution across the wells studied in Lawrence et al. (2015). The arrows indicate paleocurrent data (open arrows indicate low-angle accretion surfaces and black arrow small scale cross-set) discussed in the chapter 3.3.3 of this thesis (modified from Lawrence et al., 2015). The same wells studied in Lawrence et al. (2015) and in this thesis are reported with the same nomenclature. The remaining ones are named in a generic way ($X_1$, $X_2$ and $X_3$).*

## 2.5 Diagenesis of the Arab Fm. D Member in the onshore Abu Dhabi field

A systematic assessment of the distribution and impact of various diagenetic processes between the flank and the crest of the onshore studied field (Figure 2.4) is the topic of a comprehensive study by Morad et al. (in review) in which I am one of the co-authors (see Chapter 1). The paper focuses on the diagenesis of the Arab D Member, revealing important findings in the reservoir quality evolution. The samples analyzed belong to four of the five wells studied in this thesis, where wells A1, A3 and A5 are located on the crest (i.e. the gas zone), and well A2 on the flank (i.e. the water zone) of the field. Cores from the A-B-C members were recovered mainly in the crest wells, preventing to insert the upper part of the Arab Fm. on this comparative analysis. To be consistent, the nomenclature of the wells in Morad et al. (in review) is adapted to the one used on this thesis. A very short summary of the paper is reported on this section (and in the 2.5.1 sub-section), illustrating the workflow and the main achievements.

The research combined integrated petrography, stable isotope analyses (carbon, oxygen, strontium and sulfur), and microthermometry of fluid inclusions. The thin sections were analyzed by conventional, cathodoluminescence (CL), fluorescence (UV-light) and backscattered electron (SEM-BSE) microscopy. For isotopes studies, a dental drill and a micro-mill (computer-automated) were employed to obtain micro-samples from polished rock slabs. Unstained wafers were used for the petrographic analyses of the fluid inclusions, focusing on the study of primary and pseudosecondary ones.

Micritization and dissolution of allochems, cementation by calcite and saddle dolomite, mechanical and chemical compaction, and cementation by minor non-carbonate phases are the main diagenetic phases and events that affected the Arab D Member, both in the crest and in the flank of the studied field.

Micritization (nil to complete) affected ooids and skeletal fragments. The micritized allochems are often dissolved (partly or completely) resulting in the formation of moldic or enlarged intergranular pores (most common macropore type). These pores types are observed mainly in the packstones and grainstones (upper Arab D Member: mid-ramp/shoal complex), and they are less common in the floatstones (storm deposits in the outer/mid-ramp). In the flank of the anticline, the moldic pores are completely cemented, whereas in crest they are either empty, or partly to completely filled with calcite cement. Stylolites (dissolution and wispy seams) are more common in mudstones and wackestones (lower Arab D: outer/mid-ramp) than in the packstones and grainstones, and are more frequent and have higher amplitude in the flank than in the crest.

Petrographic studies, together with the isotopic and fluid inclusion analyses were combined with the burial-tectonic history of the basin in order to reveal the timing and origin of the diagenetic processes (Figure 2.9).

Diagenesis initially took place in the marine realm, immediately below the seafloor, where the micritization of the allochems occurred in a pre-compactional setting, resulting in a similar extent of micritization between the flank and the crest of the anticline. Oolitic grainstones at the top of the Arab D Member may unravel an incursion of meteoric water, registered by low $\delta^{13}C_{VPDB}$ (see section 3.2.2 for a possible interpretation).

Micritization of the allochems resulted in the formation of micropores between micrite particles, increasing the water-rock interaction, hence resulting in enhanced dissolution of the micritized allochems compared to the non-micritized. The dissolved micrite crystals were re-precipitated in the vicinity of the micritized allochems as more stable fine to medium equant calcite (Ostwald ripening theory, Volery et al., 2010).

Circumgranular calcite cement is suggested to have precipitated in the near-surface marine preathic realm. This suggestion is based on the crystal shape and lack of luminescence of the circumgranular calcite rims (e.g. James and Jones, 2016). The equal abundance of this cement in the crest and flank packstones/grainstones suggests an early diagenetic (eogenetic) origin.

Similar ranges of homogenization temperatures ($T_h$) in fluid inclusions suggest that fine to medium equant ($T_h$=55-130°C), syntaxial ($T_h$=80-125°C) and drusy ($T_h$=65-125°C) calcite were probably formed at similar conditions and the precipitation was continuous during burial. However, the wide ranges of $T_h$, the presence of all-liquid together with two-phase fluid inclusions and inconsistent liquid-vapor ratios in the same fluid inclusion assemblages indicate that these cements have been recrystallized (Goldstein and Reynolds, 1994). Allochems engulfed by these cements have occasionally large intergranular volume, which indicates that precipitation started before significant mechanical compaction. The source of these cements could be linked to dissolution of peloids (shallow burial realm) or to the stylolitization of the host limestone (deep burial domain).

Saddle dolomite can be related to precipitation from hot basinal brines that probably flowed along faults and fractures during the obduction of the Oman ophiolites. Evidence supporting the formation from hot brines includes the relative high $T_h$ (=140 to 175°C) and high salinity (=25.6 to 26.3 wt% NaCl eq.).

After saddle dolomite precipitation, coarse blocky calcite might have formed during cooling of the hot dolomitizing basinal brines, as result of a shift in composition of the brines (i.e. from Mg-rich to Ca-rich). The $\delta^{13}C_{VPDB}$ values (+0.6 to +2.1‰) and the $^{87}Sr/^{86}Sr$ ratios

(0.70698 to 0.70710) suggest dissolution of the host limestone as the source for the coarse blocky calcite.

Both the saddle dolomite and the coarse blocky calcite reveal presence of gas in fluid inclusions, proposing that gas migration occurred during and/or shortly after the Oman ophiolites obduction, as previously evidenced in a nearby field (cf. Paganoni et al., 2016).

Anhydrite nodules, blocky/poikilotopic anhydrite and celestine cements have replaced host limestones and skeletal fragments mainly in the some floatstones of the outer ramp in the crest and rare in the grainstones of the shoal facies.

Fluid inclusion microthermometry on celestine of the outer ramp facies (mode $T_h$=110°C) could suggests a deep burial origin or hot fluids flux to shallower depths.

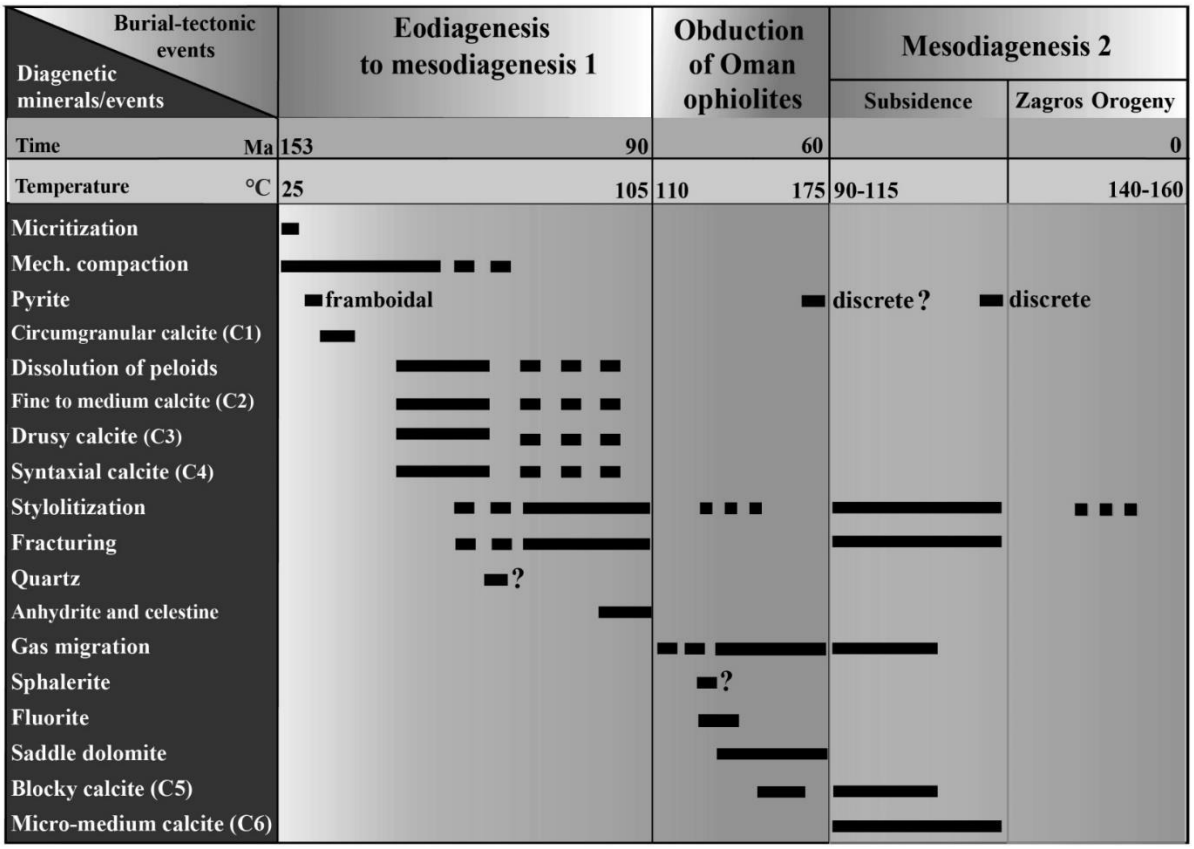


**Figure 2.9** *Paragenetic sequence from Morad et al. (in review) for the Arab Fm. in relation to burial and tectonic events (? = uncertain event; from Morad et al. in review).*

### 2.5.1 The Arab D Member reservoir quality evolution

Prior to the anticline formation and gas emplacement, diagenesis similarly affected the rocks across the field in both the crest and the flank of the present-day anticline. Among the different processes micritization, subsequent dissolution and concomitant re-precipitation of equant calcite cements had a considerable impact on reservoir quality.

During the anticline formation (related to the Oman ophiolites obduction), the diagenesis was probably mediated by the flux of hot basinal brines, and saddle dolomite and coarse blocky calcite cemented the crest and the flank limestones.

Stylolitization of the limestones is more common in the flank than the crest. More extensive stylolitization in the flank can be due to the rapid subsidence that followed the obduction of the Oman ophiolites, whereas the gas emplacement stopped further stylolitization in the crest. Consequently, more calcite cement was released in the flank, which resulted in far lower, reservoir quality in the flank than crest. Gas emplacement has been suggested to have a retarding effect on diagenesis, including stylolitization (Feazel and Schatzinger, 1985; Oswald et al., 1995; Neilson et al., 1998; Heasley et al., 2000; Cox et al., 2010). Moreover, grainstones of the flank present a far higher presence of equant calcite cement in micropores and intergranular pores compared to the same rock in the crest.

Saddle dolomite and blocky calcite (related to the flux of hot basinal brines) have negatively affected the reservoir quality mainly in the floatstones of the outer/mid-ramp, but only marginally the packstones/grainstones of the shoal complex.

# Chapter 3

# FACIES ANALYSIS AND FIELD-SCALE CONCEPTUAL DEPOSITIONAL MODEL

The greater part of this chapter is taken from an article published on Marine and Petroleum Geology (2018, vol. 89, part 2, pp. 350-369), here adapted and integrated with some additional material. The article is entitled: "Field-scale depositional evolution of the Upper Jurassic Arab Formation (onshore Abu Dhabi, UAE)" by **Marchionda, E**., Deschamps, R., Cobianchi, M., Nader, F.H., Di Giulio, A., Morad, D.J., Al Darmaki, F., Ceriani, A. http://dx.doi.org/10.1016/j.marpetgeo.2017.10.006 For the introduction and the geological setting refer to the comprehensive information in the Chapter 1 and 2. The main achievements are summarized at the end of this chapter and then reported in the conclusive Chapter 5.

## 3.1 Methods

### 3.1.1 Core and thin section analysis

Macroscopic core analysis and micropaleontologic/petrographic thin section studies were integrated together in order to obtain a detailed facies analysis of the Arab Formation.

In this chapter, a facies is defined by its lithology, texture, components and primary sedimentary structures. Subsequently the different facies were spatially and genetically assembled in facies associations that represent unique depositional environments (*sensu* Dalrymple, 2010 with references therein).

Core analysis was performed on about 540 m (1772 ft) of cores slabs from the five wells considered in this thesis (Figure 2.4B). In all the investigated wells the bottom and the top portions of the Arab Fm. are not recovered, i.e. the boundary between Diyab Fm. and Arab Fm., and Arab Fm. and Hith Formation. The cores were analyzed for sedimentological and stratigraphic perspectives focusing on: lithology, texture, dominant sedimentary structures, allochemical components and bed contacts (sedimentary classification based on Dunham, 1962; Embry and Klovan, 1971). As a significant example, the core log of well A4 is reported in this chapter. The core drawings of all the available wells are included in the Appendix 1.

These investigations were supported by the microfacies analysis on 277 thin sections available for all the wells except for well A4 (the main components detected for each thin

section are reported in the range charts of the Appendix 2). Thin sections are impregnated with blue epoxy, and stained with alizarin red S and potassium potassium ferricyanide to distinguish dolomite and calcite and their iron content. The thin sections were studied with an attention on the micropaleontological content in order to possibly recognize the main biozones defined by Al-Silwadi et al. (1996).

### 3.1.2 Well log analysis and correlations

Results obtained from cores and thin section analyses were integrated with the geological interpretation of geophysical well logs available for all the studied wells (Figure 2.4B).

A Well Log is a continuous recording, against depth, of geophysical parameters along a borehole (Rider, 2002). The logs are acquired by lowering on a cable the measuring equipment into the well (Serra, 1984).

On this research, the well logs were studied with the aim to unravel with an acceptable degree of confidence the entire vertical stacking pattern of the Arab Formation. The Gamma Ray and the combination of Density and Neutron Logs have been taken to account to identify the main facies associations (and their thicknesses) in accordance with the core description.

The Gamma Ray (GR) Log measures the radiation emitted by uranium, potassium and thorium occurring in the formation (API unit; Rider, 2002; Lucia, 2007). Pure carbonate series are not radioactive but the presence of clay minerals (containing potassium and thorium) and organic matter (containing uranium) can produce higher Gamma Ray responses (Rider, 2002). The log shape evolution, reflecting the shale/clay content, can be interpreted in terms of textural changes and in turn on facies variations (Rider, 2002). The Density Log (RHOB; g/cc) records the bulk density of the formation (including the solid matrix and the fluids in the pores; Rider, 2002). The log measures the attenuation between the tool source and the detectors of medium-high energy collimated gamma rays used to bombard the formation (Rider, 2002). The Neutron Log (NPHI; frac) records the reaction of a formation to high-energy neutron bombardment (Rider, 2002). The reduction in the neutron energy is in function of the hydrogen abundance in the rocks, because of mass equivalence between a neutron and a hydrogen nucleus. Therefore, the log principally provides a response of the water (bound, crystallization, free pore-water) in a formation, in turns interpreted in terms of porosity (Rider, 2002). Plotted on compatible scales, the combination of Density and Neutron Log can be used as a powerful lithology indicator (Rider, 2002). Summarizing from this last mentioned author, the two logs give a superimposable response in clean, water-filled

limestones; pure shale produces a large separation between the two log traces, with the Neutron values higher than the Density. The evaporites show a distinct trace because of their remarkable densities, and in the case of pure anhydrite the Neutron shows a log value of zero, because of no water content (Rider, 2002).

The well log peaks and shapes, and the vertical facies recurrence were fundamental to identify the key stratigraphic surfaces within the Arab Fm. and establish the sequence stratigraphic framework. Transgressive surfaces, maximum flooding surfaces and one subaerial unconformity have been detected (Catuneanu et al., 1998; Allen and Allen, 2005; Catuneanu 2006; Catuneanu et al., 2009; Catuneanu et al., 2011; and references therein).

According to the mentioned authors and the references in their works, these surfaces can be defined as follow:

- Transgressive surface (TS): it separates a progradational from a retrogradational trend, related to the change from shoreline regression to subsequent transgression. The TS is generally conformable, but presence of scouring can be associated to shoreline shift. The name “transgressive surface” placed emphasis on the onset of the transgression. The alternative term “maximum regressive surface” underlines the end of the regression.
- Maximum flooding surface (MFS): it records the end of the shoreline transgression, with retrograding strata below, and prograding ones above, that start to deposit when the sedimentation rate outpaces the sea-level rise. The MFS is generally conformable and lies inside condensed sections. When the underlying transgressive deposits are not present, the MFS shows evidences of scouring. Maximum transgressive surface or final transgressive surface are an example of alternative names.
- Subaerial unconformity (SU): it forms under subaerial conditions during base-level falls. It is usually adopted as sequence boundary, as it represents a significant break in the sedimentary deposition. The surface presents evidence of scouring, and on carbonates can be associated to karstification, process that may not develop under an arid climate. Adjacent to the exposed carbonate terrains, carbonates and evaporites could be deposited, and in a confined topography, sabkha cycles may form.

Transgressive and maximum flooding surfaces were picked at the top of coarsening and fining upward trends respectively. These trend variations are reflected by changes in the lithological textures observed in the cores, and in the uncored intervals, by the shapes of the logs, e.g. a coarsening upward trend is recorded by decreasing Gamma Ray log values.

The transgressive surfaces and the subaerial unconformity (evidences of scouring and exposure) were identified in all the wells and were used to trace reliable well correlations in the studied area and to draw several paleofacies maps that show the field-scale depositional evolution of the Arab Fm. through space and time. Transgressive and maximum flooding surfaces could be assumed as time-equivalent lines, with a low degree of diachroneity (below dating resolution) along dip, or even strike in intractratonic setting (Catuneanu, 2006 with references therein). The subaerial unconformity as well, despite its intrinsic hiatus, records an important event in the evolution of the studied area, and separates older from younger strata as a "time barrier" (Catuneanu, 2006 with references therein).

## 3.2 Results

### 3.2.1 Facies associations

Eighteen sedimentary facies (F) were distinguished based on primary textures and structures, without considering the diagenetic alterations. Their characteristics are summarized in Table 3.1. The different facies (Figure 3.1 and 3.2; additional photomicrographs are reported in Appendix 2) were grouped into five facies associations, considered to be representative of specific depositional environments of a carbonate ramp (Figure 3.3). The total thickness of each association of facies was gathered by the combination of the available cores with the well log interpretation, unraveling the vertical facies distribution for all the Arab Formation.

**Facies association OR - Outer Ramp**

**Description**: this facies association (up to 91 m in thickness) includes finer grained facies like massive mudstones and wackestones (MasMd, BioMd-Wc) with different degree of bioturbation, characterized by the presence of scattered fragments of bivalves (pelagic and shallow marine), gastropods, echinoderms remains, different taxa of foraminifera, among which *Kurnubia* spp., algae (among which dasyclad algae), ostracods and *Cladocoropsis* spp.. These deposits (Table 3.1; Figure 3.1 a, b; Figure 3.2 a, b) are often interbedded with floatstones of facies EroFl, characterized by an erosive and sharp base, and a gradational top with abundance of bivalves/gastropods, echinoderms, *Kurnubia* spp., dasyclad algae, and *Cladocoropsis* spp..

**Interpretation:** mud fallout and the high degree of bioturbation suggest a low energy depositional environment below the storm wave base in an outer ramp setting (Wright and Burchette, 1996), affected by wave-reworking only during major storm events.

**Table 3.1** *Major characteristics of the facies recognized, including lithology, structures, genetic processes and depositional environment interpretation.*

| FACIES CODE (F) | TEXTURES and MAIN COMPONENTS | SEDIMENTARY STRUCTURES | DEPOSITIONAL PROCESS | ENVIRONMENTAL INTERPRETATION |
|---|---|---|---|---|
| **MasMd** | Massive mudstone | Absence of sedimentary structures, different degree of bioturbation | Low energy mud fall out and transport | Lagoon, lower intertidal flat, mid-ramp, outer ramp |
| **BioMd-Wc** | Massive mudstone and wackestone with sporadic fragments of bivalves/gastropods, echinoderms, *Kurnubia* spp., foraminifera, ostracods, *Cladocoropsis* spp. | Absence of sedimentary structures, different degree of bioturbation | Low energy mud fall out and transport of bioclasts | Mid-ramp, outer ramp |
| **BirdMd-Wc** | Mudstone and wackestone with bird's eye porosity, presence of sporadic ostracods and algae | Massive aspect with fenestrae with cement growth in cavities (in some case silt-vadose filling) | Desiccation, gas bubbles | Intertidal zone, supratidal zone |
| **AlgMd** | Microbial algal mats mudstone (bindstone), presence of peloids | Algal mats lamination | Microbial organisms binding, trapping and producing carbonate | Intertidal zone, supratidal zone |
| **LamMd-Pc** | Laminated mudstone-packstone | Flat or cross lamination or flaser bedding | Transport under tidal currents | Subtidal lagoon, tidal channel |
| **BrcMd** | Brecciated mudstone, with mudclasts floating in a muddy matrix | Chaotic aspect | Desiccation breccia and probable tidal rework | Intertidal zone, supratidal zone |
| **DesMd** | Mudstone with desiccation features | Polygonal structures (mud-cracks) and tepee | Mudstone settling and desiccation | Intertidal zone, supratidal zone |
| **ShaleMd** | Black shaly mudstone, presence of organic matter | Massive aspect | Mud fall out deposit | Subtidal lagoon |
| **OstWc** | Wackestone (and mudstone) with ostracods and sporadic foraminifera, bivalves/gastropods, and algae (*Clypeina jurassica*) | Absence of sedimentary structures, massive aspect, presence of fenestral cavities | Low energy mud fall out and transport | Lagoon, lower intertidal flat, shallow marine |
| **BioWc-Pc** | Massive wackestone to packstone with fragments of bivalves/gastropods, echinoderms, *Kurnubia* spp., foraminifera, dasyclads/algae, peloids, intraclasts, *Cladocoropsis* spp. (ooids) | High level of bioturbation, homogenized aspect | Low energy mud fall out and transport of reworked bioclasts | Mid-ramp, outer ramp |
| **PelWc-Pc** | Peloidal wackestone/packstone, with sporadic bivalves/gastropods and foraminifera | Absence of sedimentary structures | Low energy mud fall out and transport | Lagoon, intertidal flat |
| **EroFl** | Poorly sorted floatstone, rich in bivalves/gastropods, echinoderms, *Kurnubia* spp., foraminifera, dasyclads/algae, *Cladocoropsis* spp. peloids and scattered mudclasts | Basal erosive and sharp surface and gradational top | Transport during storm events | Mid-ramp, outer ramp |

**Table 3.1** *continued from the previous page*

| FACIES CODE (F) | TEXTURES and MAIN COMPONENTS | SEDIMENTARY STRUCTURES | DEPOSITIONAL PROCESS | ENVIRONMENTAL INTERPRETATION |
|---|---|---|---|---|
| **BioPelPc-Gr** | Bioclastic-peloidal packstone to grainstone with bivalves/gastropods, echinoderms, intraclasts, ooids, *Kurnubia* spp., foraminifera, algae and cortoids | Sub horizontal or cross bedded lamination or massive aspect | High energy traction currents alternated to quiescent/fair weather production of carbonate | Shallow marine/shoal environment |
| **OoBioGr** | Oolitic grainstone (and packstone-grainstone) with bivalves, echinoderm fragments, intraclasts, *Kurnubia* spp., foraminifera and cortoids | Cross bedded lamination or massive aspect | High energy traction currents alternated to quiescent/fair weather production of carbonate | Shallow marine/shoal environment |
| **OoGr** | Oolitic grainstone (and packstone-grainstone) well sorted and classed, with cortoids | Cross bedded lamination or massive aspect | High energy traction currents alternated to quiescent/fair weather production of carbonate | Shallow marine/shoal environment |
| **CwSulf** | Chicken wire sulfates | Chicken wire structures irregular in shape separated by thin film or surrounded by dolomitized mudstones/wackestones | Displacive growth of sulfates | Supratidal/sabkha, upper intertidal zone |
| **EnSulf** | Enterolithic sulfates | Enterolithic folds (contorted/folded beds) separated by dolomitized mudstones/wackestones | *In situ* growth of sulfates | Supratidal/sabkha, upper intertidal zone |
| **FLag** | Poorly sorted lag deposit, characterized by scattered granules, small pebbles and lithoclasts | Erosive base | Wave rework and condensation of coarser sediments | Lagoon/intertidal, top of the shoal |

The storm events are represented by the erosive and sharp based coarser deposits (Aigner, 1982; Tucker and Wright, 1990; Flügel, 2004), where the presence of *Kurnubia* spp., *Cladocoropsis* spp. (such as *Cladocoropsis mirabilis*) and foraminifera, such as the species *Nautiloculina oolithica*, is significant of transported sediments washed from proximal shallow to deep lagoon/inner ramp environment (Sartorio and Venturini, 1988; Hughes 2004a; Hughes 2004b; Leinfelder et al., 2005) into deeper distal environments. Dasyclads fragments identify as well sediments transported from lagoon or shallow shoals (Flügel, 2004). These bioclasts are then scattered and included as sporadic components in the mud rich facies (BioMd-Wc), possibly due by subsequent rework of the tempestites by internal waves (for internal waves and related deposits description see Pomar et al., 2012; Al-Awwad and Pomar, 2015). The resulting deposits could be then masked and homogenized by bioturbation.

**Log response:** the clay content (mainly linked to the stylolites) and the possible presence of organic matter in these deposits are recorded by relative high values of the Gamma Ray response (Figure 3.4).

**Facies association MD - Mid Ramp**

**Description:** this assemblage (2.5-17 m in thickness) is formed by massive mudstones and wackestones (facies MasMd and BioMd-Wc) interbedded with packstones with presence of peloids and intraclasts (BioWc-Pc; Table 3.1). The bioclastic content increases according to the coarser textures and is characterized by fragments of bivalves (pelagic and shallow marine), different taxa of foraminifera (e.g. *Kurnubia* spp.), echinoderms remains, gastropods, algae (e.g. dasyclad algae), *Cladocoropsis* spp. and ostracods. These deposits are cut by erosive and sharp based floatstones (EroFl), typified by the presence of bivalves/gastropods, echinoderms, *Kurnubia* spp., *Cladocoropsis* spp., and dasyclad algae. Some sporadic ooids have been detected in the stratigraphically upper part of this association of facies.

**Interpretation:** these deposits show analogies with the facies association OR (outer ramp facies), but they contain a higher amount of bioclastic components disseminated within wackestones or forming packstones. All the above described features suggest a mid-ramp, a transitional environment between fair-weather wave base and storm wave base (Wright and Burchette, 1996; Flügel, 2004; Peters and Loss, 2012), often washed and reworked by waves (storm events of facies EroFl) and under increasing currents energy (packstones of facies BioWc-Pc). The numerous bivalves and gastropods are coming from an adjacent bivalve-shelly shoal, instead the *Kurnubia* spp., *Cladocoropsis* spp., *Nautiloculina oolithica*, dasyclads association is transported and winnowed out from an inner ramp/lagoonal environment same as for the OR facies association. Notwithstanding, these deposits are still subjected to calm periods (presence of mud and bioturbation of facies MasMd and BioMd-Wc) during fair-weather conditions (Flügel, 2004).

**Log response:** mid-ramp deposits are characterized by a similar Gamma Ray response as the outer ramp ones due to the similar clay and organic matter content (Figure 3.4).

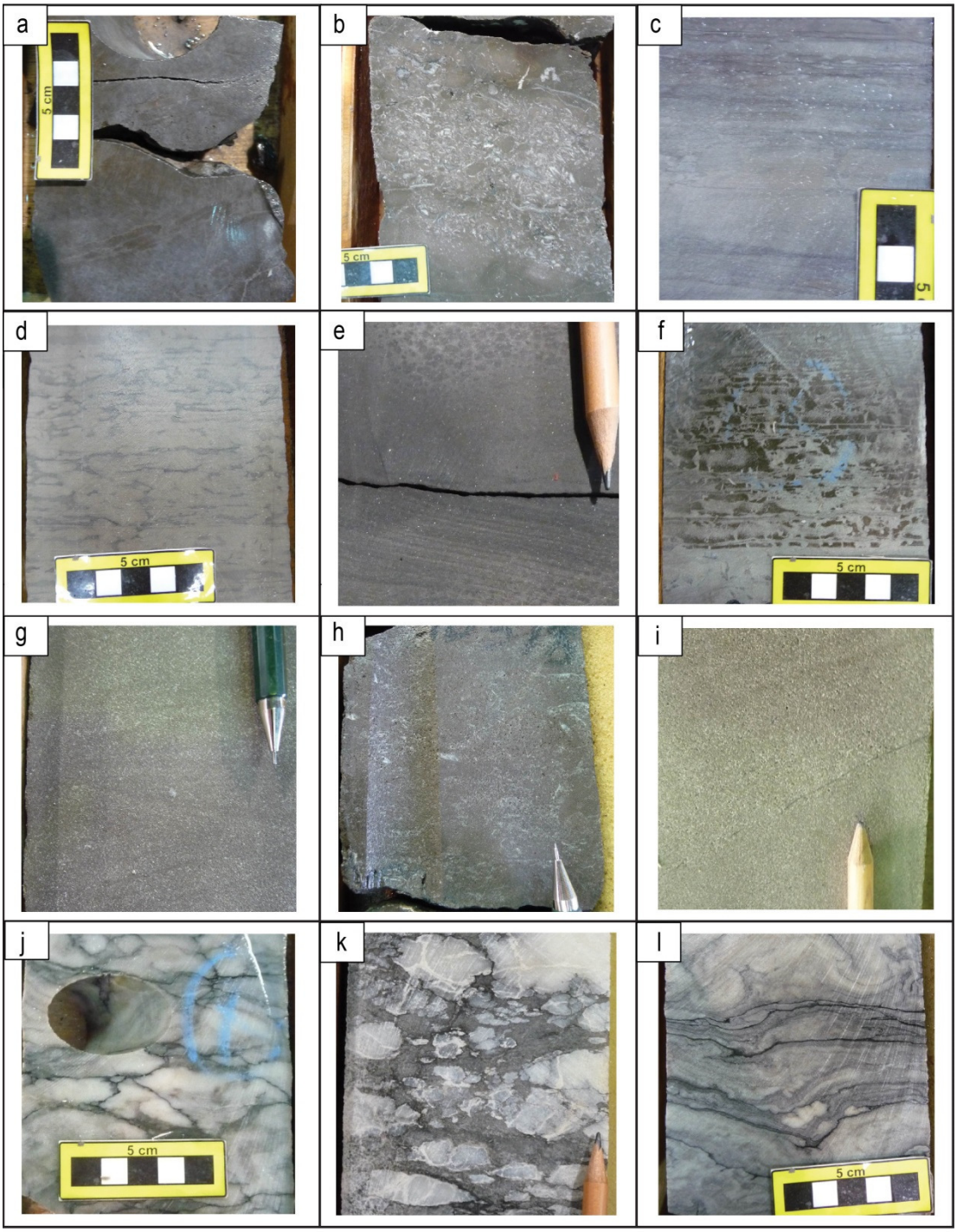


**Figure 3.1** *Core pictures. Some examples of the identified facies. On the brackets the facies code referred to Table 3.1: a) massive mudstone/wackestone (MasMd/BioMd-Wc); b) cm-scale floatstone rich in bioclastic material (EroFl). The layer is erosive sharp based; c) algal mudstone/bindstone (AlgMd); d) bioturbated mudstone/wackestone (MasMd/OstWc); e) laminated mudstone-packstone (LamMd-Pc) at the bottom of the frame that grades into a bioturbated mudstone; f) mud-cracks in a mudstone (DesMd); g) bioclastic cross laminated grainstone (BioPelPc-Gr); h) massive bioclastic packstone (BioPelPc-Gr); i) oolitic grainstone (OoGr); j) chicken-wire sulfates (CwSulf) separated by thin films of mudstone; k) chicken-wire sulfates (CwSulf) surrounded by mudstone; l) enterolithic folds of sulfates (EnSulf). In the frames c-f, j-l the sediment is dolomitized.*

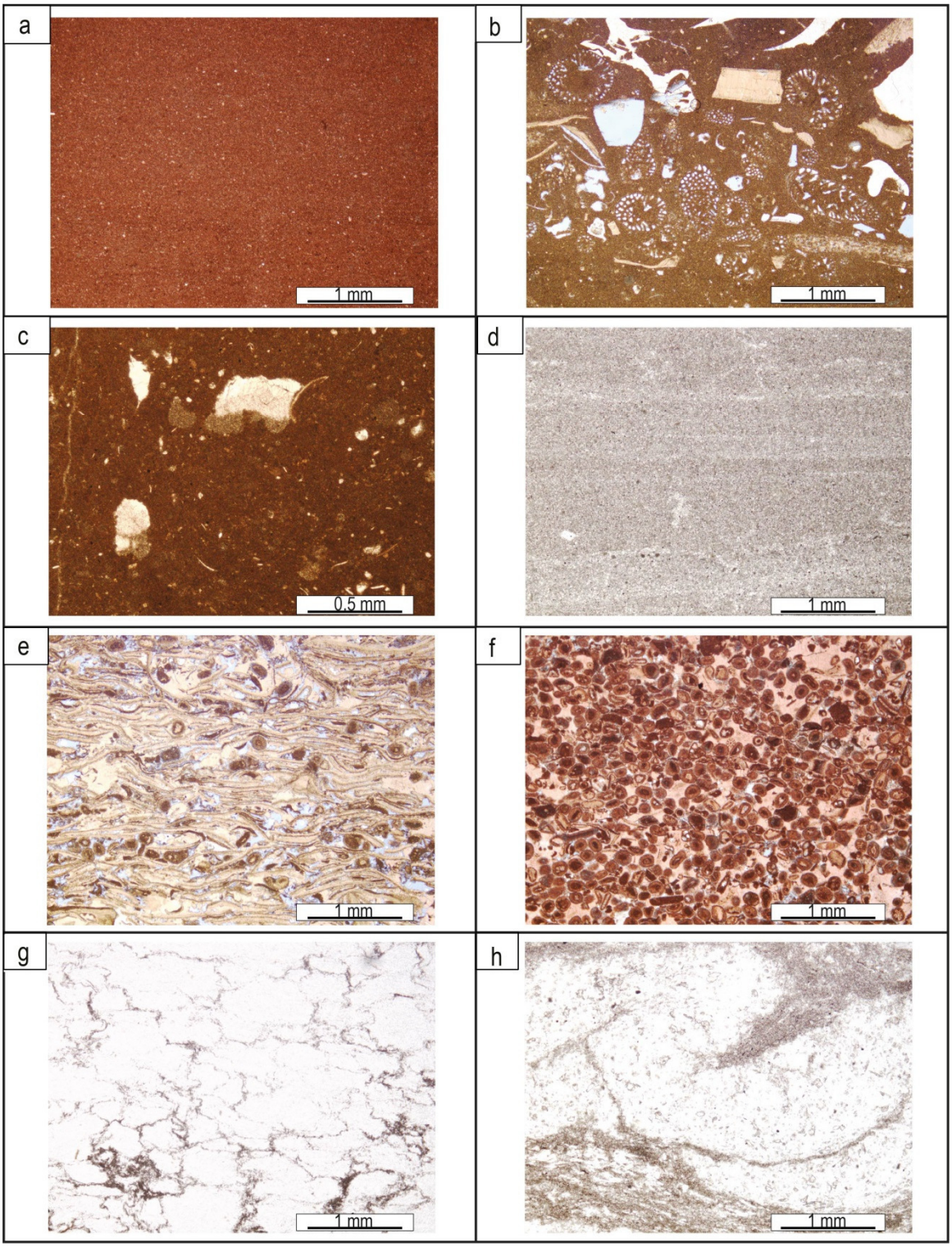


**Figure 3.2** *Optical photomicrographs in plane polarized light. Some examples of the identified facies. On the brackets the facies code referred to Table 3.1: a) massive mudstone (MasMd); b) floatstone characterized by abundance of bivalves fragments, and Kurnubia spp. (EroFl); c) mudstone-wackestone with ostracods and bird's eye fenestrae filled with vadose silt (BirdMd-Wc); d) laminated algal mats mudstone/bindstone (AlgMd); e) laminated bioclastic grainstone with bivalves, echinoderms, peloids and ooids (BioPelPc-Gr); f) oolitic grainstone with cortoids, bivalves, echinoderms and intraclasts (OoBioGr); g) chicken-wire evaporites (CwSulf); h) enterolithic fold of sulfates (EnSulf). In the frames d, g, and h the sediment is dolomitized.*

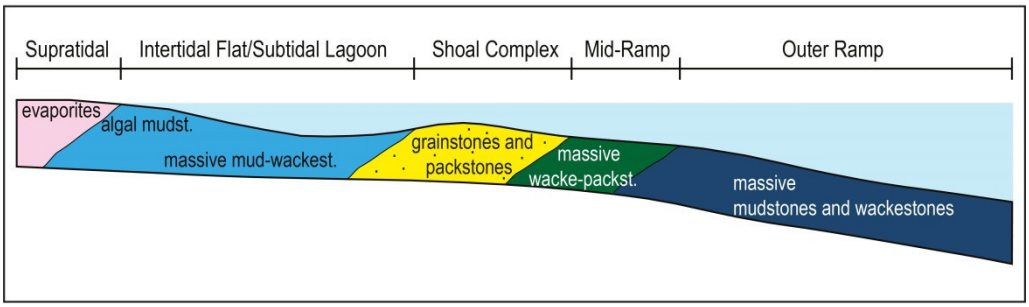


**Figure 3.3** *Schematic carbonate ramp model with the prevalent textures of the Arab Fm. for the different environments encompassed (modified from the depositional model in Morad et al., 2012).*

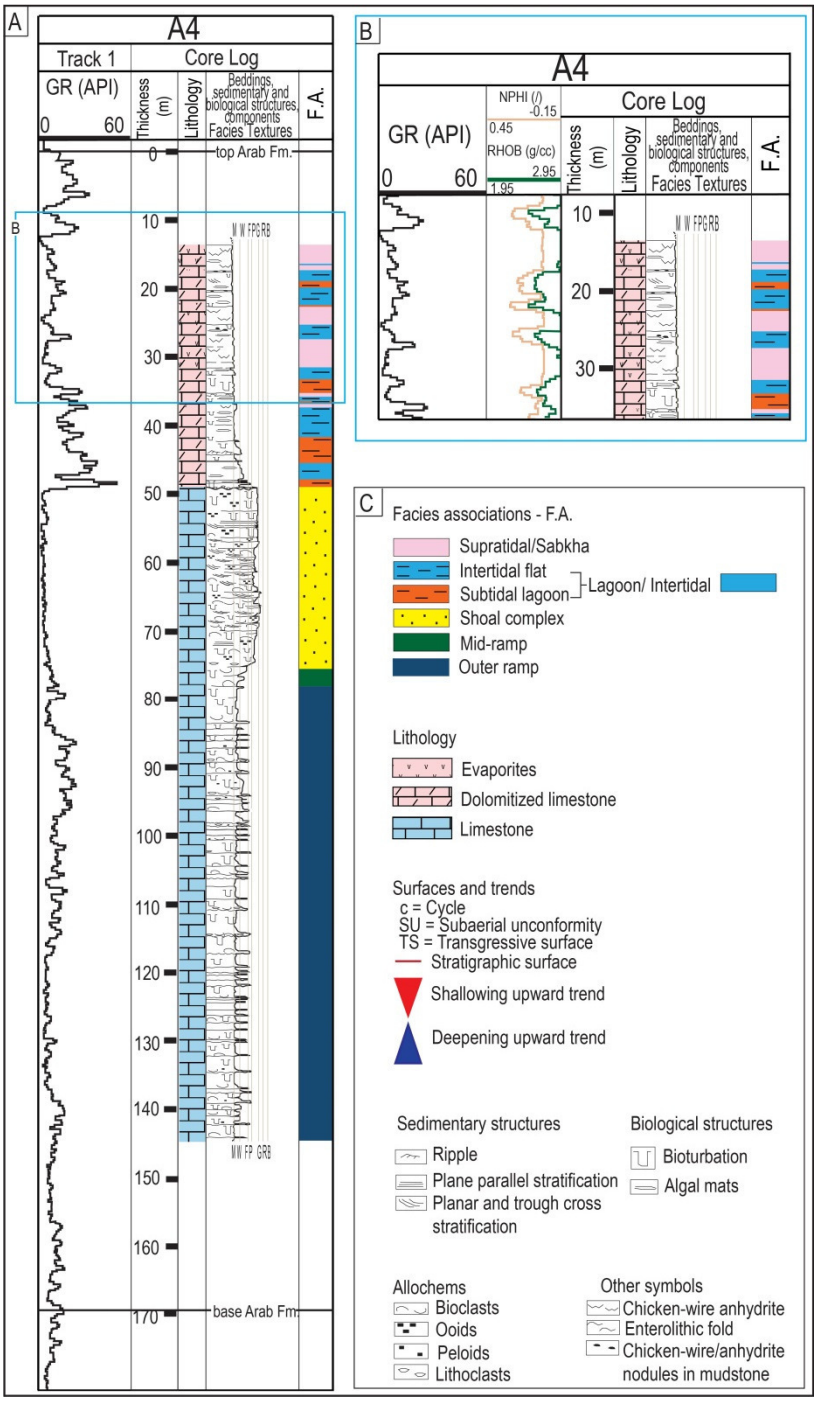


**Figure 3.4** *A) Core log drawing of well A4, representing: the Gamma Ray track (GR), the main components and sedimentary structures of the cores, and the alternation of the associations of facies. The "Thickness" column represents the vertical thickness of the Arab Fm. encountered in the well (the zero value corresponds to the top of the Arab Fm., with a possible error of a couple of meters). B) Highlight of the upper part of the core drawing of well A4, with the addition of Neutron Log (NPHI) and Density Log (RHOB) tracks. The two logs, combined together, are diagnostic to identify the supratidal/sabkha facies association, showing a particular shape in correspondence to the evaporitic strata. C) Legend comprehensive of all the symbols used in all the Figures of this chapter. For the location of well A4 see Figure 2.4. The core drawings of all the studied well are reported in the Appendix 1.*

**Facies association SH - Shoal Complex**

**Description:** this association (18.5-31 m in thickness) is made of laminated (cross or parallel) or massive packstones and grainstones (facies BioPelPc-Gr, OoBioGr, OoGr, FLag; Table 3.1). The cross lamination is visible throughout these deposits, instead the parallel one (where preserved) is present in the lower part. The laminated beds are alternated to massive bioturbated ones, that exclusively prevail at the top of this association. The deposits are characterized in the lower part by a bivalves/gastropods and peloidal association, with presence of echinoderms, intraclasts, foraminifera, such as *Kurnubia* spp., and algae. The ooids are in minor fraction at the bottom, but increase toward the top of this assemblage, which is dominated by ooids with nuclei made by peloids, foraminifera, shell fragments, echinoderm debris and algae. Ooids present a concentric, micritic or radial microfabric, not always easily observable.

**Interpretation:** the main textures (packstones and grainstones), the lack of mud and abundance of allochems and intraclasts suggest deposition in the inner ramp setting, where wave and current activity are permanent (Wright and Burchette, 1996). The inner ramp can be characterized by oolitic and bioclastic shoals (Burchette and Wright, 1992), where a shoal system can be considered as a shallow subtidal heterogeneous carbonate body, where sand-size particles are sorted by the action of waves and tidal currents (Harris, 2009; Pomar et al., 2015). The bioclastic-peloidal packstones/grainstones in the lower part of the studied association could be considered as a shelly shoal fringe, in a seaward position respect to a central cross-bedded oolitic shoal body (e.g. Ruf and Aigner, 2004; Aigner et al., 2007; Palermo et al., 2010; Esrafili-Dizaji and Rahimpour-Bonab, 2014) represented by the cross-laminated oolitic grainstones. The uppermost bioturbated oolitic grainstones could instead represent a landward shoal fringe/relative calm area characterized by a decrease in the environmental energy (presence of radial/radial-concentric ooids; see Tucker and Wright, 1990; Flügel, 2004). According to Lawrence et al. (2015), this shoal complex has been defined as a tidally influenced system (e.g. evidences of bidirectional trough cross-bedding interpreted as tide dominated parabolic bars), comparable to the modern Bahamian analogue (e.g. Gonzalez and Eberli, 1997; Rankey et al., 2006; Rankey and Reeder, 2011; Sparks and Rankey, 2013). A few examples of facies contained in this facies association are pictured in Figure 3.1 g-i, and Figure 3.2 e, f.

**Log response:** the clean coarse grain-size textures are identified also through a left shift in the Gamma Ray registration towards lower values (Figure 3.4).

**Facies association LGIN – Lagoon and intertidal flat**

This assemblage includes a great variety of mudstones to wackestones facies (MasMd, ShaleMd, OstWc, PelWc-Pc, BirdMd-Wc, AlgMd, LamMd-Pc, BrcMd, DesMd, and FLag) (Table 3.1; Figure 3.1 c-f, Figure 3.2 c-d) that shows different degrees of diagenetic alterations (e.g. dolomitization), which make sometimes difficult to identify the primary features (i.e. textures and allochems content). The facies can be associated in two groups, significant of a specific environment:

• **Description:** different facies characterized an association (0.15-6 m in thickness) mainly formed by mudstones and wackestones with possible abundance of ostracods and sporadic foraminifera, bivalves, gastropods and algae (MasMd and OstWc facies). Peloidal wackestones-packstones (PelWc-Pc) and black shaly mudstones with probable abundance of organic matter (ShaleMd) are also constituent of this association. All the deposit is characterized by different degree of bioturbation and a massive aspect with absence of sedimentary structures, except in some beds (mudstones to packstones) where the lamination (flat or crossed) is visible and underlined by coarser sediment (LamMd-Pc).

**Interpretation:** the low variety of allochems together with the abundance of peloids could be significant of a low energy subtidal lagoon poorly connected with the open sea (Tomašových, 2004; Hashmie et al., 2016), and occasionally cut by higher energy tidal channel (presence of flaser bedding; see Reineck and Wunderlich, 1968). The presence of ostracods and (two samples) of *Clypeina jurassica* highlights a restricted environment with probable great salinity fluctuations (Flügel, 2004; Tomašových, 2004).

• **Description:** facies BirdMd-Wc, AlgMd, BrcMd, DesMd, build an association (0.15-4.5 m in thickness) mainly made by microbial mats with presence of peloids (AlgMd), interbedded with massive mudstones/wackestones showing evidences of subaerial exposure, like the presence of mud cracks, tepee (DesMd), bird's eye fenestrae (BirdMd-Wc), or desiccation breccia (BrcMd; see Norton, 1917).

**Interpretation:** all these features are typically interpreted as diagnostic of an intertidal flat (e.g. in the Lofer sequences by Fischer, 1964; and Enos and Samankassou, 1998). An identified oogonium of Characeae could prove circulation of brackish waters (Flügel, 2004). The intertidal deposits are often intercalated with muddy burrowed facies (MasMd, OstWc) that could be referred to a lower intertidal/subtidal environment.

**Log response:** lagoonal and intertidal facies associations are characterized by similar Gamma Ray profiles due to the higher content of organic matter and clay. The similar Gamma Ray response made difficult to identify with precision the alternation of subtidal and intertidal deposits on the uncored intervals of the five studied wells. For this reason, the two facies associations are represented as a single "super" association of facies here in the description and in the well correlations, and they are pictured with a single color (light blue) in the panels presented in this thesis (Figure 3.4).

**Facies association SA – Supratidal/Sabkha**

**Description:** this facies association (thin lenses to deposit 0.25-6 m in thickness) includes evaporites of facies CwSulf and EnSulf (Table 3.1, Figure 3.1 j-l, Figure 3.2 g-h). These two facies are characterized by chicken wire and enterolithic sulfates respectively. The chicken wire structures are separated by thin films or surrounded by dolomitized limestones. The sulfates layers are intercalated by massive mudstones or microbial mats (AlgMd facies), where the mud is usually completely dolomitized.

**Interpretation:** this facies association is typical of the supratidal zone of coastal sabkhas (Tucker and Wright, 1990; Warren, 2006). In this setting, salts precipitate and sulfates grow by displacement within the sediments, forming characteristic chicken-wire structures (Tucker and Wright, 1990; Nichols, 2009). In the uppermost part of this sabkha deposits, coalescent beds of sulfates form contorted layers known as enterolithic structures as a consequence of minerals growth (Tucker and Wright, 1990; Nichols, 2009). We could not exclude the possible precipitation of sulfates in salinas environments (e.g. the Arab Fm. in Al-Silwadi et al., 1996; Grötsch et al., 2003; Morad et al., 2012) for the uncored intervals (especially for the thickest interpreted evaporitic beds).

**Log response:** in the uncored intervals, the combination of the Density and Neutron Log was fundamental to identify the evaporitic beds. The response (Figure 3.4) is characterized by high Density Log values (due to the higher density of the evaporites) and low Neutron Log values (due to the lower porosity of evaporites).

### 3.2.2 Field-scale stratigraphy and sedimentary evolution of the Arab Fm.

From bottom to top, all the wells show a succession that ranges from outer ramp to supratidal/intertidal deposits, where a shoal complex encloses and protects a lagoonal environment. This succession corresponds to the progradation of a carbonate ramp,

characterized by an overall shallowing upward trend. According to the local lithostratigraphic scheme (e.g. the one pictured in Lawrence at al., 2015), in each well the Arab D Member is composed by outer ramp, mid-ramp and shoal facies associations, and the Arab A-B-C by lagoonal, intertidal and supratidal environments.

The vertical stacking pattern of the formation is described in the following from bottom to top. The outer ramp mudstones/wackestones grade up into the mid-ramp facies. The latter shows a transitional increase in energy, proved by the presence of coarser facies (i.e. bioclastic packstones). Outer ramp and mid-ramp were winnowed by storm events, containing abundant shell fragments and biota typical of a lagoonal setting. The abundance of shells and the almost completely absence of ooids suggest the landward presence (out of the study area) of a shoal made (almost) exclusively by skeletal allochems, equivalent in time to the outer ramp and mid-ramp deposits detected in the studied wells. Landward to the shoal an open lagoonal environment was populated by organisms such as: *Kurnubia* spp., dasyclad algae, *Nautiloculina oolithica* and *Cladocoropsis* spp., (e.g. Hughes, 2004b) washed down by the storms into the mid-ramp and outer ramp environments. The storm deposits show the proximality gradient spatial relationship (Aigner, 1982; Seilacher and Aigner, 1991), with thicker-coarser beds in the mid-ramp and thinner-finer beds in the more distal outer ramp. The composition of the shoal changed through time during the deposition of the Arab Fm. from shelly to oolitic dominated. The ooids are the main components of the packstones-grainstones characterizing the shoal complex located stratigraphically above the mid-ramp succession in the studied wells. In all the wells, the shoal complex is characterized in the lower part by the presence of shell fragments mixed with peloids, foraminifera, echinoderms fragments, intraclasts and minor ooids. This association gradually passes upwards to oolitic packstones/grainstones (with cortoids, intraclasts and minor shells/echinoderm fragments and foraminifera), that become well-sorted oolitic grainstones (with some cortoids) at the top. The shoal could have been composed by mobile carbonate barriers (Harris, 2009) cut by tidal channels connecting the shoal with the lagoon, testified by the presence of sporadic and highly micritized *Kurnubia* spp.. The shoal complex detected in the cores could be interpreted to act as a submarine barrier with a positive topographic relief (e.g. Ruf and Aigner, 2004; Aigner et al., 2007), protecting the adjacent shallow lagoon and intertidal flat. The progradation of the shoal and the decrease in the accommodation space resulted in the subaerial exposure of the complex (e.g. Esrafili-Dizaji and Rahimpour-Bonab, 2014) registered only at the top of the shoal deposits. In correspondence to this subaerial exposure the shoal could have assumed a transient morphology similar to a beach-barrier (see Otvos,

2000). The emersion caused erosion and influx of meteoric waters, proved by the presence of an erosive surface as well as by considerably low $\delta^{13}C_{VPDB}$ values in correspondence to an oolitic layer at the top of the shoal grainstones (Morad et al., in review; see section 2.5). Lawrence et al. (2015) proposed the presence of a proto-soil in correspondence to this surface related to depletion in carbon. This erosive surface (visible in the cores of some wells) is interpreted as a subaerial unconformity and is located at the top of the oolitic grainstones. Resting onto this surface a lag deposit is present (facies Flag) due to a subsequent concentration of scattered pebbles and lithoclasts. In the cores the subaerial unconformity marks the boundary between shoal and lagoonal/intertidal deposits, corresponding to a shift in the Gamma Ray response, due to the increase in the amount of organic matter and clay in the lagoon. The lagoonal deposits show low diversity and paucity of life (presence of ostracods, rare bivalves and gastropods, and just two specimens of *Clypeina jurassica*), with no more evidence of *Kurnubia* spp. and dasyclad algae. The change and decrease in diversity of the lagoonal muds faunal assemblage could be explained with a change in water circulation (from open to restricted) and an increase in salinity (Harris, 2009). Lagoonal facies are alternated to intertidal and supratidal ones, where evaporitic facies capped the deposits. This succession of facies associations has a cyclic arrangement, identified as peritidal cycles (e.g. Read and Goldhammer, 1988; Wright, 1992; Pratt 2010) resulting from the gradual or sharp alternation between the lagoon/intertidal and supratidal/sabkha deposits.

The detected biota in the available thin sections allowed a comparison with the biozonation scheme presented by Al-Silwadi et al. in 1996 (see section 2.4 and Figure 2.7; Figure 3.5; complete range charts in Appendix 2). It was not possible to identify the seven biozones established by those authors for the following reasons: i) the thin sections do not cover all the cored intervals, that in turn do not cover all the Arab Fm. (the top and the bottom of the Arab succession were not available); and ii) the members A-B-C are largely dolomitized and they are almost barren of fossils.

*Cladocoropsis* spp. (probably *C. mirabilis*) was used to identify the Stromatoporoid Zone of Al-Silwadi et al. (1996). In all the wells, *Cladocoropsis* spp. occur already at the bottom of the cored outer ramp interval. The last occurrence of *Cladocoropsis* spp. was located inside the mid-ramp deposits and correlated through all the wells. *Kurnubia* spp. (probably *K. jurassica* and *K. palestiniensis*, with *Nautiloculina* spp.) cover all the Arab D Member from the bottom of the cored outer ramp up to the shoal facies association. The interval above the Stromatoporoid Zone with *Kurnubia* spp. specimens represents the *Kurnubia jurassica* Zone 1 of Al-Silwadi et al. (1996). The uppermost cored interval is assigned to the indistinct

*Alveosepta powersi* and *Clypeina jurassica* Zones (Al-Silwadi et al., 1996) being *A. powersi* not preserved in the sections studied and *C. jurassica* recorded only in two samples (lagoon environment of well A5).

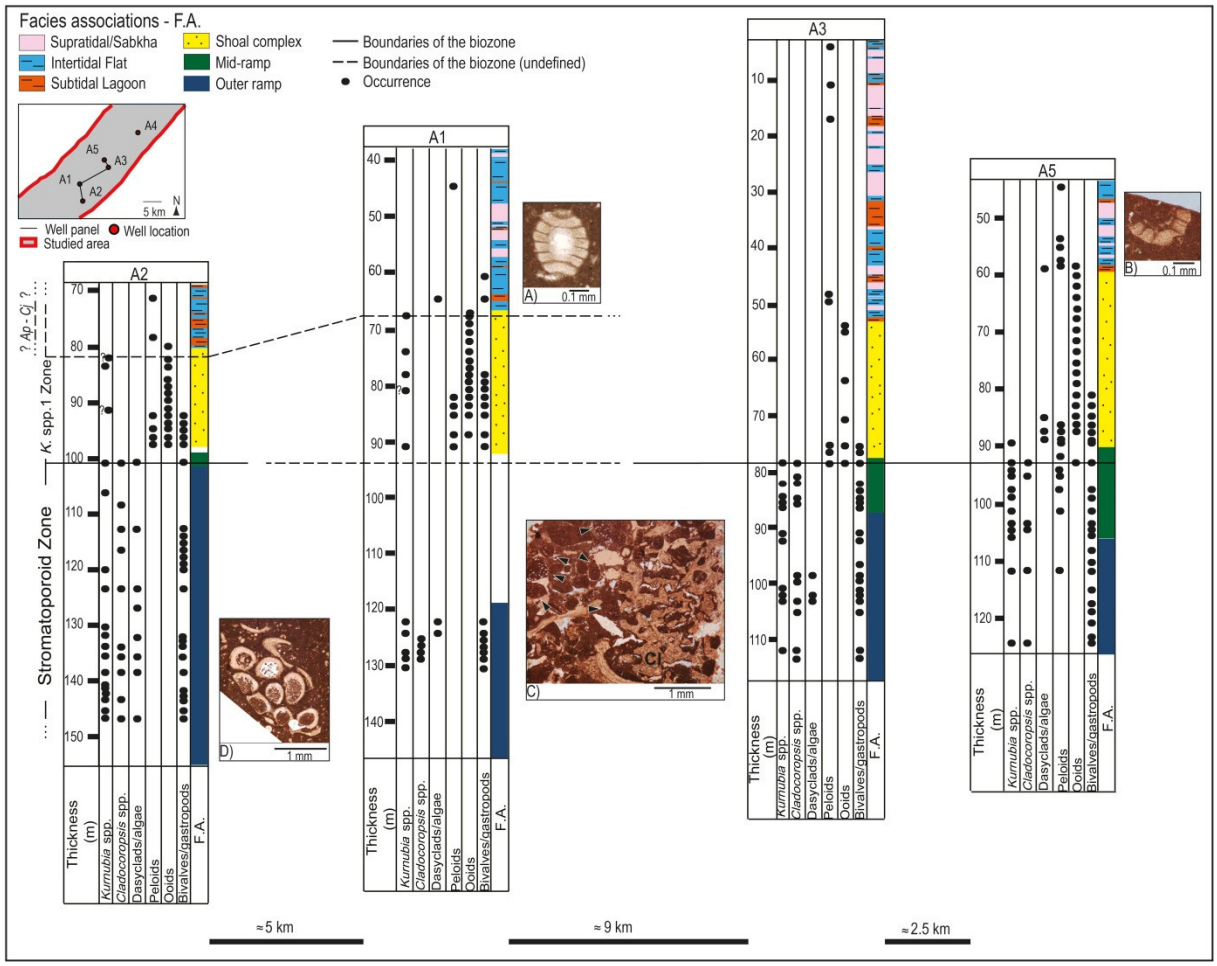


**Figure 3.5** *Micropaleontological distribution in the well A1, A2, A3, A5. The biozones refer to the work of Al-Silwadi et al. (1996). The Stromatoporoid Zone and the Kurnubia (K.) spp. 1 Zone have been identified. Indistinct Alveosepta powersi (Ap) and Clypeina jurassica (Cj) Zones are assigned to the upper part of the Arab Formation. The black dots show the stratigraphic distribution of the main biota and components identified: Kurnubia spp., Cladocoropsis spp., algae (among which dasyclads), peloids, ooids, and bivalves/gastropods. The wells are flattened on the top of the Stromatoporoid Zone. Optical photomicrographs in plane polarized light of some samples of the main biota: A) Oogonium of Characeae in the intertidal flat of well A1. B) Clypeina jurassica in the lagoonal environment of well A5. C) Cladocoropsis sp. (Cl) and Kurnubia sp. (black triangles) transported in the outer ramp of well A5. D) dasyclad algae transported in the outer ramp of well A2. The "Thickness" column represents the vertical thickness of the Arab Fm. encountered in the well with the zero value corresponding to the top of the Arab Fm. (not encompassed by the available cores, not reported in the pictured. For the complete vertical scale see Figure 3.6 and Figure 3.7) with a possible error of a couple of meters. Lateral distance of the wells not on scale.*

### 3.2.3 Well correlations

Eleven transgressive surfaces (TS) and one subaerial unconformity (SU5) were identified within the investigated succession (Figure 3.6, 3.7 and 3.8). The transects cut the study area from northeast to southwest. These stratigraphic surfaces are recognized in all the wells, allowing tracing them all over the study area. The transgressive surfaces are labelled from bottom to top TS0 to TS11, where TS0 coincides with the base of the Arab Fm., and SU5 instead coincides with the boundary between the oolitic packstones-grainstones of the shoal and the mudstones-wackestones of the lagoonal/intertidal environment.

From bottom to top, the stratigraphic surfaces divide the overall long-term shallowing upward trend of the Arab Fm. in twelve shorter cycles, where each cycle shows a similar response in terms of well log pattern, and it is also calibrated with well core data.

Between TS0 and SU5 (Arab D), five probable mid-term cycles are characterized by a lower part with a thin deepening upward trend followed by a thick shallowing upward part.

The deepening upward lower part is not always recorded, and the maximum flooding surface coincides with the transgressive surface. Above SU5 (Arab A-B-C), seven possible short-term (peritidal) cycles are made up by shallowing upward deposits, clearly visible in cores, where these cycles correspond to the lagoonal/intertidal facies capped by the supratidal/sabkha evaporites. The last cycle, c 12, in the upper part of the Arab Fm. is interpreted to be composed by lagoonal/intertidal sediments that are stratigraphically capped above by the evaporites of the Hith Formation. The transgressive surface that should bound cycle c 12 could be located inside the Hith Fm. at a depth not identified in this study, and the cycle has been left undefined in its upper part (dashed line).

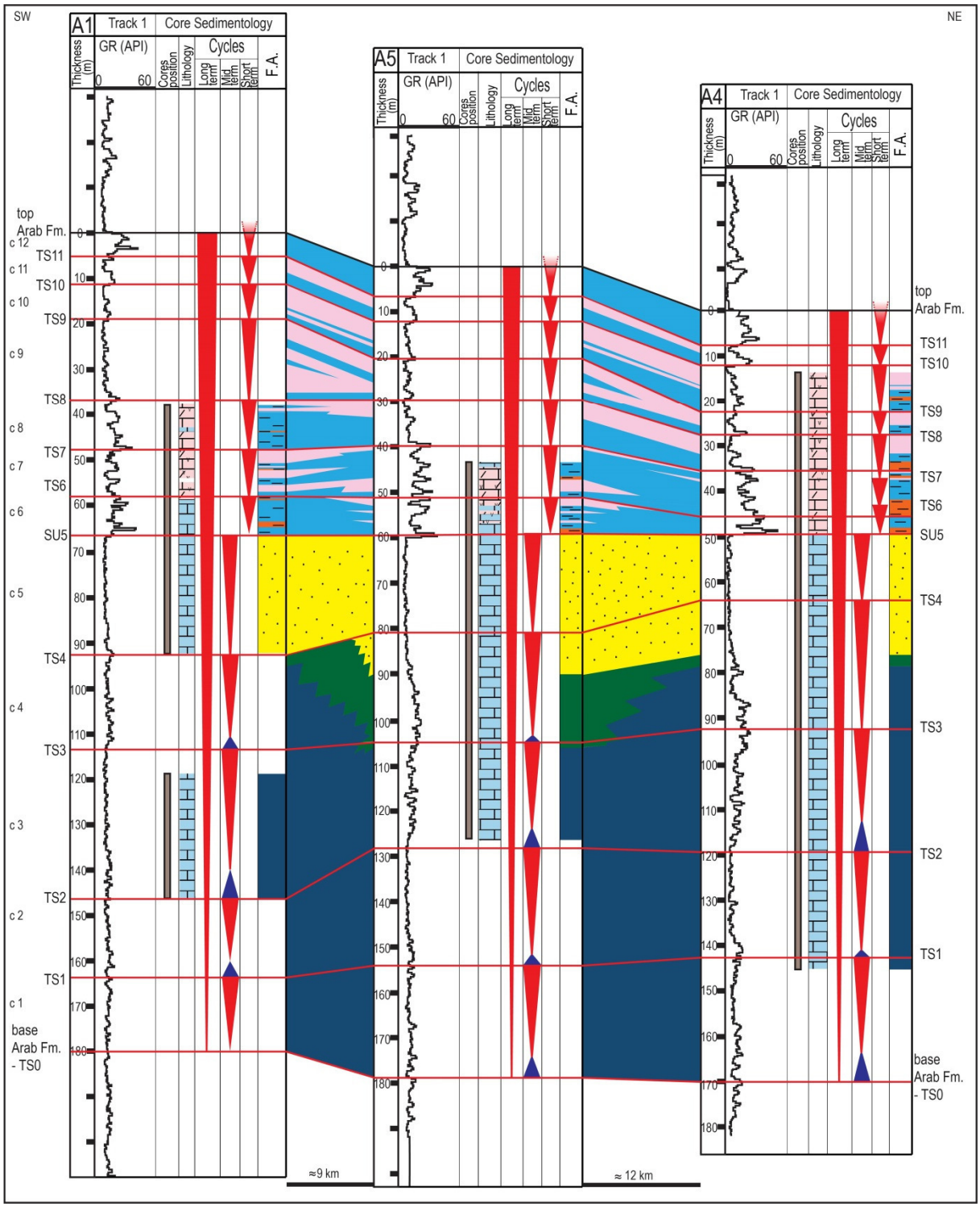


**Figure 3.6** *Correlation panel CP1 encompassing wells A1, A5 and A4 as reported in Figure 2.4. The panel shows the sequence stratigraphic pattern, the vertical and lateral distribution of the facies between the wells, with the interpretation of the uncored intervals (only the Gamma Ray track is shown). The "Thickness" column represents the vertical thickness of the Arab Fm. encountered in the well (the zero value corresponds to the top of the Arab Fm., with a possible error of a couple of meters). In the correlations the lagoonal and intertidal flat deposits are pictured together with a single color (light blue). For the legend see Figure 3.4C. Lateral distance of the wells not on scale.*

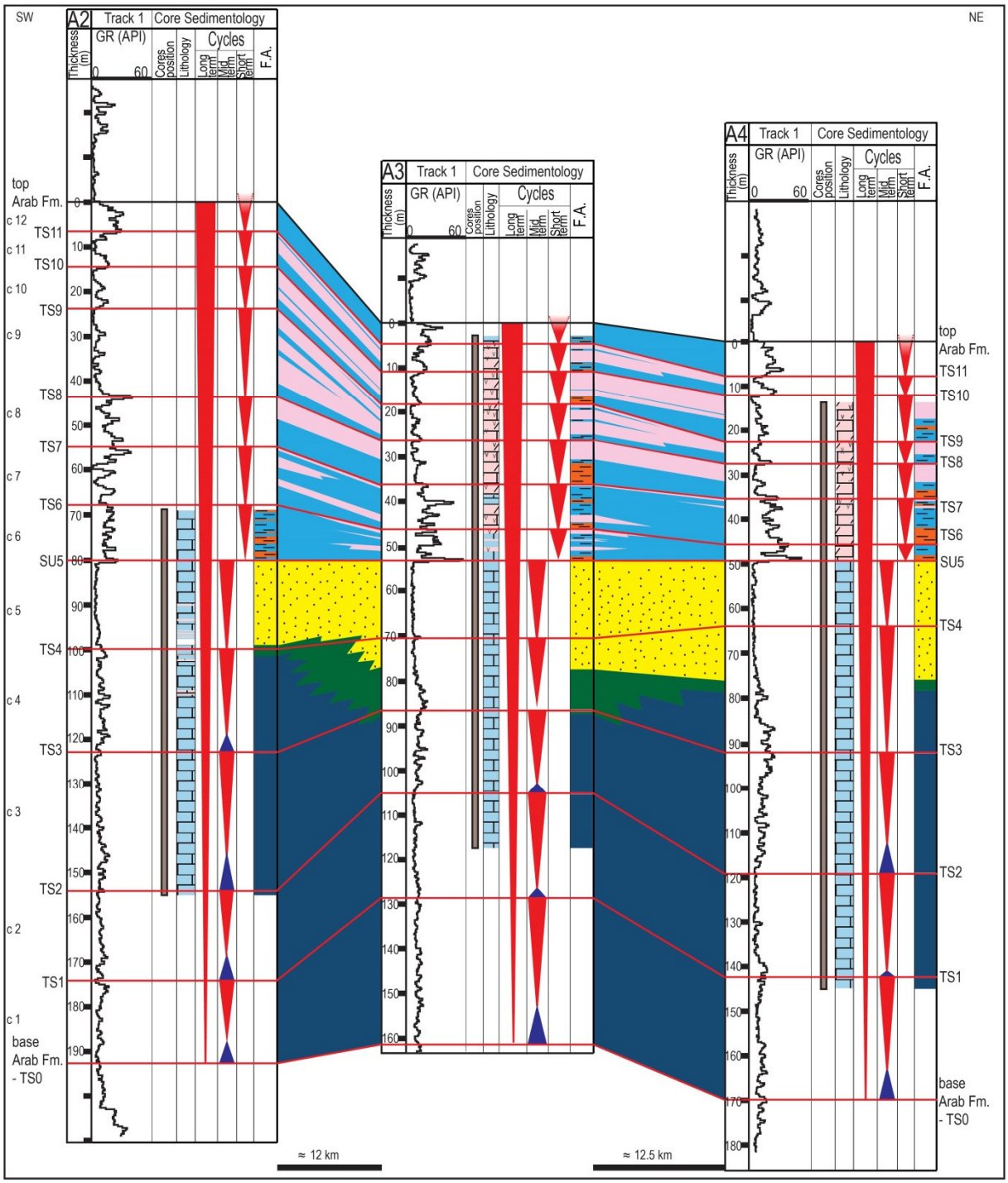


**Figure 3.7** *Correlation panel CP2 encompassing wells A2, A3 and A4 as reported in Figure 2.4. The panel shows the sequence stratigraphic pattern, the vertical and lateral changes in distribution of the facies between the wells, with the interpretation of the uncored intervals (only the Gamma Ray track is shown). The "Thickness" column represents the vertical thickness of the Arab Fm. encountered in each well (the zero value corresponds to the top of the Arab Fm. with a possible error of a couple of meters). In the correlations the lagoonal and intertidal flat deposits are pictured together with a single color (light blue). For the legend see Figure 3.4C. Lateral distance of the wells not on scale.*

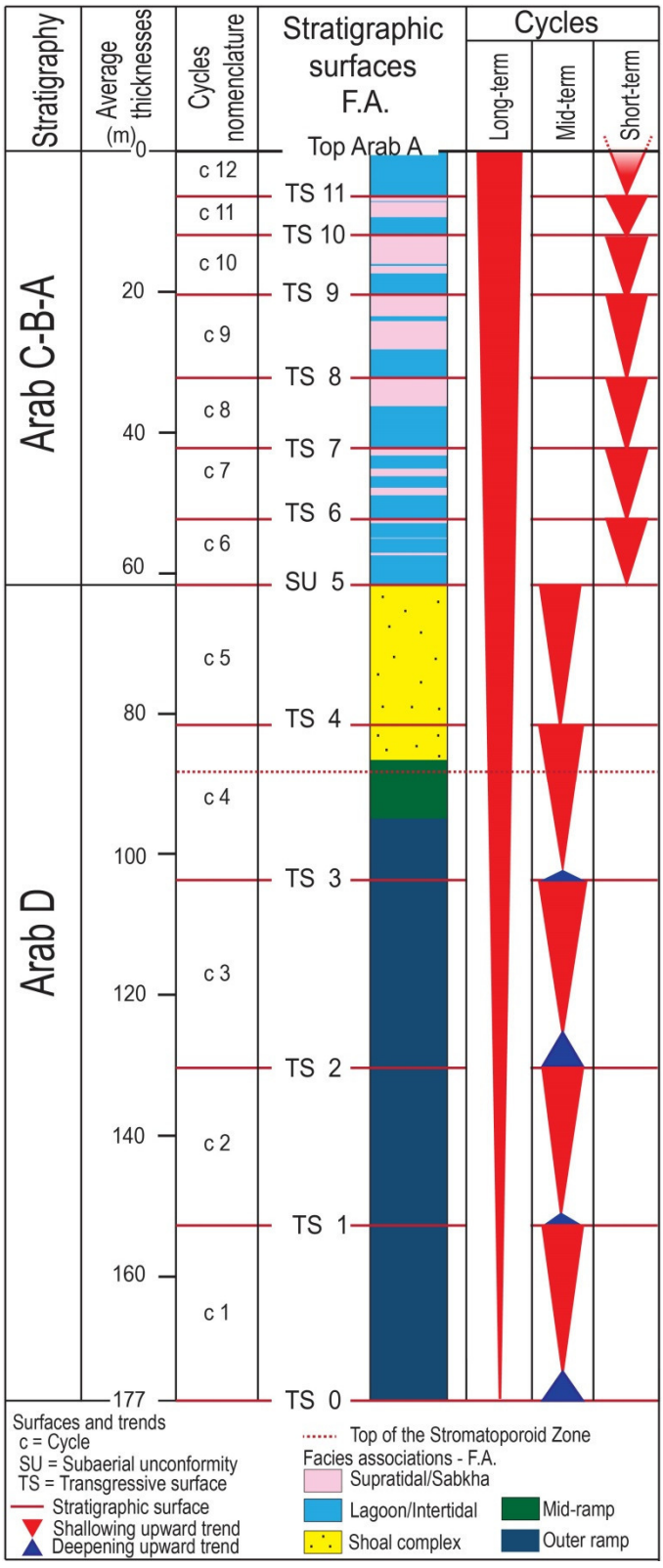


**Figure 3.8** *Schematic summary of the Arab Fm. representing the eleven transgressive surfaces, the subaerial unconformity, and the division in cycles and the top of the Stromatoporoid Zone. The vertical facies distribution is pictured in a synthetic/schematic column. The scale reports the average thickness of each cycle, considering the five available wells. The top of the Stromatoporoid Zone is comprised between TS3 and TS4 and encompassed mid ramp sediments. The division in members refers to the work of Lawrence et al. (2015). In the correlations the lagoonal and intertidal flat deposits are pictured together with a single color (light blue).*

### 3.2.4 Lateral changes and paleofacies maps

The correlation panels of Figure 3.6 (CP1) and Figure 3.7 (CP2) show the lateral changes in terms of facies distribution and thickness of the different cycles.

The thickness of each cycle changes from well to well. For example cycle c1 is thinner in wells A1 and A2 (average thickness 17 m), and it is thicker in wells A4 and A5, with a maximum of thickness in well A3 (around 32 m). On the contrary, between TS2 and TS3 (cycle c3) well A3, and A5 accumulate thinner deposits (average of 21 m). A different trend can be seen from cycle c6 to c12, where the thinnest succession is deposited in well A4 with a total thickness of around 50 m.

The facies associations show differences in terms of thickness forming stratal terminations and stratigraphic pinch-outs. The outer ramp deposits are thicker in well A1, A2 and A4. The

mid-ramp strata of the cycle c4 are made up by thick deposits (around 15 m) in wells A3 and A5, and they thin towards the well A1, A2 and A4. The shoal complex becomes thinner toward wells A1 and A2. The succession between SU5 and TS12 (alternation of lagoon and supratidal/sabkha facies) thickens towards southwest.

The combination of the vertical and lateral facies changes provides the base for twelve paleofacies maps (Figure 3.9; note that the maps representing the same distribution of facies are shown in a single frame for a total of six different maps) in correspondence to the twelve key stratigraphic surfaces (TS0 to TS11, SU5).

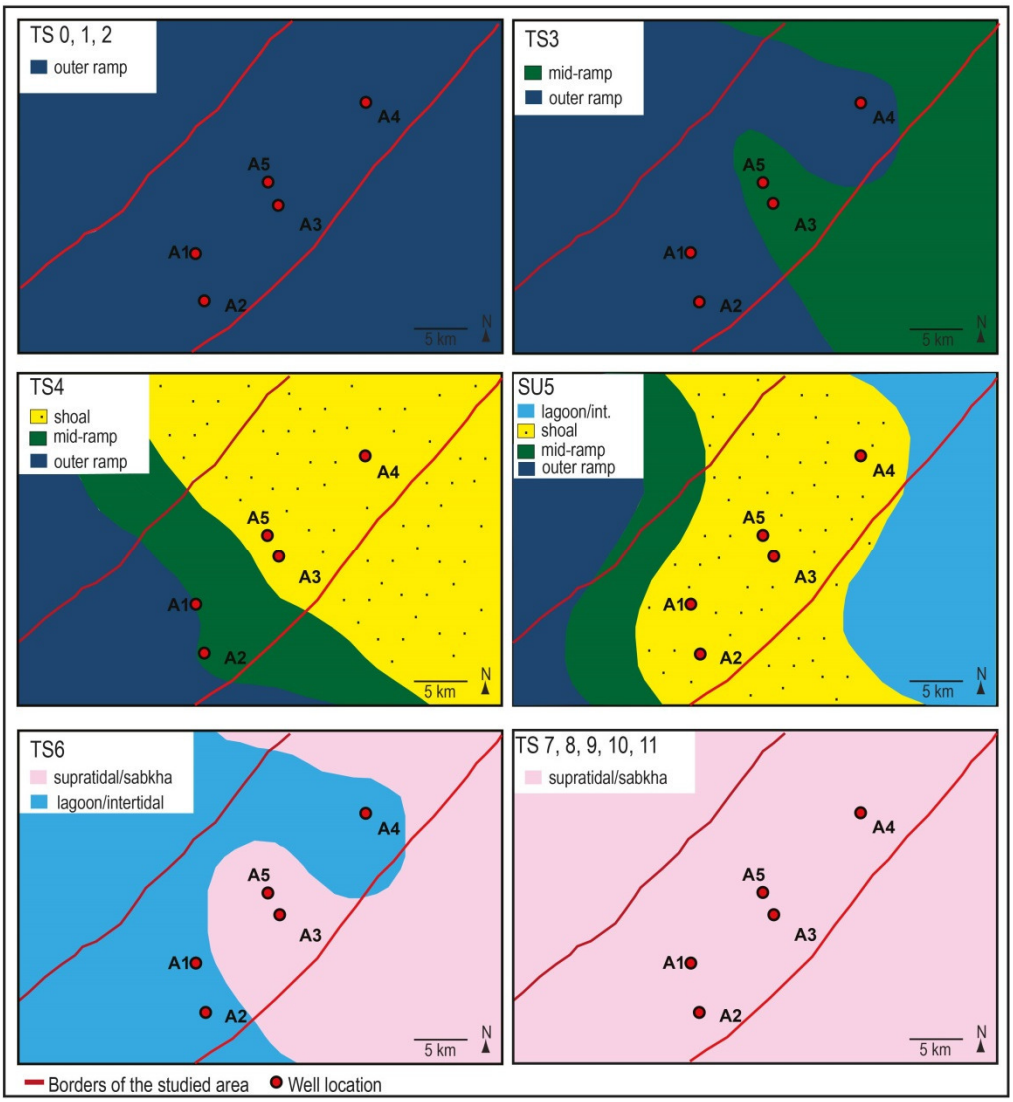


**Figure 3.9** *Paleofacies maps showing the distribution of the facies associations through time across the area. The maps are pictured in correspondence to the eleven transgressive surfaces and the subaerial unconformity identified within the Arab Formation. The well data were correlated between the wells and extended to all the field and outside area. No other constraints were used to interpret the facies distribution, except the well data. The maps representing the same distribution of facies are shown in a single frame (e.g. since TS7 to TS11). In all frames red line borders bound the studied field area.*

The maps picture the simplest suggested scenario, extending the well data (with no other constraints) across the field (between the red lines in the maps) and in the surrounding area. In most of the maps a single association of facies can be spread across all the area which means that the setting can be dominated by a specific depositional environment (e.g. the outer ramp for the maps at TS0, TS1 and TS2). The maps drawn in the upper part of the Arab Fm., from TS7 to TS10, show a depositional scenario that could be dominated by the evaporites of the supratidal/sabkha environment. These maps evidence the cyclic alternation between lagoonal and supratidal environments, where each cycle is capped by the sabkha evaporites.

## 3.3 Discussion

The vertical/ lateral facies distribution and the thickness variations described above suggest a possible conceptual field-scale depositional model for the Arab Fm. with the peculiarities highlighted in the following sub-sections.

### 3.3.1 Progradational trend

The facies distribution at the different sequence stratigraphic surfaces (paleofacies maps of Figure 3.9 and 3.10) infers a field-scale main progradation of the Arab D Member towards southwest. The paleofacies map at TS4 (Figure 3.9 and 3.10) shows that the shoal nucleates in the northeast (well A4, A5 and A3), and later (SU5), the shoal covers all the study area, involving a progradation of the Arab Fm. towards southwest (black arrows in Figure 3.10). At time stage TS3 (Figure 3.9), the well constraints permit to draw an irregular margin, where the progradation can be locally and transient toward multiple directions (red arrows in Figure 3.10), but always included in the overall southwest main direction of progradation. This "multi-directional" progradation could be observed also in Figure 3.6 (CP1) and Figure 3.7 (CP2), where the mid-ramp deposits prograde towards both north-east and south-west. Stratigraphically above the mid-ramp setting, the shoal complex progrades toward southwest as depicted in the correlation panels CP1 and CP2 (Figure 3.6 and 3.7).

In the upper part of the formation, each cycle is capped by an evaporitic body (often interbedded with intertidal mud), that does not show clear lateral variations. An exception occurs at TS6 where the supratidal sulfates are detected in the central wells of the field (well A3 and A5), showing a supratidal environment surrounded by intertidal sediments (Figure 3.6, 3.7 and 3.9).

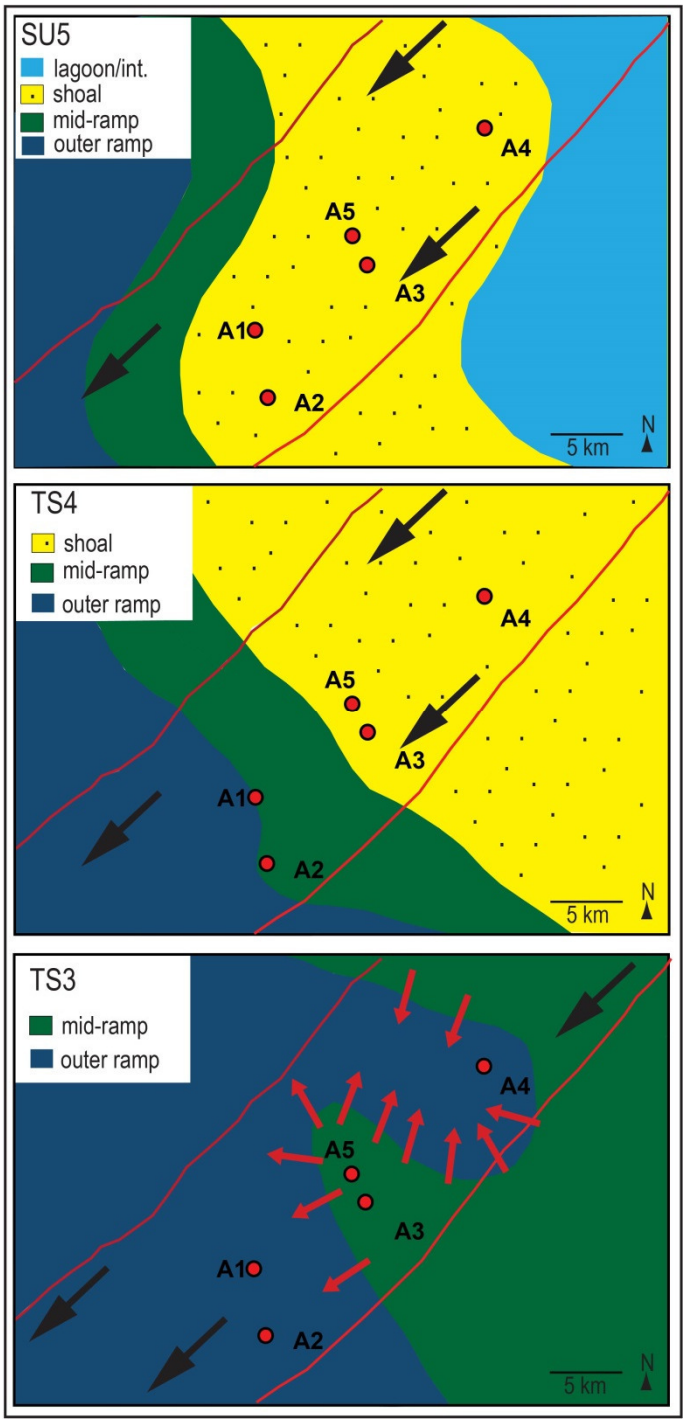


**Figure 3.10** *Progradation of the system towards southwest at time step TS4 and SU5. At TS4 the shoal facies are distributed in wells A3, A4, and A5. At SU5 the shoal complex progrades towards southwest covering all the wells. The black arrows highlight the main direction of progradation. The direction of progradation can be locally different and oriented towards many directions (little red arrows TS3), but comprises into the southwest main direction of progradation (black arrows TS3, TS4, And SU5).*

### 3.3.2 Field-scale temporal and spatial evolution

In correspondence to the available wells, the Arab Fm. started to deposit at the TS0 in an outer ramp environment, gently dipping towards the southwest. The initial topography was probably characterized by the presence of local highs, possibly due to halokinetic movements that occurred in all the Arabian Platform from the Late Paleozoic until present days (Alsharhan and Nairn, 1997). Salt movements may have affected the area during all the Arab Fm. deposition, causing the development of differential subsidence rates (Figure 3.11) due to the displacement of the salt diapirs through time and space. For example, at TS0, the wells A1 and A2 were probably placed on a local high (lower subsidence area, relatively thinner deposits), and the wells A3, A5 and A4 in a small trough of the ramp (higher subsidence rate, to some extent thicker deposits; Figure 3.11). Between TS0 and TS2 the outer ramp facies prevailed, smoothing the irregularities (thick deposits in A3/A4/A5) and filling a part of the accommodation space (Figure 3.11).

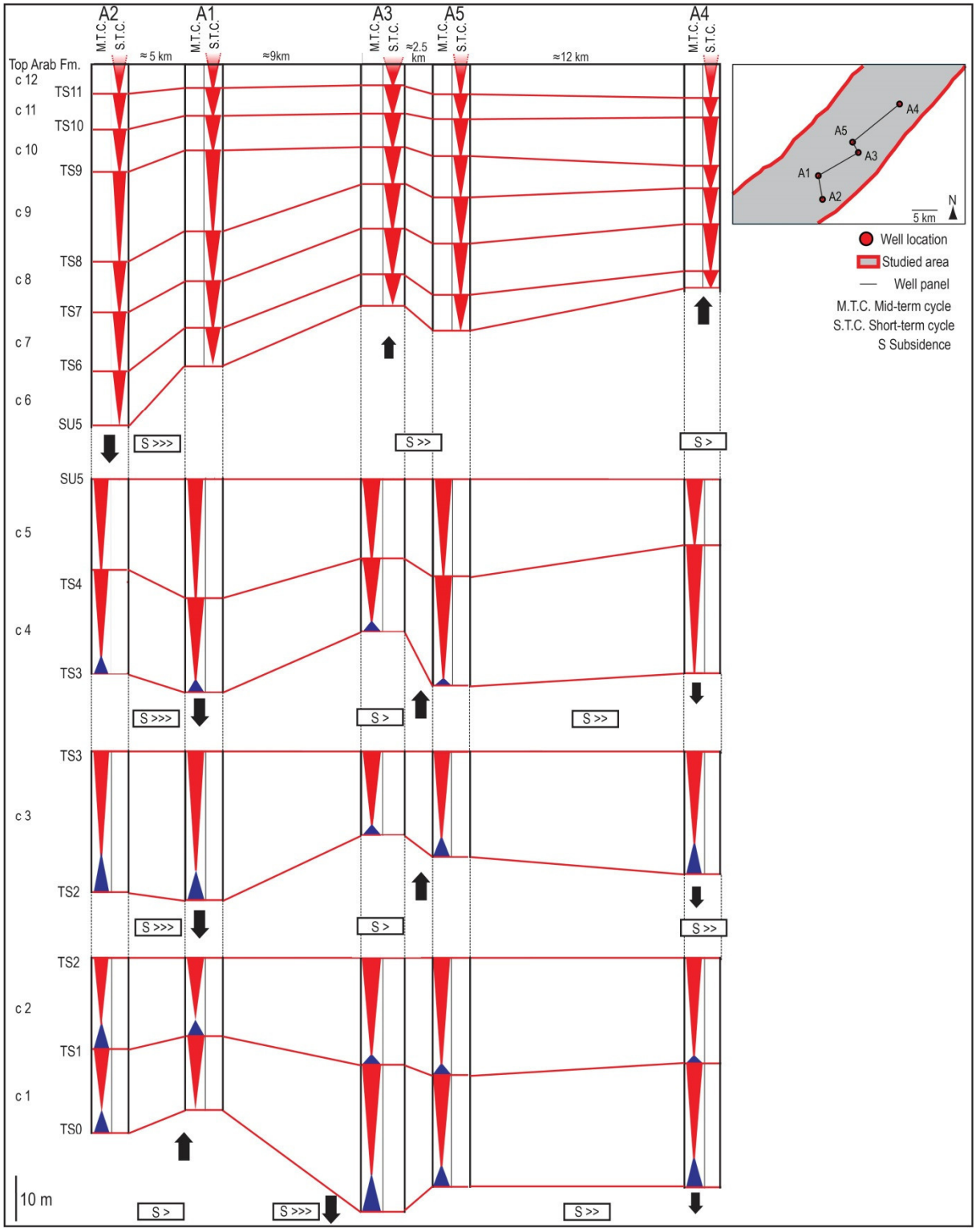


**Figure 3.11** *Well panel representing the intra-cycle thickness variations. The lateral changes in terms of thickness are related to different subsidence rates caused probably by the displacement of salt domes through time and space during the deposition of the Arab Formation. On the left: the black line represents the wells encompassed by the panel. For the legend see Figure 3.4C. Lateral distance of the wells not on scale.*

The salt rising produced subsequent migration of the local highs, situated for example under wells A3 and A5 (between TS2 and TS3) or under A3, A4 and A5 from SU5 until the top of the Arab Formation (thinner succession; Figure 3.11). The displacement of the salt diapirs could explain the presence of multiple transient directions of progradation during the deposition of the Arab Fm. (i.e. paleofacies maps at TS3 Figures 3.9 and 3.10). Between SU5 and the top of Arab Fm. the subsidence rate increases from northeast to southwest, where thicker successions were deposited (wells A1 and A2; Figure 3.11). The accommodation space was filled and the intertidal and supratidal facies were subjected to subaerial exposure (e.g. presence of mud-cracks and bird's eye). Despite the different subsidence rates and the rise of the sea level in the Upper Jurassic (Alsharhan and Magara, 1995; Ziegler, 2001) the Arab Fm. exhibit an overall shallowing upward.

### 3.3.3 A single interpretation?

The model presented here shows some discrepancies with a previous one recently developed for the Arab Fm. in the same area of study (see section 2.4.1). The model was proposed by Lawrence et al. (2015) for the Arab D Member, where a north-east progradation is invoked for the oolitic shoal complex. The facies associations identified for the Arab D are consistent in both of the works, where the Lawrence et al. (2015) foreshoal, active shoal and backshoal could be comprised in the shoal complex here defined. The Lawrence et al. (2015) interpretation is mostly based on facies correlation and paleocurrent data, and linear southeast-northwest trending features detected by the seismic analysis interpreted as depositional "beach/shoal ridges". With this respect, we observe that: i) the paleocurrent trends shown by the authors (fig. 13 in Lawrence et al., 2015 reported in Figure 2.8) are clearly bidirectional as commonly observed in tidal environments such as the Arab Fm. one; ii) the beach-ridges worked out from seismic data are consistent both with a northwest direction of progradation (Lawrence et al., 2015) and the southwest main direction of progradation suggested here.

In addition, some doubts can be expressed on the key stratigraphic surfaces identified in Lawrence at al. (2015), specifically on the Lower Sequence Boundary (LSB), represented by a dolomitized layer. They stated that the LSB evidences are present in the southwest part of the area (in wells not available for our study), but they traced the LSB across all the wells. The LSB could be tentatively guessed to coincide with a dolomite layer comprised in the cycle c4 of the here studied well A2 (Figure 3.7), in outer ramp sediments. The absence of

dolomites layers in the Arab D in the other wells makes difficult to relay on the stratigraphic depth position of the LSB defined by Lawrence et al. (2015). The new model, here proposed, is based on correlations that strictly combine the similar electrofacies signal and the core facies, highlighting trends and cyclicity. The correlations show the lateral variation of environments and progradation of the system, with the TS4 cutting mid-ramp deposits in the southwest of the area and shoal deposits on the northeast, with subsequent progradation of the shoal complex all over the studied wells (Figure 3.6, 3.7, 3.9 and 3.10). If we combine the LSB stratigraphic depth defined by Lawrence et al. (2015) with our vertical interpretation of facies (in the wells available in both the studies), we can prove the multiple directions of progradation detected by our study at the local scale due to the basin paleo-topography.

### 3.3.4 The Arab Fm. cyclicity: local controls

A cyclic stratigraphic pattern was recognized in all the wells, making possible the correlations of the Arab Fm. at the field scale (correlation panels and Figure 3.8). According to their hierarchical stack, the identified cycles have been labelled “long”, “mid” or “short” term cycles. The “long term” includes the entire Arab Fm. and reflects a shallowing upward trend, interpreted by different authors (summarized in Morad et al., 2012) as the regressive part of a second-order supersequence; thus in the Arab Fm. only the progradational part of the cycle is included. The mid-term cycles have been identified in the Arab D Member. They mainly correspond to prograding strata (i.e. highstand system tracts) that thicken towards the top of the Arab D Member. This mid-term cyclicity could be compared with the sequence stratigraphic pattern established in Morad et al. (2012), in an offshore Abu Dhabi field. In Morad et al. (2012) the identified stratigraphic surfaces in the Arab D bound shallow water facies associations (supratidal/intertidal and lagoonal environments). Instead in the field of interest for this thesis, the lagoonal and supratidal facies were deposited and preserved only at the top of the Arab Fm., i.e. in members A-B-C. This discrepancy suggests that field here studied was located in a deeper area of the intrashelf basin. Consequently, the stratigraphic surfaces identified in the field by Morad et al. (2012) may not be recorded (or not clearly evident) in the field studied for this thesis, as it was in a more basinal location. The cycles detected in the here studied onshore field could be bounded by conformable surfaces and the cyclicity could be recorded only at the field scale.

In the Arab A-B-C, short-term cycles are observed, marked by the distinct alternation of the lagoonal/intertidal and the evaporitic facies. This short-term cyclicity is similar to the one

recorded in another onshore Abu Dhabi field studied by Grötsch et al. (2003), that they refer to variations in accommodation through time. The possible discrepancy in the number of cycles detected could be linked to local emersions due to subtle variations in subsidence that could not necessarily be recorded everywhere in the onshore Abu Dhabi area. The presence of some local subsidence variations, due to substratum diapiric motions, could lead to local changes in accommodation space/fluctuations in the relative sea level, inducing a local scale cyclicity.

### 3.3.5 A regional overview: a new piece of the puzzle

The stratigraphic pattern established for the field studied in this thesis can be tentatively used for tracing some correlations to several other fields in the so-called Rub' Al Khali basin reported in the literature (e.g. Al-Silwadi et al., 1996; Al-Emadi et al., 2009; Morad et al., 2012; Grötsch et al., 2003).

In particular the top of the Stromatoporoid Zone (Al-Silwadi et al., 1996) reported in a well panel drawn in Al-Silwadi et al. (1996) for the Abu Dhabi offshore area (just a portion of the west-east cross section of Al-Silwadi et al., 1996) was considered for this study, here after called offshore transect (Figure 3.12). It can be used as the best chronologically constrained timeline to draw a regional scale correlation, together with the last occurrence of stromatoporoids (*Cladocoropsis* spp.) detected in the onshore field studied here (hereafter called onshore studied field/present thesis; Figure 3.12). The top of the zone encompasses lagoonal and shoal deposits in the offshore transect (from west to east), and mid-ramp facies in the studied field (southward Abu Dhabi City; Figure 3.12A).

That correlation highlights a facies distribution in the Abu Dhabi area (Figure 3.12B) different from the Kimmeridgian-Tithonian paleofacies maps proposed by Ziegler (2001) (reported simplified in Figure 2.4). Specifically, according to Ziegler (2001), the studied field should have been placed in the eastern margin of an intrashelf basin with deep carbonate facies in the depocenter, surrounded by shallow marine deposits (Figure 2.4). Conversely, the correlation of the top of the Stromatoporoid Zone suggests that, at that time, the intrashelf basin was shifted somewhere toward east (as yet inferred by Grötsch, et al., 2003), possibly connected with the deep marine basin occurring along the present-day of the Gulf of Oman area according to Ziegler (2001) (Figure 2.4).

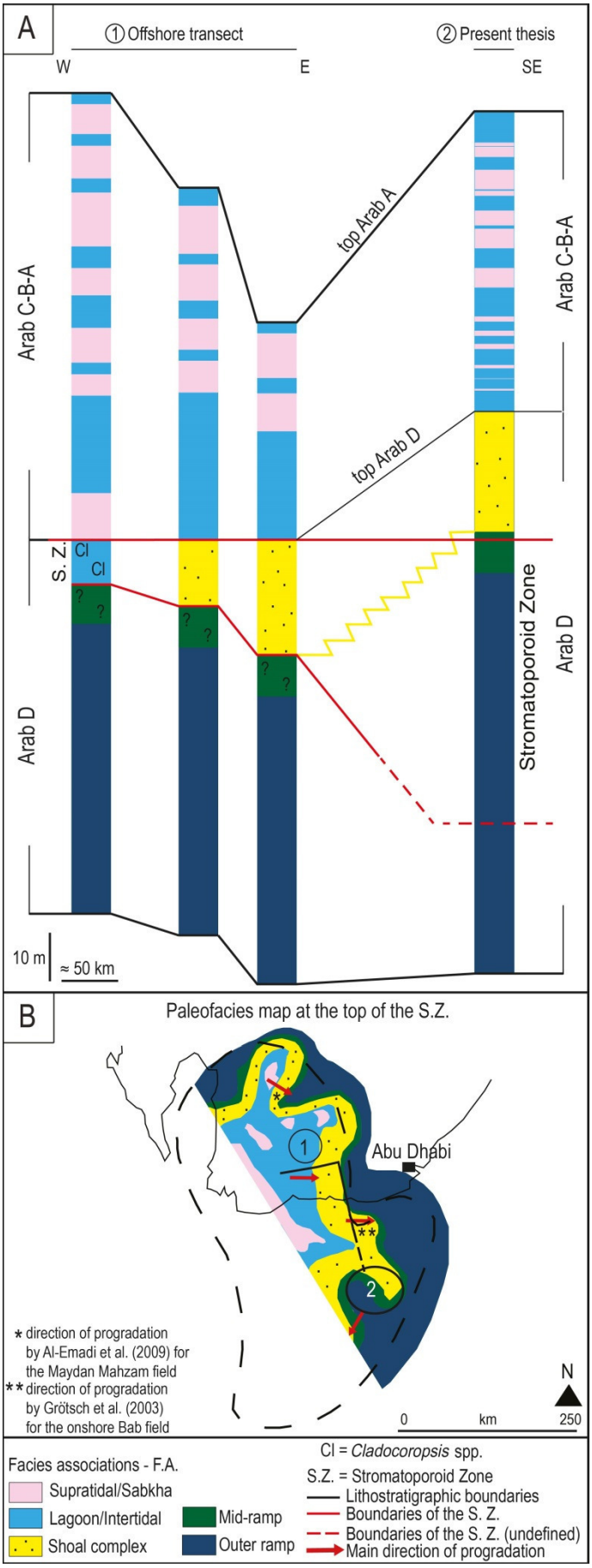


**Figure 3.12** *A) Correlation of the Stromatoporoid Zone from the "offshore transect" (number 1; redrawn, modified and simplified from Al-Silwadi et al., 1996) and the onshore studied field (number 2 "present thesis" schematic well of Figure 3.8). The wells are flattened on the top of the Stromatoporoid Zone (S.Z.). The lower boundary of the S.Z. is undefined. In the offshore transect the thickness of the mid-ramp in not defined. For the location of the transect see frame B. B) Interpretation of the paleofacies distribution at the top of the S.Z. of the Arab Fm. in a regional overview according to the correlation in frame A. The black dashed line represents the boundaries of the Rub' Al Khali intrashelf basin redrawn from Ziegler (2001) (see Figure 2.4 for more details on the geological setting). The red arrows represent the main directions of progradation of the Arab Fm. gathered from literature (Al-Silwadi et al., 1996; Grötsch et al., 2003; Al-Emadi et al., 2009) and from this study. The area of study for this thesis is roughly located inside the circle number 2. The location and the distance of the field of study depicted in the frames A, and B are on purpose approximated and imprecise.*

The here proposed regional paleofacies map (Figure 3.12B) significantly modifies the one suggested by Ziegler (2001) and explains the different directions of progradation reported for the Arab Fm. in the literature (towards east according to Al-Silwadi et al., 1996; toward east in the onshore Bab field

according to Grötsch et al., 2003; toward south-east for the Maydan Mahzam field in offshore Qatar according to Al-Emadi et al., 2009). Within this regional scale frame, local differences, as for instance the southwest directions of progradation suggested in this thesis at the local scale (Figure 3.12B), can be explained through shoreline promontories and embayments possibly due to differential subsidence related to halokinetic activity in the substratum.

## 3.4 Conclusions

The main peculiarities of the new established depositional model for the Arab Fm. (members A-B-C-D) in an onshore Abu Dhabi field can be summarized as follows:

- Eighteen sedimentary facies grouped into five facies associations highlight a succession deposited in a shallow marine carbonate ramp, comprised in an overall long term shallowing upward trend. The D Member is characterized by outer ramp, mid-ramp and shoal deposits organized in five mid-term cycles. The Arab A-B-C is defined by seven short-term cycles, showing alternation of peritidal environments (subtidal lagoon, intertidal flat and supratidal/sabkha).

- During the deposition of the outer ramp and mid-ramp, a shelly-rich shoal and an open lagoon were located in a landward position not recorded in the available wells. The outer ramp and mid-ramp environments are often interbedded with erosive and sharp based floastones identified as storm events, characterized by transported inner ramp originated bioclasts (such as *Kurnubia* spp., *Cladocoropsis* spp., *Nautiloculina oolitica* and dasyclad algae).

- The shelly-rich shoal evolves into an ooid-rich shoal complex, detected in the wells used in this study. This shoal complex encloses a protected lagoon, no more open, but characterized by restricted water circulation and salinity variations (low abundance and diversity of biota, presence of ostracods and peloids). The lagoon is constantly subjected to (local) emersion with the deposition of intertidal and supratidal deposits (microbial mats, desiccation cracks, bird's eye fenestrae, and precipitation of sulfates/sabkha facies).

- At the scale of the studied field, the evolution of the Arab Fm. was gathered by correlating eleven transgressive surfaces and one subaerial unconformity through all

the wells. The paleofacies maps pictured in their correspondence show a main progradation of the Arab D member towards southwest, but different directions of progradation can be detected at local scale, related to the presence of topographic irregularities.

- A new paleogeographic picture is tentatively proposed at the regional scale for the Arab Formation time, correlating the top of the Stomatoporoid Zone in the on- and offshore Abu Dhabi regions. According to this new picture a NNW-SSE running, eastward prograding basin margin existed west of Abu Dhabi City, possibly connected with the deep marine basin located in the present-day area of the Gulf of Oman.

# Chapter 4

# 3D FORWARD MODELLING OF A PROGRADING CARBONATE RAMP: A QUANTITATIVE ANALYSIS

This chapter mainly derives from a paper submitted to Sedimentary Geology, here adapted and integrated with some additional material. The article is entitled: "3D stratigraphic forward modelling of a carbonate ramp: a quantitative field-scale analysis of the Arab Formation (Upper Jurassic, onshore Abu Dhabi, UAE)", by **Marchionda, E**., Deschamps, R., Nader, F.H., Di Giulio, A., Al Darmaki, F., Ceriani, A. Similarly to Chapter 3, the introduction and the geological setting are reported in Chapter 1 and 2. The main achievements are summarized at the end of this chapter and then reported in the conclusive Chapter 5.

## 4.1 Model set up

### 4.1.1 3D stratigraphic forward modelling

The second part of this thesis was developed by means of DionisosFlow™ (Granjeon, 1997; Granjeon and Joseph, 1999; IFPEN/Beicip-Franlab; www.beicip.com), a 3D deterministic dynamic-slope model, where the sediment distribution is simulated by the use of a generalized, modified diffusion equation (Burgess et al., 2006; Burgess et al., 2008).

A deterministic approach is based on physical equations to constrain as far as possible the physical parameters on the available data (from exploration or appraisal processes) in contrast to the probabilistic laws of stochastic models (Granjeon and Joseph, 1999; Rabineau et al., 2005). Among the different forward simulations, a dynamic-slope model is intermediary between a geometrical and a fluid-flow one (Granjeon and Joseph, 1999). The former reproduces 2D stratigraphy, without considering the dynamic of sediment transport, the latter computes very detailed physical equations to simulate the 3D movement of the sediments, hardly constrainable on well log or seismic (Granjeon and Joseph, 1999). On the contrary a dynamic model, due to its simplicity, fits real data with the combination of an empirical transport law and the continuity equation for sediment (Granjeon and Joseph, 1999).

DionisosFlow™ has been developed (by IFPEN/Beicip-Franlab) in order to quantify the average geometry of sedimentary units and their average facies content, but it does not simulate each geological process in detail (e.g. each tidal bar; Granjeon and Joseph, 1999).

The model can be used as a tool in order to represent the dynamic and the filling of a sedimentary basin at a scale from several to hundreds of kilometers, and from several hundreds of thousands to tens of million years (Granjeon and Joseph, 1999; Granjeon, 2014).
The 3D architecture is built by the step by step quantification of accommodation space, sediment supply and/or *in situ* marine production (as in this work), and transport for each cell (square mesh) of the basin (Granjeon, 2014; Bruneau et al., 2016), simulating the geological processes from a fixed age in the past and moving forward in time (Granjeon and Joseph, 1999; 4D diffusion modelling).
In the simulations here presented, a slope gravity-driven diffusion equation was computed for each cell of the model grid: $Q = \kappa S$ (Granjeon, 1997; Granjeon and Joseph, 1999, Williams et al., 2011). The equation proportionally links the sediment supply rate Q ($km^2/kyr$) to the surface gradient S at a point in the model grid, where $\kappa$ is the gravity-driven diffusion coefficient ($km^2/kyr$), defined by the user for each type of sediment grain.
The transport, linked to the surface gradient, is related to the *in situ* carbonate production: steep slopes formed by sediment production are affected by higher transport rates, but the removing of sediments influences depositional depths and in turn the carbonate production (Williams et al., 2011).
Up to now DionisosFlow™ modelling has been applied to different cases of study on carbonate or siliciclastic (or mixed) systems (Rabineau et al., 2005; Alzaga-Ruiz et al., 2009; Sømme et al., 2009; Williams et al., 2011; Csato et al., 2013; Seard et al., 2013; Gvirtzman et al., 2014; Montaggioni et al., 2015; Kolodka et al., 2016), providing different cases of study such as atoll, reef or shelf break development, or insights in the Messinian salinity crisis in the circum-Mediterranean region. Here it is used to model and discuss the factors driving the evolution of a carbonate ramp system.

### 4.1.2 Workflow

Several parameters were inserted in the model editors and tuned by trial and error, until to reach a model calibrated on the five available wells, here presented as the Reference Model (hereafter REF). The model portrays a possible depositional scenario for the Arab Fm., where the input data are summarized in Table 4.1 and the most important are explained in the next sections. Initial topography and subsidence maps were combined with the eustatic oscillations in order to establish the available accommodation space; in addition the carbonate production curves and transport parameters were defined for each lithology involved in the model.

**Table 4.1** *List of the Reference Model (REF) input parameters.*

| REFERENCE MODEL - REF | |
|---|---|
| **PROPERTIES** | **VALUES** |
| Domain; Simulation Interval | Area: 100x80 km; Square mesh: 2x2 km; 154.6 Ma-148.5 Ma |
| Sediment Classes (grain sizes) | Carbo_Grains (CG): 1 mm (sand granulometry)<br>Carbo_Mud (CM): 0.04 mm (silt granulometry)<br>Carbo_Evapo (CE): 0.001 mm (mud granulometry) |
| Eustatic Curve (combination of two curves) | First curve - sinusoidal curve: Period: 0.4 Ma; Amplitude: 2 m<br>Second curve: Long Term Haq (Haq et al., 1987) |
| Maximum production rate (constant through time) | CG CM CE<br>(m/Ma): 212 44 16 |
| Environmental constraints on the production | CG: Wave Energy (kW/m) 20 – max<br>CE: Wave Energy (kW/m) min – 10 |
| Waves | Wave 1 (W1): wave base 15 m; Azimuth 50°;<br>Frequency (year) 100%<br>Wave 2 (W2): wave base 20 m; Azimuth 50°; Frequency (year) 10% |
| Transport parameters | Gravity-driven diffusion coefficient CG CM CE<br>*K* ($km^2$/kyr) Continental: 0.005 0.01 0.0001<br>Marine: 0.005 0.01 0.0001 |
| Evaporation (constant per simulation interval) | 1500 mm/yr |
| Simulation Time Step | 0.1 Ma |

The calibration was done organizing the observed facies associations of the five available wells (hereafter called real wells) into macro environments, in turn compared with the modelled ones in the simulated wells in terms of thickness and stratigraphic distribution. The simulated wells are the result of the vertical succession of cells in correspondence of the locations of the real wells. If a simulated macro environment (macroenv) is equal in term of thickness to the corresponding one in the real well, the calibration match is of 100%; the percentage decreases with poorer fits. The average of the matches percentages was evaluated according to this formula for each defined macro environment (equation n. 1):

*eq. 1*

$$macroenvAverageMacth = \frac{1}{5} \times \sum_{n=A1}^{A5} macroenvMatch(n)$$

(with *n* corresponding to the available wells: A1, A2, A3, A4, and A5)

A satisfactory model calibration was considered when the average of the matches between all the different macro environments between the five wells (TOT value) was above the 80%.

The REF model was the starting point of the sensitivity analysis that was carried out testing different ranges of parameters (including the values of the REF model) defined randomly by the user, changing one input value per time.

The following input parameters were tested: i) initial topography; ii) subsidence; iii) carbonate production; and iv) diffusion coefficients. At each test the response of the model was evaluated in terms of facies distribution and thickness, always in respect with the five available wells. The sensitivity analysis followed a "waterfall workflow", i.e. if a tuned parameter simulates a better calibrated model, this parameter is kept fixed for the subsequent analyses, obtaining gradually improved best-fitting models. In each 3D model pictured in the following paragraphs (and in the related cross sections) the length and the width are cut of 10 km at each side in order to avoid representing possible boundary effects. The vertical axis (m) represents all the deposits simulated in the entire computed time interval (154.6-148.5 Ma).

## 4.2 Dataset and inputs

### 4.2.1 Sediment classes and carbonate production

Three sediment classes based on different grain sizes were defined (from coarser to finer: Carbo_Grains, Carbo_Mud, and Carbo_Evapo), that can be considered as the basic lithologies building up the carbonate ramp in the Arab Fm. case of study (Table 4.1). For each sediment class, coefficients of sediment production versus depth were fixed (Figure 4.1A; negative depth values below the average sea-level fixed at 0 m and positive above it), i.e. a curve of values (dimensionless) that ranges from 0 (nil production) to 1 (maximum production). These coefficients were multiplied for a maximum production rate (m/Ma) chosen by trial and error for each sediment class and kept constant for the entire simulation time interval (Table 4.1). For the Carbo_Grains (CG) class the curve starts at 0 m with a nil production that rapidly increases toward the maximum coefficient of production at -5 m of depth. From this maximum value, the curve decreases toward nil production (depth of -20 m). This curve represents a factory of coarse carbonates located at shallow depths, with maximum production in shallow subtidal/submerged setting (e.g. production curves of: Read et al., 1991; Demicco, 1998; Pomar, 2001; Boylan et al., 2002). For the Carbo_Mud (CM) class the production slowly increases with depth until to reach its maximum value at -20 m and then it is steadily kept constant toward deeper bathymetries. An opposite trend was established for the Carbo_Evapo (CE) sediment class: the production was constrained at shallow bathymetries from 0 to -10 m that could be identified with the production of lagoonal/intertidal fine sediment (e.g. microbial mud) or with the evaporitic sediment precipitated. The combination of Carbo_Evapo and Carbo_Mud curves provides a more or less uniform production with depth of fine sediments (e.g. the mud-producing biota curve in Pomar, 2001). In addition, the

production of Carbo_Evapo and Carbo_Grains was constrained according to the wave energy; a minimum of 20 km/W and a maximum of 10 km/W thresholds were set for the Carbo_Grains and for the Carbo_Evapo production respectively.

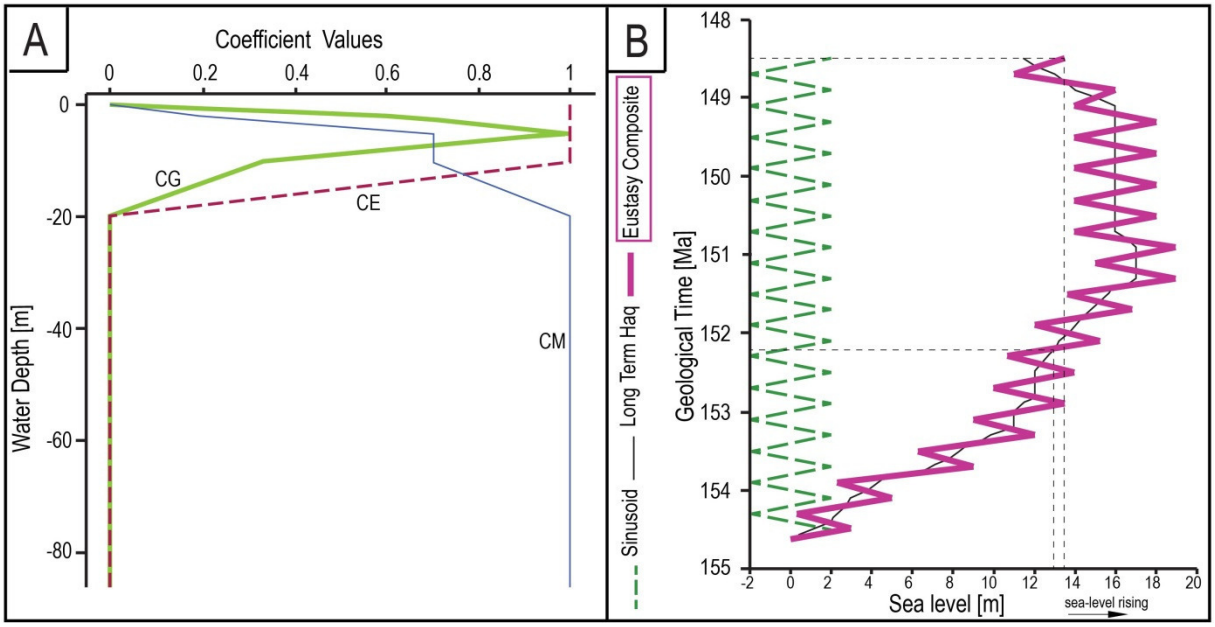


**Figure 4.1** *A) Curves of production versus depth for each sediment class. The values represented in the curves need to be multiplied for the maximum production rates inserted in the different simulations (Table 4.1 and 4.3). Negative depth values below 0 m. B) Composite eustatic curve computed in the simulations (lilac curve). The curve is the combination of a sinusoidal ("sinusoid" green color) curve (period 0.4 Ma and 2 m in amplitude) and the Long Term Haq curve (Haq et al., 1987). Positive values refer to the sea-level rising above 0 m. The black dashed lines represent the values of the eustatic curve in correspondence of the key ages that constrain the model. At 152.2 Ma (top Arab D) and 148.5 Ma (top of the Arab Fm.), values of +13 m and +13.5 m correspond in the composite eustatic curve respectively. See the text for further details.*

### 4.2.2 Age model, eustasy and greenhouse conditions

The simulation time interval was defined according to the orbital forcing AROS J/C chart and following updates, where the Arab Fm. could be comprised between 154.6 Ma and 148.5 Ma, with the top of the Arab D at 152.2 Ma (Al-Husseini and Matthews, 2008; Al-Husseini, 2008; Al-Husseini 2009). These ages were used to constrain the simulation, even if they probably cover a depositional interval larger than the Arab Formation (Figure 2.6). According to these ages, a composite eustatic curve was defined (Figure 4.1B; positive values above 0 m corresponding to sea-level rising) in order to simulate the relative sea-level oscillations that could have affected the deposition of the Arab Formation. The curve combines a sinusoidal constant curve with the Long Term Haq curve (Haq et al., 1987). The sinusoidal curve was inserted with a fixed period of 400 ky and a constant amplitude of 2 m. The oscillation period

of 0.4 Ma can be compared to the term of largest amplitude in the eccentricity of 0.405 Ma proposed by Laskar et al. (2004) for the calibration of the Mesozoic times scale and suggested to form the fourth-order depositional sequence in the AROS J/C chart (Al-Husseini and Matthews, 2008; Al-Husseini, 2008; Al-Husseini 2009). The 2 m amplitude should reproduce the slight sea-level fluctuations into an arid region during a greenhouse climate period (e.g. Williams et al., 2011) that should have characterized the Late Jurassic (Al-Saad and Sadooni, 2001; Rameil, 2005; Rameil, 2008).

### 4.2.3 Domain and basinal settings

A bathymetry map was inserted (light blue circle; Figure 4.2) at the beginning of the simulation (154.6 Ma) representing the initial topography at the base of the Arab Formation (negative bathymetric depth values below the average sea-level fixed at 0 m and positive above are displayed for all the bathymetry inputs and outputs of this thesis). The map covers an area of 100x80 km (domain of the model), with square meshes of 2x2 km. The area depicts a south-west dipping carbonate ramp, ranging from -2 m to -50 m. The modelled area was chosen larger than the field of study (wells locations reported in Figure 4.2), in order to visualize the temporal evolution of the main depositional environments on the entire ramp. At the bottom of the Arab Fm., all the wells show evidences of a relative deep outer ramp setting (see section 3.2.2), and an initial bathymetric range from -21 to -32 m was computed across the wells. The map was bounded in its north and east side by two "walls" (100x4 km and 4x80 km respectively; +500 m in elevation; the walls will be not represented in the output models), with the aim to avoid any possible sedimentary/water flux coming from northeast (Figure 4.2). At 152.2 Ma (top Arab D member) a second bathymetry map depicts a shallower environment, where potential salt dome rising produces a morphology of the margin with embayements and promontories (Figure 4.2). This morphology could be probably related to the deep-seated salt movements occurring in all the Arabian Platform since the Late Paleozoic until present days (Alsharhan and Nairn, 1997; see Chapter 3). Two thickness maps were defined for the Arab D (154.6-152.2 Ma) and the Arab A-B-C members (152.2-148.5 Ma; green squares; Figure 4.2). Thickness and bathymetry maps are based on user interpolations on the well thicknesses and bathymetric interpretations from the observed facies associations.
By the combination of bathymetry and thickness maps, the software automatically computes two subsidence maps at 152.2 Ma (top of the Arab D) and 148.5 Ma (top of the Arab Fm.). The two maps report the subsidence values in meters, considering for the first one the interval

of deposition between 154.6 and 152.2 Ma, for the second one the entire simulated time interval. The subsidence maps, together with the initial bathymetry and the eustatic curve, are taken in account to simulate the evolution of the accommodation space through time.

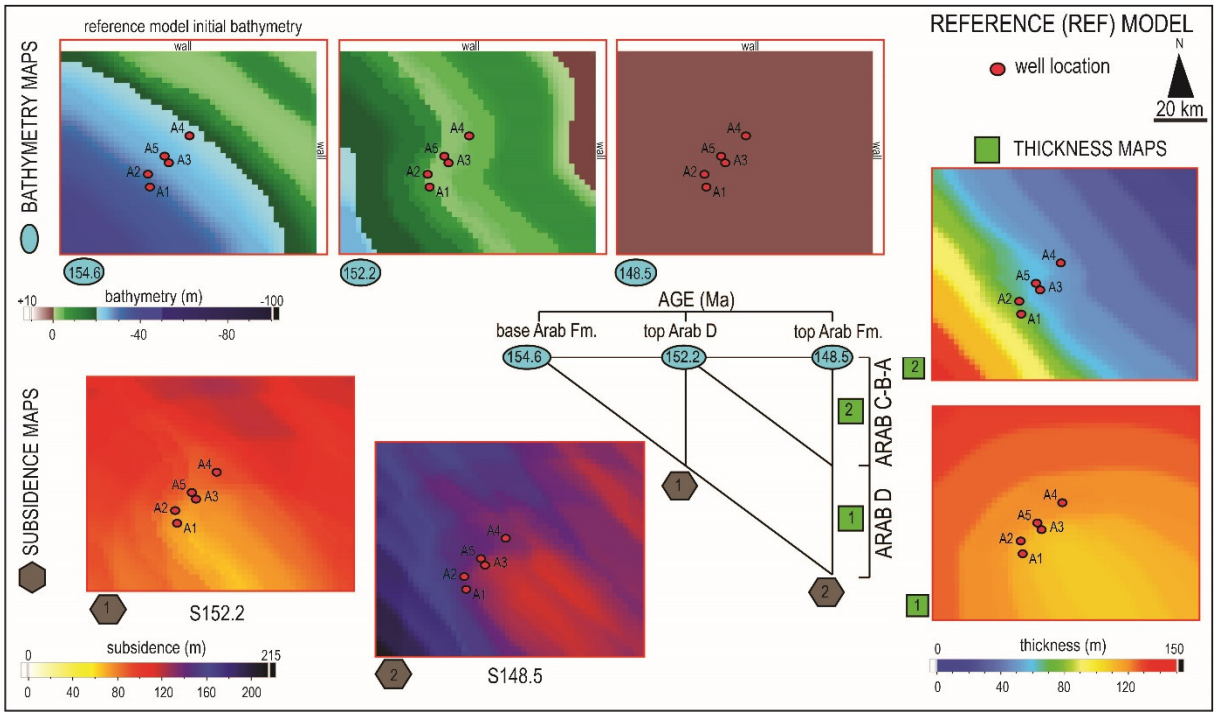


**Figure 4.2** *Bathymetry, thickness and subsidence maps inserted in the Reference Model (REF). At each map a number is associated corresponding to a time step in the age model diagram (center of the Figure). Bathymetry (negative bathymetric depth values below the average sea-level fixed at 0m and positive above it) and thickness maps are drawn starting from the available wells, interpreting the surrounding area with no other constraints. Combining these two kind of maps, the software automatically computed two subsidence maps, that in the REF model were corrected for values of -13 m (S152.2 map) and -13.5 m (S148.5 map) to account for the eustatic sea-level change. The corrected maps are pictured in the Figure.*

In the REF model, the automatically computed subsidence maps were corrected for values of -13 m and -13.5 m at 152.2 Ma and 148.5 Ma respectively (hereafter named S152.2 and S148.5 maps), as a software requirement, in order to balance the increase in accommodation space related to the composite eustatic curve (Figure 4.1B). The curve shows a gradual sea-level rising from 0 m at 154.6 Ma to +13 m (152.2 Ma) and +13.5 m at 148.5 Ma (positive values above 0 m). In the S152.2 and S148.5 the wells are comprised between subsidence values of 74-92 m and 122-146 m respectively.

## 4.3 Results

### 4.3.1 The Reference Model (REF)

The REF model displays an overall southwest progradation of a carbonate ramp, where the main part of the simulated strata has an inclination lower than 0.15°. The deepest bathymetry is reached at the bottom of the model, with a maximum depth of -46 m. Toward the top of the simulation the sediments are deposited in shallower environments, oscillating between values above and under 0 m (brown and light green colors respectively). Slight higher steep strata break the slope (greenish colors, with an estimated slope comprised between 0.15° and 0.5°) that divide the 3D geological simulation in a relative deep and a shallow domain, in front and behind the slope break respectively (Figure 4.3A). The slight slope break partitions the block according to several output properties as shown in Figure 4.3. At the slight slope break, highest percentages of Carbo_Grains sediment class are present with a maximum value of 91%, and the most energetic waves impact at a maximum of 135 kW/m.

In front of the slight slope break (toward the southwest), the relative deep domain is characterized by normal salinity, lower wave energies and higher Carbo_Mud concentration reaching the value of 100% in several cells. Behind (northeastward), the cells of the model are populated by mixtures of Carbo_Evapo and Carbo_Mud sediment classes, with minor Carbo_Grains percentages. This shallow domain is characterized by low waves energies and high salinity (Figure 4.3).

- ***Facies distribution***

According to the distributions of the output properties, the facies (Table 4.2) that build the REF model were defined (Figure 4.4). Six facies were established, mainly based on textural properties that we are going to call simulated facies (hereafter SF). The SF were mainly defined according to the Carbo_Grains distribution. Mudstones, Wackestones, Packstones and Grainstones SF display an increasing content in Carbo_Grains, and can be deposited until the maximum values above sea-level at which water can be simulated by the model (i.e. +3 m). According to the depositional domains in the 3D geological simulation (Figure 4.4), the Grainstones and the Packstones SF are deposited mainly at the slight slope breaking strata. These strata could simulate the shoal complex, detected in the Arab Fm. real wells, acting as a submerged margin barrier (e.g. Ruf and Aigner, 2004; Aigner et al., 2007; see section 3.2.2).

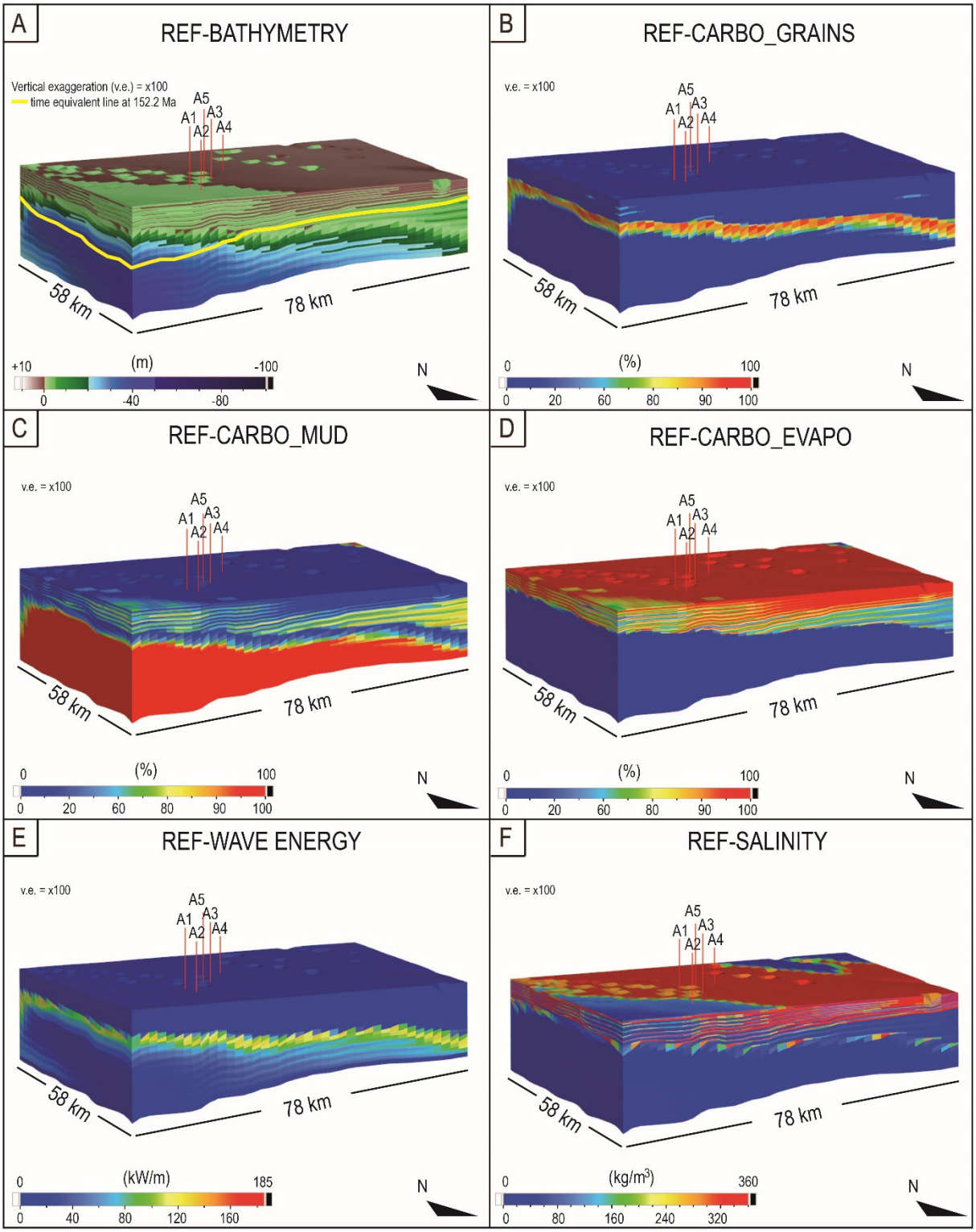


**Figure 4.3** *3D representation of the Reference Model (REF), according to different simulated output parameters: A) bathymetry (negative values below 0 m); sediment classes distribution of B) Carbo_Grains; C) Carbo_Mud; D) Carbo_Evapo; variations in E) wave energy; and F) salinity. In each 3D model, the length and the width are cut of 10 km at each side in order to avoid representing possible boundary effects. In each model the vertical scale is exaggerated 100 times. In the frame A, the 152.2 Ma time equivalent line cutting the model is also displayed.*

**Table 4.2** *Properties of the different simulated facies (SF) defined in each model presented in this thesis. The SF are comparable with the observed facies associations (F.A.) detected in the real wells, and grouped in order to represent different depositional macro environments.*

| **SIMULATED FACIES (SF)** | **MUDSTONES** | **WACKESTONES** | **PACKSTONES** | **GRAINSTONES** | **EVAPORITES A** | **EVAPORITES B** |
|---|---|---|---|---|---|---|
| BATHYMETRY | +3 – -130 m | +3 – -130 m | | | | |
| CARBO_GRAINS | 0-20 % | 20-50% | 50-70 % | 70-100% | 0-3.45 % | 0-3.45 % |
| CARBO_EVAPO | | | | | 55-100 % | |
| SALINITY | | | | | 360 kg/m$^3$ | |
| **OBSERVED F.A.** | | | | | | |
| OUTER RAMP | X | X | | | | |
| MID-RAMP | X | X | | | | |
| SHOAL COMPLEX | | | X | X | | |
| LAGOON/ INTERTIDAL | X | X | | | | |
| SUPRATIDAL/ SABKHA | | | | | X | X |
| **GROUP OF SF (macro environment)** | | | | | | |
| OMR (outer + mid-ramp) | X | X | | | | |
| SHC (shoal complex) | | | X | X | | |
| LIST (lagoon/inter + supratidal) | X | X | | | X | X |

The Mudstones and the Wackestones SF represent both the outer and mid ramp deposits (relative deep domain in front and at the base of the slight slope break), or the lagoonal/intertidal ones (shallow domain, northeastward to the shoal complex). Concerning the evaporitic layers, identified in the Arab succession, two SF were defined (called Evaporites A and Evaporites B; Table 4.2). The Evaporites A SF displays a fine sediment deposited under simulated high salinity, linked with the intertidal/supratidal evaporitic precipitation. The Evaporites B SF is computed in the modeled area above +3 m (where the software does not allow simulating water and thus salinity), in order to represent sediment deposited in a supratidal/continental setting. The Evaporites A and B SF are repeatedly intercalated to Mudstones and Wackestones SF in the shallow domain behind the grainy shoal complex (low wave energy with salinity fluctuations; Figure 4.4).

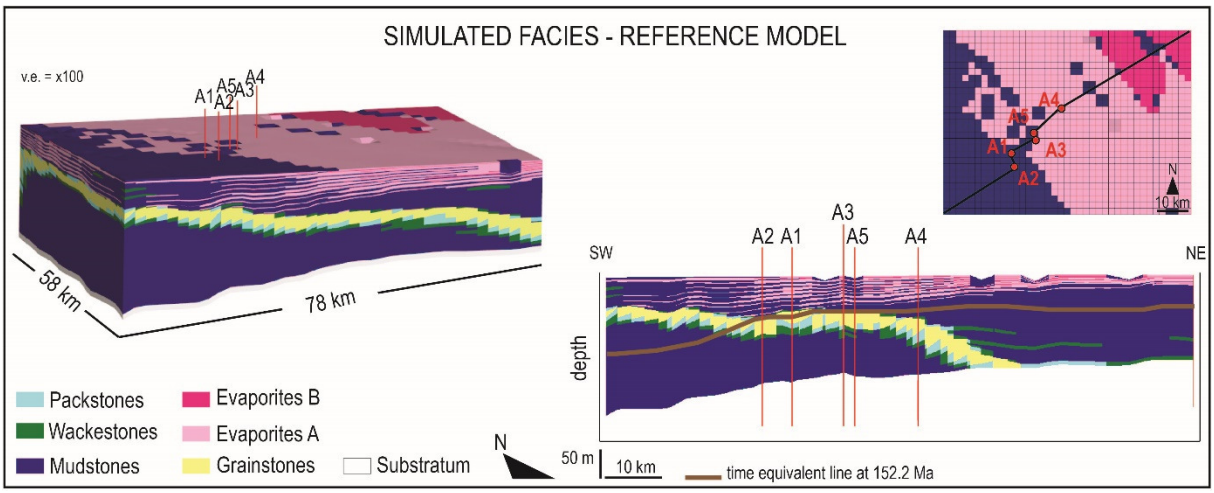


**Figure 4.4** *Distribution of the simulated facies in the Reference Model. The facies are displayed in 3D and according to a cross section that encompasses the available wells, in a SW-NE transect. The 3D model (and the related cross section) is cut in the length and in the width at each side of 10 km in order to avoid representing possible boundary effects. The substratum represents strata older than the Arab Formation.*

- ***Calibration: simulated vs. real wells***

In the simulated wells, the simulated facies were arranged in facies associations descriptive of a specific depositional setting and grouped in three macro environments (OMR: outer + mid-ramp; SHC: shoal complex; LIST: lagoon/inter + supratidal; see Table 4.2). The vertical simulated stacking pattern is comparable with the vertical distribution of environments in the real wells. Considering the five wells, the REF model has an average match between simulated and observed groups of facies associations (eq. 1) of: 85.5% for the OMR, 80.4% for the SHC, and 82.4% for the LIST (Figure 4.5).

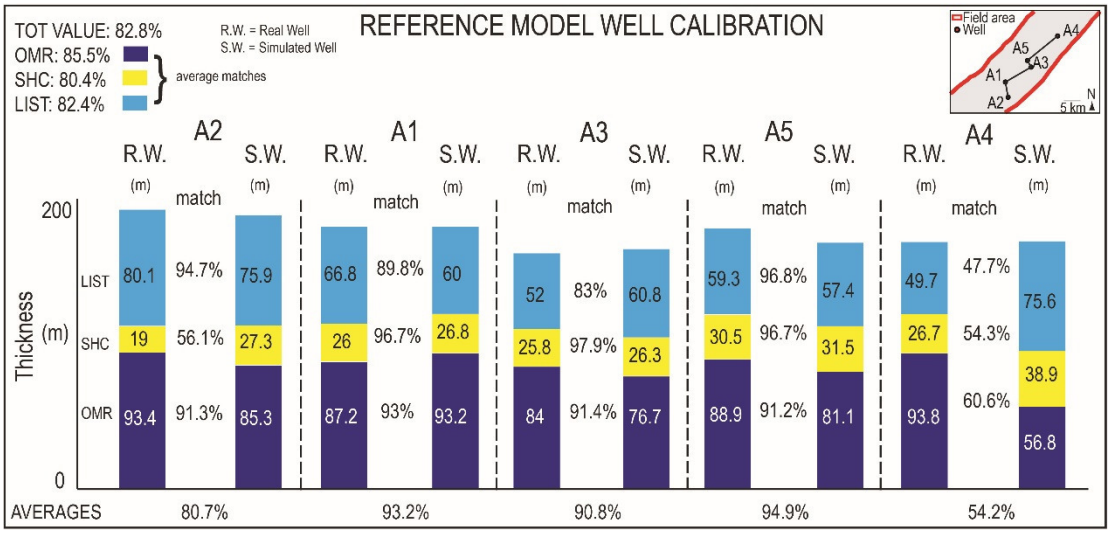


**Figure 4.5** *Comparison between the real (R.W.) and simulated wells (S.W.), according to the distribution and thickness of the three macro environments (LIST, SHC, OMR). The wells are reported in a southwest to northeast transect. The lateral distance between the wells is not on scale.*

For the REF model, the average (TOT value) between the three average matches has a value of 82.8%. Punctually, each simulated well shows an average match between the macro environments above 80% except for well A4 with an average match of 54% (Figure 4.5).

### 4.3.2 Sensitivity analysis

Initial topography, subsidence, carbonate production and diffusion coefficients were tested, according to random user defined ranges, in order to understand how these parameters impact on the deposition of the Arab Formation. For each set of simulations, a graph is reported showing the average in percentage between the matches of each macro environment between the five wells (eq. 1) and the TOT value. Each tested model with the related main parameters is listed in Table 4.3 (the data sheets of the sensitivity analysis are reported in Appendix 3; for all the models not graphically reported on this chapter refer to Appendix 4).

**Table 4.3** *List of the models presented in the thesis with the values assigned at the main inputs. For the parameters not reported here refer to the ones of the Reference Model (Table 4.1). In all the models the evaporation is set at 1500 mm/yr except for the E500 and E2500 models. Underlined the simulations that provided a better refinement (higher calibration).*

| PARAMETER TESTED | MODEL NAME | MAIN PARAMETERS |
|---|---|---|
| Initial topography | Salt Dome SD | Initial bathymetry: salt dome initial bathymetry<br>Subsidence maps: S152.2b – S148.5b (S0 maps -13m and -13.5m)<br>Maximum production: CG CM CE<br>(m/Ma) 212 44 16<br>Gravity-driven diffusion coefficient CG CM CE<br>*K* ($km^2$/kyr) Continental: 0.005 0.01 0.0001<br>Marine: 0.005 0.01 0.0001<br>Evaporation: 1500 mm/yr |
| Subsidence | S0 | Initial bathymetry: salt dome initial bathymetry<br>Subsidence maps: S0 maps (computed by the software)<br>Maximum production: CG CM CE<br>(m/Ma) 212 44 16<br>Gravity-driven diffusion coefficient CG CM CE<br>*K* ($km^2$/kyr) Continental: 0.005 0.01 0.0001<br>Marine: 0.005 0.01 0.0001 |
| Subsidence | S12 | Initial bathymetry: salt dome initial bathymetry; Subsidence maps: S0 maps -12m<br>Maximum production: CG CM CE<br>(m/Ma) 212 44 16<br>Gravity-driven diffusion coefficient CG CM CE<br>*K* ($km^2$/kyr) Continental: 0.005 0.01 0.0001<br>Marine: 0.005 0.01 0.0001 |
| Subsidence | S14 | Initial bathymetry: salt dome initial bathymetry; Subsidence maps: S0 maps -14m<br>Maximum production: CG CM CE<br>(m/Ma) 212 44 16<br>Gravity-driven diffusion coefficient CG CM CE<br>*K* ($km^2$/kyr) Continental: 0.005 0.01 0.0001<br>Marine: 0.005 0.01 0.0001 |

**Table 4.3** *continued from the previous page*

| PARAMETER TESTED | MODEL NAME | MAIN PARAMETERS |
|---|---|---|
| Subsidence | S26 | Initial bathymetry: salt dome initial bathymetry; Subsidence maps: S0 maps -26m<br>Maximum production: CG CM CE<br>(m/Ma) 212 44 16<br>Gravity-driven diffusion coefficient CG CM CE<br>*K* ($km^2$/kyr) Continental: 0.005 0.01 0.0001<br>Marine: 0.005 0.01 0.0001 |
| Carbo_Grains production | G106 | Initial bathymetry: salt dome initial bathymetry; Subsidence maps: S0 maps -14m<br>Maximum production: CG CM CE<br>(m/Ma) 106 44 16<br>Gravity-driven diffusion coefficient CG CM CE<br>*K* ($km^2$/kyr) Continental: 0.005 0.01 0.0001<br>Marine: 0.005 0.01 0.0001 |
| Carbo_Grains production | G206 | Initial bathymetry: salt dome initial bathymetry; Subsidence maps: S0 maps -14m<br>Maximum production: CG CM CE<br>(m/Ma) 206 44 16<br>Gravity-driven diffusion coefficient CG CM CE<br>*K* ($km^2$/kyr) Continental: 0.005 0.01 0.0001<br>Marine: 0.005 0.01 0.0001 |
| Carbo_Grains production | G218 | Initial bathymetry: salt dome initial bathymetry; Subsidence maps: S0 maps -14m<br>Maximum production: CG CM CE<br>(m/Ma) 218 44 16<br>Gravity-driven diffusion coefficient CG CM CE<br>*K* ($km^2$/kyr) Continental: 0.005 0.01 0.0001<br>Marine: 0.005 0.01 0.0001 |
| Carbo_Grains production | G318 | Initial bathymetry: salt dome initial bathymetry; Subsidence maps: S0 maps -14m<br>Maximum production: CG CM CE<br>(m/Ma) 318 44 16<br>Gravity-driven diffusion coefficient CG CM CE<br>*K* ($km^2$/kyr) Continental: 0.005 0.01 0.0001<br>Marine: 0.005 0.01 0.0001 |
| Carbo_Mud production | M22 | Initial bathymetry: salt dome initial bathymetry; Subsidence maps: S0 maps -14m<br>Maximum production: CG CM CE<br>(m/Ma) 218 22 16<br>Gravity-driven diffusion coefficient CG CM CE<br>*K* ($km^2$/kyr) Continental: 0.005 0.01 0.0001<br>Marine: 0.005 0.01 0.0001 |
| Carbo_Mud production | M42 | Initial bathymetry: salt dome initial bathymetry; Subsidence maps: S0 maps -14m<br>Maximum production: CG CM CE<br>(m/Ma) 218 42 16<br>Gravity-driven diffusion coefficient CG CM CE<br>*K* ($km^2$/kyr) Continental: 0.005 0.01 0.0001<br>Marine: 0.005 0.01 0.0001 |
| Carbo_Mud production | M46 | Initial bathymetry: salt dome initial bathymetry; Subsidence maps: S0 maps -14m<br>Maximum production: CG CM CE<br>(m/Ma) 218 46 16<br>Gravity-driven diffusion coefficient CG CM CE<br>*K* ($km^2$/kyr) Continental: 0.005 0.01 0.0001<br>Marine: 0.005 0.01 0.0001 |
| Carbo_Mud production | M66 | Initial bathymetry: salt dome initial bathymetry; Subsidence maps: S0 maps -14m<br>Maximum production: CG CM CE<br>(m/Ma) 218 66 16<br>Gravity-driven diffusion coefficient CG CM CE<br>*K* ($km^2$/kyr) Continental: 0.005 0.01 0.0001<br>Marine: 0.005 0.01 0.0001 |
| Carbo_Evapo production | CE8 | Initial bathymetry: salt dome initial bathymetry; Subsidence maps: S0 maps -14m<br>Maximum production: CG CM CE<br>(m/Ma) 218 44 8<br>Gravity-driven diffusion coefficient CG CM CE<br>*K* ($km^2$/kyr) Continental: 0.005 0.01 0.0001<br>Marine: 0.005 0.01 0.0001 |

**Table 4.3** *continued from the previous page*

| PARAMETER TESTED | MODEL NAME | MAIN PARAMETERS |
|---|---|---|
| Carbo_Evapo production | CE24 | Initial bathymetry: salt dome initial bathymetry; Subsidence maps: S0 maps -14m<br>Maximum production: CG CM CE<br>(m/Ma) 218 44 24<br>Gravity-driven diffusion coefficient CG CM CE<br>*K* ($km^2$/kyr) Continental: 0.005 0.01 0.0001<br>Marine: 0.005 0.01 0.0001 |
| Transport parameters | T0.01-0.05 | Initial bathymetry: salt dome initial bathymetry; Subsidence maps: S0 maps -14m<br>Maximum production: CG CM CE<br>(m/Ma) 218 44 16<br>Gravity-driven diffusion coefficient CG CM CE<br>*K* ($km^2$/kyr) Continental: 0.01 0.05 0.0001<br>Marine: 0.01 0.05 0.0001 |
| Transport parameters | T0.002-0.01 | Initial bathymetry: salt dome initial bathymetry; Subsidence maps: S0 maps -14m<br>Maximum production: CG CM CE<br>(m/Ma) 218 44 16<br>Gravity-driven diffusion coefficient CG CM CE<br>*K* ($km^2$/kyr) Continental: 0.002 0.01 0.0001<br>Marine: 0.002 0.01 0.0001 |
| Transport parameters | T0.005-0.025 | Initial bathymetry: salt dome initial bathymetry; Subsidence maps: S0 maps -14m<br>Maximum production: CG CM CE<br>(m/Ma) 218 44 16<br>Gravity-driven diffusion coefficient CG CM CE<br>*K* ($km^2$/kyr) Continental: 0.005 0.025 0.0001<br>Marine: 0.005 0.025 0.0001 |
| Evaporation | E500 | Initial bathymetry: salt dome initial bathymetry; Subsidence maps: S0 maps -14m<br>Maximum production: CG CM CE<br>(m/Ma) 218 44 16<br>Gravity-driven diffusion coefficient CG CM CE<br>*K* ($km^2$/kyr) Continental: 0.005 0.01 0.0001<br>Marine: 0.005 0.01 0.0001<br>Evaporation: 500 mm/yr |
| Evaporation | E2500 | Initial bathymetry: salt dome initial bathymetry; Subsidence maps: S0 maps -14m<br>Maximum production: CG CM CE<br>(m/Ma) 218 44 16<br>Gravity-driven diffusion coefficient CG CM CE<br>*K* ($km^2$/kyr) Continental: 0.005 0.01 0.0001<br>Marine: 0.005 0.01 0.0001<br>Evaporation: 2500 mm/yr |

- ***Initial bathymetry***

To test a different possible depositional scenario, a new bathymetry map was substituted as input at the base of the model (Figure 4.6A). The new initial topography map represents a southwest dipping carbonate ramp, with a bathymetric range from -66 m to -1 m. Compared to the REF model, this map is characterized by a relative local high under well A1 and A2. This high aims to reproduce the presence of a salt diapir in the substratum (as proposed in the section 3.3.2) that already affects the morphology of the sea floor at the beginning of the Arab Fm. deposition. In the bathymetric map inserted at 152.2 Ma, the relative high was drawn under wells A3, A4 and A5, to represent the relative shift of the salt diapir through time and space that should affect the main southwest direction of progradation of the shoal. The thickness maps used to compute the subsidence of the basin are the same of the REF model.

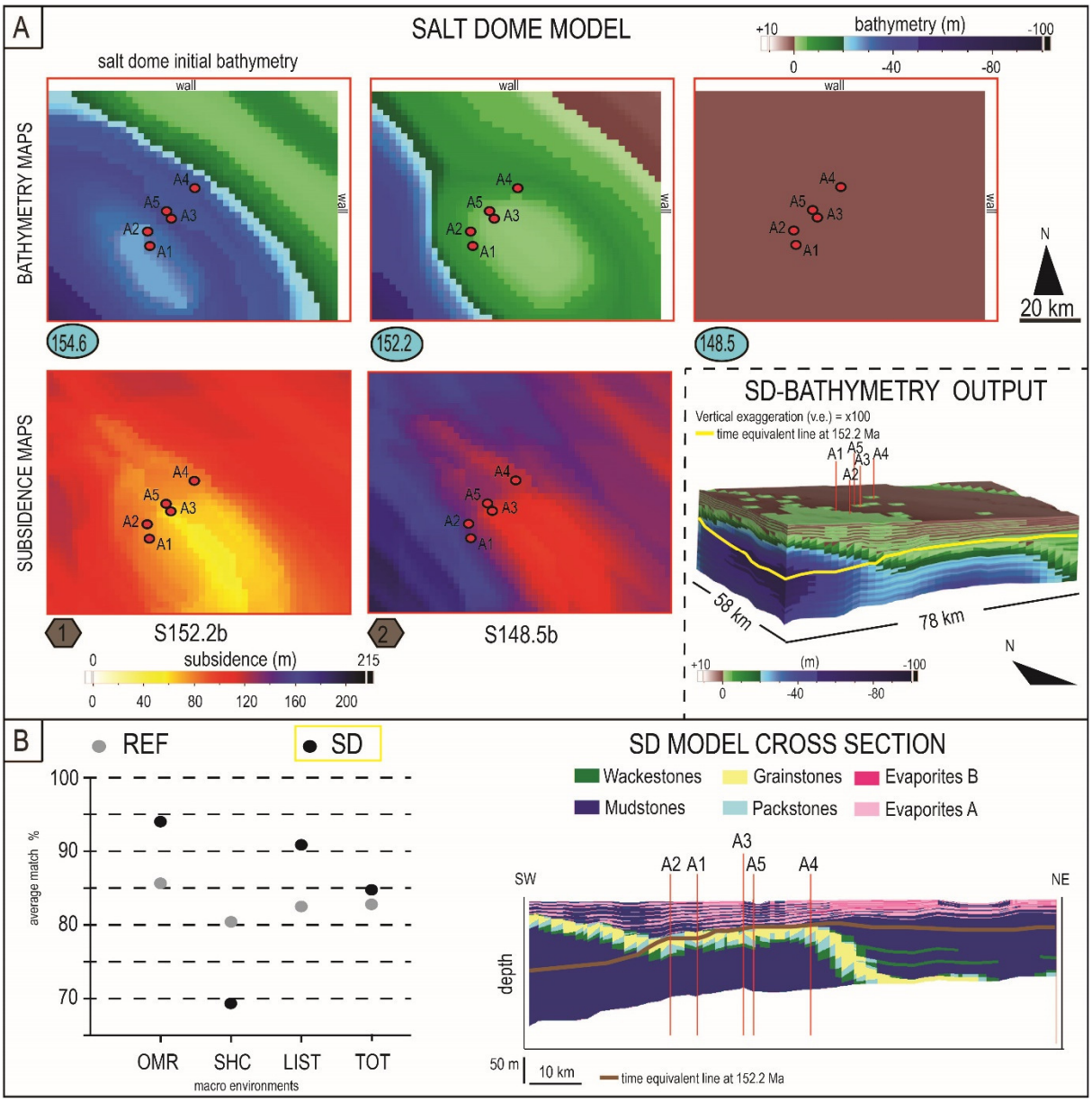


**Figure 4.6** *A) Bathymetry (negative values below 0 m) and subsidence maps inserted in the Salt Dome (SD) model. The thickness maps and the age model are the same shown in Figure 4.2. On the right: 3D output model displaying the variations in bathymetry (output) through the deposition of the Arab Formation (negative values below 0 m). B) Diagram comparing the REF and SD models, showing the percentage in match of the different macro environments considering the five available wells and the TOT values. On the right: cross section cutting the SD model across the five wells, picturing the distribution of facies. The 3D model (and the related cross section) is cut in the length and the width at each side of 10 km in order to avoid representing possible boundary effects.*

The new automatically computed subsidence maps (hereafter called S0 maps) were corrected, as previously, for a values of -13 m and -13.5 m respectively to account for the eustatic contribution to the accommodation space. The new corrected subsidence maps, S152.2b and S148.5b (Figure 4.6A) depict slight different morphologies compared to those inserted in the

REF model. In the S152.2b and S148.5b the wells are bracketed between subsidence values of 57 to 79 m (time interval: 154.6-152.2 Ma) and 105 to 149 m (time span: 154.6-148.5 Ma) respectively. The output model, named Salt Dome model (SD; Table 4.3; Figure 4.6A), shows geometries similar to the REF model, illustrating an overall progradation of the Arab Fm. carbonate ramp through time (Figure 4.6A; slight steeper strata at the shoal complex have an inclination between 0.01° and 0.6°), that ranges from -62 to +7 m. According to the distribution of the simulated facies (Table 4.2), the calibration of the SD model reaches a TOT value of 84.8% (Figure 4.6B). Singularly, each simulated well shows an average match between all the macro environments above 90% except for well A2 with an average match of 57.4%. The TOT value resulting from the SD simulation provides a higher calibration compared to the REF model (Figure 4.6B), due to the new initial bathymetry that, on the consequence, was kept for all the following tests.

- ***Subsidence***

For testing the impact of subsidence, the two S0 maps computed automatically by the software were analyzed and then modified with correction values of -12 m (S12 model), -14 m (S14), and -26 m (S26) applied to both maps, running four different models (Table 4.3). The values to test were chosen in the nearby of the correction values applied to the SD model subsidence maps (-13 m; -13.5 m) and doubled.

The S0 maps imply an increase in the accommodation space, with a consequent high accumulation of outer ramp deposits and slow progradation rates compared to the SD model. On the contrary the S26 maps imply a reduced accommodation space, causing the rapid deposition of the outer/mid ramp deposit with higher progradation rates. The top of the shoal complex is encompassed by the wells (top Arab D Member; Lawrence et al., 2015) between 151.7-151.3 Ma, and 153.1-152.9 Ma, in the S0 and S26 models respectively, without respecting the age suggested in literature for the top Arab D (i.e. 152.2 Ma; Al-Husseini, 2009). The TOT values of these two simulations (67.9% for the S0; 72.9% for the S26) show a poorer and unsatisfactory calibration in respect with the SD model (Figure 4.7A).

The S12 and S14 simulations, where the values of corrections are similar to the ones applied to the SD subsidence maps, gave similar TOT values of 88.2% and 89% (Figure 4.7A) respectively. The S14 provides a better match. On the consequence the subsidence maps corrected both for a value of -14 m are kept for the subsequent tests. Considering the five wells, the average subsidence rates (m/Ma) applied by the software for each simulation at the different time intervals are reported in Table 4.4.

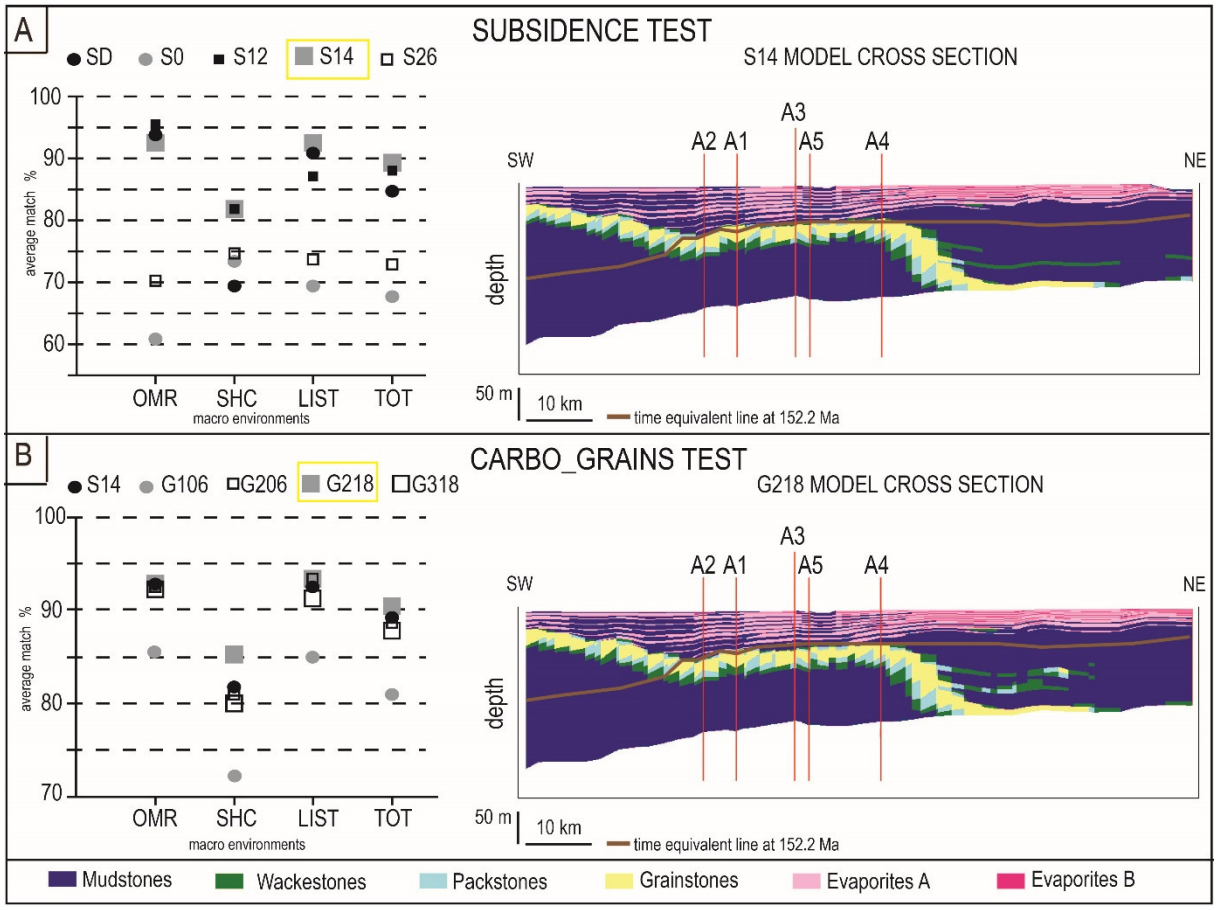


**Figure 4.7** *A) Diagrams that compares the models in which the subsidence (A) and the Carbo_Grains production (B) were tested, showing the percentages of the average matches of the different macro environments considering the five available wells and the TOT values. The S14 and the G218 models (highlighted in yellow) gave a higher TOT value (higher calibration). On the right: cross section cutting the S14 model (A) and the G218 model (B) across the five wells, picturing the distribution of facies. The cross sections are sliced from 3D models cut in the length and the width at each side of 10 km in order to avoid representing possible boundary effects.*

**Table 4.4** *Different subsidence rates applied by the software for the simulations: S0, S12, SD, S14 and S26 (average between the wells values).*

| | | MODELS | | | | |
|---|---|---|---|---|---|---|
| | **SUBSIDENCE RATES (m/Ma)** | **S0** | **S12** | **SD** | **S14** | **S26** |
| **TIME INTERVALS (Ma)** | **154.6 – 152.2** | 35.9 | 30.9 | 30.5 | 30.1 | 25.1 |
| | **152.2 -148.5** | 15.1 | 15.1 | 14.9 | 15.1 | 15.1 |
| | **154.6 – 148.5** | 23.3 | 21.3 | 21.1 | 21 | 19 |

- ***Carbonate production***

Each sediment class was tested for different sets of maximum carbonate production (constant for the entire simulation interval) analyzing values randomly close or far from those of the S14 model (Table 4.3).

The Carbo_Grains production (CG) was investigated at first, testing values of (m/Ma): 106; 206; 218; and 318 (Table 4.3). All the simulations returned similar values of average matches for each macro environment (Figure 4.7B) except for the SHC, where the average of the matches between the five wells show a higher value (85.1%), when the carbonate production is set at 218 m/Ma (G218 model). In the G218 model the top of the shoal is reached by the wells between 152.5 and 151.1 Ma, and the simulation returns a TOT value of 90.4% (higher in respect with the S14 model). No further simulations have produced a higher calibration (TOT value) electing the G218 as the best-fitting model developed.

The Carbo_Mud (CM; Figure 4.8A) was tested for values of (m/Ma): 22; 42; 46; and 66 (Table 4.3) keeping for the Carbo_Grains production the value of 218 m/Ma. Low and high production rates consistently affected the model. In the M22 simulation the model reaches shallow bathymetries only in its northeast corner at the end of the simulation, involving just the well A4. The other wells are composed only by Mudstones and Wackestones SF. As a consequence, the average match for the shoal complex and the lagoon/inter-supratidal is very low (19.6%) or 0% (Figure 4.8A) respectively. The higher Carbo_Mud production (simulation M66) on the contrary provides thinner outer/mid ramp deposits and thicker lagoon/inter-supratidal ones, whose matches are unsatisfactory with respect to the G218 model with a Carbo_Mud production of 44 m/Ma.

The effects of Carbo_Evapo production variations (Figure 4.8B) are mainly reflected on the thickness of the Evaporites A and B layers inside the lagoonal/inter-supratidal macro environment, but they do not affect the total thickness of the different groups of facies associations (TOT value > 85%).

- ***Transport parameters***

The gravity diffusion coefficients, inserted in the REF model and kept in all the previous simulations, set a ratio of 1:2:0.02=CG:CM:CE, meaning that the Carbo_Mud is two times more transportable than the Carbo_Grains (Williams et al., 2011), than in turn is fifty times more transportable than the Carbo_Evapo. The diffusion coefficients for the Carbo_Evapo were set nearly at zero, in order to reproduce a potential sediment (the evaporites) that can precipitate only under specific conditions (i.e. evaporation, salts saturated solutions; Bosellini

et al., 1989; Schreiber and El Tabakh, 2000; Warren 2006; Warren, 2010; Bąbel and Schreiber, 2014), that can just locally occur in the basin. At the same time, the Carbo_Evapo could also evoke sediments of microbial origin, for which can be thought that no significant transport occurred in a restricted lagoonal/intertidal environment like the one where the upper part of the Arab Fm. was deposited. For these reasons the Carbo_Evapo transport parameters were left invariant, and the Carbo_Grains and Carbo_Mud diffusion coefficients were tuned in respect to a ratio of 1:5 (Table 4.3). All the simulations resulted in similar TOT values with matches around 85% (Figure 4.8C).

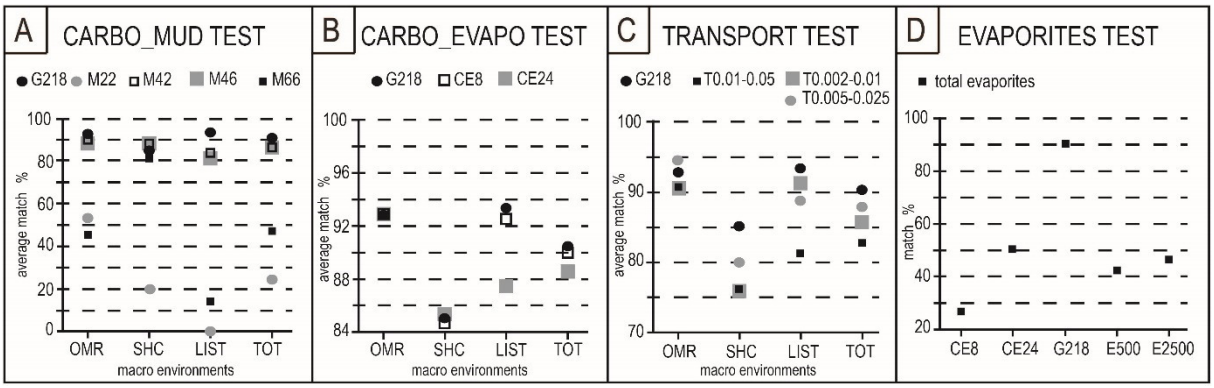


**Figure 4.8** *Diagrams showing the percentages in average matches of the different macro environments considering the five available wells and the TOT values, according to the parameters tested: production rate of A) Carbo_Mud; B) Carbo_Evapo; and C) diffusion coefficients (transport). D) Comparison of the percentages of the matches between the total thickness of the simulated and real evaporites, testing the Carbo_Evapo production and the evaporation rate.*

- ***Evaporites calibration***

In all the previous simulations the Evaporites A and B layers (alternated to the simulated Mudstones - Wackestones SF) were considered part of the macro environment composed by lagoon/intertidal + supratidal facies (LIST). The average of the total thickness of the simulated Evaporites (A+B) between the five wells was compared with the same kind of average considering the real wells (25 m). The model with the higher calibration in terms of group of facies, G218, presents a match of the Evaporites layers of 90% (Figure 4.8D). The Evaporites SF deposition was tested tuning one per time: i) the evaporation parameter (mm/yr) for values of 500 and 2500 (1/3; and 5/3 the evaporation value of 1500 mm/yr inserted in all the previous simulations, that roughly reflects the actual evaporation in the Abu Dhabi coastline of 1240 mm/yr; Alsharhan and Kendall, 2003; see section 2.3); and ii) the Carbo_Evapo (CE) production rate (m/Ma) for values of 8 and 24 (Table 4.3). The lower inserted values of evaporation and production rate produced less deposition of Evaporites SF

(around 1/3 and 1/4 of the evaporitic layers in the real wells) with matches of 42.1% (E500) and 26.8% (CE8) respectively (Figure 4.8D). On the contrary the high values set produced an increase in Evaporites SF achieving an average in thickness of around 38 m, i.e. 50% higher than the drilled evaporitic beds, with unsatisfactory matches of 46.3% (E2500) and 50.5% (CE24; Figure 4.8D). The variation in evaporation does not affect the total thicknesses of the three macro environments (TOT Values 90.4 %)

## 4.4 Discussion

The REF model represents a possible simple depositional scenario for the Arab Fm. based and calibrated on the properties measured or gathered from the wells such as thicknesses and facies associations. Tuning by trial the parameters of the REF model, according to different ranges of values, other sixteen calibrated models (TOT Value > 80%) were produced. These simulations could as well represent evaluable sedimentary settings, with the achievement of higher calibrations (such as the SD and S14 models) and of the G218 best-fitting model. The lack in constraints on several input values (e.g. bathymetric range, carbonate production), gave the possibility to test and refine the REF model, understanding how the different parameters might have affected the Arab Fm. deposition.

### 4.4.1 Salt dome evolution: two depositional scenarios

The initial bathymetry maps tested (at 154.6 Ma; Figure 4.2 and 4.6) portray two depositional scenarios that yield two models (REF and SD) both calibrated on the wells (TOT values more than 80%). Despite the satisfactory calibration, the concepts and the shape of the simulated geological bodies are different between the REF and SD model. The SD model illustrates a diapiric movement that deforms the seafloor before and during the Arab Fm. sedimentation (Figure 4.6A). The REF model shows instead the development of a salt dome entirely coeval to the deposition of the Arab Fm. (Figure 4.2). In the SD model, the input bathymetry maps allow to locate with precision the salt dome in order to compute the different local subsidence suggested by the correlations of the real wells (see section 3.3.2 and Figure 3.11). In the maps S152.2b and S148.5b (SD model), the difference in subsidence is higher between the wells, in respect with the maps of the REF model (S152.2 and S148.5). Considering for example the S152.2b map (SD model; Figure 4.6), the wells A3 and A2 (center and south-west part of the field) display a difference in subsidence of 22 m, where in the S152.2 (REF model; Figure 4.2) is almost zero. The differences in subsidence are reflected in the output bathymetric

evolution of the basin, and in turn on the Carbo_Grains production and distribution of simulated facies. Analyzing the two simulated models at several time steps (Figure 4.9), we can observe that at 154.3 Ma (almost at the base of the Arab Fm.) a shoal complex (Packstones + Grainstones SF) of around 5.5 km in width cuts from northwest to southeast the north-east part of the modeled area.

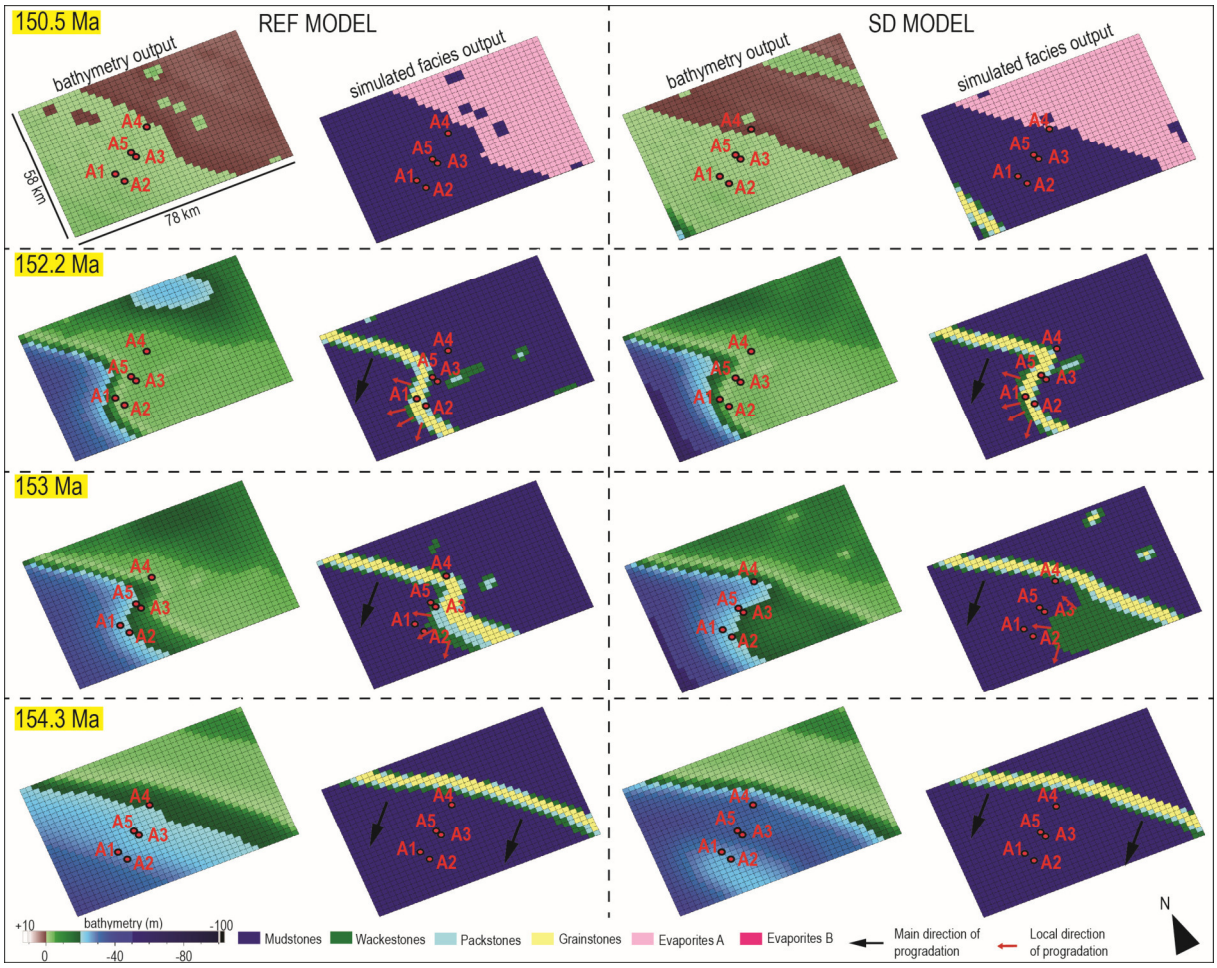


**Figure 4.9** *Evolution of the output bathymetries (negative values below 0 m) and facies distribution in the REF and SD models according to certain time steps. The sizes of the models are kept fixed in all the representations; the models are cut in the length and the width at each side of 10 km in order to avoid representing possible boundary effects.*

Southwestward to the shoal, mid-ramp and outer ramp environments are computed (Mudstones + Wackestones SF of the relative deep domain), where in the REF model the bathymetry gradually increases toward southwest, instead in the SD model the wells are located on relative high (A1, and A2) and depocenter position (A3, A4 and A5), due to the presence of a pre-sedimentary salt dome.

At 153 Ma (SD model) the salt dome is shifted and raised southward to the field area, with consequent deposition of mid-ramp deposits surrounded by outer ramp ones (Mudstones +

Wackestones SF of the relative deep domain; similar distribution of facies of map TS3 in Figure 3.9) in front of the shoal complex, still located northwest-southeast. In the REF model, at the same time step, the shoal complex covers part of the field area, with a promontory under well A4 and relative deeper bathymetries around the other wells. At 152.2 Ma (top Arab D) the shoal complex has gradually prograded toward southwest developing in both models an irregular margin that displays multiple directions of progradation. In the SD model, the shoal encompasses almost all the wells (for well A4 and A3 the shoal complex facies is displayed in one cell close; similar to paleofacies map at SU5 in Figure 3.9) displaying sinuous geometries. On the contrary in the REF model at 152.2 Ma the shoal cuts the field of study almost north to south, encompassing only well A1. Compared to the conceptual model, the multiple and transient directions of progradation are clearly observable in the simulated models not only when outer and mid-ramp facies intercept the wells (as in map TS3 in Figure 3.9), but also when the shoal complex covers them as a consequence of the salt diapirsm.

In the SD model the top of the shoal across the wells is comprised between 152.4 and 152 Ma, with a difference of 0.4 Ma. This slight diachrony is comprised within the 0.4 Ma time-resolution of the model related to the adopted eustatic curve, therefore the top of the shoal, across the wells, can be considered to approximate a time-line (see section 3.1.2) that separates the shoal complex from the lagoon/intertidal environment. Instead in the REF model, the top of the shoal is reached in a doubled time interval (152.9-152.1 Ma) by the wells. Proceeding with the simulation, the shoal keeps prograding southwestward, and the shoal takes up again a straight northwest-southwest trend, enclosing landward the lagoonal/intertidal and supratidal facies (i.e. at 150.6 Ma; Mudstones + Wackestones + Evaporites (A+B) SF in the shallow domain). At the scale of the model, the top of the shoal complex is clearly diachronic (Figure 4.3 and 4.6).

The higher accuracy in the depositional evolution of the SD model, together with a better calibration (TOT value of 84.8%), makes its initial bathymetry map a more successful input, in respect with the regularly dipping carbonate ramp of the REF model.

The “sinuous” shoal complex is similarly represented in all the simulations which have the same initial bathymetry of the Salt Dome model. An exception is made by the T0.01-0.05 model (Table 4.3), that computes higher gravity-driven diffusion rates both for the Carbo_Grains (two times more than the other models) and the Carbo_Mud sediment classes (five times more than the other simulations). These rates distribute the sediments smoothing the slight topographic variations induced by the salt dome rising at the early stage of the Arab Formation. The result is an almost north-south distribution of the shoal complex facies

(Figure 4.10) with geometries similar to the REF model where a gradually dipping carbonate ramp was imposed at the beginning of the simulation (Figure 4.9). This result proves that a successful input (the salt dome initial bathymetry) is not sufficient for obtain a satisfactory model, but it is fundamental the interplay between all the parameters.

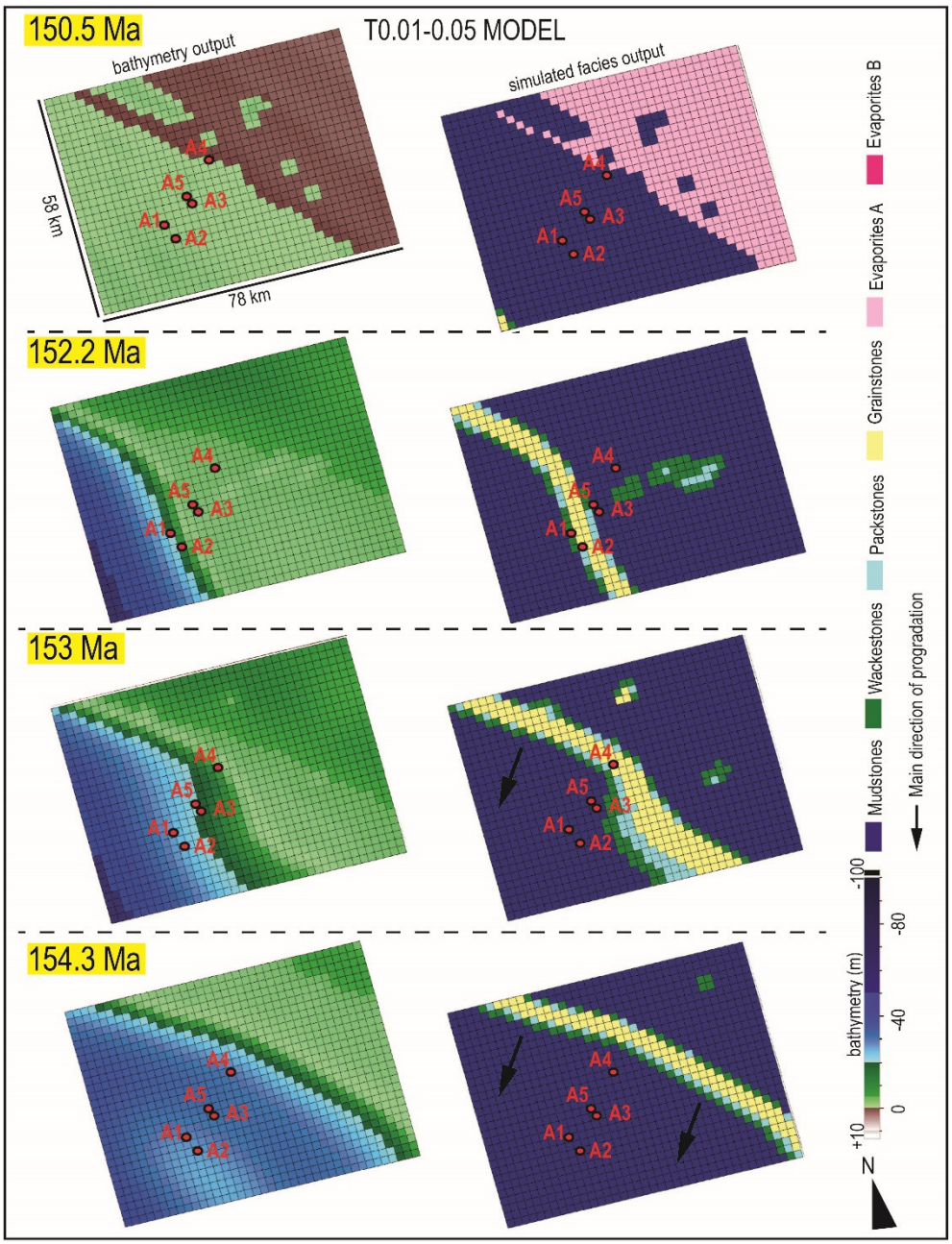


**Figure 4.10** *Evolution of the bathymetries (negative values below 0 m) and facies distribution of the model T0.01-0.05, according to four time-steps. The model is cut in the length and the width at each side of 10 km in order to avoid representing possible boundary effects.*

### 4.4.2 Subsidence and carbonate production rates

The computed subsidence and carbonate production rates were two key parameters in order to simulate the present-day (fully compacted) thickness and facies distribution of the Arab Fm. in the studied wells. The present-day wells are the result of early and deep burial diagenetic

alterations (such as for instance mechanical and chemical compaction) that were not taken in account in the modelling, but are known to affect the studied wells (Morad et al., in review; see sections 2.5-2.5.1) and the Arab Fm. reservoirs in different fields throughout the Arabian Platform (Cantrell et al., 2001; Ehrenberg et al., 2007; Morad et al., 2012; Nader et al., 2013).

Considering the entire simulation interval, the average subsidence rate between the wells applied by the software in the different models (Table 4.4) has a value of around 21 m/Ma, in agreement with the rate imposed in the cratonic-based simulations of Williams et al. (2011). Higher subsidence rates (Table 4.4) were computed in the Arab D depositional interval (154.6-152.2 Ma) respect to the Arab A-B-C one (152.2-148.5 Ma). These rates were necessary to simulate a thicker succession in a shorter time (around 115 m in 2.4 Ma) for the former, and a thinner one in a larger time interval for the latter (around 62 m in 3.7 Ma).

Except for the possible local differences in subsidence from well to well due to the salt movements in the substratum, it could be difficult to explain a reduction of the 50% in the real subsidence rates between the Arab D and A-B-C (Table 4.4). On the contrary, we can assume a constant subsidence during the deposition of the Arab Fm. (as suggested for the central part of the Arabian Platform by Le Nindre et al., 2003 in the Late Jurassic), where sedimentation was mainly controlled by the different carbonate production rates.

The carbonate production actively contributed to obtain the vertical stacking pattern of the present-day wells. All the production rates tested for the different sediment classes are comparable with the ranges of values in Williams et al. (2011) for cratonic settings.

The maximum total production rate of the G218 best-fitting model (average 92.6 m/Ma) is comparable with the minimum production rate of similar modern environments (average 88-90 m/Ma), but shows a decrease of the 82-84% in respect with the modern average rates summarized in Kolodka et al. (2016). The simulated Carbo_Grains production (218 m/Ma) is comprised in the present-day ooids production ranges, but the Carbo_Mud rate (44 m/Ma) is around 1/3 less than the minimum modern lagoon and outer ramp production rates (see Kolodka et al., 2016 with references therein). Assuming that the Late Jurassic rates could have been similar to the modern ones, the lower computed production (necessary to simulate the present-day thickness of the compacted and lithified succession) could address to a major loss in thickness of the original deposited Arab Fm. that affected more the finer Carbo_Mud than the coarser Carbo_Grains deposits. This result demonstrates that the carbonate ramp mudstones/wackestones were affected by more considerable compaction than the oolitic grainstones (see Brown, 1997; Goldhammer, 1997).

Related to the carbonate production, the simulated sedimentation rates in the G218 model are higher for the shoal complex macro environment (SHC; with an average sedimentation rate of 72 m/Ma) and minor for the outer/mid-ramp (OMR; average sedimentation rate of 46 m/Ma) and for the lagoon/inter-supratidal (LIST; average sedimentation rate of 16 m/Ma) macro environments (Figure 4.11).

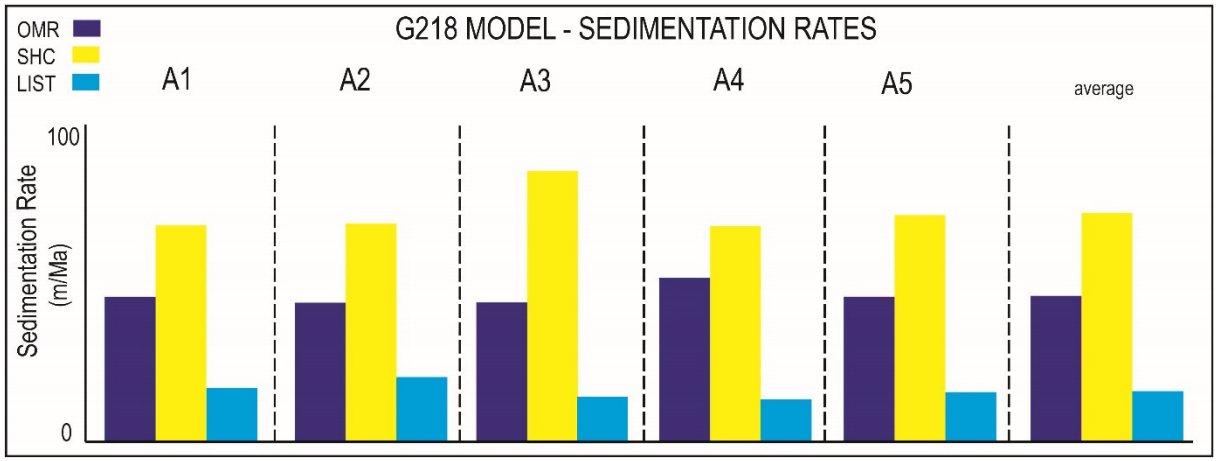


**Figure 4.11** *Simulated sedimentation rates for the three macro environments according to the different wells and their averages in the G218 model* (LIST = lagoon/inter-supratidal, SHC = shoal complex, OMR = outer/mid-ramp).

The difference in the simulated sedimentation rates between the different macro environments is linked to minor production rates in the LIST and OMR (mainly composed of Carbo_Mud and Carbo_Evapo sediments) environments as well related to diagenetic alterations (such as compaction and porosity loss mechanisms) that could have affected differently the several textures and lithologies (Brown, 1997; Goldhammer, 1997; Croizé et al., 2013 with references therein).

The different trials on carbonate production rates highlighted the Carbo_Mud production to affect the most the simulated models, because it is the only sediment class produced even at relative deep bathymetries (from -20 to -100 m) and at low wave energies. When the Carbo_Mud production is highly reduced (22 m/Ma in the M22 model), the carbonate ramp develops an aggrading shoal complex only in correspondence to shallower bathymetries imposed by the initial topography map, but all the surrounding area records a deepening upward trend caused by the low Carbo_Mud production rate. The shoal complex starts to prograde around 151.2 Ma, when the sea-level is steady (Figure 4.1B) and the Carbo_Mud production can outpace the accommodation space. On the contrary, a high Carbo_Mud production (66 m/Ma in the model M66) produces thin outer/mid-ramp deposits (average of

41 m between the wells) with a rapid progradation of the shoal (top of Arab D reached by the wells between 153.8 -153.4 Ma).

The trials done on the production rates of the other sediment classes (Carbo_Grains and Carbo_Evapo) did not affect substantially the models with a calibration always higher than 80 % (TOT value).

### 4.4.3 Cyclicity and evaporites precipitation

Seven progradational cycles (Figure 4.12A) characterize the upper part of the Arab Fm. in the real wells (A-B-C members; see section 3.2.3).

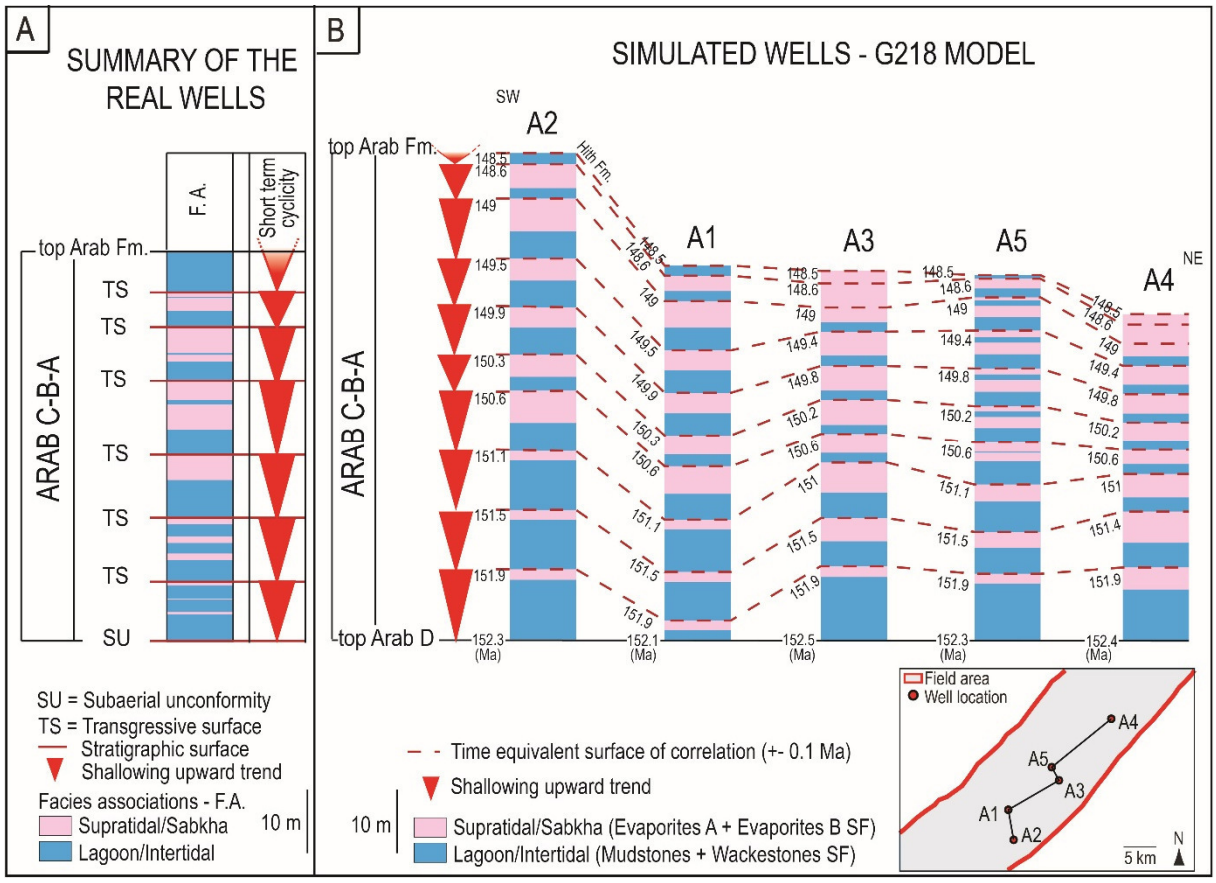


**Figure 4.12** *A) Summary of the vertical stacking pattern of the Arab A-B-C in the real wells, where the association of facies can be organized in seven cycles (modified from Figure 3.8 in Chapter 3). Each cycle is capped by evaporitic deposits, except the last one capped by the Hith Fm. evaporites (not modeled). Six transgressive surfaces were identified, bounding each cycle (except the last one whose top is within the Hith Fm. and thus not modelled), and a subaerial unconformity was identified at the base of the Arab A-B-C (see Chapter 3). B) Panel of correlation of the simulated wells (G218 model), where the top of the Evaporites SF beds could be linked by time equivalent lines (+-0.1 Ma). The simulated top of the Arab D has a time equivalence of +- 0.2 Ma. The lateral distance between the wells is not on scale.*

Each cycle is defined by the peritidal alternation of lagoonal/intertidal and supratidal deposits, except the last one at the top of the Arab succession composed by lagoonal/intertidal facies associations capped by the evaporites of the Hith Formation. In the Arab A-B-C members, the evaporites form several layers in each cycle, and some of them, especially the ones at the top of each parasequence, can be traced and their top can be considered time equivalent all over the available wells (see section 3.1.2).

Analyzing the sediment distribution in the computed wells of the best-fitting G218 model (Carbo_Grains production of 218 m/Ma; Figure 4.12B), the simulated facies are organized in a cyclic pattern in the upper part of the succession.

It is possible to distinguish ten cycles, generally characterized by Mudstones-Wackestones SF, capped by Evaporites A and/or B SF, except in wells A1, A2 and A5, where the last cycle is made by the Arab A Mudstones SF (lagoon/intertidal environment) capped by the overlying Hith evaporites. In wells A3 and A5, the last two cycles are made up only by simulated evaporites. Nine Evaporites SF layers, distributed from the bottom of the Arab A-B-C toward the top, can be traced all over the five wells, showing time equivalent or similar ages (maximum difference of around 0.1 Ma). The tops of the correlated Evaporites are deposited from 151.9 Ma to 148.6 Ma with a period of 0.4 Ma (+- 0.1 Ma) related to the adopted eustatic curve. Nine are the resulting cycles, and the last one toward the top of the Arab Fm. (number ten) is not complete and covers a depositional time of 0.1 Ma. The top of this last cycle belongs to the overlying Hith Fm., which is not simulated in this work. Compared to the seven cycles identified in the real wells (see section 3.2.3), it is possible to speculate that the slight difference in number of cycles can be due to a larger computed time interval, in respect with the poorly constrained Arab Fm. depositional ages.

In the simulations results, the deposition of the Evaporites SF provides an example of allocyclic controls on peritidal parasequences under greenhouse conditions related to the adopted eustatic curve (small see-level oscillation of 2 m in amplitude). Despite the successful modelling of the Arab A-B-C members in relation with eustatic oscillations, we could not exclude autocyclic mechanisms partly controlling the stacking pattern. As suggested by many authors (e.g. Burgess, 2001; Yang and Lehrmann, 2014), peritidal cyclicity can develop under greenhouse conditions even without invoking relative sea-level oscillations, but as a result in changes in carbonate productivity and/or transport processes.

In the Arab D member the 0.4 Ma cyclicity is not detected. The possible cause of this observation is that the small sea-level oscillations did not cause significant facies variations in

the relative distal environments of the Arab D Member. On the contrary in the Arab A-B-C members, metric scale sea-level changes were able to trigger evident facies changes.

### 4.4.4 Conceptual vs. 3D stratigraphic forward model

The models presented in this thesis, both conceptual (Chapter 3) and dynamic-slope based (Chapter 4), were developed in order to honor the five available wells, defined as control points, necessary to evaluate the robustness of the resulting models.

In the conceptual model the time-step evolution of the Arab Fm. was depicted by twelve paleofacies maps pictured in correspondence of the time-equivalent key stratigraphic surfaces. These maps were built extending the core and well log data throughout the studied area, and the geometries of the geological bodies were based on interpretation.

The results gathered from the conceptual model, such as the lateral and vertical facies distribution, direction of progradation and the stratigraphic framework were fundamental in order to develop the 3D forward models. In these latter, the spatial and temporal evolution of the Arab Fm. is not based on the user interpretation, but is the outcome of the interplay of the several inputs ruled by the quantification of accommodation space, *in situ* marine production, and transport for each square mesh of the simulated domain (Granjeon, 2010; Granjeon, 2014; Bruneau et al., 2016).

The shape of the geological bodies in the conceptual model was refined by the 3D forward modelling. In the conceptual paleofacies map at TS4 (Figure 3.9 and 3.10), the shoal complex (drawn with no other constraints beyond the wells) has a northwest-southeast strike, covering a vast area of around 700 $km^2$ (considering the entire frame). In correspondence of SU5 (Figure 3.9 and 3.10) the shoal complex was drawn with a sinuous shape and it covers an extended area of the map as well (around 650 $km^2$ considering the entire frame). In the simulated models such as the SD one (Figure 4.9), it is possible to observe a narrower shape of the shoal complex that along its length encompasses the available wells (e.g. at 152.2 Ma), covering a less extended area (estimated area of around 120 $km^2$ covering the wells; Figure 4.9) compared to the one suggested in the conceptual paleofacies maps. The sinuous and narrow shoal complex could be considered as a more reasonable and less speculative morphology to be applied to understand the field-scale evolution of the Arab Formation.

The investigation and quantification on the physical, chemical, and biological parameters by means of DionisosFlow$^{TM}$ highlight another possible inaccuracy of the conceptual model. As explained in the above section, the upper part of the simulated Arab Fm. (A-B-C members) is

punctuated by a cyclicity of 0.4 Ma reflected in the facies alternation. In the conceptual model this cyclicity was defined as “short-term” in comparison with the “mid-term” one identified in the Arab D Member (see section 3.2.3 and 3.3.4). This different hierarchical stack was suggested supposing a different depositional time period for the cycles in the Arab D Member in respect with the ones in the Arab A-B-C. The lack in chronological constraints led to propose that the thicker cycles of the Arab D Member where deposited in a longer time interval. The short-term cyclicity, related to low amplitude relative sea-level oscillations, could not be visible in the relative deeper deposits of the Arab Fm. (Arab D) with no evident facies associations contrasts as in the shallower A-B-C members.

Contrary to this concept, it is also possible to suggest that all the detected cycles could have been deposited during similar time intervals. The differences in thickness could be related to different carbonate production rates and/or diagenetic alterations for each lithology and depositional environment. According to the inputs of the forward modelling a minor carbonate production is computed for the Carbo_Mud and Carbo_Evapo sediment classes that populate the A-B-C members (peritidal deposits; average input of production rate in the G218 model: 30 m/Ma). A major carbonate production is instead simulated for the D Member (Carbo_Grains + Carbo_Mud sediment classes; average input of production rate in the G218 model: 131 m/Ma). Finally, considering the uncertain age boundaries for the simulations, the five Arab D Member cycles, identified in the conceptual model and deposited in a time interval supposed of 2.4 Ma, could as well cover a period of around 0.4 Ma each, same as for the cycles in the Arab A-B-C members.

## 4.5 Conclusions

A 3D stratigraphic forward modelling tool was applied in order to simulate the time and space evolution of the Upper Jurassic Arab Formation carbonate ramp in an onshore Abu Dhabi field and in the surrounding area. The main achievements can be summarized as follow:

- Twenty models picture an overall progradation (toward southwest) of a shoal complex that is recorded in all the studied wells (control points), and divides the simulated geological volume in a southwestward relative deep domain (outer and mid-ramp deposits), and in a northeastward shallow macro environment where lagoonal and intertidal facies are alternated to supratidal ones.

- Seventeen models with a calibration in terms of facies and thickness above the 80% (TOT values) were produced. The models correctly simulate the vertical and lateral distribution of facies identified in the real wells. Between them, the best-fitting model reaches a calibration of 90.4% representing the best depositional scenario simulated for the Arab Formation. This model shows an 85.1% calibration of the shoal complex, where the top intercepts the wells between 152.5 and 152.1 Ma.

- An initial topography characterized by a local high, due to salt rising was substituted as a more successful input to a gently southwest dipping ramp. This scenario implies that the Arab Fm. started to accumulate on a substratum already affected by local salt diapirism that continued during the deposition of the Arab Formation. The resulting model better reproduces a top of the shoal approximately time equivalent across the studied wells with transient and local multiple directions of progradation, within a main southwest prograding scenario.

- Despite a difference in the modelled subsidence rates between the Arab D and A-B-C members, necessary to simulate the present-day well thickness and facies distribution, a constant subsidence can be assumed during the deposition of the Arab Formation, consistently with the regional tectonic setting.

- Assuming that modern and Late Jurassic carbonate production rates could be similar, the lower computed average production in the simulations could address to a major significant loss in thickness of the original deposited Arab Fm. that affected more the finer sediments than the coarser deposits.

- Between the parameters tested, a low Carbo_Mud (finer sediments) production substantially affected the output model, preventing the progradation of the shoal complex. The low Carbo_Mud production rates caused the retrogradation of all the relative deep and calm area on the carbonate ramp, because this sedimentary class is the only one produced even at relative deep bathymetries under low wave energies.

- The evaporitic layers in the upper part of the succession (Arab A-B-C) could be the result of a possible allocyclical control on the peritidal deposits, due to the oscillations of the eustatic curve with an amplitude of 2 m (greenhouse conditions) and an average period of 0.4 Ma linked to orbital forcing.

# Chapter 5

# CONCLUSIONS

A strict combination of qualitative and quantitative analyses led to unravel new stratigraphic and sedimentological insights into the spatial and temporal evolution of an ancient carbonate ramp depositional system. Conceptual and dynamic-slope based models were developed in order to implement the scientific knowledge of this kind of carbonate setting, useful for addressing modern and ancient analogue studies.

Specifically, the research adds new data and interpretations into the study of the Upper Jurassic Arab Fm., which comprises one of the most economically important oil and gas reservoir in the world. In the study area (onshore Abu Dhabi field) the Arab Fm. illustrates an overall shallowing upward trend typified by carbonate deposits, alternated to evaporitic ones in the upper part of the succession. The ramp is characterized by an oolitic/shelly shoal complex that separates relative distal mid- and outer ramp environments from shallower intertidal/lagoonal and supratidal/sabkha settings.

The conceptual depositional model not only put the basis for the 3D forward dynamic-slope simulations, but it provides an excellent overview of the evolution of the carbonate system, unraveling important achievements and interpretations.

Point of interest is the heterogeneous carbonate ramp setting that has been observed by means of the micropaleontological analysis. During the deposition of the Arab Fm., the ramp dynamically changed. At the beginning, the ramp was characterized by a shelly shoal with behind an open lagoon, where the former evolved through time into an oolitic/shelly one, acting as a barrier, and causing restricted water circulation and salinity increase in the landward lagoon. The last occurrence of *Cladocoropsis spp.* allowed correlating several scattered wells and fields in the Abu Dhabi area, providing a possible distribution of facies associations during the Arab Fm. depositional time. This correlation made possible to move from the local case history of this thesis and to extend the interpretations to a wider-regional scale, merging together different data previously fragmented in literature.

The 3D forward modelling, based on the conceptual interpretations, provided important findings concerning the parameters that control the stratigraphic architecture and the lateral and vertical distribution of facies on a carbonate ramp.

The sensitivity analysis, performed on several main inputs, confirmed the importance of the interplay between all the different parameters that rule the sedimentation in a basin. The

balance between accommodation space, due to the subsidence and to the eustatic curve, the carbonate production and the transport coefficients was fundamental to recreate the 3D depositional geometries.

Orbital forcing (e.g. the long-term eccentricity) was used as the driving mechanism to reproduce the evident alternation of facies associations that characterizes the upper part of the succession. The slight sea-level oscillations (2 m in amplitude) and a period of 0.4 Ma were able to trigger the peritidal deposits under greenhouse conditions. The period of 0.4 Ma probably ruled even the cycles identified in the lower part of the formation (Arab D Member), where the small sea-level fluctuations did not cause substantial changes in facies, and it is evident only the overall shallowing upward trend. This outcome suggests that, even the small global sea-level changes, driven by orbital forcing in a greenhouse climate state, are enough to explain the cyclicity observed in the studied carbonate ramp system.

Different sediment classes filled the accommodation space, created under a supposed constant subsidence (during time). The different production/sedimentation rates were necessary to determine the thicknesses and facies distribution of the deposits in the simulated wells. Between the sediment classes inserted in the models, the one produced in the deepest range of bathymetries (Carbo_Mud) played a key role in controlling the progradation of the ramp. A low Carbo_Mud production caused (during time) a deepening upward trend in several parts of the carbonate ramp, failing in reproducing the shallowing upward trend observed in all the available wells.

The carbonate production rates inserted in the simulations for the different sediment classes revealed lower values than the modern production rates. For example the Carbo_Mud is 1/3 less than the minimum modern lagoon and outer ramp production rates. This observation was linked to the fact that modelling aimed to reproduce the present-day thicknesses of the different associations of facies, without a quantitative user-control on the diagenetic alterations. The differences in the successfully modeled carbonate production rates and the ones observed in similar present-day depositional environments address a major thickness loss of the finer than the coarser deposits.

The 3D modelled distribution of facies was better constrained by the use of a specific initial bathymetry that located a salt dome under certain wells. Deep-seated salt movements were supposed in the field-scale conceptual sedimentary model, analyzing the lateral thickness variations of the detected cycles across the wells. In the forward models, higher calibrations were reached when the salt diapirism was suggested to affect the Arab Fm. before and during its deposition. The salt rising affected the morphology of the sedimentary bodies as

represented both in the conceptual paleofacies maps and in the simulations. In correspondence of the salt dome, the salt activity produced topographic irregularities. The mid-ramp and shoal complex deposits display multiple local and transient directions of progradation, comprised in the south-west main direction of progradation.

In conclusion, it is possible to affirm that this kind of forward modelling improved the knowledge on the factors controlling the depositional evolution of the carbonate ramp in exam, enhancing the conceptual model. Moreover, the 3D stratigraphic assessment and distribution of facies could be used to potentially predict and define the various parts of a petroleum system (in synergy with other specific studies), in accordance with hydrocarbon exploration and production purposes (see Chapter 6).

# Chapter 6

# FUTURE WORKS

The results obtained during the Ph.D. and described in this thesis open to new research opportunities that could be developed in scientific cutting-edge projects. The possible ideas are summarized in the following paragraphs.

## 6.1 The predictive power of the model: blind well tests

The 3D forward facies distribution and stratigraphic framework of the Arab Fm. were modeled for an area larger than the onshore Abu Dhabi studied field. The simulated area far from the wells (control points) can provide a prediction on the assessment of the environments and architectures useful for potential definition of the different part of the petroleum system. To cross-validate and verify the degree of accuracy of the simulated properties far from the control points, it is necessary to check the correspondence between observed and simulated facies in other wells not used as an input to build and calibrate the models (i.e. a blind well test, see Hyne, 2014). The consistency between the new well data and the properties extracted from the 3D stratigraphic forward simulation will prove the predictive power of the model. One or more wells could be used for the blind-test. These wells, if not already described in literature, need to be study in detail with the same workflow adopted in this thesis: cores, petrography of thin sections, and well log analysis in order to reconstruct the vertical facies distribution.

## 6.2 Regional forward stratigraphic assessment

The workflow used on this thesis could be extended to the regional scale in order to produce for the first time a 3D stratigraphic forward modelling of the Arab Fm. at the scale of the Rub' Al Khali basin (Figure 2.4). The model could be centered on the basin with an area of 300x500 km and it will combine all the data available in the different fields scattered on the Rub' Al Khali basin. The detailed 3D field evolution provided within this thesis, the well logs and stratigraphies of other fields (e.g. Al-Silwadi et al., 1996; Al-Emadi et al., 2009; Morad, et al., 2012; Grötsch et al., 2003), and the new regional paleogeographic picture at the top of the Stromatoporoid Zone (Figure 3.12) could be used as key constraints for the modelling.

The first challenge of the project will be the definition of the regional bathymetry and thickness maps, needed by the DionisosFlow™ software to compute the subsidence variations. To overcome this problem a 3D modelling software could be used (e.g. move™ by Midland Valley) to interpolate the data available at the control points, by means of a range of statistic algorithms. The second main challenge consists in the assessment of all the inputs that control the deposition of the Arab Formation. The first trial could be attempted using the values inserted in the best-fitting model presented in this thesis. Different ranges could be then tested and changed in order to reach a regional calibrated model. To quantify the uncertainties and optimize the model, the huge set of parameters could be tested by multiple simulations with an uncertainty modelling tool (e.g. CougarFlow™; see Hawie et al., 2015; www.beicip.com). The multiple-realizations produce a sensitivity analysis on all the uncertain parameters, allowing to select the most influential and important ones (Hawie et al., 2015). The higher calibrated models will be analyzed and the geological consistent ones will be chosen to represent possible 3D depositional-time evolution scenarios for the Arab Fm. at the regional scale.

## 6.3 Thermal-burial history and basin modelling: new insights on the diagenetic impact

The sedimentological and stratigraphic data gathered within this Ph.D. project could be used to develop a 3D forward thermal-burial model, in order to dynamically simulate the evolution of the Arab Fm. sedimentary basin through the geological time. The model will be generated at the same scale (100x80 km) of the 3D stratigraphic forward simulation of this thesis with the aim to focus on the development of the onshore field anticline structure and gas emplacement. For example, the simulation could be held by TemisFlow® software (IFPEN; www.beicip.com), a next generation basin-modelling tool that allows to simulate the thermal history, as well as the pressure evolution and the multiphase flow migration, assessing hydrocarbons generation, migration and accumulation (Schneider et al., 2000; www.beicip.com). The investigation time will span from the Diyab Fm. deposition (Oxfordian-Kimmeridgian) until the present-day, in order to comprise in the simulation the main source rock of the Arab Formation. The geological succession will be defined by a series of selected horizons and erosion maps, populated by sedimentary facies converted in petrophysical properties; after a backstripping process the forward simulation of the basin is ready to be performed (e.g. Teles et al., 2014).

The developed thermal-burial history together with the hydrocarbon expulsion and migration simulations will be fundamental to provide a quantitative high-detail picture of the parameters (and their timing) that impact on the Arab Fm. reservoirs quality distribution. Processes such as the anticline development and gas emplacement have been proved to exert a significant control on the diagenetic alterations on the Arab Fm. reservoir in the field of study (Morad et al., in review).

# ACKNOWLEDGEMENTS

First of all I would like to thank for funding this Ph.D. project the Petroleum Institute of Abu Dhabi (PIRC project nr. LTR14012) and the Department of Earth and Environmental Sciences of University of Pavia (Research Project "Burial diagenesis and thermochemical sulfate reduction in the Arab gas reservoirs", P.I. Prof. A. Di Giulio), and Al Hosn Gas Company for giving us access to samples and necessary data.

I would like to express my deep gratitude to my supervisors Prof. Andrea Di Giulio and Dr. Andrea Ceriani for their constructive revisions, suggestions and enormous patience during these three years. A lot of thanks to my co-supervisors Dr. Fadi H. Nader and Dr. Rémy Deschamps for their enthusiastic help, encouragement, positive attitude and precious guide.

I am thankful to Daniel Morad for sharing with me his work and doubts, and a lot of enriching discussions.

I am grateful to Prof. Miriam Cobianchi for her substantial scientific contribution in my Ph.D., constructive discussions and constant optimism.

Special thanks to Dr. Marta Gasparrini and Professor Sadoon Morad for their evaluable help in the core-logging activity, and to Dr. Didier Granjeon and Dr. Christine Souque (IFPEN) for their important advices in the initial assessment of the 3D forward modelling.

Big thanks to the two anonymous reviewers of the first paper for improving the scientific quality of my work with their fruitful comments.

Sincere thanks to Fatima Al Darmaki, Stan Stearns, and David Lawrence (Al Hosn Gas) for the constructive meeting and the help with the papers bureaucracy.

Finally, but not less important, a deeply acknowledgement to Beicip-Franlab and the technical team for providing DionisosFlow™ and a constant fundamental support.

# REFERENCES

Abdolmaleki, J., Tavakoli, V., Asadi-Eskandar, A., 2016. Sedimentological and diagenetic controls on reservoir properties in the Permian–Triassic successions of Western Persian Gulf, Southern Iran. Journal of Petroleum Science and Engineering, vol. 141, pp. 90-113

Aigner, T., 1982. Calcareous tempestites: storm-dominated stratification in Upper Muschelkalk limestones (Middle Trias, SW-Germany). In: Einsele G., Seilacher A. (eds.), Cyclic and Event Stratification. Springer-Verlag, Berlin, Heidelberg, pp. 180-198

Aigner, T., Braun, S., Palermo, D., Blendinger, W., 2007. 3D geological modelling of a carbonate shoal complex: reservoir analogue study using outcrop data. EAGE First Break, vol. 25, pp. 65-72

Al-Awwad, S.F., Collins, L.B., 2013. Carbonate-platform scale correlation of stacked high-frequency sequences in the Arab-D reservoir, Saudi Arabia. Sedimentary Geology, vol. 294, pp. 205-218

Al-Awwad, S.F., Pomar, L., 2015. Origin of the rudstone-floatstone beds in the Upper Jurassic Arab-D reservoir, Khurais Complex, Saudi Arabia. Marine and Petroleum Geology, vol. 67, pp. 743-768

Al-Emadi, A., Jorry, S.J., Chautru J.M., Caline, B., Blum, M.S., Jeddaan, N., Fryer, V., Léandri, P., Fraisse, C., 2009. 3D modeling of the Arab Formation (Maydan Mahzam field, Offshore Qatar): an integrated approach. International Petroleum Technology Conference, 7-9 December, Doha, Qatar. IPTC 13461, pp. 1-17

Al-Husseini, M.I., 1997. Jurassic sequence stratigraphy of the western and southern Arabian Gulf. GeoArabia, vol. 2, no. 4, pp. 361-382

Al-Husseini, M.I. 2008. Launch of the Middle East geologic time scale. GeoArabia, vol. 13, no. 4, p. 11 and 185-188

Al-Husseini, M., 2009. Update to Late Triassic-Jurassic stratigraphy of Saudi Arabia for the Middle East geologic time scale. GeoArabia, vol. 14, no. 2, pp. 145-186

Al-Husseini, M.I., Matthews, R.K., 2008. Jurassic-Cretaceous Arabian orbital stratigraphy: the AROS-JK chart. GeoArabia, vol. 13, no. 1, pp. 89-94

Allen, P.A., Allen, J.R., 2005. Basin Analysis: Principles and Applications. Second edition, Wiley-Blackwell, 560 p.

Al-Saad, H., Ibrahim, M.I.A., 2005. Facies and palynofacies characteristics of the Upper Jurassic Arab D reservoir in Qatar. Revue de Paléobiologie, Genève, vol. 24, no. 1, pp. 225-241

Al-Saad, H., Sadooni, F.N., 2001. A new depositional model and sequence stratigraphic interpretation for the Upper Jurassic Arab "D" reservoir in Qatar. Journal of Petroleum Geology, vol. 24, no. 3, pp. 243-264

Alsharhan, A.S., 1989. Petroleum geology of the United Arab Emirates. Journal of Petroleum Geology, vol. 12, no. 3, pp. 253-288

Alsharhan, A.S., Kendall, C.G.St.C., 1994. Depositional setting of the Upper Jurassic Hith anhydrite of the Arabian Gulf: an analog to Holocene evaporites of the United Arab Emirates and Lake MacLeod of western Australia. AAPG Bulletin, vol. 78, no. 7, pp. 1075-1096

Alsharhan, A.S., Kendall, C.G.St.C., 2003. Holocene coastal carbonates and evaporites of the southern Arabian Gulf and their ancient analogues. Earth-Science Reviews, vol. 61, pp. 191-243

Alsharhan, A.S., Kendall, C.G.St.C., 2011. Introduction to Quaternary carbonate and evaporite sedimentary facies and their ancient analogues. In: Kendall, C.G.St.C., Alsharhan, A.S. (eds.), Quaternary carbonate and evaporite sedimentary facies and their ancient analogues: A Tribute to Douglas James Shearman. Special Publication no. 43 of the International Association of Sedimentologists, Wiley-Blackwell, pp. 1-10

Alsharhan, A.S., Magara, K., 1995. Nature and distribution of porosity and permeability in Jurassic Carbonate reservoirs of the Arabian Gulf Basin. Facies, vol. 32, pp. 237-254

Alsharhan, A.S., Nairn, A.E.M., 1997. Sedimentary basins and petroleum geology of the Middle East. Elsevier, Amsterdam, 878 p.

Alsharhan, A.S., Scott, R.W., 2000. Hydrocarbon potential of Mesozoic carbonate platform-basin systems, U.A.E.. In: Alsharhan A.S., Scott, R.W. (eds.), Middle East Models of Jurassic/Cretaceous Carbonate Systems. SEPM Special Publication, no. 69, pp. 335-358

Alsharhan, A.S., Whittle, G.L., 1995. Carbonate-evaporite sequences of the Late Jurassic, southern and southwestern Arabian Gulf. AAPG Bulletin, vol. 79, no. 11, pp. 1608-1630

Al-Silwadi, M.S., Kirkham, A., Simmons, M.D., Twombley, B.N., 1996. New insights into regional correlation and sedimentology, Arab Formation (Upper Jurassic), offshore Abu Dhabi. GeoArabia, vol. 1, no. 1, pp. 6-27

Al-Suwaidi, A.S., Aziz, S.K., 2002. Sequence stratigraphy of Oxfordian and Kimmeridgian shelf carbonate reservoirs, offshore Abu Dhabi. GeoArabia, vol. 7, no. 1, pp. 31-44

Al-Suwaidi, A.S., Taher, A.K., Alsharhan, A.S., Salah, M.G., 2000. Stratigraphy and geochemistry of Upper Jurassic Diyab Formation, Abu Dhabi, U.A.E.. In: Alsharhan A.S., Scott, R.W. (eds.), Middle East Models of Jurassic/Cretaceous Carbonate Systems. SEPM Special Publication, no. 69, pp. 249-271

Alzaga-Ruiz, H., Granjeon, D., Lopez, M., Seranne, M., Roure, F., 2009. Gravitational collapse and Neogene sediment transfer across the western margin of the Gulf of Mexico: insights from numerical models. Tectonophysics, vol. 470, pp. 21-41

Ayoub, M.R., En Nadi, I.M., 2000. Stratigraphic framework and reservoir development of the Upper Jurassic in Abu Dhabi area, U.A.E.. In: Alsharhan A.S., Scott, R.W. (eds.), Middle East Models of Jurassic/Cretaceous Carbonate Systems. SEPM Special Publication, no. 69, pp. 229-248

Azer, S.R., Peebles, R.G., 1995. Sequence stratigraphy of the Hith/Upper Arab formations offshore Abu Dhabi, U.A.E.. Proceedings of the 9th Society of Petroleum Engineers Middle East Oil Show, 11-14 March, Bahrain. SPE 29799, pp. 277-292

Bąbel, M., Schreiber, B.C., 2014. Geochemistry of evaporites and evolution of seawater. In: Holland, H., Turekian, K. (eds.), Treatise on Geochemistry (Second edition). Elsevier, pp. 483-560

Beigi, M., Jafarian, A., Javanbakht, M., Wanas, H.A., Mattern, F., Tabatabaei, A., 2017. Facies analysis, diagenesis and sequence stratigraphy of the carbonate-evaporite succession of the Upper Jurassic Surmeh Formation: impacts on reservoir quality (Salman Oil Field, Persian Gulf, Iran). Journal of African Earth Sciences, vol. 129, pp. 179-194

Beydoun, Z.R., 1998. Arabian plate oil and gas: why so rich and so prolific? Episodes, vol. 21, no. 2, pp. 74-81

Bosellini, A., Mutti, E., Ricci Lucchi, F., 1989. Rocce e successioni sedimentarie. UTET Torino, 395 p.

Boylan, A.L., Waltham, D.A., Bosence, D.W.J., Bádenas, B., Aurell, M., 2002. Digital rocks: linking forward modelling to carbonate facies. Basin Research, vol. 14, pp. 401-415

Brown, A., 1997. Porosity variation in carbonates as a function of depth: Mississippian Madison Group, Williston Basin. In: Kupecz, J.A., Gluyas, J., Bloch, S. (eds.), Reservoir quality prediction in sandstones and carbonates. AAPG Memoir 69, pp. 29-46

Bruneau, B., Chauveau, B., Duarte, L.V., Desaubliaux, G., Moretti, I., Baudin, F., 2016. 3D numerical modelling of marine organic matter distribution: example of the Early Jurassic sequences of the Lusitanian Basin (Portugal). Basin Research, doi:10.1111/bre.12210

Burchette, T.P., Wright, V.P., 1992. Carbonate ramp depositional systems. Sedimentary Geology, vol. 79, pp. 3-57

Burchette, T.P., Wright, V.P., Faulkner, T.J., 1990. Oolitic sandbody depositional models and geometries, Mississippian of southwest Britain: implications for petroleum exploration in carbonate ramp settings. Sedimentary Geology, vol. 68, pp. 87-115

Burgess, P.M., 2001. Modeling carbonate sequence development without relative sea-level oscillations. Geology, vol. 29, no. 12, pp. 1127-1130

Burgess, P.M., Steel, R.J., Granjeon, D., 2008. Stratigraphic forward modeling of basin-margin clinoforms systems: implications for controls on topset and shelf width and timing on formation of shelf-edge deltas. In: Hampson, G.J., Steel, R.J., Burgess, P.M., Dalrymple, R.W. (eds.), Recent Advances in Models of Siliciclastic Shallow-Marine Stratigraphy. SEPM Special Publication, no. 90, pp. 35-45

Burgess, P.M., Lammers, H., Van Oosterhout, C., Granjeon, D., 2006. Multivariate sequence stratigraphy: tackling complexity and uncertainty with stratigraphic forward modeling, multiple scenarios, and conditional frequency maps. AAPG Bulletin, vol. 90, no. 12, pp. 1883-1901

Cantrell, D.L., Hagerty, R.M., 2003. Reservoir rock classification, Arab-D reservoir, Ghawar field, Saudi Arabia. GeoArabia, vol. 8, no. 3, pp. 435-462

Cantrell, D.L., Swart, P.K., Handford, R.C., Kendall, C.G., Westphal, H., 2001. Geology and production significance of dolomite, Arab-D reservoir, Ghawar Field, Saudi Arabia. GeoArabia, vol. 6, no.1, pp. 45-60

Catuneanu, O., 2006. Principles of Sequence Stratigraphy. Elsevier, Amsterdam, 386 p.

Catuneanu, O., Willis, A.J., Miall, A.D., 1998. Temporal significance of sequence boundaries. Sedimentary Geology, vol. 121, pp.157-178

Catuneanu, O., Galloway, W.E., Kendall, C.G.St.C., Miall, A.D., Posamentier H.W., Strasser, A., Tucker, M.E., 2011. Sequence stratigraphy: methodology and nomenclature. Newsletters on Stratigraphy, vol. 44, no. 3, pp. 173-245

Catuneanu, O., Abreu, V., Bhattacharya, J.P., Blum, M.D., Dalrymple, R.W., Eriksson, P.G., Fielding, C.R., Fisher, W.L., Galloway, W.E., Gibling, M.R., Giles, K.A., Holbrook, J.M., Jordan, R., Kendall, C.G.St.C., Macurda, B., Martinsen, O.J., Miall, A.D., Neal, J.E., Nummedal, D., Pomar, L., Posamentier, H.W., Pratt, B.R., Sarg, J.F., Shanley, K.W., Steel, R.J., Strasser, A., Tucker, M.E., Winker, C., 2009. Towards the standardization of sequence stratigraphy. Earth-Science Reviews vol. 92, pp. 1-33

Cox, P.A., Wood, R.A., Dickson, J.A.D., Al Rougha, H.B., Shebl, H., Corbett, P.W.M., 2010. Dynamics of cementation in response to oil charge: evidence from a Cretaceous carbonate field, UAE. Sedimentary Geology, vol. 228, pp. 246-254

Croizé, D., Renard, F., Gratier, J., 2013. Compaction and porosity reduction in carbonates: a review of observations, theory, and experiments. Advances in Geophysics, vol. 54, pp. 181-238

Csato, I., Granjeon, D., Catuneanu, O., Baum, G.R., 2013. A three-dimensional stratigraphic model for the Messinian crisis in the Pannonian Basin, eastern Hungary. Basin research, vol. 25, pp. 121-148

Dalrymple, R.W., 2010. Interpreting sedimentary successions: facies, facies analysis and facies models. In: James, N.P., Dalrymple, R.W. (eds.), Facies Model 4. GEOtext6, St. John's, Newfoundland, Geological Association of Canada, pp. 3-18

Daraei, M., Rahimpour-Bonab, H., Fathi, N., 2014. Factors shaping reservoir architecture in the Jurassic Arab carbonates: a case from the Persian Gulf. Journal of Petroleum Science and Engineering, vol. 122, pp.187-207

Demicco, R.V., 1998. CYCOPATH 2D - A two-dimensional, forward model of cyclic sedimentation on carbonate platforms. Computers & Geosciences, vol. 24, no. 5, pp. 405-423

Dunham, R.J., 1962. Classification of carbonate rocks according to depositional texture. In: Ham W.E. (ed.), Classification of Carbonate Rocks - A Symposium. AAPG Memoir 1, pp. 108-121

Durham, L.S., 2005. Saudi Arabia's Ghawar field: the elephant of all elephants. AAPG Explorer, 26, pp. 4-7 [archives.aapg.org]

Ehrenberg, S.N., Nadeau, P.H., Aqrawi, A.A.M., 2007. A comparison of Khuff and Arab reservoir potential throughout the Middle East. AAPG Bulletin, vol. 91, no. 3, pp. 275-286

Embry III, A.F., Klovan, J.E., 1971. A Late Devonian reef tract on Northeastern Banks Island, N.W.T.. Bulletin of Canadian Petroleum Geology, vol. 19, no. 4, pp. 730-781

Enos, P., Samankassou, E., 1998. Lofer cyclothems revisited (Late Triassic, northern Alps, Austria). Facies, vol. 38, pp. 207-228

Esrafili‐Dizaji, B., Rahimpour‐Bonab, H., 2014. Generation and evolution of oolitic shoal reservoirs in the Permo‐Triassic carbonates, the South Pars Field, Iran. Facies, vol. 60, pp. 921-940

Feazel, C.T., Schatzinger, R.A., 1985. Prevention of carbonate cementation in petroleum reservoirs. In: Schneidermann, N., Harris, P.M. (eds.), Carbonate Cements. SEPM Special Publication, no. 36, pp. 97-106

Fischer, A.G., 1964. The Lofer cyclothems of the Alpine Triassic. In: Merriam, D.F. (ed.), Symposium on cyclic sedimentation. Kansas Geological Survey, Bulletin 169, pp. 107-149

Flügel, E., 2004. Microfacies of Carbonate Rocks. Analysis, Interpretation and Application. Springer-Verlag Berlin Heidelberg, 976 p.

Glennie, K.W., 2010. Structural and stratigraphic evolution of Abu Dhabi in the context of Arabia. Arabian Journal of Geosciences, vol. 3, pp. 331-349

Goldhammer, R.K., 1997. Compaction and decompaction algorithms for sedimentary carbonates. Journal of Sedimentary Research, vol. 67, no. 1, pp. 26-35

Goldstein, R.H., Reynolds, T.J., 1994. Systematics of fluid inclusions in diagenetic minerals. SEPM Short Course 31. Society for Sedimentary Geology, 199 p.

Gonzalez, R., Eberli, G.P., 1997. Sediment transport and bedforms in a carbonate tidal inlet; Lee Stocking Island, Exumas, Bahamas. Sedimentology, vol. 44, pp. 1015-1030

Granjeon, D., 1997. Modélisation stratigraphique déterministe: conception et applications d'un modèle diffusif 3-D multilithologique. Ph.D. dissertation, Memoires Geosciences Rennes, vol. 78, Université de Rennes 1, France, 197 p.

Granjeon, D., 2010. Dionisos - 3D stratigraphic modelling of sedimentary basins. AAPG-ER Newsletter, vol. 5, pp. 4-5

Granjeon, D., 2014. 3D forward modelling of the impact of sediment transport and base level cycles on continental margins and incised valleys. In: Martinius, A.W., Ravnås, R., Howell, J.A., Steel, R.J., and Wonham, J.P. (eds.), From Depositional Systems to Sedimentary Successions on the Norwegian Continental Margin, First edition. Int. Assoc. Sedimentol. Spec. Publ., vol. 46, pp. 453-472

Granjeon, D., Joseph, P., 1999. Concepts and applications of a 3-D multiple lithology, diffusive model in stratigraphic modeling. In: Harbaugh, J.W., Watney, W.L., Rankey, E.C., Slingerland, R., Goldstein, R.H., and Franseen, E.K. (eds.), Numerical Experiments in Stratigraphy: Recent Advances in Stratigraphic and Sedimentologic Computer Simulations. SEPM Special Publication, no. 62, pp. 197-210

Griffiths, C.M., Dyt, C., Paraschivoiu, E., Liu, K., 2001. Sedsim in hydrocarbon exploration. In: Merriam, D., Davis, J.C. (eds.), Geologic Modeling and Simulation. Kluwer Academic, New York, pp. 71-97

Grötsch, J., Suwaina, O., Ajlani, G., Taher, A., El-Khassawneh, R., Lokier, S., Coy, G., Van der Weerd, E., Masalmeh, S., Van Dorp, J., 2003. The Arab Formation in central Abu Dhabi: 3-D reservoir architecture and static and dynamic modeling. GeoArabia, vol. 8, no. 1, pp. 47-86

Gvirtzman, Z., Csato, I., Granjeon, D., 2014. Constraining sediment transport to deep marine basins through submarine channels: the Levant margin in the Late Cenozoic. Marine Geology, vol. 347, pp. 12–26

Haq, B.U., Al-Qahtani A.M., 2005. Phanerozoic cycles of sea-level change on the Arabian Platform. GeoArabia, vol. 10, no. 2, pp. 127-160 + enclosures

Haq, B.U., Hardenbol, J., Vail, P.R., 1987. Chronology of fluctuating sea levels since the Triassic. Science, vol. 235, pp. 1156-1166

Harris, P.M., 2009. Depositional environments of carbonate platforms. Search and Discovery Article #60032, pp. 31-60

Hashmie, A., Rostamnejad, A., Nikbakht, F., Ghorbanie, M., Rezaie, P., Gholamalian, H., 2016. Depositional environments and sequence stratigraphy of the Bahram Formation (middle-late Devonian) in north of Kerman, south-central Iran. Geoscience Frontiers, vol. 7, pp. 821-834

Hawie, N., Barrois, A., Marfisi, E., Murat, B., Hall, J., El-Wazir, Z, Al-Madani, N., Aillud, G., 2015. Forward stratigraphic modelling, deterministic approach to improve carbonate heterogeneity prediction; Lower Cretaceous, Abu Dhabi. Abu Dhabi International Petroleum Exhibition and Conference, 9-12 November, Abu Dhabi, UAE. SPE-177519-MS, pp. 1-15

Hawie, N., Dubille, M., Guyomar, N., Maury, G., Thomas, V., Vidal, O., Carayon, V., Cuilhe, L., Al-Sahlan, G., Al-Ali, S., Al-Khamis, A., Dawwas Al-Ajmi, M., 2016. Innovative and integrated multi-disciplinary workflow for mature basins exploration: the Arabian Platform case study. Abu Dhabi International Petroleum Exhibition and Conference, 7-10 November, Abu Dhabi, UAE. SPE-183193-MS, pp. 1-20

Hawie, N., Deschamps, R., Granjeon, D., Nader, F.H., Gorini, C., Müller, C., Montadert, L., Baudin, F., 2017. Multi-scale constraints of sediment source to sink systems in frontier basins: a forward stratigraphic modelling case study of the Levant region. Basin Research, vol. 29, pp. 418-445, doi:10.1111/bre.12156

Heasley, E.C., Worden, R.H., Hendry, J.P., 2000. Cement distribution in a carbonate reservoir: recognition of a palaeo oil-water contact and its relationship to reservoir quality in the Humbly Grove field, onshore, UK. Marine and Petroleum Geology, vol. 17, pp. 639-654

Huang, X., Griffiths, C.M., Liu, J., 2015. Recent development in stratigraphic forward modelling and its application in petroleum exploration. Australian Journal of Earth Sciences, vol. 62, pp. 903-919

Hughes, G.W., 2004a. Middle to Late Jurassic biofacies of Saudi Arabia. Rivista Italiana di Paleontologia e Stratigrafia, vol. 110, no. 1, pp. 173-179

Hughes, G.W., 2004b. Middle to Upper Jurassic Saudi Arabian carbonate petroleum reservoirs: biostratigraphy, micropaleontology and palaeoenvironments. GeoArabia, vol. 9, no. 3, pp. 79-114

Hyne, N.J., 2014. Dictionary of Petroleum Exploration, Drilling & Production. PennWell corporation, Second edition, 778 p.

James, N.P., Jones, B., 2016. Origin of Carbonate Sedimentary Rocks. Wiley, United Kingdom, 446 p.

Kendall, C.G.St.C., Alsharhan, A.S., 2011a. Holocene geomorphology and recent carbonate-evaporite sedimentation of the coastal region of Abu Dhabi, United Arab Emirates. In: Kendall, C.G.St.C., Alsharhan, A.S. (eds.), Quaternary carbonate and evaporite sedimentary facies and their ancient analogues: A Tribute to Douglas James Shearman. Special Publication no. 43 of the International Association of Sedimentologists, Wiley-Blackwell, pp. 45-88

Kendall, C.G.St.C., Alsharhan, A.S., 2011b. Coastal Holocene carbonates of Abu Dhabi, UAE: depositional setting, sediment distribution, and role of cyanobacteria in micritization. In: Kendall, C.G.St.C., Alsharhan, A.S. (eds.), Quaternary carbonate and evaporite sedimentary facies and their ancient analogues: A Tribute to Douglas James Shearman. Special Publication no. 43 of the International Association of Sedimentologists, Wiley-Blackwell, pp. 205-220

Kietzmann, D.A., Palma, R.M., Riccardi, A.C., Martín-Chivelet, J., López-Gómez, J., 2014. Sedimentology and sequence stratigraphy of a Tithonian–Valanginian carbonate ramp (Vaca Muerta Formation): a misunderstood exceptional source rock in the Southern Mendoza area of the Neuquén Basin, Argentina. Sedimentary Geology, vol. 302, pp. 64-86

Kolodka, C., Vennin, E., Bourillot, R., Granjeon, D., Desaubliaux, G., 2016. Stratigraphic modelling of platform architecture and carbonate production: a Messinian case study (Sorbas Basin, SE Spain). Basin Research, vol. 28, pp. 658-684

Konert, G., Afifi, A.M., Al-Hajri, S.A., Droste, H.J., 2001. Paleozoic stratigraphy and hydrocarbon habitat of the Arabian Plate. GeoArabia, vol. 6, no. 3, pp. 407-442

Laskar, J., Robutel, P., Joutel, F., Gastineau, M., Correia, A.C.M., Levrard, B., 2004. A long term numerical solution for the insolation quantities of the Earth. Astronomy & Astrophysics, vol. 428, pp. 261-285

Lawrence, D.A., Hollis, C., Green, D., Deville de Perière, M., Al Darmaki, F., Bouzida, Y., 2015. Palaeogeographic reconstruction of a tide-dominated oolite shoal complex in the Lower Arab Formation, Onshore UAE. Abu Dhabi International Petroleum Exhibition and Conference, 9-12 November, Abu Dhabi, UAE. SPE 172769-MS, pp. 1-21

Le Nindre, Y., Vaslet, D., Le Métour, J., Bertrand, J., Halawani, M., 2003. Subsidence modelling of the Arabian Platform from Permian to Paleogene outcrops. Sedimentary Geology, vol. 156, pp. 263-285

Lehmann, C.T., Al Hosany, K.I., Cobb, D.O., Al-Hendi, A., 2008. Rock-typing of Upper Jurassic (Arab) carbonates offshore Abu Dhabi. Abu Dhabi International Petroleum Exhibition and Conference, 3-6 November, Abu Dhabi, UAE. SPE 117889, pp. 1-20

Leinfelder, R.R., Schlagintweit, F., Werner, W., Ebli, O., Nose, M., Schmid, D.U., Hughes, G.W., 2005. Significance of stromatoporoids in Jurassic reefs and carbonate platforms - concepts and implications. Facies, vol. 51, pp. 287-325

Lindsay, R.F., Cantrell, D.L., Hughes, G.W., Keith, T.H., Mueller III, H.W., Russell, S.D., 2006. Ghawar Arab-D reservoir: widespread porosity in shoaling-upward carbonate cycles, Saudi Arabia. In: Harris, P.M., Weber, L.J. (eds.), Giant hydrocarbon reservoirs of the world: From rocks to reservoir characterization and modeling. AAPG Memoir 88/SEPM Special Publication, pp. 97–137

Lucia, F.J., 2007. Carbonate reservoir characterization: an integrated approach, Second edition. Springer-Verlag Berlin Heidelberg, 336 p.

Marchionda, E., Deschamps, R., Nader, F.H., Di Giulio, A., Al Darmaki, F., Ceriani, A.. 3D stratigraphic forward modelling of a carbonate ramp: a quantitative field-scale analysis of the Arab Formation (Upper Jurassic, onshore Abu Dhabi, UAE). *Submitted to Sedimentary Geology*

Marchionda, E., Deschamps, R., Cobianchi, M., Nader, F.H., Di Giulio, A., Morad, D.J., Al Darmaki, F., Ceriani, A., 2018. Field-scale depositional evolution of the Upper Jurassic Arab Formation (onshore Abu Dhabi, UAE). Marine and Petroleum Geology, vol. 89, part 2, pp. 350-369 http://dx.doi.org/10.1016/j.marpetgeo.2017.10.006

Matthews, R.K., Frohlich, C., 1998. Forward modeling of sequence stratigraphy and diagenesis: application to rapid, cost-effective carbonate reservoir characterization. GeoArabia, vol. 3, no. 3, pp. 359-384

Montaggioni, L.F., Borgomano, J., Fournier, F., Granjeon, D., 2015. Quaternary atoll development: new insights from the two-dimensional stratigraphic forward modelling of Mururoa Island (Central Pacific Ocean). Sedimentology, vol. 62, pp. 466-500

Morad, D., Nader, F.H., Gasparrini, M., Morad, S., Rossi, C., Marchionda, E., Al Darmaki, F., Martines, M., Hellevang, H.. Comparison of the diagenetic and reservoir quality evolution between the anticline crest and flank of an Upper Jurassic carbonate gas reservoir, Abu Dhabi, United Arab Emirates. *In review at Sedimentary Geology.*

Morad, S., Al-Aasm, I.S., Nader, F.H., Ceriani, A., Gasparrini, M., Mansurbeg, H., 2012. Impact of diagenesis on the spatial and temporal distribution of reservoir quality in the Jurassic Arab D and C members, offshore Abu Dhabi oilfield, United Arab Emirates. GeoArabia, vol. 17, no. 3, pp. 17-56

Murris, R.J., 1980. Middle East: stratigraphic evolution and oil habitat. AAPG Bulletin, vol. 64, no. 5, pp. 597-618

Nader, F.H., De Boever, E. Gasparrini, M., Liberati, M., Dumont, C., Ceriani, A., Morad, S., Lerat, O., Doligez, B., 2013. Quantification of diagenesis impact on the reservoir properties of the Jurassic Arab D and C members (Offshore, U.A.E.). Geofluids, vol. 13, pp. 204-220

Neilson, J.E., Oxtoby, N.H., Simmons, M.D., Simpson, I.R., Fortunatova, N.K., 1998. The relationship between petroleum emplacement and carbonate reservoir quality: examples from Abu Dhabi and the Amu Darya Basin. Marine and Petroleum Geology, vol. 15, pp. 57-72

Nichols, G., 2009. Sedimentology and Stratigraphy. Second edition, Wiley-Blackwell, 432 p.

Nordlund, U., 1999. FUZZIM: forward stratigraphic modeling made simple. Computers & Geosciences, vol. 25, pp. 449-456

Norton, W.H., 1917. A classification of breccias. The Journal of Geology, vol. 25, no. 2, pp. 160-194

Oswald, E.J., Mueller III, H.W., Goff, D.F., Al-Habshi, H., Al-Matroushi, S., 1995. Controls on porosity evolution in Thamama Group carbonate reservoirs in Abu Dhabi, UAE. Middle East Oil Show, 11-14 March, Bahrain. SPE paper 29797-MS, pp. 1-15

Otvos, E.G., 2000. Beach ridges-definitions and significance. Geomorphology vol. 32, pp. 83-108

Paganoni, M., Al Harthi, A., Morad, D., Morad, S., Ceriani, A., Mansurbeg, H., Al Suwaidi, A., Al-Aasm, I.S., Ehrenberg, S.N., Sirat, M., 2016. Impact of stylolitization on diagenesis of a Lower Cretaceous carbonate reservoir from a giant oilfield, Abu Dhabi, United Arab Emirates. Sedimentary Geology, vol. 335, pp. 70-92

Palermo, D., Aigner, T., Nardon, S., Blendinger, W., 2010. Three-dimensional facies modeling of carbonate sand bodies: outcrop analog study in an epicontinental basin (Triassic, southwest Germany). AAPG Bulletin, vol. 94, no. 4, pp. 475-512

Peters, S.E., Loss, D.P., 2012. Storm and fair-weather wave base: a relevant distinction? Geology, vol. 40, no. 6, pp. 511-514

Pollastro, R.M., 2003. Total petroleum systems of the Paleozoic and Jurassic, greater Ghawar uplift and adjoining provinces of central Saudi Arabia and northern Arabian-Persian Gulf. U.S. Geological Survey Bulletin 2202-H, 100 p.

Pomar, L., 2001. Types of carbonate platforms: a genetic approach. Basin Research, vol. 13, pp. 313-334

Pomar, L., Hallock, P., 2008. Carbonate factories: a conundrum in sedimentary geology. Earth-Science Reviews, vol. 87, pp. 134-169

Pomar, L., Haq, B.U., 2016. Decoding depositional sequences in carbonate systems: concepts vs experience. Global and Planetary Change, vol. 146, pp. 190-225

Pomar, L., Kendall, C.G.St.C., 2008. Architecture of carbonate platforms: a response to hydrodynamics and evolving ecology. In: Lukasik, J., Simo, A., (eds.), Controls on Carbonate Platform and Reef Development. SEPM Special Publication, no. 89, pp. 187-216

Pomar, L., Morsilli, M., Hallock, P., Bádenas, B., 2012. Internal waves, an under-explored source of turbulence events in the sedimentary record. Earth-Sciences Reviews, vol. 111, pp. 56-81

Pomar, L., Aurell, M., Bádenas, B., Morsilli, M., Al-Awwad, S.F., 2015. Depositional model for a prograding oolitic wedge, Upper Jurassic, Iberian basin. Marine and Petroleum Geology, vol. 67, pp. 556-582

Powers, R.W., Ramirez, L.F., Redmond, C.D., Elberg, E.L.Jr., 1966. Geology of the Arabian Peninsula: Sedimentary Geology of Saudi Arabia. U.S. Geological Survey Professional Paper no. 560-D, pp. 60-65

Pratt, B.R., 2010. Peritidal carbonates. In: James, N.P., Dalrymple, R.W. (eds.), Facies Model 4. GEOtext6, St. John's, Newfoundland, Geological Association of Canada, pp. 401-420

Rabineau, M., Berné, S., Aslanian, D., Olivet, J., Joseph, P., Guillocheau, F., Bourillet, J., Ledrezen, E., Granjeon, D., 2005. Sedimentary sequences in the Gulf of Lion: a record of 100,000 years climatic cycles. Marine and Petroleum Geology, vol. 22, pp. 775-804

Rameil, N., 2005. Carbonate sedimentology, sequence stratigraphy, and cyclostratigraphy of the Tithonian in the Swiss and French Jura mountains: a high-resolution record of changes in sea level and climate. GeoFocus, vol. 13, 246 p.

Rameil, N., 2008. Early diagenetic dolomitization and dedolomitization of late Jurassic and earliest Cretaceous platform carbonates: a case study from the Jura Mountains (NW Switzerland, E France). Sedimentary Geology, vol. 212, pp. 70-85

Rankey, E.C., Reeder, S.L., 2011. Holocene oolitic marine sand complexes of the Bahamas. Journal of Sedimentary Research, vol. 81, pp. 97-117

Rankey, E.C., Riegl, B., Steffen, K., 2006. Form, function and feedbacks in a tidally dominated ooid shoal, Bahamas. Sedimentology, vol. 53, pp. 1191-1210

Read, J.F., Goldhammer, R.K., 1988. Use of Fischer plots to define third-order sea-level curves in Ordovician peritidal cyclic carbonates, Appalachians. Geology, vol. 16, no. 10, pp. 895-899

Read, J.F., Osleger, D., Elrick, M., 1991. Two-dimensional modeling of carbonate ramp sequences and component cycles. In: Franseen, E.K., Watney, W.L., Kendall, C.G.St.C.,

Ross, W. (eds.), Sedimentary modeling: computer simulations and methods for improved parameter definition. Kansas Geological Survey Bulletin 233, pp. 473-488

Reineck, H., Wunderlich, F., 1968. Classification and origin of flaser and lenticular bedding. Sedimentology, vol. 11, pp. 99-104

Rider, M.H., 2002. The geological interpretation of well logs. Rider-French Consulting Ltd, Second edition, 280 p.

Ruf, M., Aigner, T., 2004. Facies and poroperm characteristics of a carbonate shoal (Muschelkalk, South German Basin): a reservoir analogue investigation. Journal of Petroleum Geology, vol. 27, no. 3, pp. 215-239

Sartorio, D., Venturini, S., 1988. Southern Tethys Biofacies. Agip S.p.A., S. Donato Milanese, 235 p.

Schneider, F., Wolf, S., Faille, I., Pot., D., 2000. A 3D basin model for hydrocarbon potential evaluation: application to Congo offshore. Oil & Gas Science and Technology - Rev. IFP, vol. 55, no. 1, pp. 3-13

Schreiber, B.C., El Tabakh, M., 2000. Deposition and early alternation of evaporites. Sedimentology, vol. 47, suppl. 1, pp. 215-238

Seard, C., Borgomano, J., Granjeon, D., Camoin, G., 2013. Impact of environmental parameters on coral reef development and drowning: forward modelling of the last deglacial reefs from Tahiti (French Polynesia; IODP Expedition #310). Sedimentology, vol. 60, pp. 1357-1388

Seilacher, A., Aigner, T., 1991. Storm deposition at the bed, facies, and basin scale: the geologic perspective. In: Einsele, G., Ricken, W., Seilacher, A. (eds.), Cycles and Events in Stratigraphy. Springer-Verlag, Berlin, pp. 249-267

Serra, O., 1984. Fundamentals of well-log interpretation: 1. The acquisition of logging data. Elsevier, 423 p.

Shafie, K.R.K., Madon, M., 2008. A review of stratigraphic simulation techniques and their applications in sequence stratigraphy and basin analysis. Bulletin of Geological Society of Malaysia, vol. 54, pp. 81-89

Sømme, T.O., Helland-Hansen, W., Granjeon, D., 2009. Impact of eustatic amplitude variations on shelf morphology, sediment dispersal, and sequence stratigraphic interpretation: icehouse versus greenhouse systems. Geology, vol. 37, no. 7, pp. 587-590

Sparks, A.G., Rankey, E.C., 2013. Relations between geomorphic form and sedimentologic-stratigraphic variability: Holocene ooid sand shoal, Lily Bank, Bahamas. AAPG Bulletin, vol. 97, no. 1, pp. 61-85

Stern, R.J., Johnson, P., 2010. Continental lithosphere of the Arabian Plate: a geologic, petrologic, and geophysical synthesis. Earth-Science Reviews, vol. 101, pp. 29–67

Swart, P.K., Cantrell, D.L., Westphal, H., Handford, C.R, Kendall, C.G., 2005. Origin of dolomite in the Arab-D reservoir from the Ghawar field, Saudi Arabia: evidence from petrographic and geochemical constraints. Journal of Sedimentary Research, vol. 75, no. 3, pp. 476-491

Teles, V., Fornel, A., Houel, P., Delmas, J., Mengus, J.M., Michel, A., Maurand, N., 2014. Coupling basin and reservoir simulators for an improved $CO_2$ injection flow model. Energy Procedia, vol. 63, pp. 3665-3675

Tomašových, A., 2004. Microfacies and depositional environment of an Upper Triassic intra-platform carbonate basin: the Fatric Unit of the West Carpathians (Slovakia). Facies, vol. 50, pp. 77-105

Tucker, M.E., Wright, V.P., 1990. Carbonate sedimentology. Wiley-Blackwell, Oxford, 496 p.

Volery, C., Davaud, E., Foubert, A., Caline, B., 2010. Lacustrine microporous micrites of the Madrid Basin (Late Miocene, Spain) as analogues for shallow-marine carbonates of the Mishrif reservoir Formation (Cenomanian to Early Turonian, Middle East). Facies, vol. 56, pp. 385-397

Wang, J., Guo, R., Zhao, L., Li, W., Zhou, W., Duan, T., 2016. Geological features of grain bank reservoirs and the main controlling factors: a case study on Cretaceous Mishrif Formation, Halfaya Oilfield, Iraq. Petroleum Exploration Development, vol. 43, no. 3, pp. 404-415

Warren, J.K., 2006. Evaporites: Sediments, Resources and Hydrocarbons. Springer-Verlag, 1036 p.

Warren, J.K., 2010. Evaporites through time: tectonic, climatic and eustatic controls in marine and nonmarine deposits. Earth-Science Reviews, vol. 98, pp. 217-268

Warrlich, G.M.D., Waltham, D.A., Bosence, D.W.J., 2002. Quantifying the sequence stratigraphy and drowning mechanisms of atolls using a new 3-D forward stratigraphic modelling program (CARBONATE 3D). Basin Research, vol. 14, pp. 379-400

Warrlich, G., Bosence, D., Waltham, D., Wood, C., Boylan, A., Bádenas, B., 2008. 3D stratigraphic forward modelling for analysis and prediction of carbonate platform stratigraphies in exploration and production. Marine and Petroleum Geology, vol. 25, pp. 35-58

Williams, H.D., Burgess, P.M., Wright, V.P., Della Porta, G., Granjeon, D., 2011. Investigating carbonate platform types: multiple controls and a continuum of geometries. Journal of Sedimentary Research, vol. 81, pp. 18-37

Wright, V.P., 1992. Speculations on the controls on cyclic peritidal carbonates: ice-house versus greenhouse eustatic controls. Sedimentary Geology, vol. 76, pp. 1-5

Wright, V.P., Burchette, T.P., 1996. Shallow-water carbonate environments. In: Reading, H.G. (ed.), Sedimentary Environments: Processes, Facies and Stratigraphy. Third edition, Wiley-Blackwell, pp. 325-394

Yang, W., Lehrmann, D.J., 2014. Peritidal carbonate cycles induced by carbonate productivity variations: a conceptual model for an isolated Early Triassic greenhouse platform in South China. Journal of Palaeogeography, vol. 3, no. 2, pp. 115-126

Ziegler, M.A., 2001. Late Permian to Holocene paleofacies evolution of the Arabian Plate and its hydrocarbon occurrences. GeoArabia, vol. 6, no. 3, pp. 445-504

www.beicip.com

www.eia.gov Country Analysis Brief: United Arab Emirates. Last update: March 21, 2017

# APPENDIX 1 - CORE LOGGING

In the following appendix, the drawing of the core logs of all the studied wells is pictured (Figure A11), including the one already reported in the thesis (Figure 3.4). Core logging activity was performed in the cores lab in Abu Dhabi, where around 540 m (1772 ft) of cores slabs from the five wells (A1, A2, A3, A4 and A5) were investigated. For the main micropalentological components refer to Figure 3.5.

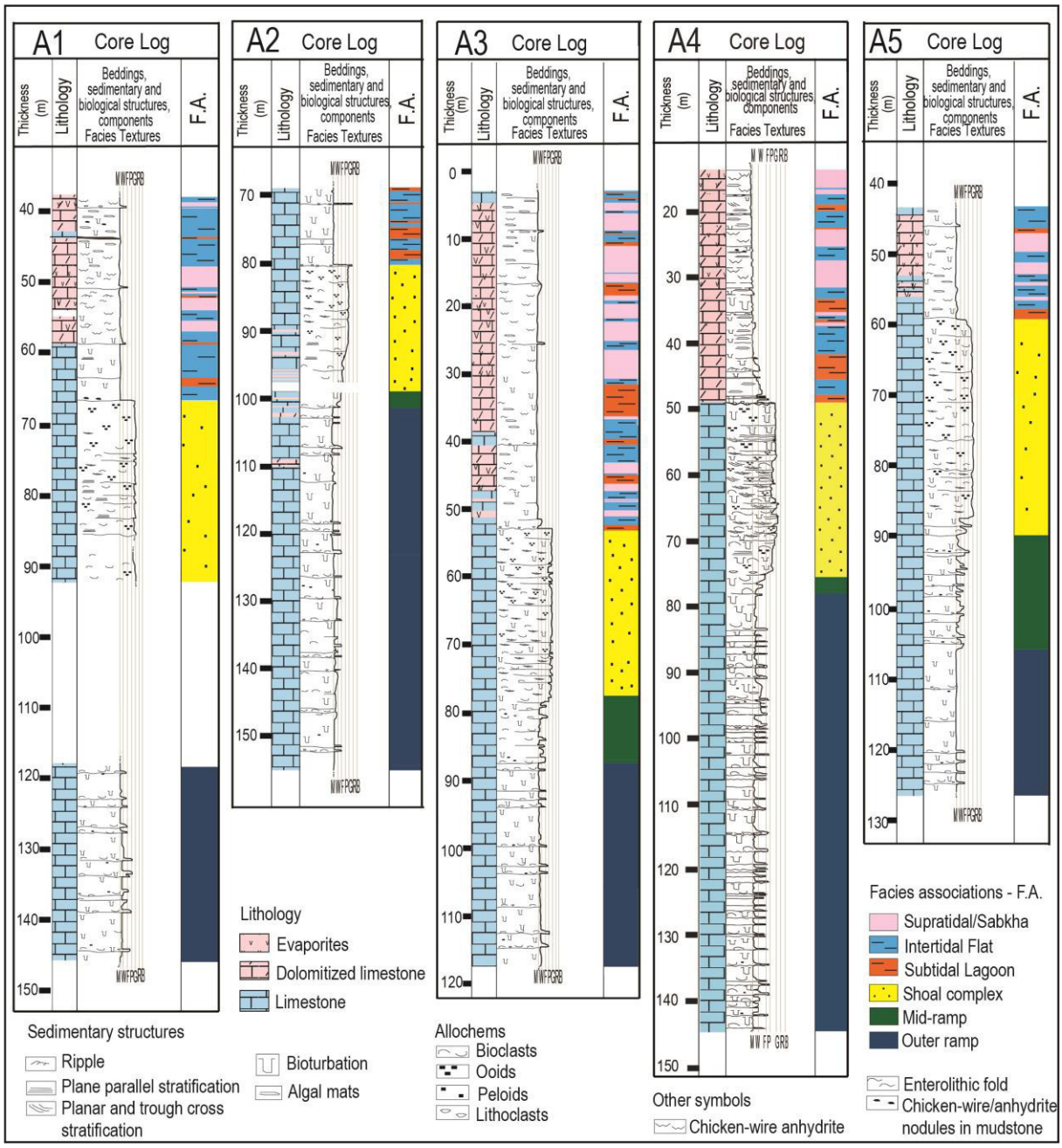


**Figure A11** *Core logs*

# APPENDIX 2 - THIN SECTIONS ANALYSIS

For the PhD research, 277 thin sections were analyzed under a polarizing microscope at the laboratories of IFPEN and University of Pavia, in order to identify: lithology, textures, main allochemical components, and biological and physical features of the Arab Formation.

For each well (except for the well A4 where no thin sections were available) a range chart is reported, that shows the biological and mineralogical components detected in the thin sections. The depth column displays the depth of each sample respect to the top of the Arab Fm. conventionally located at 0 m, with increasing positive values toward the bottom of the succession. The depth values were corrected for the core-log shift, in order to compare these charts with the well logs pictured in Figure 3.5, 3.6 and 3.7 of this thesis. For the well A3, the depth values correspond to the deviated MD log, and not to the TVD log reported in Figure 3.5 and 3.7.

A selection of microscope photographs (plane and cross polarized light) is presented for each well, with the aim to add some examples of the microfacies that characterized the succession. The microfacies codes (reported in brackets of the figures captions) refer to Table 3.1 of Chapter 3 reported again in this appendix.

LEGEND:

| | | | |
|---|---|---|---|
| **Clad** | *Cladocoropsis* spp. | **Lag** | Lagenidae |
| **Biv/Gas** | Bivalves/Gastropods | **Pel** | Peloids |
| **Das/Alg** | Dasyclads/Algae | **Oo** | Ooids |
| **Cly** | *Clypeina jurassica* | **Ost** | Ostracods |
| **Oog** | Oogonium of Characeae | **Micr** | Microbialites |
| **For** | Foraminifera | **Fen** | Fenestrae |
| **Kur** | *Kurnubia* spp. | **Brec** | Breccia |
| **Naut** | *Nautiloculina oolithica* | **Intra** | Intraclasts |
| **Tex** | Textulariidae | **Dolo** | Dolomitization |
| | | **Sul** | Sulfates |

**Table 3.1** *Major characteristics of the facies recognized, including lithology, structures, genetic processes and depositional environment interpretation.*

| FACIES CODE (F) | TEXTURES and MAIN COMPONENTS | SEDIMENTARY STRUCTURES | DEPOSITIONAL PROCESS | ENVIRONMENTAL INTERPRETATION |
|---|---|---|---|---|
| **MasMd** | Massive mudstone | Absence of sedimentary structures, different degree of bioturbation | Low energy mud fall out and transport | Lagoon, lower intertidal flat, mid-ramp, outer ramp |
| **BioMd-Wc** | Massive mudstone and wackestone with sporadic fragments of bivalves/gastropods, echinoderms, *Kurnubia* spp., foraminifera, ostracods, *Cladocoropsis* spp. | Absence of sedimentary structures, different degree of bioturbation | Low energy mud fall out and transport of bioclasts | Mid-ramp, outer ramp |
| **BirdMd-Wc** | Mudstone and wackestone with bird's eye porosity, presence of sporadic ostracods and algae | Massive aspect with fenestrae with cement growth in cavities (in some case silt-vadose filling) | Desiccation, gas bubbles | Intertidal zone, supratidal zone |
| **AlgMd** | Microbial algal mats mudstone (bindstone), presence of peloids | Algal mats lamination | Microbial organisms binding, trapping and producing carbonate | Intertidal zone, supratidal zone |
| **LamMd-Pc** | Laminated mudstone-packstone | Flat or cross lamination or flaser bedding | Transport under tidal currents | Subtidal lagoon, tidal channel |
| **BrcMd** | Brecciated mudstone, with mudclasts floating in a muddy matrix | Chaotic aspect | Desiccation breccia and probable tidal rework | Intertidal zone, supratidal zone |
| **DesMd** | Mudstone with desiccation features | Polygonal structures (mud-cracks) and tepee | Mudstone settling and desiccation | Intertidal zone, supratidal zone |
| **ShaleMd** | Black shaly mudstone, presence of organic matter | Massive aspect | Mud fall out deposit | Subtidal lagoon |
| **OstWc** | Wackestone (and mudstone) with ostracods and sporadic foraminifera, bivalves/gastropods, and algae (*Clypeina jurassica*) | Absence of sedimentary structures, massive aspect, presence of fenestral cavities | Low energy mud fall out and transport | Lagoon, lower intertidal flat, shallow marine |
| **BioWc-Pc** | Massive wackestone to packstone with fragments of bivalves/gastropods, echinoderms, *Kurnubia* spp., foraminifera, dasyclads/algae, peloids, intraclasts, *Cladocoropsis* spp. (ooids) | High level of bioturbation, homogenized aspect | Low energy mud fall out and transport of reworked bioclasts | Mid-ramp, outer ramp |
| **PelWc-Pc** | Peloidal wackestone/packstone, with sporadic bivalves/gastropods and foraminifera | Absence of sedimentary structures | Low energy mud fall out and transport | Lagoon, intertidal flat |
| **EroFl** | Poorly sorted floatstone, rich in bivalves/gastropods, echinoderms, *Kurnubia* spp., foraminifera, dasyclads/algae, *Cladocoropsis* spp. peloids and scattered mudclasts | Basal erosive and sharp surface and gradational top | Transport during storm events | Mid-ramp, outer ramp |

**Table 3.1** *continued from the previous page*

| FACIES CODE (F) | TEXTURES and MAIN COMPONENTS | SEDIMENTARY STRUCTURES | DEPOSITIONAL PROCESS | ENVIRONMENTAL INTERPRETATION |
|---|---|---|---|---|
| **BioPelPc-Gr** | Bioclastic-peloidal packstone to grainstone with bivalves/gastropods, echinoderms, intraclasts, ooids, *Kurnubia* spp., foraminifera, algae and cortoids | Sub horizontal or cross bedded lamination or massive aspect | High energy traction currents alternated to quiescent/fair weather production of carbonate | Shallow marine/shoal environment |
| **OoBioGr** | Oolitic grainstone (and packstone-grainstone) with bivalves, echinoderm fragments, intraclasts, *Kurnubia* spp., foraminifera and cortoids | Cross bedded lamination or massive aspect | High energy traction currents alternated to quiescent/fair weather production of carbonate | Shallow marine/shoal environment |
| **OoGr** | Oolitic grainstone (and packstone-grainstone) well sorted and classed, with cortoids | Cross bedded lamination or massive aspect | High energy traction currents alternated to quiescent/fair weather production of carbonate | Shallow marine/shoal environment |
| **CwSulf** | Chicken wire sulfates | Chicken wire structures irregular in shape separated by thin film or surrounded by dolomitized mudstones/wackestones | Displacive growth of sulfates | Supratidal/sabkha, upper intertidal zone |
| **EnSulf** | Enterolithic sulfates | Enterolithic folds (contorted/folded beds) separated by dolomitized mudstones/wackestones | *In situ* growth of sulfates | Supratidal/sabkha, upper intertidal zone |
| **FLag** | Poorly sorted lag deposit, characterized by scattered granules, small pebbles and lithoclasts | Erosive base | Wave rework and condensation of coarser sediments | Lagoon/intertidal, top of the shoal |

**Table A21** *Range chart of well A1.*

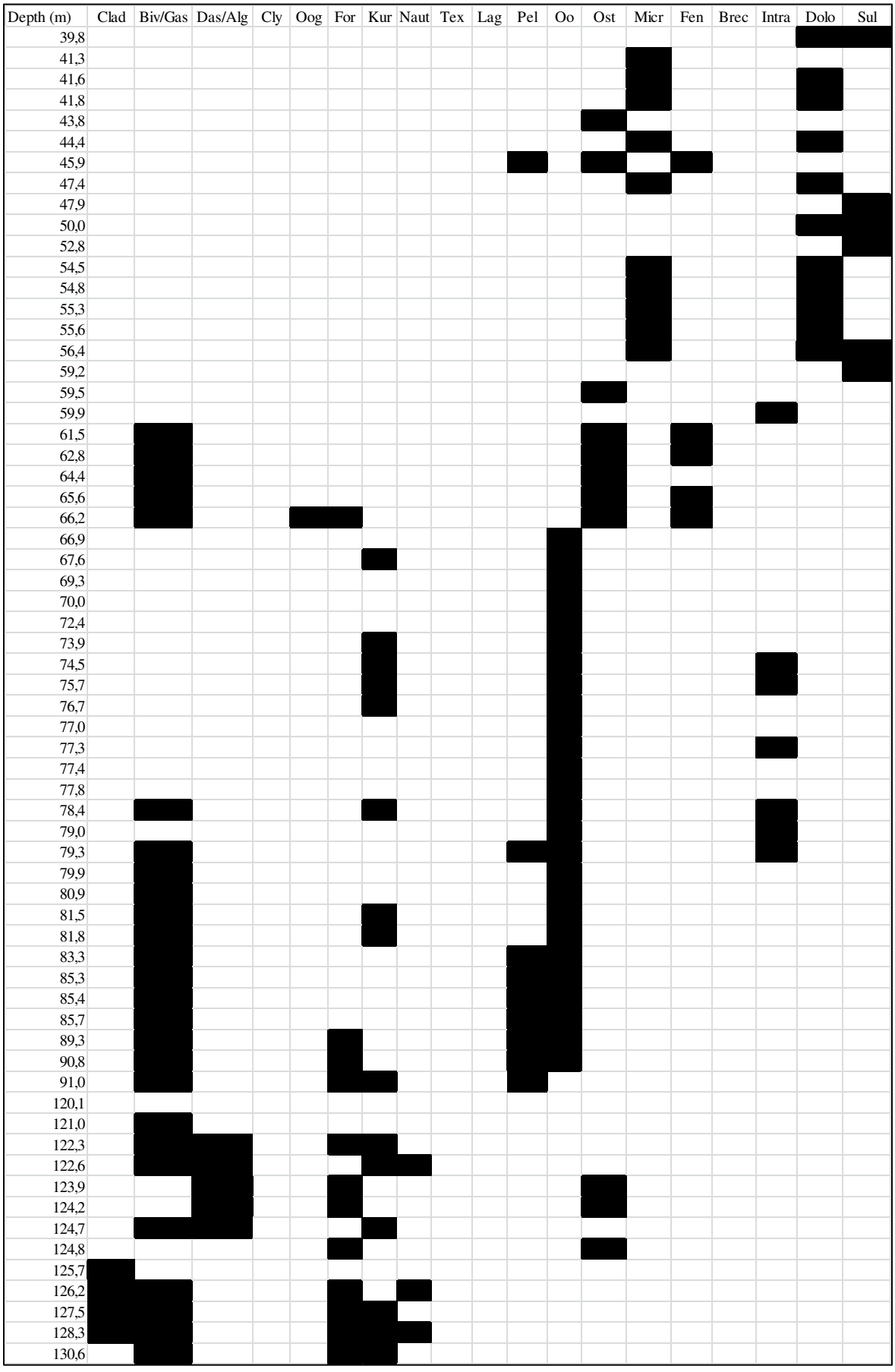

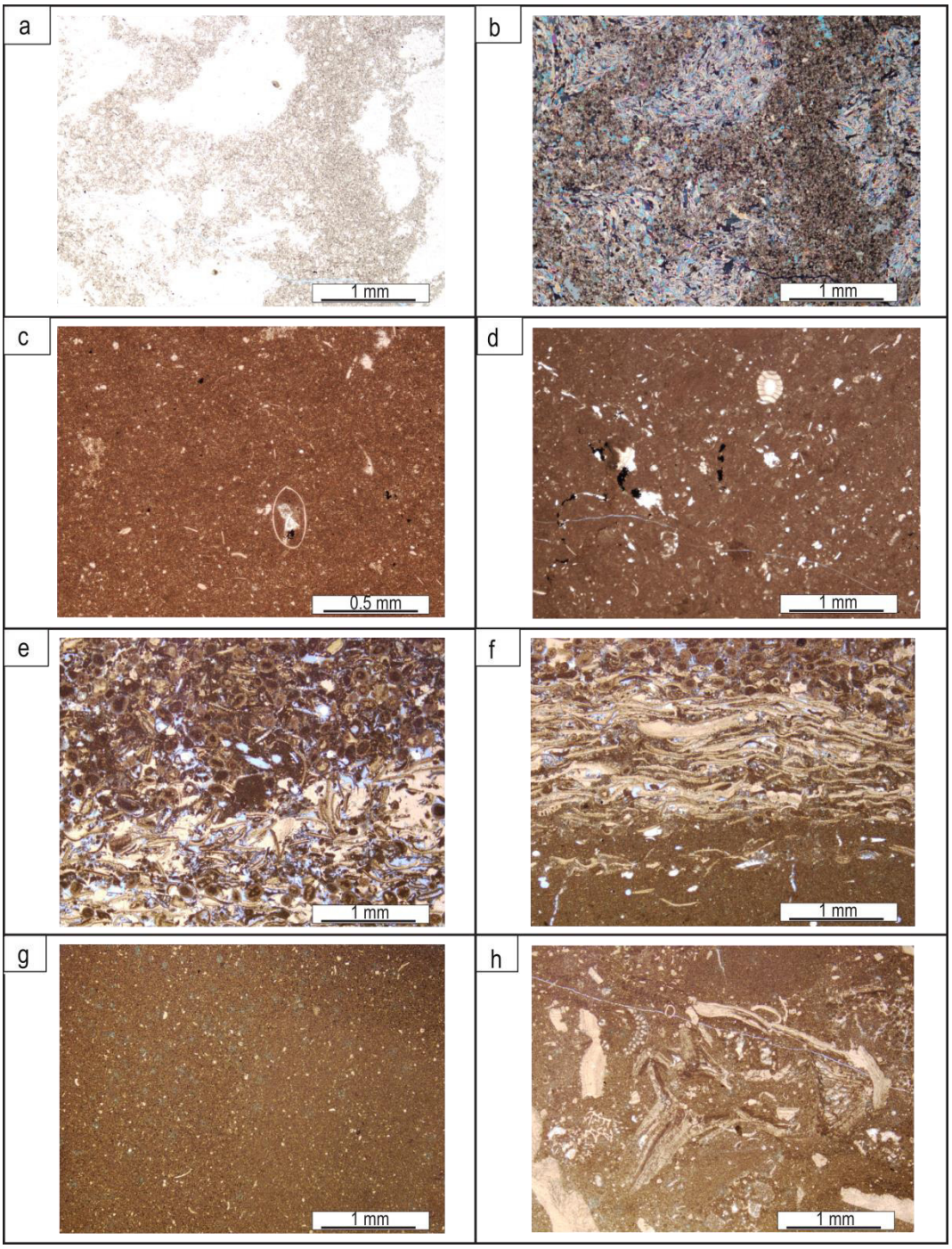


**Figure A21** *Well A1: a) chicken-wire evaporites (CwSulf), surrounded by dolomitized mudstone; b) cross polarized view of the frame a); c) mudstone/wackestone with ostracods (OstWc); d) Oogonium of Characeae in a mudstone/wackestone with ostracods fragments (OstWc); e) Bioclastic packstone/grainstone (BioPelPc-Gr) with abundant bivalves and few ooids (bottom). At the top: oolitic packstone with bivalves fragments, peloids and echinoderms (OoBioGr); f) Transition between a bioclastic wackestone (BioWc-Pc) into a cross laminated bioclastic packstone (BioPelPc-Gr) with increasing abundance of ooids toward the top of the frame; g) massive mudstone (MasMd); h) floatstone with abundant shell fragments of bivalves, Kurnubia spp. and rare Cladocoropsis spp.*

**Table A22** *Range chart of well A2.*

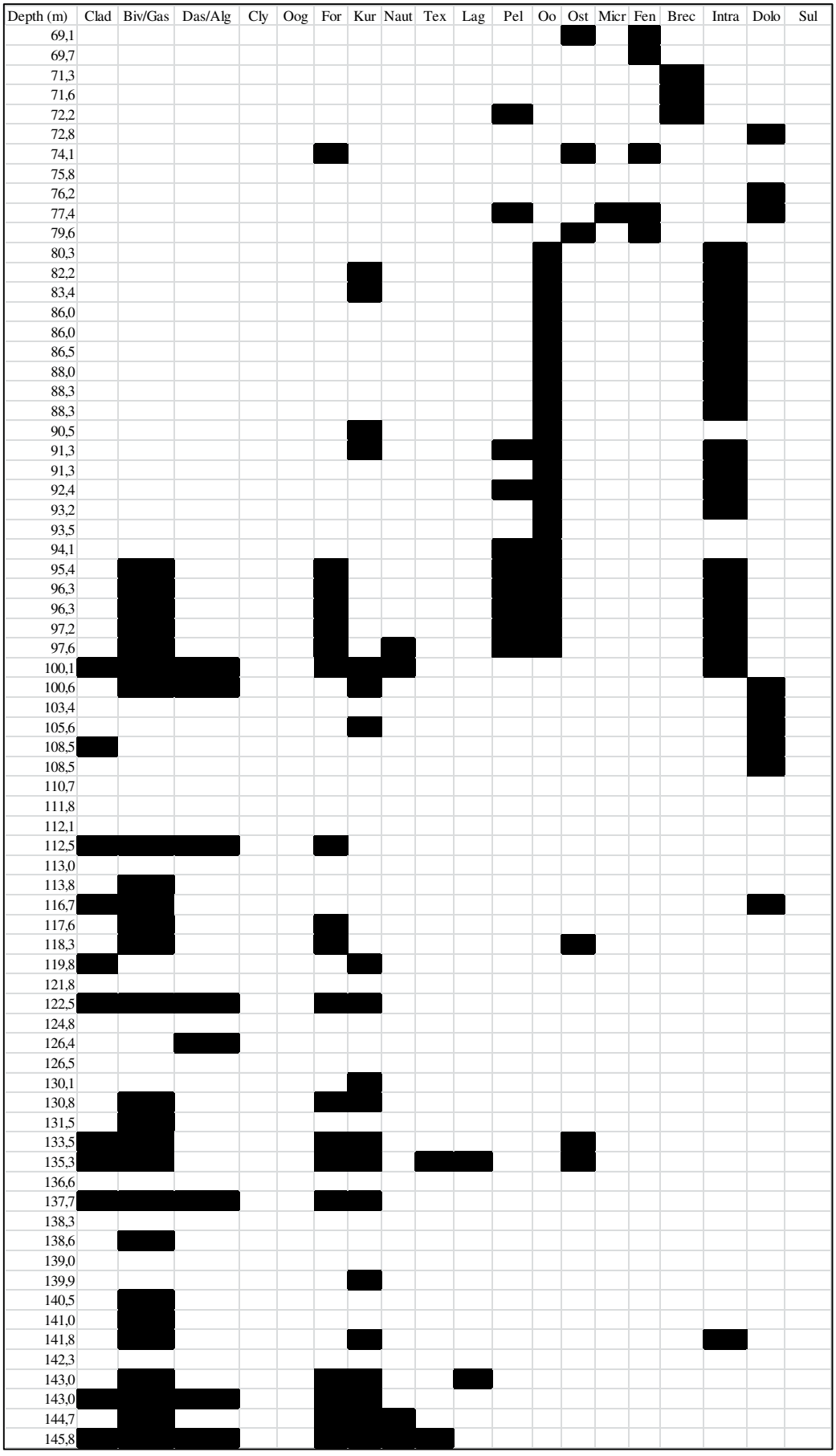

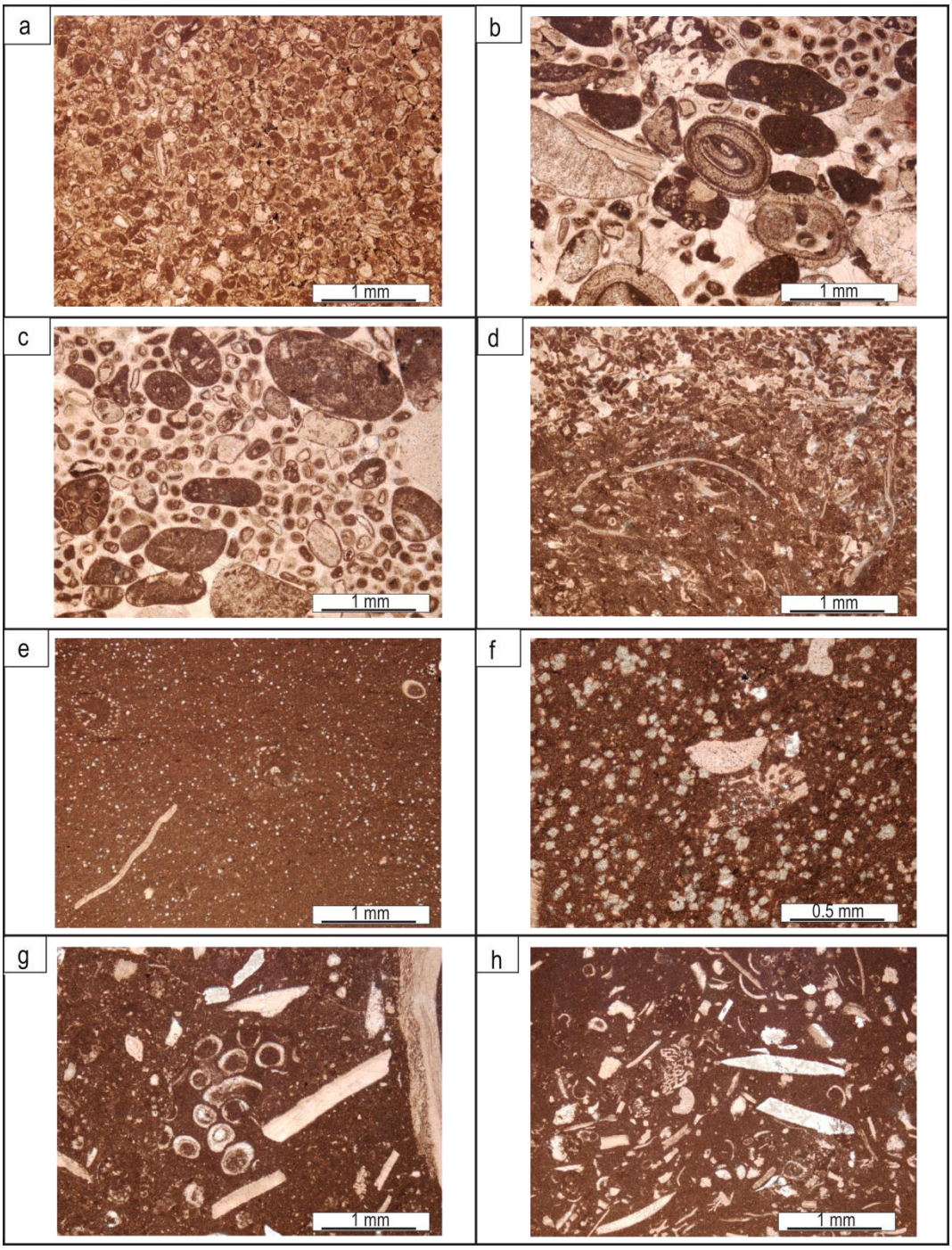


**Figure A22** *Well A2: a) oolitic grainstone (OoGr); b) and c) oolitic grainstone with intraclasts and cortoids (OoGr); d) bioclastic (bivalves) peloidal packstone, with ooids (BioPelPc-Gr); e) massive wackestones, locally dolomitized, with Kurnubia spp. and bivalves (BioMd-Wc); f) dolomitized mudstone (BioMd-Wc) with Cladocoropsis spp.; g) floatstone with bivalves, dasyclad algae and Kurnubia spp.; h) floatstone with bivalves and Cladocoropsis spp. (EroFl).*

**Table A23** *Range chart of well A3 (MD values corrected for core-log shift).*

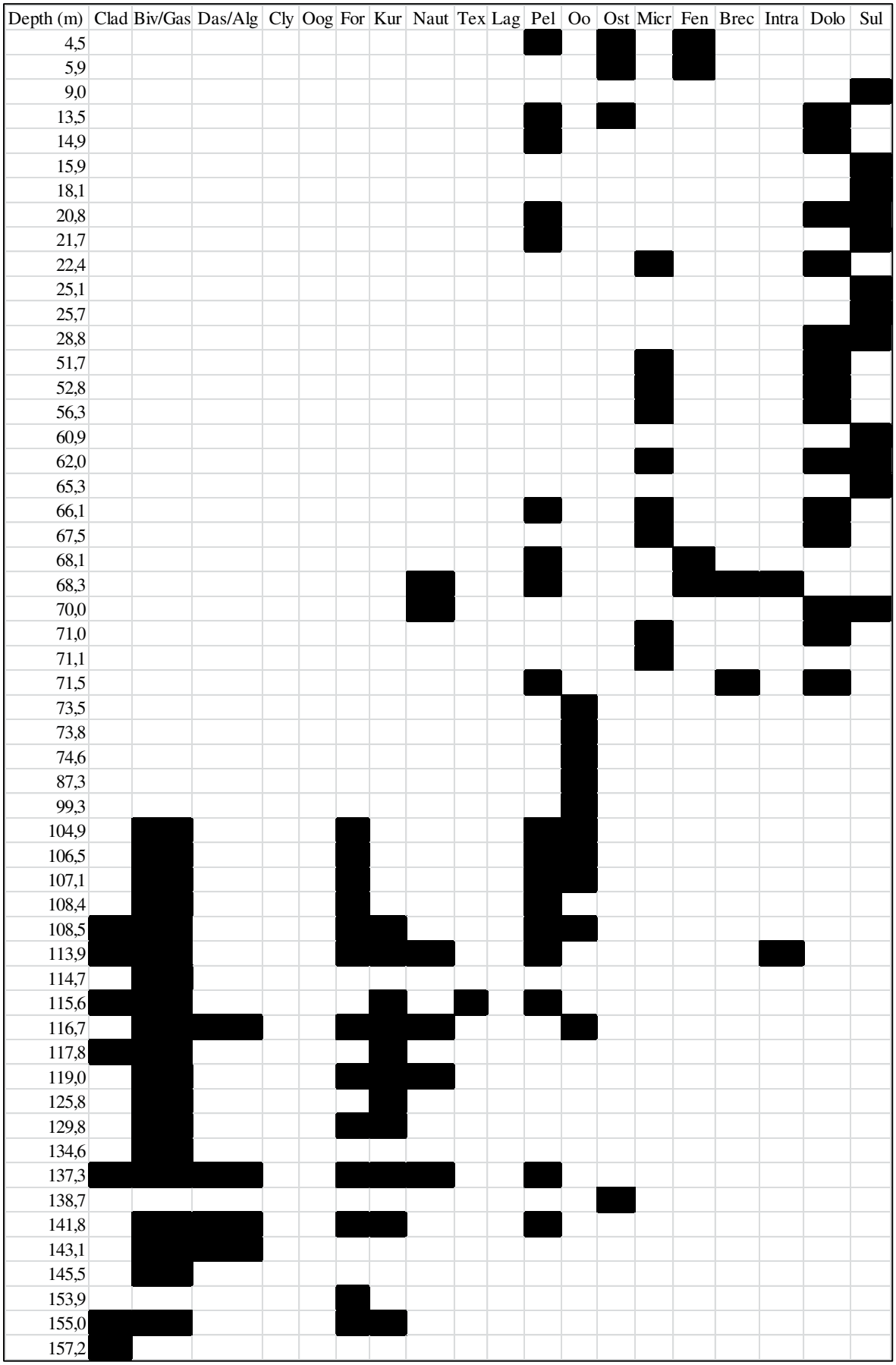

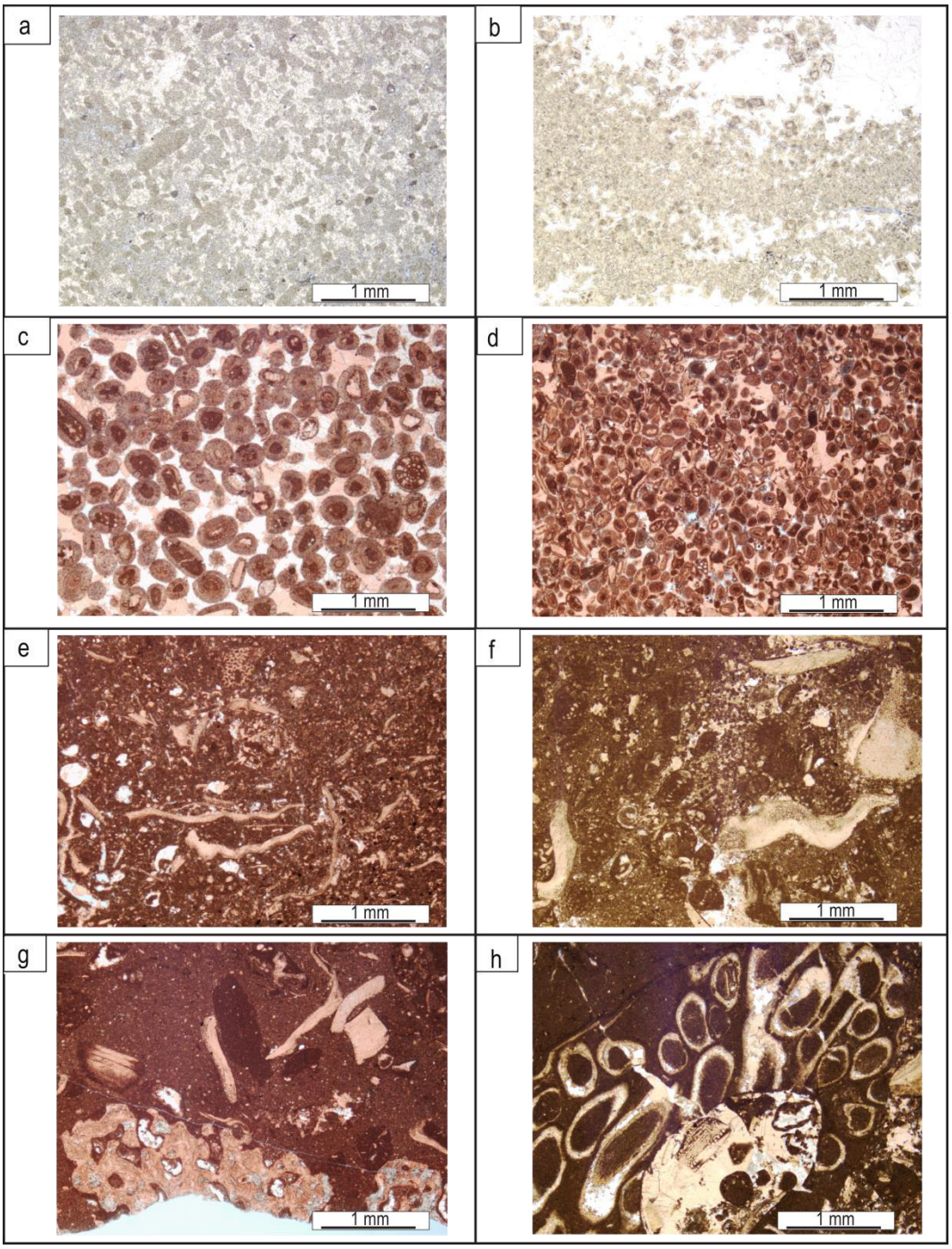


**Figure A23** *Well A3: a) dolomitized peloidal wackestones (PelWc-Pc); b) Dolomitized mudstone with some sulfates in chicken wires structures (CwSulf); c) oolitic grainstone (OoGr); d) oolitic grainstone with bivalves, and foraminifera (OoBioGr); e) floatstone with bivalves and Cladocoropsis spp. (EroFl); f) floatstone with Nautiloculina oolithica, Kurnubia spp., bivalves, gastropods, and echinoderms (EroFl); g) floatstone with Cladocoropsis spp., echinoderms, shell fragments and intraclasts (EroFl); h) detail on a sample of dasyclad algae.*

**Table A24** *Range chart of well A5.*

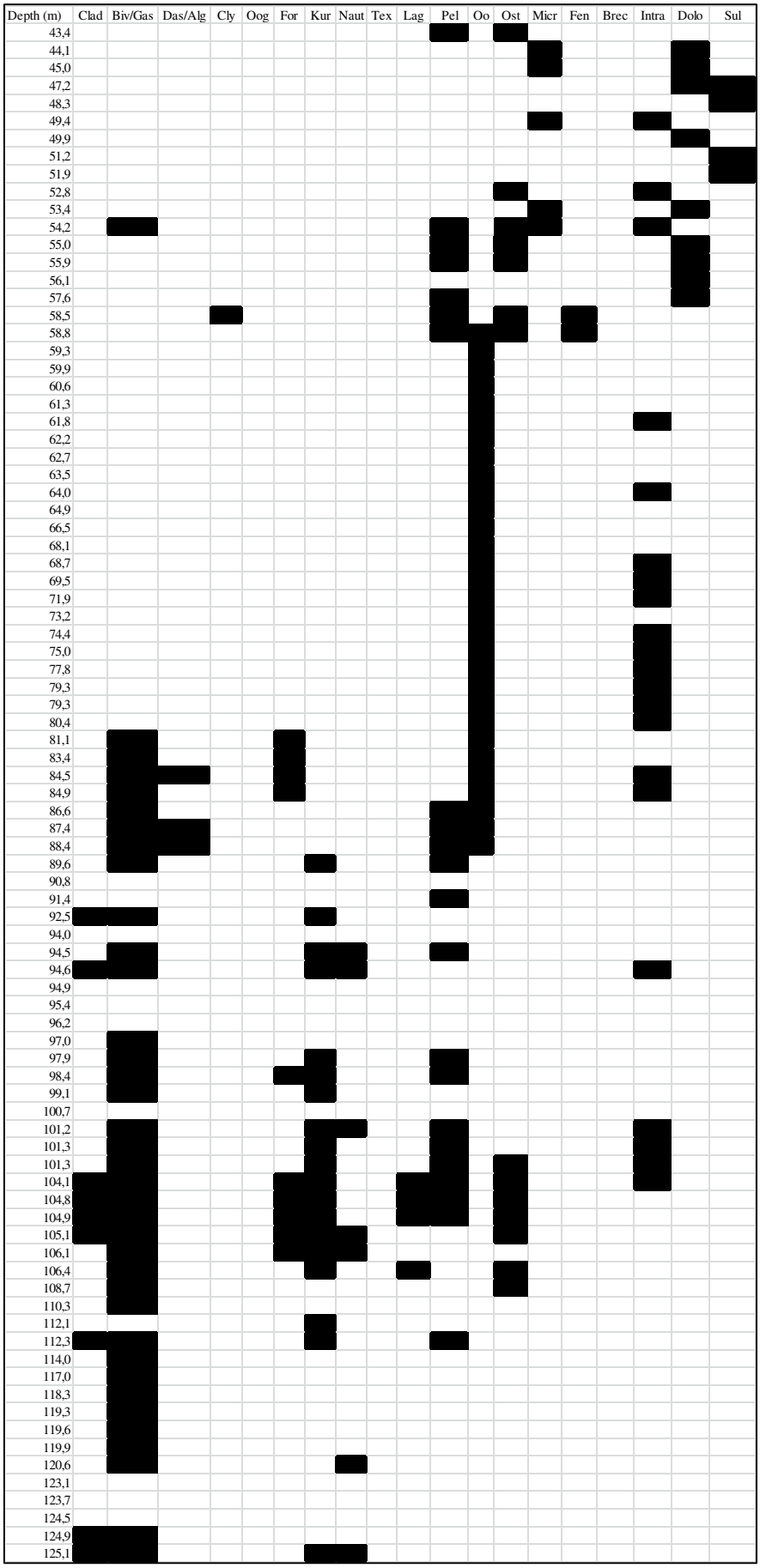

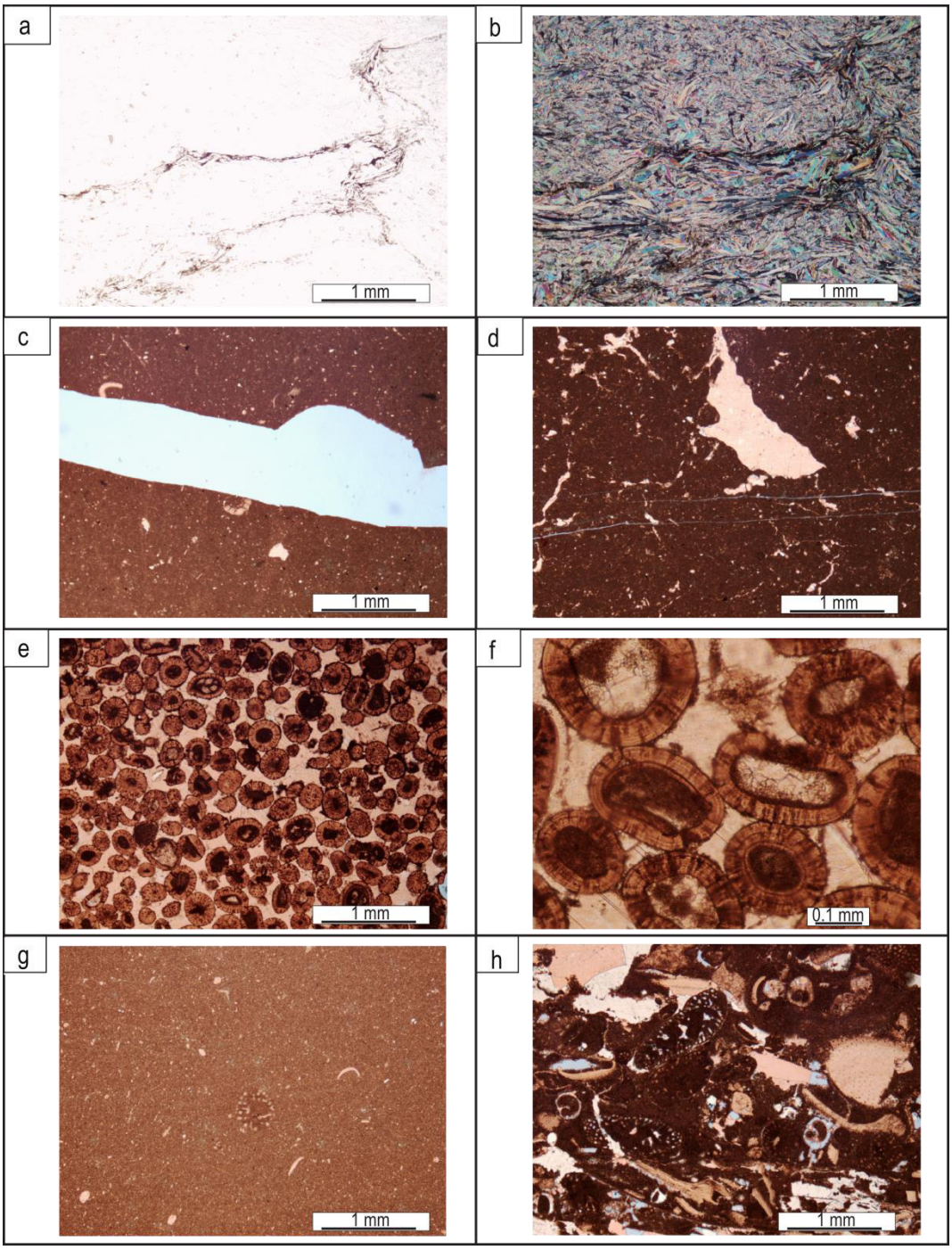


**Figure A24** *Well A5: a) Sulfates separated by thin film of mudstone (CwSulf); b) cross polarized view of the frames a); c) mudstone-wackestone with ostracods and Clypeina jurassica (OstWc); d) mudstone with fenestrae (BirdMd-Wc/OstWc); e) oolitic grainstone (OoGr); f) oolitic grainstone (OoGr); g) mudstone-wackestone with Kurnubia spp. (BioMd-Wc); h) floastone with bivalves, Kurnubia spp., echinoderms, gastropods.*

# APPENDIX 3 - SENSITIVITY ANALYSIS

In this appendix the matches, for each well, of the different macro environments are reported for all the sensitivity analyses done. The code of each model refers to Table 4.3 (Chapter 4; reported here again). For each simulation the different macro environments are listed according to the thicknesses (expressed in meters) detected in the real (R.W.) and simulated wells (S.W.), with the relative matches and their averages (AV.). The TOTAL item represents the total thickness of the real and simulated wells (not computed in the AV. value). Table A36 reports the total thickness of the evaporitic deposits for each well (real and simulated) and the average (AV.) for the different analyses and the matches. In the Table A37 the averages for each macro environment between the five wells (eq.1 Chapter 4) and the TOT value (TOT) are listed. All the matches are reported in fraction of 1.

**Table 4.3** *List of the models presented in the thesis with the values assigned at the main inputs. For the parameters not reported here refer to the ones of the Reference Model (Table 4.1). In all the models the evaporation is set at 1500 mm/yr except for the E500 and E2500 models. Underlined the simulations that provided a better refinement (higher calibration).*

| PARAMETER TESTED | MODEL NAME | MAIN PARAMETERS |
|---|---|---|
| Initial topography | Salt Dome SD | Initial bathymetry: salt dome initial bathymetry<br>Subsidence maps: S152.2b – S148.5b (S0 maps -13m and -13.5m)<br>Maximum production: CG CM CE<br>(m/Ma) 212 44 16<br>Gravity-driven diffusion coefficient CG CM CE<br>$K$ (km$^2$/kyr) Continental: 0.005 0.01 0.0001<br>Marine: 0.005 0.01 0.0001<br>Evaporation: 1500 mm/yr |
| Subsidence | S0 | Initial bathymetry: salt dome initial bathymetry<br>Subsidence maps: S0 maps (computed by the software)<br>Maximum production: CG CM CE<br>(m/Ma) 212 44 16<br>Gravity-driven diffusion coefficient CG CM CE<br>$K$ (km$^2$/kyr) Continental: 0.005 0.01 0.0001<br>Marine: 0.005 0.01 0.0001 |
| Subsidence | S12 | Initial bathymetry: salt dome initial bathymetry; Subsidence maps: S0 maps -12m<br>Maximum production: CG CM CE<br>(m/Ma) 212 44 16<br>Gravity-driven diffusion coefficient CG CM CE<br>$K$ (km$^2$/kyr) Continental: 0.005 0.01 0.0001<br>Marine: 0.005 0.01 0.0001 |
| Subsidence | S14 | Initial bathymetry: salt dome initial bathymetry; Subsidence maps: S0 maps -14m<br>Maximum production: CG CM CE<br>(m/Ma) 212 44 16<br>Gravity-driven diffusion coefficient CG CM CE<br>$K$ (km$^2$/kyr) Continental: 0.005 0.01 0.0001<br>Marine: 0.005 0.01 0.0001 |

**Table 4.3** *continued from the previous page*

| PARAMETER TESTED | MODEL NAME | MAIN PARAMETERS |
|---|---|---|
| Subsidence | S26 | Initial bathymetry: salt dome initial bathymetry; Subsidence maps: S0 maps -26m<br>Maximum production: CG CM CE<br>(m/Ma) 212 44 16<br>Gravity-driven diffusion coefficient CG CM CE<br>*K* ($km^2$/kyr) Continental: 0.005 0.01 0.0001<br>Marine: 0.005 0.01 0.0001 |
| Carbo_Grains production | G106 | Initial bathymetry: salt dome initial bathymetry; Subsidence maps: S0 maps -14m<br>Maximum production: CG CM CE<br>(m/Ma) 106 44 16<br>Gravity-driven diffusion coefficient CG CM CE<br>*K* ($km^2$/kyr) Continental: 0.005 0.01 0.0001<br>Marine: 0.005 0.01 0.0001 |
| Carbo_Grains production | G206 | Initial bathymetry: salt dome initial bathymetry; Subsidence maps: S0 maps -14m<br>Maximum production: CG CM CE<br>(m/Ma) 206 44 16<br>Gravity-driven diffusion coefficient CG CM CE<br>*K* ($km^2$/kyr) Continental: 0.005 0.01 0.0001<br>Marine: 0.005 0.01 0.0001 |
| Carbo_Grains production | G218 | Initial bathymetry: salt dome initial bathymetry; Subsidence maps: S0 maps -14m<br>Maximum production: CG CM CE<br>(m/Ma) 218 44 16<br>Gravity-driven diffusion coefficient CG CM CE<br>*K* ($km^2$/kyr) Continental: 0.005 0.01 0.0001<br>Marine: 0.005 0.01 0.0001 |
| Carbo_Grains production | G318 | Initial bathymetry: salt dome initial bathymetry; Subsidence maps: S0 maps -14m<br>Maximum production: CG CM CE<br>(m/Ma) 318 44 16<br>Gravity-driven diffusion coefficient CG CM CE<br>*K* ($km^2$/kyr) Continental: 0.005 0.01 0.0001<br>Marine: 0.005 0.01 0.0001 |
| Carbo_Mud production | M22 | Initial bathymetry: salt dome initial bathymetry; Subsidence maps: S0 maps -14m<br>Maximum production: CG CM CE<br>(m/Ma) 218 22 16<br>Gravity-driven diffusion coefficient CG CM CE<br>*K* ($km^2$/kyr) Continental: 0.005 0.01 0.0001<br>Marine: 0.005 0.01 0.0001 |
| Carbo_Mud production | M42 | Initial bathymetry: salt dome initial bathymetry; Subsidence maps: S0 maps -14m<br>Maximum production: CG CM CE<br>(m/Ma) 218 42 16<br>Gravity-driven diffusion coefficient CG CM CE<br>*K* ($km^2$/kyr) Continental: 0.005 0.01 0.0001<br>Marine: 0.005 0.01 0.0001 |
| Carbo_Mud production | M46 | Initial bathymetry: salt dome initial bathymetry; Subsidence maps: S0 maps -14m<br>Maximum production: CG CM CE<br>(m/Ma) 218 46 16<br>Gravity-driven diffusion coefficient CG CM CE<br>*K* ($km^2$/kyr) Continental: 0.005 0.01 0.0001<br>Marine: 0.005 0.01 0.0001 |
| Carbo_Mud production | M66 | Initial bathymetry: salt dome initial bathymetry; Subsidence maps: S0 maps -14m<br>Maximum production: CG CM CE<br>(m/Ma) 218 66 16<br>Gravity-driven diffusion coefficient CG CM CE<br>*K* ($km^2$/kyr) Continental: 0.005 0.01 0.0001<br>Marine: 0.005 0.01 0.0001 |
| Carbo_Evapo production | CE8 | Initial bathymetry: salt dome initial bathymetry; Subsidence maps: S0 maps -14m<br>Maximum production: CG CM CE<br>(m/Ma) 218 44 8<br>Gravity-driven diffusion coefficient CG CM CE<br>*K* ($km^2$/kyr) Continental: 0.005 0.01 0.0001<br>Marine: 0.005 0.01 0.0001 |

**Table 4.3** *continued from the previous page*

| PARAMETER TESTED | MODEL NAME | MAIN PARAMETERS |
|---|---|---|
| Carbo_Evapo production | CE24 | Initial bathymetry: salt dome initial bathymetry; Subsidence maps: S0 maps -14m<br>Maximum production: CG CM CE<br>(m/Ma) 218 44 24<br>Gravity-driven diffusion coefficient CG CM CE<br>*K* ($km^2$/kyr) Continental: 0.005 0.01 0.0001<br>Marine: 0.005 0.01 0.0001 |
| Transport parameters | T0.01-0.05 | Initial bathymetry: salt dome initial bathymetry; Subsidence maps: S0 maps -14m<br>Maximum production: CG CM CE<br>(m/Ma) 218 44 16<br>Gravity-driven diffusion coefficient CG CM CE<br>*K* ($km^2$/kyr) Continental: 0.01 0.05 0.0001<br>Marine: 0.01 0.05 0.0001 |
| Transport parameters | T0.002-0.01 | Initial bathymetry: salt dome initial bathymetry; Subsidence maps: S0 maps -14m<br>Maximum production: CG CM CE<br>(m/Ma) 218 44 16<br>Gravity-driven diffusion coefficient CG CM CE<br>*K* ($km^2$/kyr) Continental: 0.002 0.01 0.0001<br>Marine: 0.002 0.01 0.0001 |
| Transport parameters | T0.005-0.025 | Initial bathymetry: salt dome initial bathymetry; Subsidence maps: S0 maps -14m<br>Maximum production: CG CM CE<br>(m/Ma) 218 44 16<br>Gravity-driven diffusion coefficient CG CM CE<br>*K* ($km^2$/kyr) Continental: 0.005 0.025 0.0001<br>Marine: 0.005 0.025 0.0001 |
| Evaporation | E500 | Initial bathymetry: salt dome initial bathymetry; Subsidence maps: S0 maps -14m<br>Maximum production: CG CM CE<br>(m/Ma) 218 44 16<br>Gravity-driven diffusion coefficient CG CM CE<br>*K* ($km^2$/kyr) Continental: 0.005 0.01 0.0001<br>Marine: 0.005 0.01 0.0001<br>Evaporation: 500 mm/yr |
| Evaporation | E2500 | Initial bathymetry: salt dome initial bathymetry; Subsidence maps: S0 maps -14m<br>Maximum production: CG CM CE<br>(m/Ma) 218 44 16<br>Gravity-driven diffusion coefficient CG CM CE<br>*K* ($km^2$/kyr) Continental: 0.005 0.01 0.0001<br>Marine: 0.005 0.01 0.0001<br>Evaporation: 2500 mm/yr |

**Table A31** *Punctual matches for the simulations computed for well A1.*

| | (m) | (m) | | | (m) | (m) | | | | | | | | | |
|---|---|---|---|---|---|---|---|---|---|---|---|---|---|---|---|
| **REF** | **R.W.** | **S.W.** | **Match** | **SD** | **R.W.** | **S.W.** | **Match** | | | | | | | | |
| TOTAL | 179.9 | 180.0 | 0.999 | TOTAL | 179.9 | 180.3 | 0.998 | | | | | | | | |
| OMR | 87.2 | 93.2 | 0.930 | OMR | 87.2 | 95.7 | 0.902 | | | | | | | | |
| SHC | 26.0 | 26.8 | 0.967 | SHC | 26.0 | 27.3 | 0.948 | | | | | | | | |
| LIST | 66.8 | 60.0 | 0.898 | LIST | 66.8 | 57.3 | 0.858 | | | | | | | | |
| AV. | | | 0.932 | AV. | | | 0.903 | | | | | | | | |
| | | | | | | | | | (m) | (m) | | | | (m) | (m) | |
| **S0** | **R.W.** | **S.W.** | **Match** | **S12** | **R.W.** | **S.W.** | **Match** | **S14** | **R.W.** | **S.W.** | **Match** | **S26** | **R.W.** | **S.W.** | **Match** |
| TOTAL | 179.9 | 193.7 | 0.923 | TOTAL | 179.9 | 181.8 | 0.989 | TOTAL | 179.9 | 179.7 | 0.999 | TOTAL | 179.9 | 167.9 | 0.933 |
| OMR | 87.2 | 129.8 | 0.511 | OMR | 87.2 | 101.5 | 0.836 | OMR | 87.2 | 99.2 | 0.862 | OMR | 87.2 | 60.3 | 0.692 |
| SHC | 26.0 | 20.9 | 0.804 | SHC | 26.0 | 23.4 | 0.903 | SHC | 26.0 | 21.3 | 0.821 | SHC | 26.0 | 25.1 | 0.966 |
| LIST | 66.8 | 43.0 | 0.644 | LIST | 66.8 | 56.9 | 0.852 | LIST | 66.8 | 59.1 | 0.886 | LIST | 66.8 | 82.5 | 0.764 |
| AV. | | | 0.653 | AV. | | | 0.864 | AV. | | | 0.856 | AV. | | | 0.807 |
| | | | | | | | | | | | | | | | |
| **G106** | **R.W.** | **S.W.** | **Match** | **G206** | **R.W.** | **S.W.** | **Match** | **G218** | **R.W.** | **S.W.** | **Match** | **G318** | **R.W.** | **S.W.** | **Match** |
| TOTAL | 179.9 | 179.7 | 0.999 | TOTAL | 179.9 | 179.7 | 0.999 | TOTAL | 179.9 | 179.7 | 0.999 | TOTAL | 179.9 | 179.7 | 0.999 |
| OMR | 87.2 | 112.9 | 0.704 | OMR | 87.2 | 98.6 | 0.869 | OMR | 87.2 | 99.9 | 0.854 | OMR | 87.2 | 88.0 | 0.991 |
| SHC | 26.0 | 11.3 | 0.433 | SHC | 26.0 | 21.9 | 0.844 | SHC | 26.0 | 20.4 | 0.786 | SHC | 26.0 | 31.1 | 0.803 |
| LIST | 66.8 | 55.5 | 0.831 | LIST | 66.8 | 59.1 | 0.886 | LIST | 66.8 | 59.3 | 0.889 | LIST | 66.8 | 60.6 | 0.908 |
| AV. | | | 0.656 | AV. | | | 0.866 | AV. | | | 0.843 | AV. | | | 0.900 |
| | | | | | | | | | | | | | | | |
| **M22** | **R.W.** | **S.W.** | **Match** | **M42** | **R.W.** | **S.W.** | **Match** | **M46** | **R.W.** | **S.W.** | **Match** | **M66** | **R.W.** | **S.W.** | **Match** |
| TOTAL | 179.9 | 125.3 | 0.697 | TOTAL | 179.9 | 179.7 | 0.999 | TOTAL | 179.9 | 179.7 | 0.999 | TOTAL | 179.9 | 179.7 | 0.999 |
| OMR | 87.2 | 125.3 | 0.562 | OMR | 87.2 | 103.9 | 0.808 | OMR | 87.2 | 81.3 | 0.933 | OMR | 87.2 | 31.1 | 0.356 |
| SHC | 26.0 | 0.0 | 0.000 | SHC | 26.0 | 23.7 | 0.913 | SHC | 26.0 | 26.0 | 0.998 | SHC | 26.0 | 26.4 | 0.983 |
| LIST | 66.8 | 0.0 | 0.000 | LIST | 66.8 | 52.0 | 0.780 | LIST | 66.8 | 72.3 | 0.916 | LIST | 66.8 | 122.2 | 0.169 |
| AV. | | | 0.187 | AV. | | | 0.834 | AV. | | | 0.949 | AV. | | | 0.503 |
| | | | | | | | | | | | | | | | |
| **CE8** | **R.W.** | **S.W.** | **Match** | **CE24** | **R.W.** | **S.W.** | **Match** | | | | | | | | |
| TOTAL | 179.9 | 177.9 | 0.989 | TOTAL | 179.9 | 181.7 | 0.990 | | | | | | | | |
| OMR | 87.2 | 99.9 | 0.854 | OMR | 87.2 | 99.9 | 0.854 | | | | | | | | |
| SHC | 26.0 | 20.2 | 0.777 | SHC | 26.0 | 20.7 | 0.796 | | | | | | | | |
| LIST | 66.8 | 57.8 | 0.866 | LIST | 66.8 | 61.1 | 0.915 | | | | | | | | |
| AV. | | | 0.832 | AV. | | | 0.855 | | | | | | | | |
| | | | | | | | | | | | | | | | |
| **T0,01-0,05** | **R.W.** | **S.W.** | **Match** | **T0,002-0,01** | **R.W.** | **S.W.** | **Match** | **T0,005-0,025** | **R.W.** | **S.W.** | **Match** | | | | |
| TOTAL | 179.9 | 180.2 | 0.998 | TOTAL | 179.9 | 179.7 | 0.999 | TOTAL | 179.9 | 179.8 | 1.000 | | | | |
| OMR | 87.2 | 100.1 | 0.852 | OMR | 87.2 | 97.1 | 0.887 | OMR | 87.2 | 98.2 | 0.873 | | | | |
| SHC | 26.0 | 28.1 | 0.916 | SHC | 26.0 | 25.4 | 0.978 | SHC | 26.0 | 25.9 | 0.998 | | | | |
| LIST | 66.8 | 52.0 | 0.779 | LIST | 66.8 | 57.2 | 0.858 | LIST | 66.8 | 55.7 | 0.834 | | | | |
| AV. | | | 0.849 | AV. | | | 0.907 | AV. | | | 0.902 | | | | |

**Table A32** *Punctual matches for the simulations computed for well A2.*

| | (m) | (m) | | | (m) | (m) | | | | | | | | | | |
|---|---|---|---|---|---|---|---|---|---|---|---|---|---|---|---|---|
| **REF** | **R.W.** | **S.W.** | **Match** | **SD** | **R.W.** | **S.W.** | **Match** | | | | | | | | | |
| TOTAL | 192.5 | 188.4 | 0.979 | TOTAL | 192.5 | 188.7 | 0.980 | | | | | | | | | |
| OMR | 93.4 | 85.3 | 0.913 | OMR | 93.4 | 82.2 | 0.880 | | | | | | | | | |
| SHC | 19.0 | 27.3 | 0.561 | SHC | 19.0 | 38.2 | -0.012 | | | | | | | | | |
| LIST | 80.1 | 75.9 | 0.947 | LIST | 80.1 | 68.3 | 0.853 | | | | | | | | | |
| AV. | | | 0.807 | AV. | | | 0.574 | | | | | | | | | |
| | | | | | | | | | | (m) | (m) | | | | (m) | (m) | |
| **S0** | **R.W.** | **S.W.** | **Match** | **S12** | **R.W.** | **S.W.** | **Match** | **S14** | **R.W.** | **S.W.** | **Match** | **S26** | **R.W.** | **S.W.** | **Match** | |
| TOTAL | 192.5 | 201.8 | 0.951 | TOTAL | 192.5 | 189.9 | 0.987 | TOTAL | 192.5 | 187.9 | 0.977 | TOTAL | 192.5 | 175.8 | 0.914 | |
| OMR | 93.4 | 125.5 | 0.656 | OMR | 93.4 | 92.4 | 0.989 | OMR | 93.4 | 83.1 | 0.890 | OMR | 93.4 | 49.3 | 0.528 | |
| SHC | 19.0 | 27.5 | 0.552 | SHC | 19.0 | 29.3 | 0.455 | SHC | 19.0 | 30.9 | 0.369 | SHC | 19.0 | 27.4 | 0.555 | |
| LIST | 80.1 | 48.9 | 0.610 | LIST | 80.1 | 68.2 | 0.851 | LIST | 80.1 | 73.9 | 0.923 | LIST | 80.1 | 99.2 | 0.762 | |
| AV. | | | 0.606 | AV. | | | 0.765 | AV. | | | 0.727 | AV. | | | 0.615 | |
| | | | | | | | | | | | | | | | | |
| **G106** | **R.W.** | **S.W.** | **Match** | **G206** | **R.W.** | **S.W.** | **Match** | **G218** | **R.W.** | **S.W.** | **Match** | **G318** | **R.W.** | **S.W.** | **Match** | |
| TOTAL | 192.5 | 187.9 | 0.976 | TOTAL | 192.5 | 187.8 | 0.976 | TOTAL | 192.5 | 187.8 | 0.976 | TOTAL | 192.5 | 187.9 | 0.976 | |
| OMR | 93.4 | 96.8 | 0.963 | OMR | 93.4 | 83.0 | 0.889 | OMR | 93.4 | 83.2 | 0.891 | OMR | 93.4 | 77.7 | 0.832 | |
| SHC | 19.0 | 22.4 | 0.819 | SHC | 19.0 | 31.7 | 0.328 | SHC | 19.0 | 27.6 | 0.543 | SHC | 19.0 | 29.6 | 0.441 | |
| LIST | 80.1 | 68.6 | 0.857 | LIST | 80.1 | 73.1 | 0.913 | LIST | 80.1 | 77.0 | 0.961 | LIST | 80.1 | 80.6 | 0.994 | |
| AV. | | | 0.880 | AV. | | | 0.710 | AV. | | | 0.798 | AV. | | | 0.755 | |
| | | | | | | | | | | | | | | | | |
| **M22** | **R.W.** | **S.W.** | **Match** | **M42** | **R.W.** | **S.W.** | **Match** | **M46** | **R.W.** | **S.W.** | **Match** | **M66** | **R.W.** | **S.W.** | **Match** | |
| TOTAL | 192.5 | 130.3 | 0.677 | TOTAL | 192.5 | 187.8 | 0.976 | TOTAL | 192.5 | 187.8 | 0.976 | TOTAL | 192.5 | 187.9 | 0.976 | |
| OMR | 93.4 | 130.3 | 0.605 | OMR | 93.4 | 95.7 | 0.975 | OMR | 93.4 | 75.2 | 0.805 | OMR | 93.4 | 36.6 | 0.392 | |
| SHC | 19.0 | 0.0 | 0.000 | SHC | 19.0 | 24.4 | 0.711 | SHC | 19.0 | 22.2 | 0.828 | SHC | 19.0 | 12.2 | 0.645 | |
| LIST | 80.1 | 0.0 | 0.000 | LIST | 80.1 | 67.7 | 0.845 | LIST | 80.1 | 90.4 | 0.871 | LIST | 80.1 | 139.1 | 0.263 | |
| AV. | | | 0.202 | AV. | | | 0.844 | AV. | | | 0.835 | AV. | | | 0.433 | |
| | | | | | | | | | | | | | | | | |
| **CE8** | **R.W.** | **S.W.** | **Match** | **CE24** | **R.W.** | **S.W.** | **Match** | | | | | | | | | |
| TOTAL | 192.5 | 185.9 | 0.966 | TOTAL | 192.5 | 189.4 | 0.984 | | | | | | | | | |
| OMR | 93.4 | 83.2 | 0.891 | OMR | 93.4 | 83.2 | 0.891 | | | | | | | | | |
| SHC | 19.0 | 27.6 | 0.547 | SHC | 19.0 | 27.8 | 0.537 | | | | | | | | | |
| LIST | 80.1 | 75.2 | 0.938 | LIST | 80.1 | 78.5 | 0.980 | | | | | | | | | |
| AV. | | | 0.792 | AV. | | | 0.803 | | | | | | | | | |
| | | | | | | | | | | | | | | | | |
| **T0,01-0,05** | **R.W.** | **S.W.** | **Match** | **T0,002-0,01** | **R.W.** | **S.W.** | **Match** | **T0,005-0,025** | **R.W.** | **S.W.** | **Match** | | | | | |
| TOTAL | 192.5 | 187.9 | 0.976 | TOTAL | 192.5 | 187.9 | 0.976 | TOTAL | 192.5 | 187.8 | 0.976 | | | | | |
| OMR | 93.4 | 93.3 | 0.999 | OMR | 93.4 | 83.0 | 0.889 | OMR | 93.4 | 88.1 | 0.944 | | | | | |
| SHC | 19.0 | 35.8 | 0.110 | SHC | 19.0 | 32.6 | 0.281 | SHC | 19.0 | 31.2 | 0.355 | | | | | |
| LIST | 80.1 | 58.7 | 0.733 | LIST | 80.1 | 72.3 | 0.902 | LIST | 80.1 | 68.5 | 0.855 | | | | | |
| AV. | | | 0.614 | AV. | | | 0.691 | AV. | | | 0.718 | | | | | |

**Table A33** *Punctual matches for the simulations computed for well A3.*

| | (m) | (m) | | | (m) | (m) | | | | | | | | | |
|---|---|---|---|---|---|---|---|---|---|---|---|---|---|---|---|
| **REF** | **R.W.** | **S.W.** | **Match** | **SD** | **R.W.** | **S.W.** | **Match** | | | | | | | | |
| TOTAL | 161.7 | 163.9 | 0.987 | TOTAL | 161.7 | 163.7 | 0.988 | | | | | | | | |
| OMR | 84.0 | 76.7 | 0.914 | OMR | 84.0 | 85.0 | 0.988 | | | | | | | | |
| SHC | 25.8 | 26.3 | 0.979 | SHC | 25.8 | 22.1 | 0.855 | | | | | | | | |
| LIST | 52.0 | 60.8 | 0.830 | LIST | 52.0 | 56.7 | 0.909 | | | | | | | | |
| AV. | | | 0.908 | AV. | | | 0.917 | | | | | | | | |
| | | | | | | | | | (m) | (m) | | | (m) | (m) | |
| **S0** | **R.W.** | **S.W.** | **Match** | **S12** | **R.W.** | **S.W.** | **Match** | **S14** | **R.W.** | **S.W.** | **Match** | **S26** | **R.W.** | **S.W.** | **Match** |
| TOTAL | 161.7 | 177.2 | 0.904 | TOTAL | 161.7 | 165.2 | 0.978 | TOTAL | 161.7 | 163.3 | 0.990 | TOTAL | 161.7 | 151.4 | 0.936 |
| OMR | 84.0 | 117.0 | 0.606 | OMR | 84.0 | 84.0 | 1.000 | OMR | 84.0 | 79.0 | 0.942 | OMR | 84.0 | 65.3 | 0.778 |
| SHC | 25.8 | 19.0 | 0.735 | SHC | 25.8 | 23.8 | 0.922 | SHC | 25.8 | 26.0 | 0.994 | SHC | 25.8 | 15.9 | 0.617 |
| LIST | 52.0 | 41.3 | 0.794 | LIST | 52.0 | 57.4 | 0.895 | LIST | 52.0 | 58.3 | 0.878 | LIST | 52.0 | 70.2 | 0.649 |
| AV. | | | 0.711 | AV. | | | 0.939 | AV. | | | 0.938 | AV. | | | 0.681 |
| | | | | | | | | | | | | | | | |
| **G106** | **R.W.** | **S.W.** | **Match** | **G206** | **R.W.** | **S.W.** | **Match** | **G218** | **R.W.** | **S.W.** | **Match** | **G318** | **R.W.** | **S.W.** | **Match** |
| TOTAL | 161.7 | 163.3 | 0.990 | TOTAL | 161.7 | 161.9 | 0.999 | TOTAL | 161.7 | 163.3 | 0.990 | TOTAL | 161.7 | 163.4 | 0.990 |
| OMR | 84.0 | 88.9 | 0.941 | OMR | 84.0 | 79.0 | 0.942 | OMR | 84.0 | 79.1 | 0.942 | OMR | 84.0 | 80.5 | 0.958 |
| SHC | 25.8 | 24.4 | 0.945 | SHC | 25.8 | 26.1 | 0.990 | SHC | 25.8 | 25.8 | 0.998 | SHC | 25.8 | 24.4 | 0.947 |
| LIST | 52.0 | 50.0 | 0.962 | LIST | 52.0 | 56.8 | 0.907 | LIST | 52.0 | 58.4 | 0.876 | LIST | 52.0 | 58.5 | 0.875 |
| AV. | | | 0.949 | AV. | | | 0.946 | AV. | | | 0.939 | AV. | | | 0.927 |
| | | | | | | | | | | | | | | | |
| **M22** | **R.W.** | **S.W.** | **Match** | **M42** | **R.W.** | **S.W.** | **Match** | **M46** | **R.W.** | **S.W.** | **Match** | **M66** | **R.W.** | **S.W.** | **Match** |
| TOTAL | 161.7 | 124.9 | 0.772 | TOTAL | 161.7 | 163.3 | 0.990 | TOTAL | 161.7 | 163.3 | 0.990 | TOTAL | 161.7 | 163.3 | 0.990 |
| OMR | 84.0 | 124.9 | 0.512 | OMR | 84.0 | 88.9 | 0.942 | OMR | 84.0 | 70.2 | 0.836 | OMR | 84.0 | 42.8 | 0.509 |
| SHC | 25.8 | 0.0 | 0.000 | SHC | 25.8 | 25.2 | 0.978 | SHC | 25.8 | 26.2 | 0.984 | SHC | 25.8 | 24.1 | 0.933 |
| LIST | 52.0 | 0.0 | 0.000 | LIST | 52.0 | 49.2 | 0.946 | LIST | 52.0 | 66.9 | 0.713 | LIST | 52.0 | 96.4 | 0.144 |
| AV. | | | 0.171 | AV. | | | 0.955 | AV. | | | 0.844 | AV. | | | 0.529 |
| | | | | | | | | | | | | | | | |
| **CE8** | **R.W.** | **S.W.** | **Match** | **CE24** | **R.W.** | **S.W.** | **Match** | | | | | | | | |
| TOTAL | 161.7 | 161.1 | 0.996 | TOTAL | 161.7 | 164.5 | 0.983 | | | | | | | | |
| OMR | 84.0 | 79.1 | 0.942 | OMR | 84.0 | 79.1 | 0.942 | | | | | | | | |
| SHC | 25.8 | 25.7 | 0.996 | SHC | 25.8 | 25.8 | 1.000 | | | | | | | | |
| LIST | 52.0 | 56.3 | 0.917 | LIST | 52.0 | 59.6 | 0.853 | | | | | | | | |
| AV. | | | 0.952 | AV. | | | 0.932 | | | | | | | | |
| | | | | | | | | | | | | | | | |
| **T0,01-0,05** | **R.W.** | **S.W.** | **Match** | **T0,002-0,01** | **R.W.** | **S.W.** | **Match** | **T0,005-0,025** | **R.W.** | **S.W.** | **Match** | | | | |
| TOTAL | 161.7 | 163.3 | 0.990 | TOTAL | 161.7 | 163.3 | 0.990 | TOTAL | 161.7 | 163.3 | 0.990 | | | | |
| OMR | 84.0 | 79.3 | 0.945 | OMR | 84.0 | 79.0 | 0.941 | OMR | 84.0 | 78.5 | 0.936 | | | | |
| SHC | 25.8 | 24.7 | 0.958 | SHC | 25.8 | 26.1 | 0.990 | SHC | 25.8 | 26.6 | 0.969 | | | | |
| LIST | 52.0 | 59.2 | 0.860 | LIST | 52.0 | 58.2 | 0.880 | LIST | 52.0 | 58.1 | 0.882 | | | | |
| AV. | | | 0.921 | AV. | | | 0.937 | AV. | | | 0.929 | | | | |

**Table A34** *Punctual matches for the simulations computed for well A4.*

| | (m) | (m) | | | | (m) | (m) | | | | | | | | | | |
|---|---|---|---|---|---|---|---|---|---|---|---|---|---|---|---|---|---|
| **REF** | **R.W.** | **S.W.** | **Match** | | **SD** | **R.W.** | **S.W.** | **Match** | | | | | | | | | |
| TOTAL | 170.2 | 171.4 | 0.993 | | TOTAL | 170.2 | 171.7 | 0.991 | | | | | | | | | |
| OMR | 93.8 | 56.8 | 0.606 | | OMR | 93.8 | 90.5 | 0.965 | | | | | | | | | |
| SHC | 26.7 | 38.9 | 0.543 | | SHC | 26.7 | 31.5 | 0.822 | | | | | | | | | |
| LIST | 49.7 | 75.6 | 0.477 | | LIST | 49.7 | 49.7 | 0.999 | | | | | | | | | |
| AV. | | | 0.542 | | AV. | | | 0.929 | | | | | | | | | |
| | | | | | | | | | | (m) | (m) | | | | (m) | (m) | |
| **S0** | **R.W.** | **S.W.** | **Match** | | **S12** | **R.W.** | **S.W.** | **Match** | **S14** | **R.W.** | **S.W.** | **Match** | **S26** | **R.W.** | **S.W.** | **Match** | |
| TOTAL | 170.2 | 185.1 | 0.912 | | TOTAL | 170.2 | 173.0 | 0.983 | TOTAL | 170.2 | 171.1 | 0.995 | TOTAL | 170.2 | 159.1 | 0.935 | |
| OMR | 93.8 | 128.2 | 0.633 | | OMR | 93.8 | 97.2 | 0.963 | OMR | 93.8 | 91.5 | 0.976 | OMR | 93.8 | 75.9 | 0.809 | |
| SHC | 26.7 | 21.1 | 0.789 | | SHC | 26.7 | 25.6 | 0.959 | SHC | 26.7 | 27.8 | 0.960 | SHC | 26.7 | 18.3 | 0.684 | |
| LIST | 49.7 | 35.8 | 0.721 | | LIST | 49.7 | 50.2 | 0.990 | LIST | 49.7 | 51.7 | 0.958 | LIST | 49.7 | 64.9 | 0.692 | |
| AV. | | | 0.714 | | AV. | | | 0.971 | AV. | | | 0.965 | AV. | | | 0.728 | |
| | | | | | | | | | | | | | | | | | |
| **G106** | **R.W.** | **S.W.** | **Match** | | **G206** | **R.W.** | **S.W.** | **Match** | **G218** | **R.W.** | **S.W.** | **Match** | **G318** | **R.W.** | **S.W.** | **Match** | |
| TOTAL | 170.2 | 171.1 | 0.994 | | TOTAL | 170.2 | 171.0 | 0.995 | TOTAL | 170.2 | 171.0 | 0.995 | TOTAL | 170.2 | 171.1 | 0.995 | |
| OMR | 93.8 | 112.4 | 0.802 | | OMR | 93.8 | 90.9 | 0.969 | OMR | 93.8 | 92.3 | 0.984 | OMR | 93.8 | 87.5 | 0.933 | |
| SHC | 26.7 | 18.4 | 0.689 | | SHC | 26.7 | 28.5 | 0.933 | SHC | 26.7 | 27.0 | 0.990 | SHC | 26.7 | 23.3 | 0.871 | |
| LIST | 49.7 | 40.3 | 0.811 | | LIST | 49.7 | 51.6 | 0.960 | LIST | 49.7 | 51.7 | 0.958 | LIST | 49.7 | 60.3 | 0.785 | |
| AV. | | | 0.767 | | AV. | | | 0.954 | AV. | | | 0.978 | AV. | | | 0.863 | |
| | | | | | | | | | | | | | | | | | |
| **M22** | **R.W.** | **S.W.** | **Match** | | **M42** | **R.W.** | **S.W.** | **Match** | **M46** | **R.W.** | **S.W.** | **Match** | **M66** | **R.W.** | **S.W.** | **Match** | |
| TOTAL | 170.2 | 167.8 | 0.986 | | TOTAL | 170.2 | 171.0 | 0.995 | TOTAL | 170.2 | 171.1 | 0.995 | TOTAL | 170.2 | 171.1 | 0.995 | |
| OMR | 93.8 | 140.6 | 0.501 | | OMR | 93.8 | 106.6 | 0.864 | OMR | 93.8 | 87.5 | 0.933 | OMR | 93.8 | 43.7 | 0.466 | |
| SHC | 26.7 | 27.2 | 0.983 | | SHC | 26.7 | 21.7 | 0.812 | SHC | 26.7 | 19.8 | 0.741 | SHC | 26.7 | 25.1 | 0.941 | |
| LIST | 49.7 | 0.0 | 0.000 | | LIST | 49.7 | 42.7 | 0.860 | LIST | 49.7 | 63.8 | 0.715 | LIST | 49.7 | 102.2 | -0.059 | |
| AV. | | | 0.495 | | AV. | | | 0.845 | AV. | | | 0.796 | AV. | | | 0.449 | |
| | | | | | | | | | | | | | | | | | |
| **CE8** | **R.W.** | **S.W.** | **Match** | | **CE24** | **R.W.** | **S.W.** | **Match** | | | | | | | | | |
| TOTAL | 170.2 | 168.8 | 0.992 | | TOTAL | 170.2 | 171.8 | 0.990 | | | | | | | | | |
| OMR | 93.8 | 92.3 | 0.985 | | OMR | 93.8 | 92.3 | 0.984 | | | | | | | | | |
| SHC | 26.7 | 26.4 | 0.988 | | SHC | 26.7 | 27.1 | 0.986 | | | | | | | | | |
| LIST | 49.7 | 50.1 | 0.992 | | LIST | 49.7 | 52.3 | 0.946 | | | | | | | | | |
| AV. | | | 0.988 | | AV. | | | 0.972 | | | | | | | | | |
| | | | | | | | | | | | | | | | | | |
| **T0,01-0,05** | **R.W.** | **S.W.** | **Match** | | **T0,002-0,01** | **R.W.** | **S.W.** | **Match** | **T0,005-0,025** | **R.W.** | **S.W.** | **Match** | | | | | |
| TOTAL | 170.2 | 171.0 | 0.995 | | TOTAL | 170.2 | 171.1 | 0.995 | TOTAL | 170.2 | 171.1 | 0.994 | | | | | |
| OMR | 93.8 | 75.4 | 0.803 | | OMR | 93.8 | 108.9 | 0.839 | OMR | 93.8 | 93.7 | 0.999 | | | | | |
| SHC | 26.7 | 31.0 | 0.841 | | SHC | 26.7 | 16.1 | 0.601 | SHC | 26.7 | 21.9 | 0.820 | | | | | |
| LIST | 49.7 | 64.7 | 0.697 | | LIST | 49.7 | 46.1 | 0.928 | LIST | 49.7 | 55.6 | 0.881 | | | | | |
| AV. | | | 0.780 | | AV. | | | 0.789 | AV. | | | 0.900 | | | | | |

**Table A35** *Punctual matches for the simulations computed for well A5.*

| | (m) | (m) | | | (m) | (m) | | | | | | | | | | |
|---|---|---|---|---|---|---|---|---|---|---|---|---|---|---|---|---|
| **REF** | **R.W.** | **S.W.** | **Match** | **SD** | **R.W.** | **S.W.** | **Match** | | | | | | | | | |
| TOTAL | 178.7 | 170.0 | 0.951 | TOTAL | 178.7 | 175.4 | 0.981 | | | | | | | | | |
| OMR | 88.9 | 81.1 | 0.912 | OMR | 88.9 | 85.8 | 0.965 | | | | | | | | | |
| SHC | 30.5 | 31.4 | 0.967 | SHC | 30.5 | 34.7 | 0.860 | | | | | | | | | |
| LIST | 59.3 | 57.4 | 0.968 | LIST | 59.3 | 54.8 | 0.924 | | | | | | | | | |
| AV. | | | 0.949 | AV. | | | 0.916 | | | | | | | | | |
| | | | | | | | | | (m) | (m) | | | | (m) | (m) | |
| **S0** | **R.W.** | **S.W.** | **Match** | **S12** | **R.W.** | **S.W.** | **Match** | **S14** | **R.W.** | **S.W.** | **Match** | **S26** | **R.W.** | **S.W.** | **Match** | |
| TOTAL | 178.7 | 187.1 | 0.953 | TOTAL | 178.7 | 171.4 | 0.959 | TOTAL | 178.7 | 173.2 | 0.969 | TOTAL | 178.7 | 161.3 | 0.902 | |
| OMR | 88.9 | 121.4 | 0.635 | OMR | 88.9 | 90.8 | 0.979 | OMR | 88.9 | 86.3 | 0.970 | OMR | 88.9 | 63.5 | 0.714 | |
| SHC | 30.5 | 24.0 | 0.789 | SHC | 30.5 | 34.6 | 0.863 | SHC | 30.5 | 28.7 | 0.943 | SHC | 30.5 | 27.5 | 0.903 | |
| LIST | 59.3 | 41.7 | 0.703 | LIST | 59.3 | 45.9 | 0.774 | LIST | 59.3 | 58.2 | 0.980 | LIST | 59.3 | 70.3 | 0.816 | |
| AV. | | | 0.709 | AV. | | | 0.872 | AV. | | | 0.964 | AV. | | | 0.811 | |
| | | | | | | | | | | | | | | | | |
| **G106** | **R.W.** | **S.W.** | **Match** | **G206** | **R.W.** | **S.W.** | **Match** | **G218** | **R.W.** | **S.W.** | **Match** | **G318** | **R.W.** | **S.W.** | **Match** | |
| TOTAL | 178.7 | 169.4 | 0.948 | TOTAL | 178.7 | 175.0 | 0.979 | TOTAL | 178.7 | 173.2 | 0.969 | TOTAL | 178.7 | 173.2 | 0.969 | |
| OMR | 88.9 | 101.2 | 0.862 | OMR | 88.9 | 86.2 | 0.970 | OMR | 88.9 | 86.3 | 0.971 | OMR | 88.9 | 81.0 | 0.911 | |
| SHC | 30.5 | 21.9 | 0.720 | SHC | 30.5 | 28.8 | 0.947 | SHC | 30.5 | 28.6 | 0.940 | SHC | 30.5 | 32.6 | 0.930 | |
| LIST | 59.3 | 46.3 | 0.781 | LIST | 59.3 | 59.9 | 0.990 | LIST | 59.3 | 58.2 | 0.981 | LIST | 59.3 | 59.6 | 0.996 | |
| AV. | | | 0.788 | AV. | | | 0.969 | AV. | | | 0.964 | AV. | | | 0.946 | |
| | | | | | | | | | | | | | | | | |
| **M22** | **R.W.** | **S.W.** | **Match** | **M42** | **R.W.** | **S.W.** | **Match** | **M46** | **R.W.** | **S.W.** | **Match** | **M66** | **R.W.** | **S.W.** | **Match** | |
| TOTAL | 178.7 | 136.2 | 0.762 | TOTAL | 178.7 | 169.9 | 0.950 | TOTAL | 178.7 | 175.5 | 0.982 | TOTAL | 178.7 | 172.9 | 0.967 | |
| OMR | 88.9 | 136.2 | 0.468 | OMR | 88.9 | 95.1 | 0.931 | OMR | 88.9 | 81.2 | 0.913 | OMR | 88.9 | 49.2 | 0.554 | |
| SHC | 30.5 | 0.0 | 0.000 | SHC | 30.5 | 29.0 | 0.951 | SHC | 30.5 | 25.7 | 0.845 | SHC | 30.5 | 16.5 | 0.541 | |
| LIST | 59.3 | 0.0 | 0.000 | LIST | 59.3 | 45.8 | 0.771 | LIST | 59.3 | 68.6 | 0.844 | LIST | 59.3 | 107.2 | 0.194 | |
| AV. | | | 0.156 | AV. | | | 0.884 | AV. | | | 0.867 | AV. | | | 0.430 | |
| | | | | | | | | | | | | | | | | |
| **CE8** | **R.W.** | **S.W.** | **Match** | **CE24** | **R.W.** | **S.W.** | **Match** | | | | | | | | | |
| TOTAL | 178.7 | 173.5 | 0.971 | TOTAL | 178.7 | 155.7 | 0.871 | | | | | | | | | |
| OMR | 88.9 | 86.3 | 0.971 | OMR | 88.9 | 86.3 | 0.971 | | | | | | | | | |
| SHC | 30.5 | 32.8 | 0.924 | SHC | 30.5 | 29.0 | 0.952 | | | | | | | | | |
| LIST | 59.3 | 54.4 | 0.916 | LIST | 59.3 | 40.4 | 0.681 | | | | | | | | | |
| AV. | | | 0.937 | AV. | | | 0.868 | | | | | | | | | |
| | | | | | | | | | | | | | | | | |
| **T0,01-0,05** | **R.W.** | **S.W.** | **Match** | **T0,002-0,01** | **R.W.** | **S.W.** | **Match** | **T0,005-0,025** | **R.W.** | **S.W.** | **Match** | | | | | |
| TOTAL | 178.7 | 173.3 | 0.970 | TOTAL | 178.7 | 174.8 | 0.978 | TOTAL | 178.7 | 173.3 | 0.970 | | | | | |
| OMR | 88.9 | 83.1 | 0.934 | OMR | 88.9 | 86.3 | 0.971 | OMR | 88.9 | 87.2 | 0.981 | | | | | |
| SHC | 30.5 | 30.8 | 0.988 | SHC | 30.5 | 28.8 | 0.947 | SHC | 30.5 | 26.0 | 0.855 | | | | | |
| LIST | 59.3 | 59.5 | 0.998 | LIST | 59.3 | 59.6 | 0.995 | LIST | 59.3 | 60.1 | 0.988 | | | | | |
| AV. | | | 0.973 | AV. | | | 0.971 | AV. | | | 0.941 | | | | | |

**Table A36** *Matches for the total thicknesses of the evaporitic deposits between real and simulated wells.*

| **CE8** | **R.W.** | **S.W.** | **Match** | **CE24** | **R.W.** | **S.W.** | **Match** | **E500** | **R.W.** | **S.W.** | **Match** | **E2500** | **R.W.** | **S.W.** | **Match** | **G218** | **R.W.** | **S.W.** | **Match** |
|---|---|---|---|---|---|---|---|---|---|---|---|---|---|---|---|---|---|---|---|
| A1 | 30.4 | 2.3 | 0.074 | A1 | 30.4 | 43.4 | 0.573 | A1 | 30.4 | 8.7 | 0.286 | A1 | 30.4 | 38.8 | 0.724 | A1 | 30.4 | 25.4 | 0.833 |
| A2 | 34.4 | 1.6 | 0.046 | A2 | 34.4 | 48.0 | 0.605 | A2 | 34.4 | 9.1 | 0.265 | A2 | 34.4 | 44.8 | 0.695 | A2 | 34.4 | 28.9 | 0.840 |
| A3 | 23.5 | 7.1 | 0.302 | A3 | 23.5 | 48.1 | -0.047 | A3 | 23.5 | 8.5 | 0.360 | A3 | 23.5 | 43.9 | 0.130 | A3 | 23.5 | 32.4 | 0.622 |
| A4 | 14.6 | 14.4 | 0.982 | A4 | 14.6 | 41.3 | -0.822 | A4 | 14.6 | 12.7 | 0.865 | A4 | 14.6 | 39.1 | -0.676 | A4 | 14.6 | 30.5 | -0.088 |
| A5 | 22.6 | 8.3 | 0.368 | A5 | 22.6 | 7.3 | 0.322 | A5 | 22.6 | 4.0 | 0.176 | A5 | 22.6 | 26.1 | 0.842 | A5 | 22.6 | 21.4 | 0.947 |
| AV. | 25.1 | 6.7 | 0.268 | AV. | 25.1 | 37.5 | 0.505 | AV. | 25.1 | 10.6 | 0.421 | AV. | 25.1 | 38.6 | 0.463 | AV. | 25.1 | 27.5 | 0.904 |

**Table A37** *Averages for each macro environment between the five wells and the TOT value.*

| **REF** | **av. match** | **SD** | **av. match** | | | | | |
|---|---|---|---|---|---|---|---|---|
| OMR | 0,855 | OMR | 0,940 | | | | | |
| SHC | 0,804 | SHC | 0,694 | | | | | |
| LIST | 0,824 | LIST | 0,908 | | | | | |
| TOT | 0,828 | TOT | 0,848 | | | | | |
| | | | | | | | | |
| **S0** | **av. match** | **S12** | **av. match** | **S14** | **av. match** | | **S26** | **av. match** |
| OMR | 0,608 | OMR | 0,953 | OMR | 0,928 | | OMR | 0,704 |
| SHC | 0,734 | SHC | 0,820 | SHC | 0,818 | | SHC | 0,745 |
| LIST | 0,694 | LIST | 0,872 | LIST | 0,925 | | LIST | 0,737 |
| TOT | 0,679 | TOT | 0,882 | TOT | 0,890 | | TOT | 0,729 |
| | | | | | | | | |
| **G106** | **av. match** | **G206** | **av. match** | **G218** | **av. match** | | **G318** | **av. match** |
| OMR | 0,854 | OMR | 0,928 | OMR | 0,928 | | OMR | 0,925 |
| SHC | 0,721 | SHC | 0,808 | SHC | 0,851 | | SHC | 0,798 |
| LIST | 0,848 | LIST | 0,931 | LIST | 0,933 | | LIST | 0,912 |
| TOT | 0,808 | TOT | 0,889 | TOT | 0,904 | | TOT | 0,878 |
| | | | | | | | | |
| **M22** | **av. match** | **M42** | **av. match** | **M46** | **av. match** | | **M66** | **av. match** |
| OMR | 0,530 | OMR | 0,904 | OMR | 0,884 | | OMR | 0,455 |
| SHC | 0,197 | SHC | 0,873 | SHC | 0,879 | | SHC | 0,809 |
| LIST | 0,000 | LIST | 0,840 | LIST | 0,812 | | LIST | 0,142 |
| TOT | 0,242 | TOT | 0,872 | TOT | 0,858 | | TOT | 0,469 |
| | | | | | | | | |
| **CE8** | **av. match** | **CE24** | **av. match** | **E500** | **av. match** | | **E2500** | **av. match** |
| OMR | 0,928 | OMR | 0,928 | OMR | 0,928 | | OMR | 0,928 |
| SHC | 0,846 | SHC | 0,854 | SHC | 0,851 | | SHC | 0,851 |
| LIST | 0,926 | LIST | 0,875 | LIST | 0,933 | | LIST | 0,933 |
| TOT | 0,900 | TOT | 0,886 | TOT | 0,904 | | TOT | 0,904 |
| | | | | | | | | |
| **T0,0,1-0,05** | **av. match** | **T0,002-0,01** | **av. match** | **T0,005-0,025** | **av. match** | | | |
| OMR | 0,907 | OMR | 0,905 | OMR | 0,946 | | | |
| SHC | 0,763 | SHC | 0,759 | SHC | 0,799 | | | |
| LIST | 0,813 | LIST | 0,913 | LIST | 0,888 | | | |
| TOT | 0,828 | TOT | 0,859 | TOT | 0,878 | | | |

# APPENDIX 4 - 3D FORWARD MODELLING

Twenty-one 3D stratigraphic forward models were obtained and analyzed during the Ph.D., in order to evaluate the parameters that impact on the deposition of the Arab Formation. In this section, nineteen of these models are represented in the figures, reporting the main input data, the 3D geological simulation according to the bathymetry distribution, a cross section encompassing the available wells and displaying the distribution of the simulated facies (SF), and a series of maps at different time steps, that compare bathymetry and simulated facies outputs. For the code of the models refer to Table 4.3 in Chapter 4 (reported also in Appendix 3). The two missing models (REF and SD) are pictured in Figure 4.3, 4.4, 4.6 and 4.9 in Chapter 4 of the thesis. The models (and the related cross-sections) are cut of 10 km in width and length at each side, in order to avoid representing possible boundary effects. The letter *K* represents the gravity-driven diffusion coefficient.

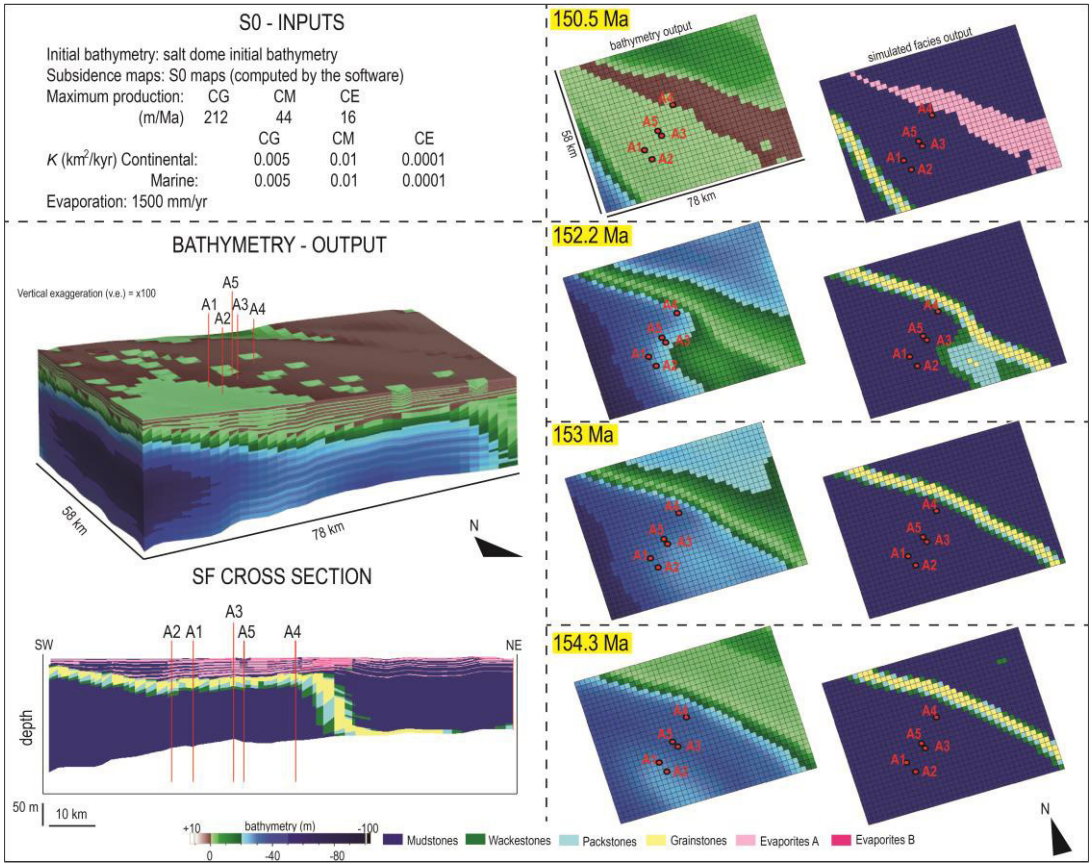


**Figure A41** *S0 model.*

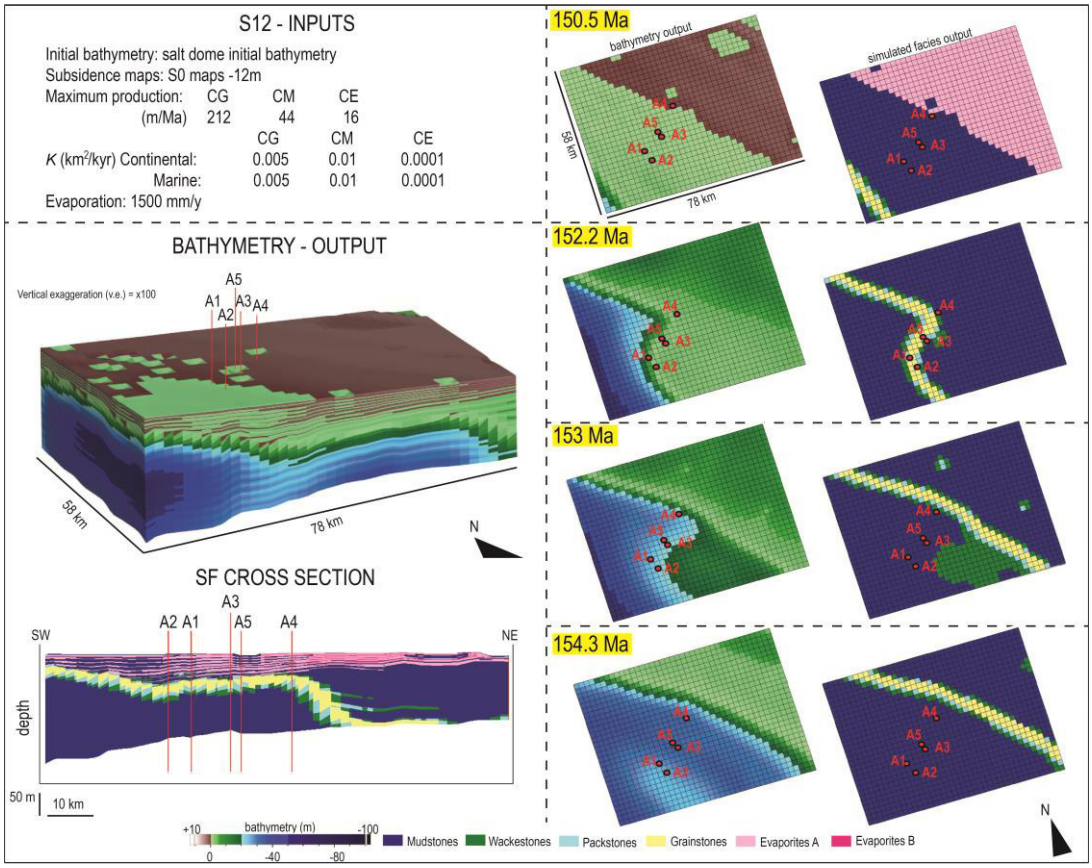


**Figure A42** *S12 model.*

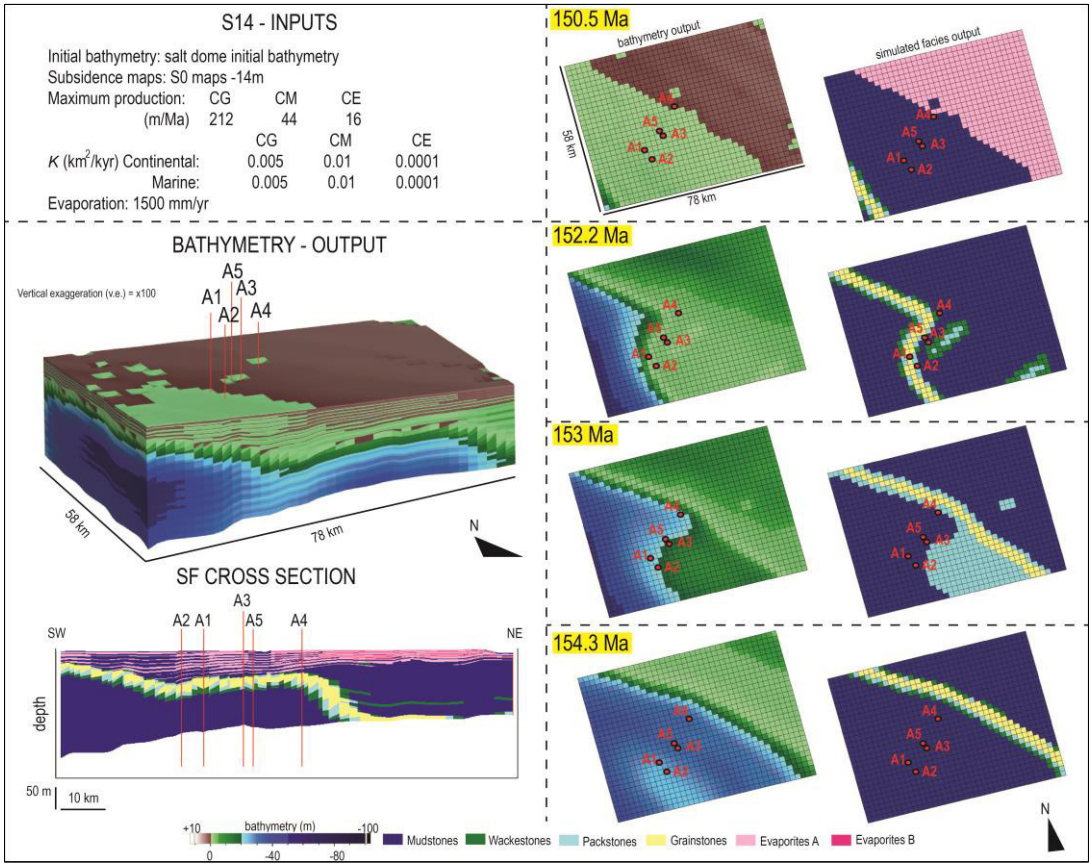


**Figure A43** *S14 model.*

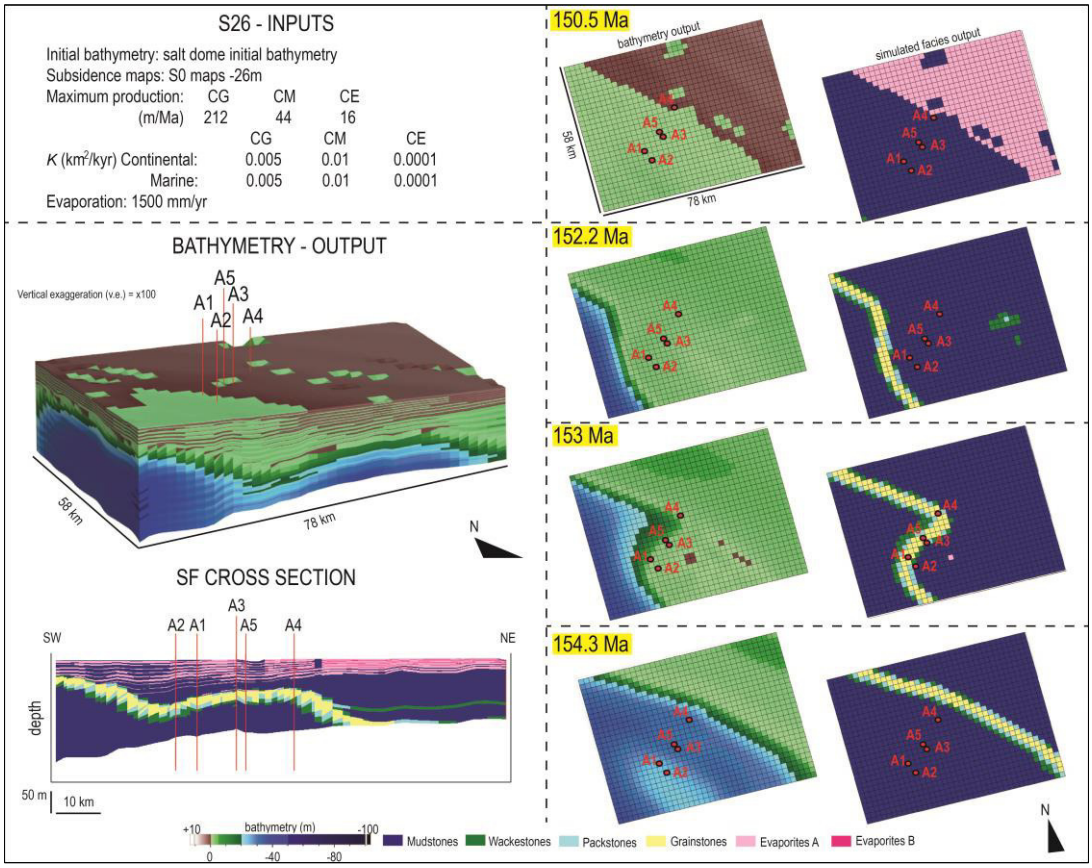


**Figure A44** *S26 model.*

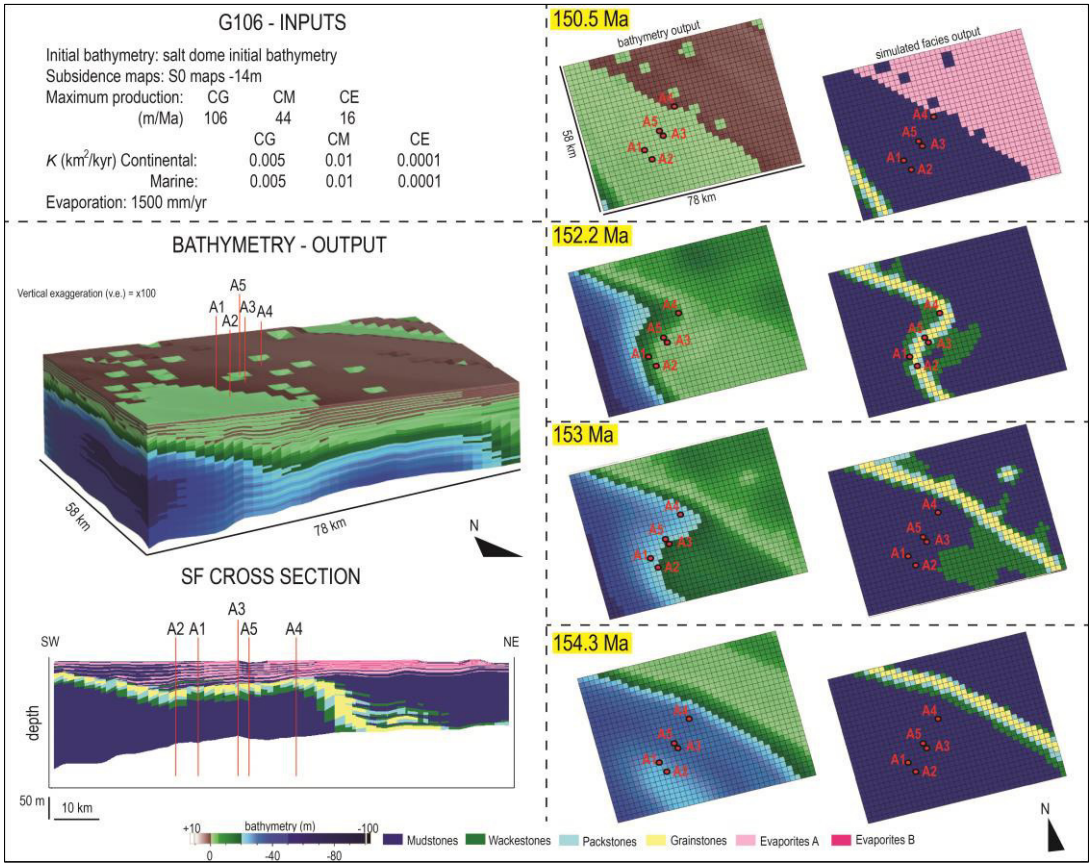


**Figure A45** *G106 model.*

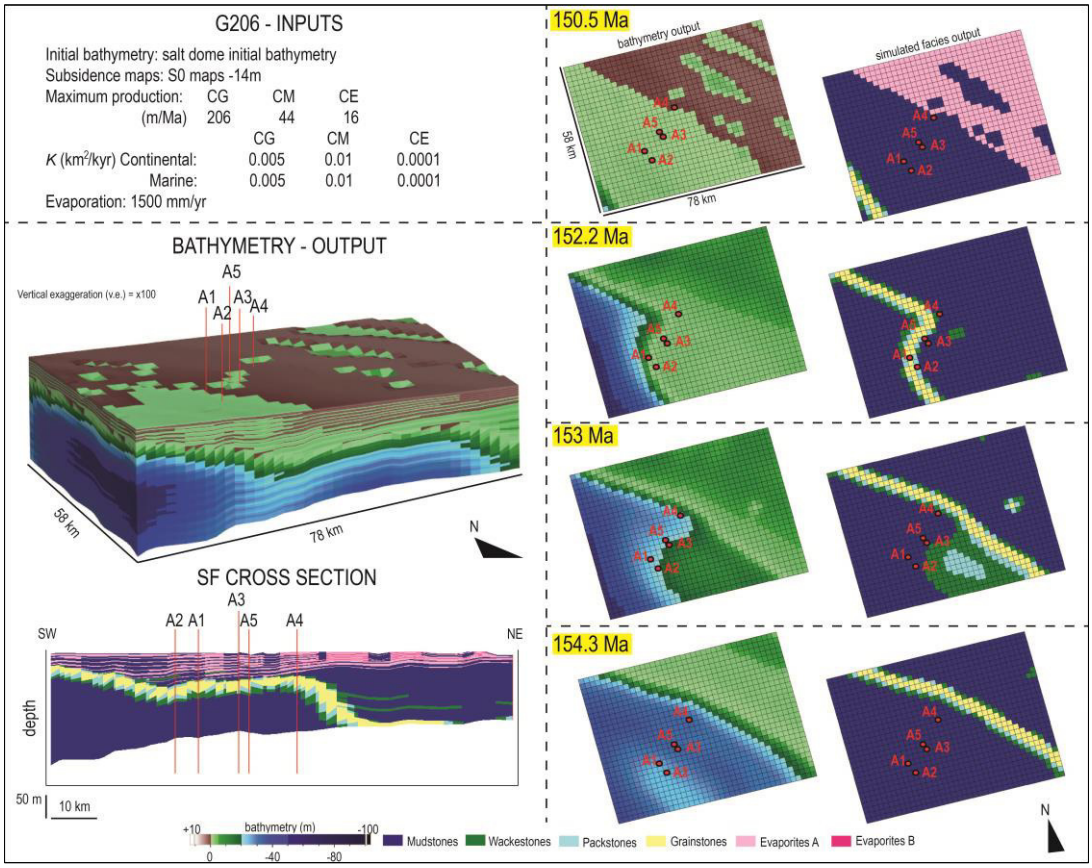


**Figure A46** *G206 model.*

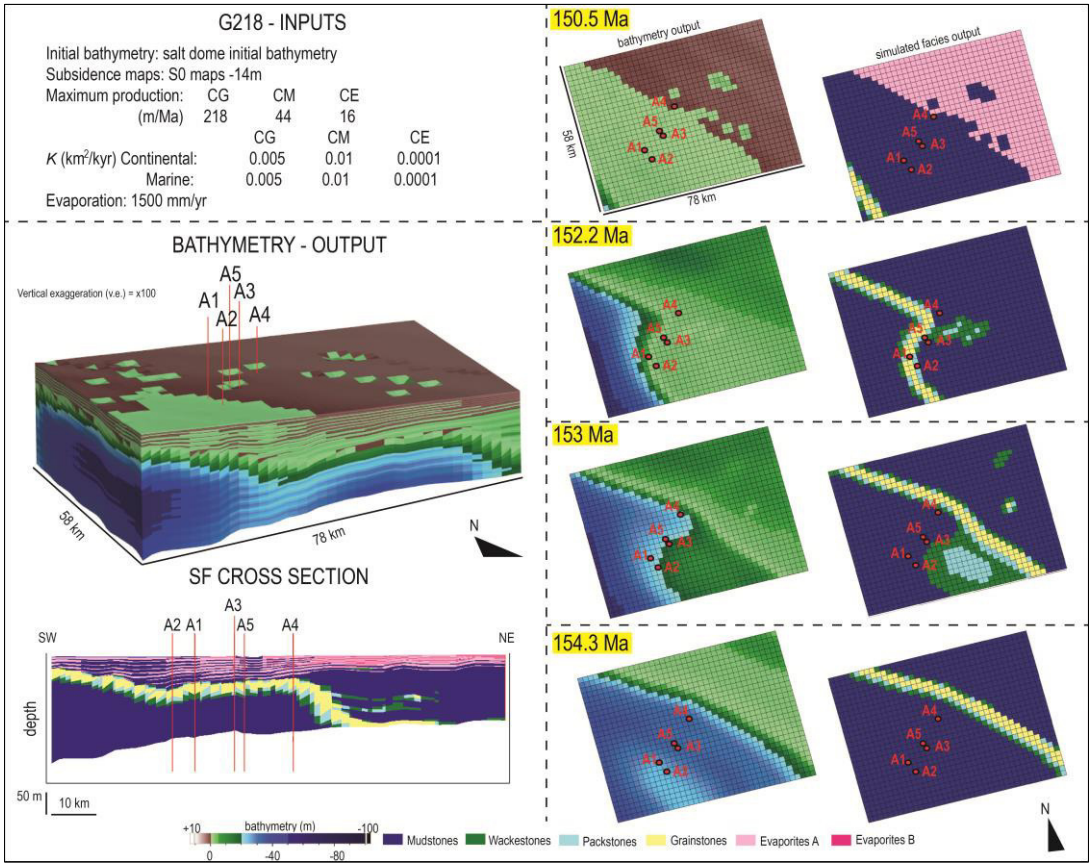


**Figure A47** *G218 model.*

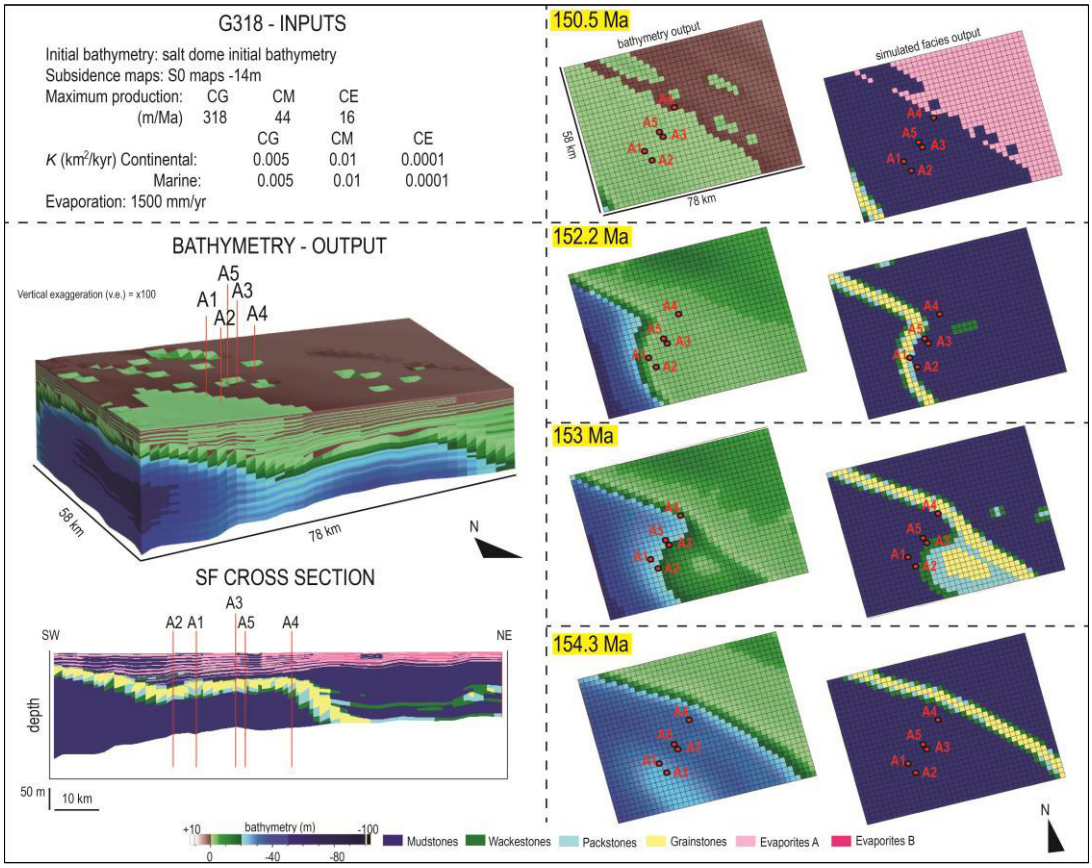


**Figure A48** *G318 model.*

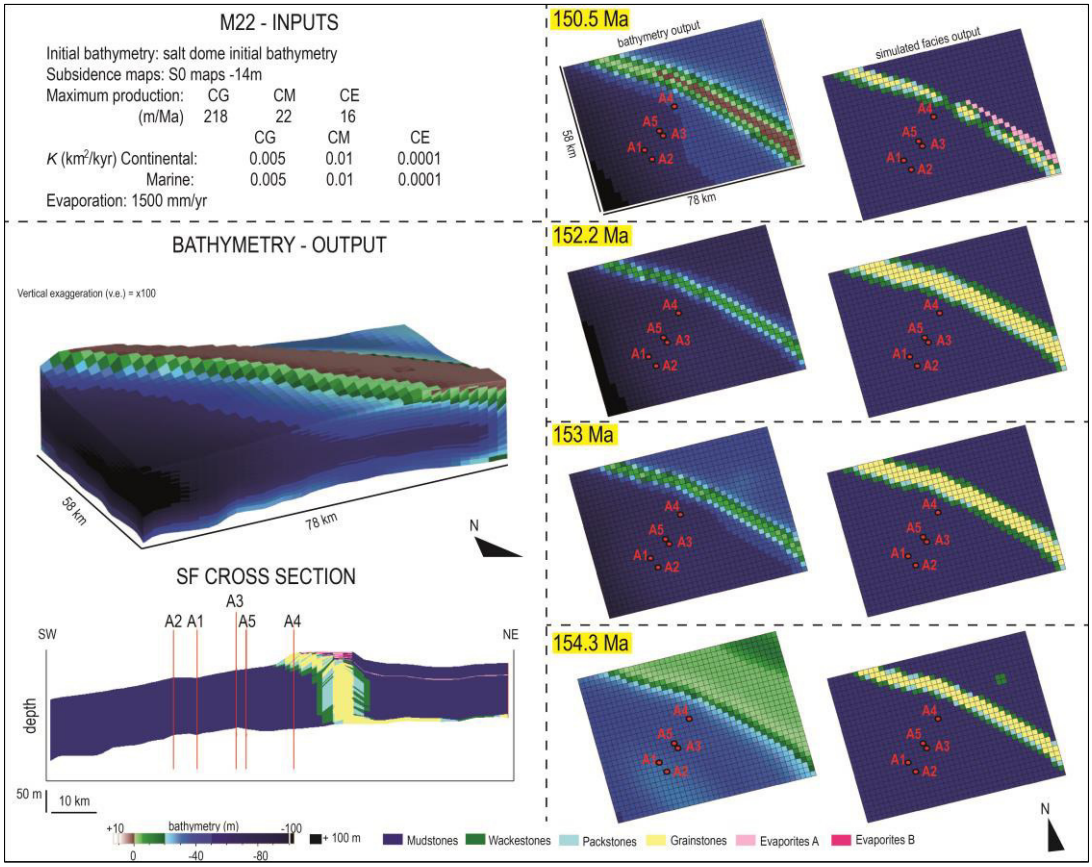


**Figure A49** *M22 model.*

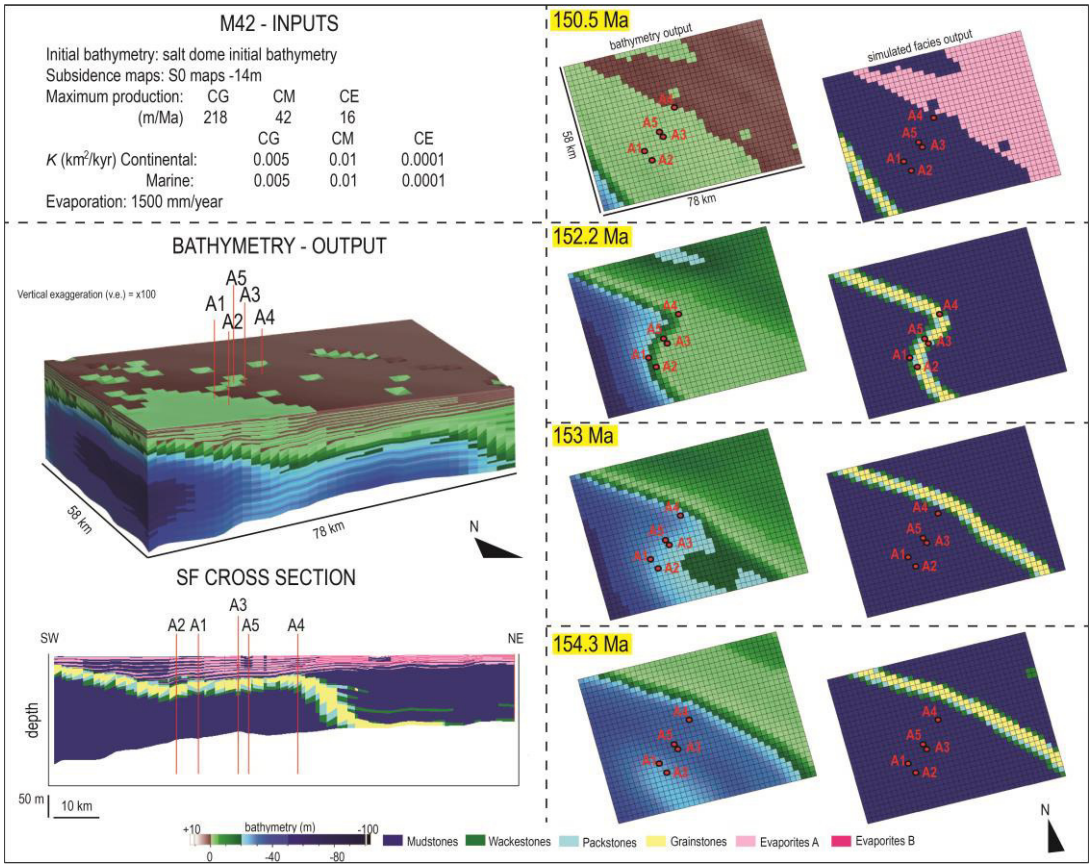


**Figure A410** *M42 model.*

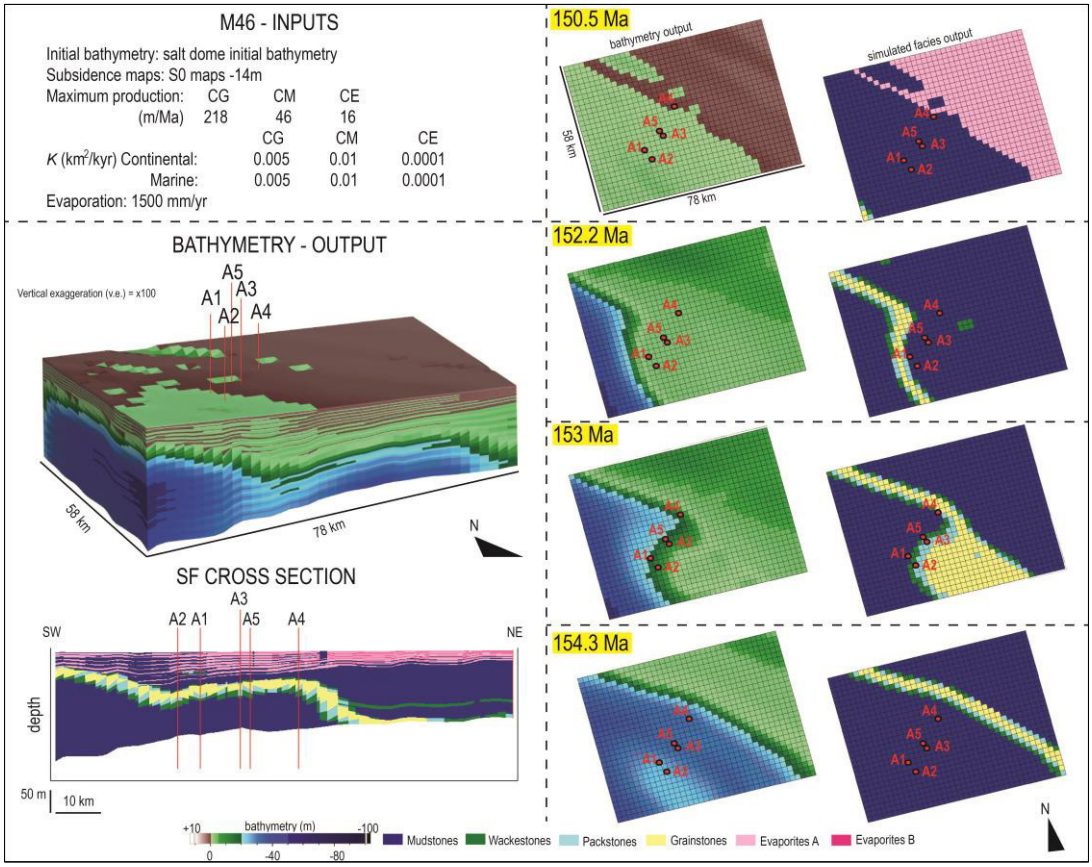


**Figure A411** *M46 model.*

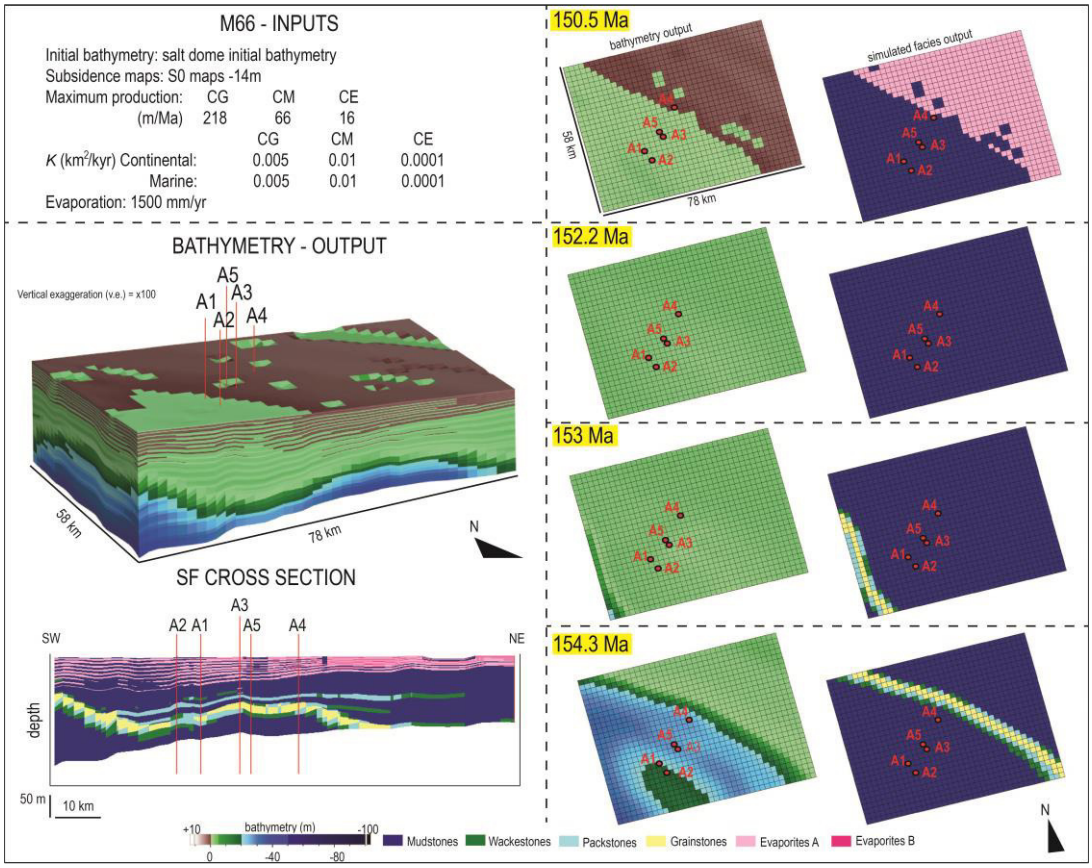


**Figure A412** *M66 model.*

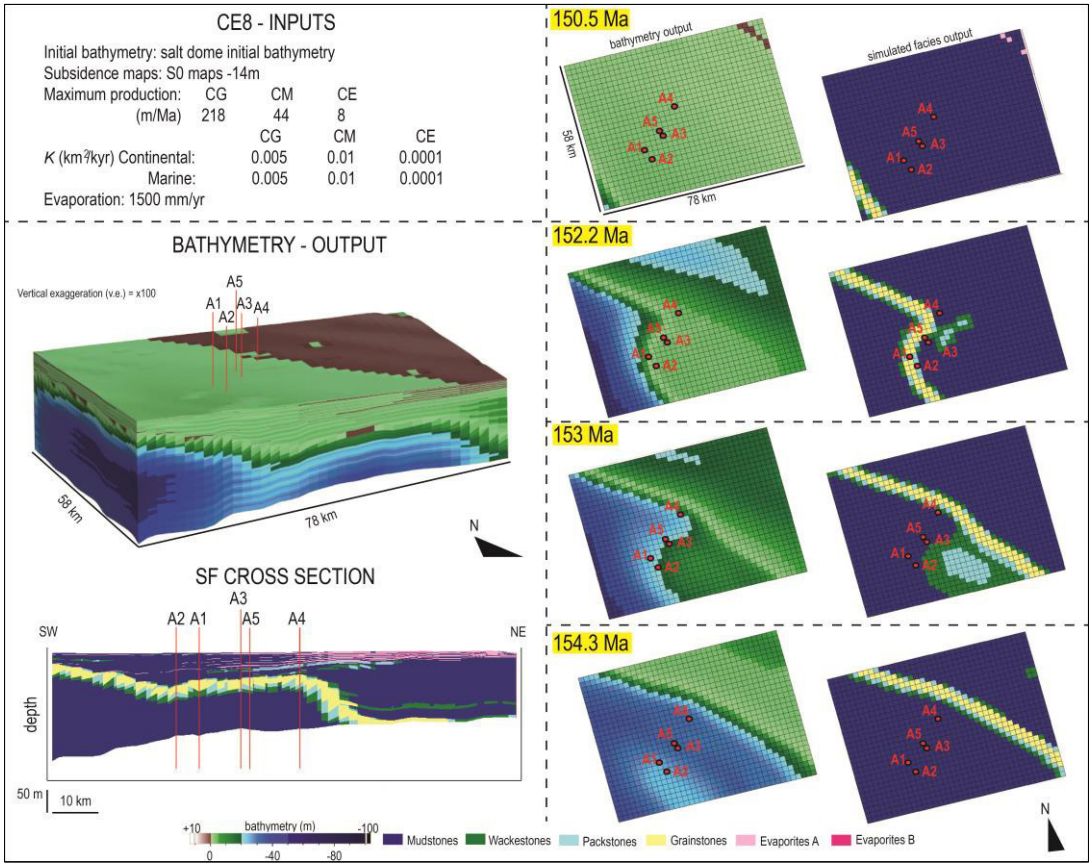


**Figure A413** *CE8 model.*

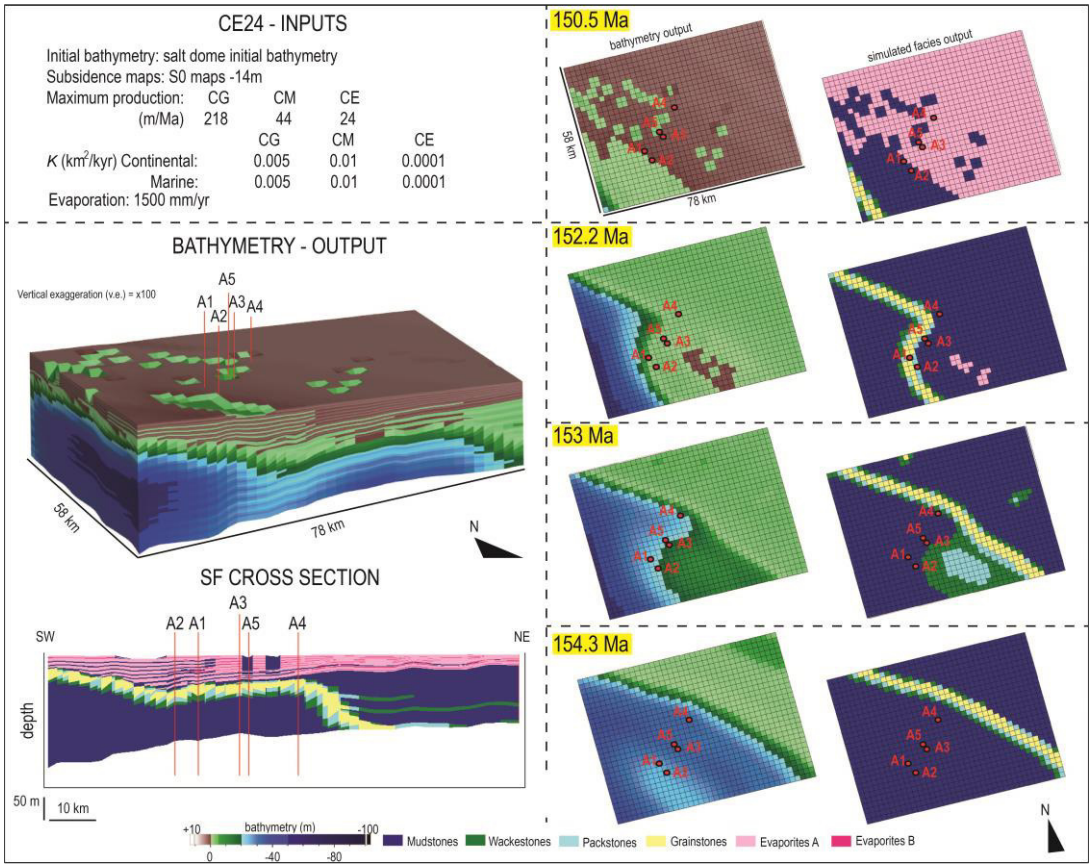


**Figure A414** *CE24 model.*

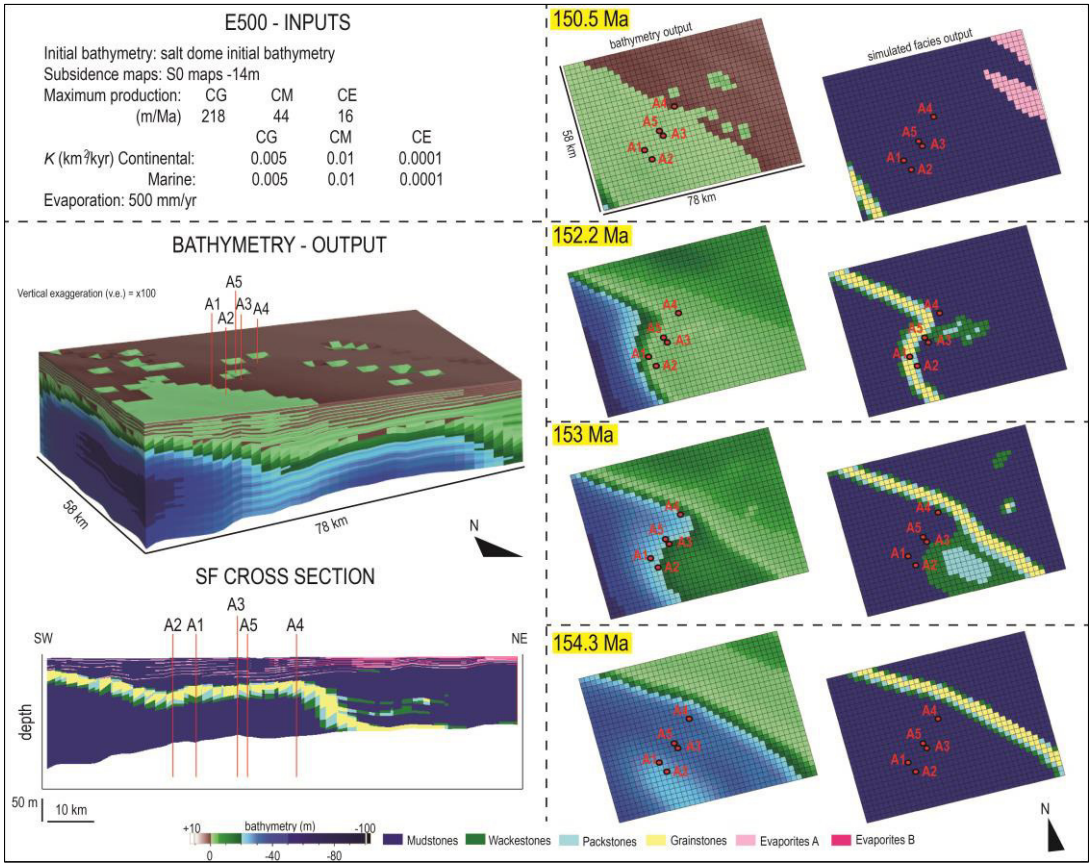


**Figure 415** *E500 model.*

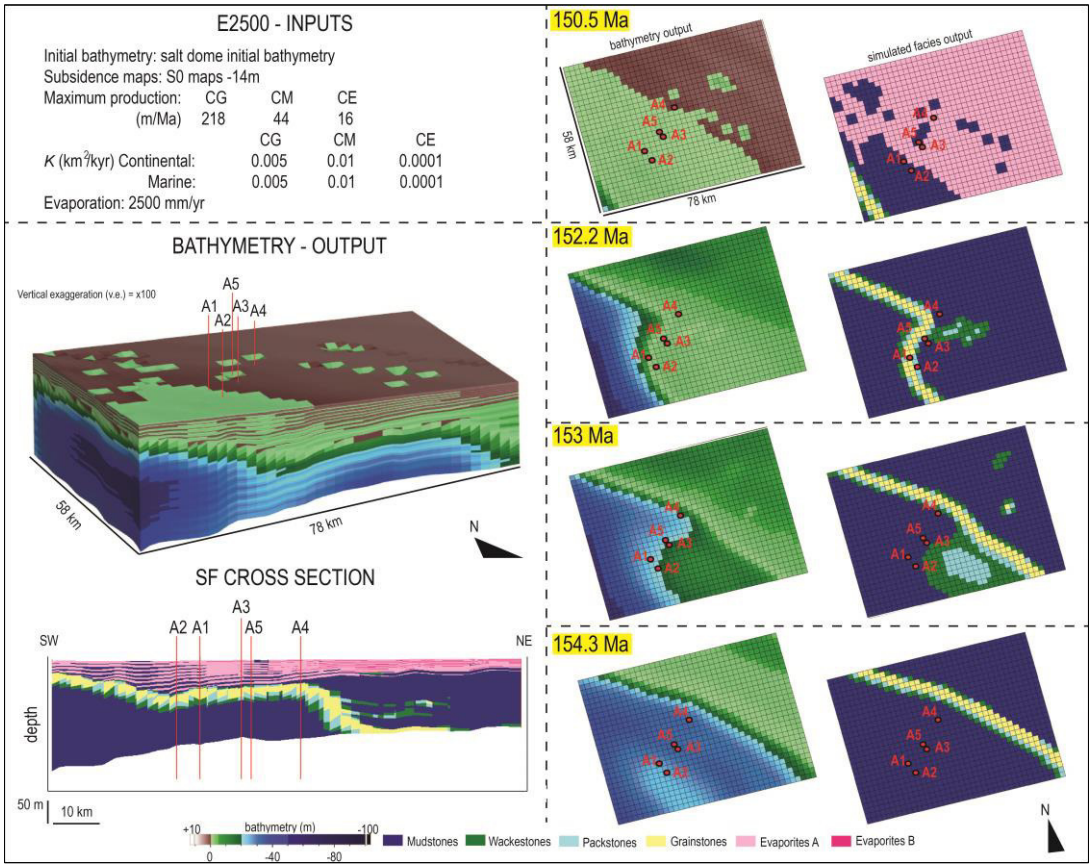


**Figure A416** *E2500 model.*

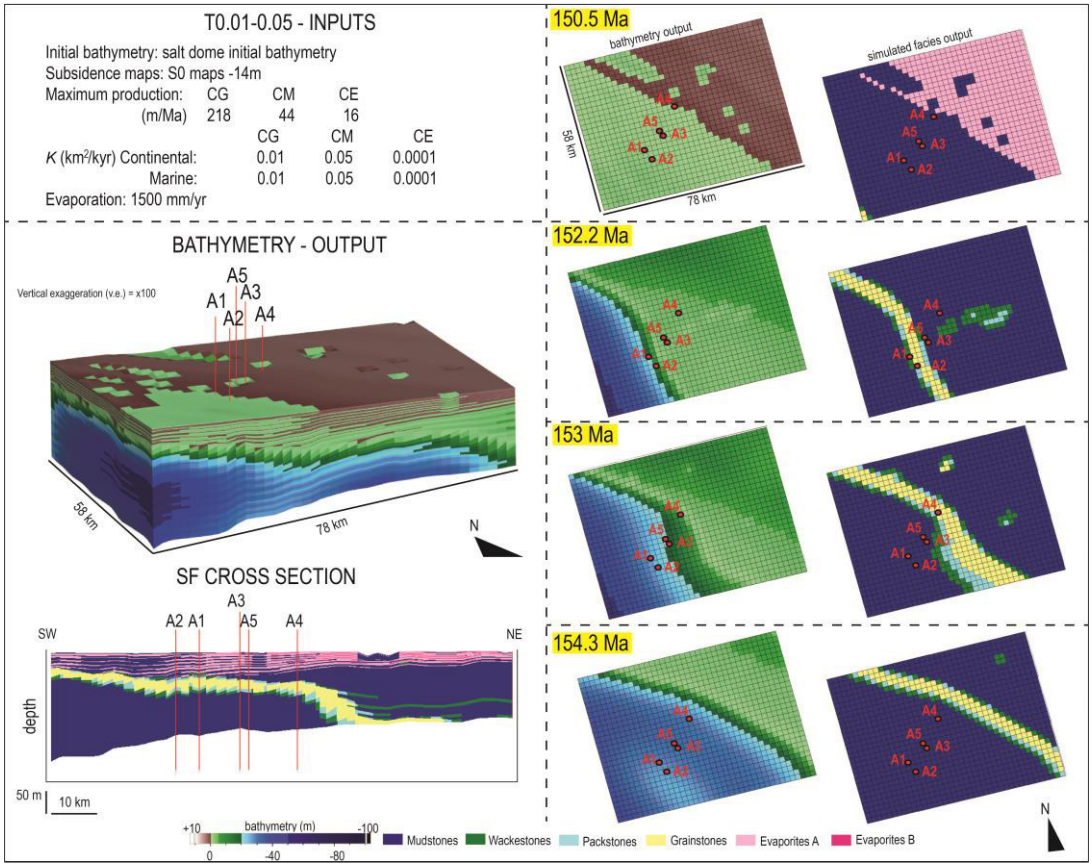


**Figure A417** *T0.01-0.05 model.*

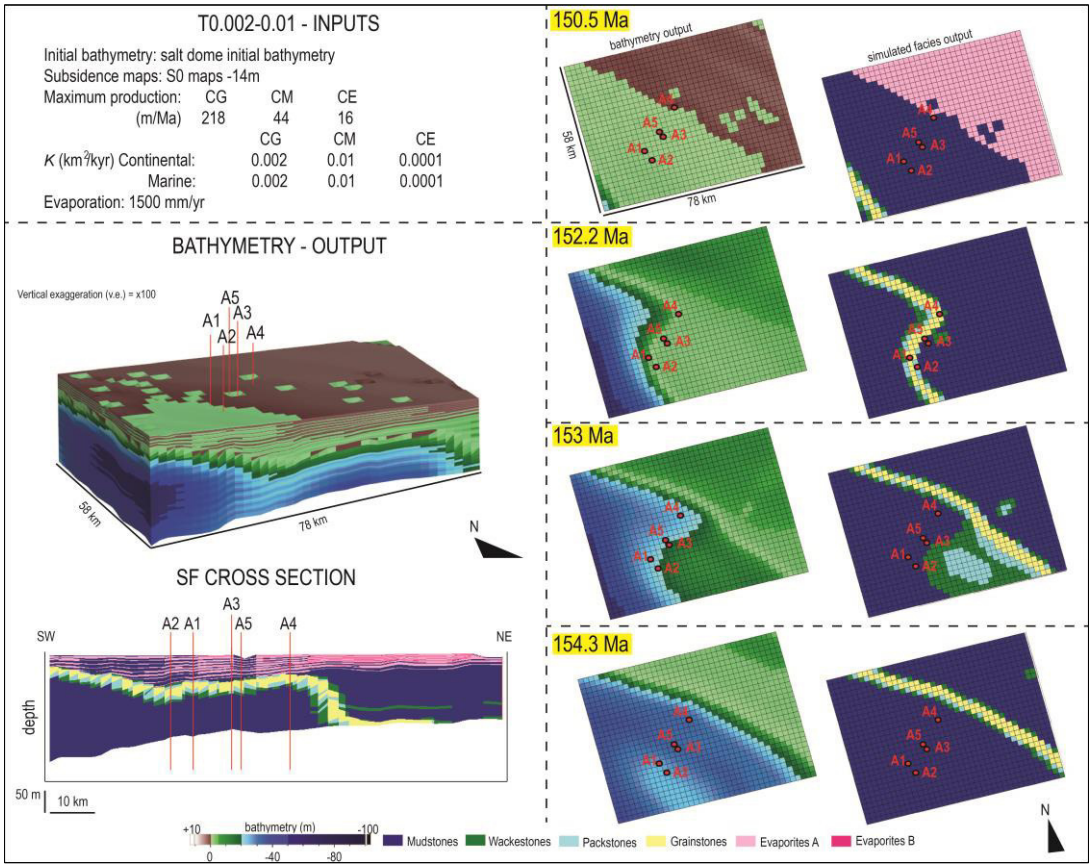


**Figure A418** *T0.002-0.01 model.*

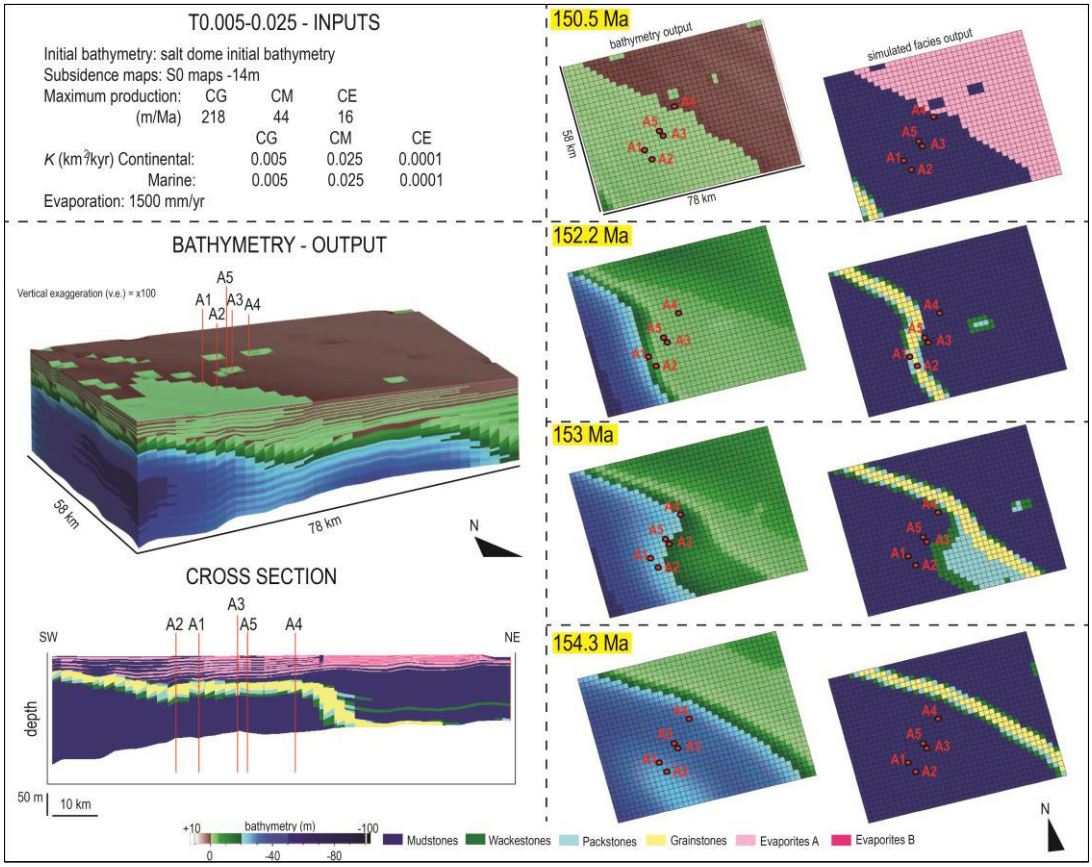


**Figure A419** *T0.005-0.025 model.*